JAAVSO

Volume 49
Number 1
2021

The Journal of the American Association of Variable Star Observers

A Spectroscopic Study of T Cen, and the Effects of TiO on Its Atmosphere

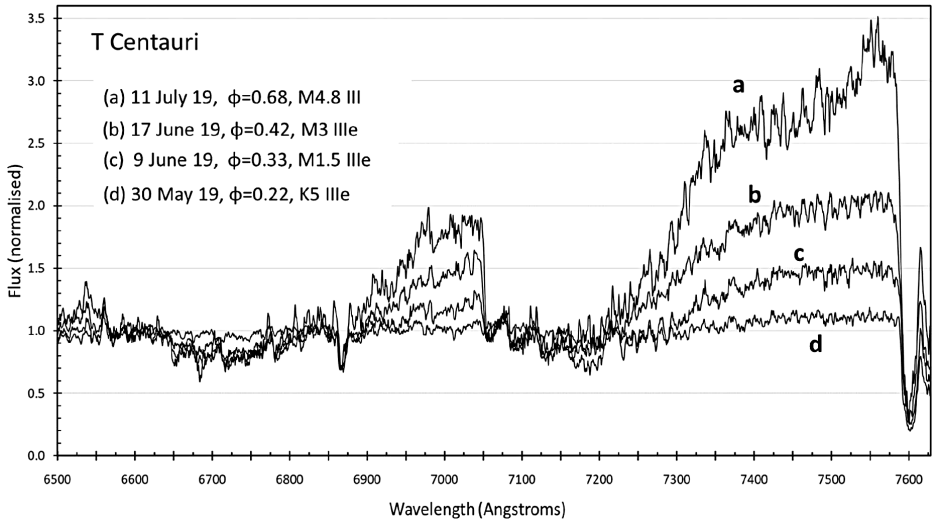

Example captured spectra, normalized at λ 6610; the legend shows phase and spectral type, illustrating both maximum light in May 2019 and minimum light in July 2019.

Also in this issue...

The American Association of Variable Star Observers
49 Bay State Road, Cambridge, MA 02138, USA

The Journal of the American Association of Variable Star Observers

The Board of the American Association of Variable Star Observers 2020–2021

ISSN 0271-9053 (print journal)
ISSN 2380-3606 (online journal)
ISSN 2768-5225 (print abstracts)
ISSN 2768-5233 (online abstracts)

JAAVSO

The Journal of
The American Association
of Variable Star Observers

Volume 49
Number 1
2021

ISSN 0271-9053 (print journal)
ISSN 2380-3606 (online journal)
ISSN 2768-5225 (print abstracts)
ISSN 2768-5233 (online abstracts)

AAVSO
49 Bay State Road
Cambridge, MA 02138
USA

Publication Schedule

The Journal of the American Association of Variable Star Observers is published twice a year, June 15 (Number 1 of the volume) and December 15 (Number 2 of the volume). The submission window for inclusion in the next issue of JAAVSO closes six weeks before the publication date. A manuscript will be added to the table of contents for an issue when it has been fully accepted for publication upon successful completion of the referee process; these articles will be available online prior to the publication date. An author may not specify in which issue of JAAVSO a manuscript is to be published; accepted manuscripts will be published in the next available issue, except under extraordinary circumstances.

Page Charges

Page charges are waived for Members of the AAVSO. Publication of unsolicited manuscripts in JAAVSO requires a page charge of US $100/page for the final printed manuscript. Page charge waivers may be provided under certain circumstances.

Publication in *JAAVSO*

With the exception of abstracts of papers presented at AAVSO meetings, papers submitted to JAAVSO are peer-reviewed by individuals knowledgeable about the topic being discussed. We cannot guarantee that all submissions to JAAVSO will be published, but we encourage authors of all experience levels and in all fields related to variable star astronomy and the AAVSO to submit manuscripts. We especially encourage students and other mentees of researchers affiliated with the AAVSO to submit results of their completed research.

Subscriptions

Institutions and Libraries may subscribe to JAAVSO as part of the Complete Publications Package or as an individual subscription. Individuals may purchase printed copies of recent JAAVSO issues via Createspace. Paper copies of JAAVSO issues prior to volume 36 are available in limited quantities directly from AAVSO Headquarters; please contact the AAVSO for available issues.

Instructions for Submissions

The *Journal of the AAVSO* welcomes papers from all persons concerned with the study of variable stars and topics specifically related to variability. All manuscripts should be written in a style designed to provide clear expositions of the topic. Contributors are encouraged to submit digitized text in MS WORD, LATEX+POSTSCRIPT, or plain-text format. Manuscripts should be submitted through the JAAVSO submission portal (https://www.aavso.org/apps/jaavso/submit/) or may be mailed electronically to journal@aavso.org or submitted by postal mail to JAAVSO, 49 Bay State Road, Cambridge, MA 02138, USA.

Manuscripts must be submitted according to the following guidelines, or they will be returned to the author for correction:

Manuscripts must be:
1) original, unpublished material;
2) written in English;
3) accompanied by an abstract of no more than 100 words.
4) not more than 2,500–3,000 words in length (10–12 pages double-spaced).

Figures for publication must:
1) be camera-ready or in a high-contrast, high-resolution, standard digitized image format;
2) have all coordinates labeled with division marks on all four sides;
3) be accompanied by a caption that clearly explains all symbols and significance, so that the reader can understand the figure without reference to the text.

Maximum published figure space is 4.5″ by 7″. When submitting original figures, be sure to allow for reduction in size by making all symbols, letters, and division marks sufficiently large.

Photographs and halftone images will be considered for publication if they directly illustrate the text.

Tables should be:
1) provided separate from the main body of the text;
2) numbered sequentially and referred to by Arabic number in the text, e.g., Table 1.

References:
1) References should relate directly to the text.
2) References should be keyed into the text with the author's last name and the year of publication, e.g., (Smith 1974; Jones 1974) or Smith (1974) and Jones (1974).
3) In the case of three or more joint authors, the text reference should be written as follows: (Smith et al. 1976).
4) All references must be listed at the end of the text in alphabetical order by the author's last name and the year of publication, according to the following format: Brown, J., and Green, E. B. 1974, *Astrophys. J.*, **200**, 765.
Thomas, K. 1982, *Phys. Rep.*, **33**, 96.
5) Abbreviations used in references should be based on recent issues of JAAVSO or the listing provided at the beginning of *Astronomy and Astrophysics Abstracts* (Springer-Verlag).

Miscellaneous:
1) Equations should be written on a separate line and given a sequential Arabic number in parentheses near the right-hand margin. Equations should be referred to in the text as, e.g., equation (1).
2) Magnitude will be assumed to be visual unless otherwise specified.
3) Manuscripts may be submitted to referees for review without obligation of publication.

Online Access

Articles published in JAAVSO, and information for authors and referees may be found online at: https://www.aavso.org/apps/jaavso/

The Journal of the American Association of Variable Star Observers
Volume 49, Number 1, 2021

Editorial

Variable Star Research

Education and Outreach

Table of Contents continued on following pages

Variable Star Data

Abstracts of Papers and Posters Presented at the 109th Annual Meeting of the AAVSO, Held as an "Online Only" Event, November 13–15, 2020

Table of Contents continued on next page

Editorial

Conference Proceedings of the AAVSO

Nancy D. Morrison
Editor-in-Chief, *Journal of the AAVSO*

Department of Physics and Astronomy and Ritter Observatory, MS 113, The University of Toledo, 2801 W. Bancroft Street, Toledo OH 43606; jaavso.editor@aavso.org

Received June 8, 2021

With the 110th meeting in November 2021, the AAVSO is pleased to launch a series of conference proceedings, tentatively entitled *Conference Proceedings of the AAVSO*. It will be an electronic publication that will be separate from *JAAVSO*.

Those who would like to make an oral presentation at the meeting are invited, as usual, to submit abstracts; see https://www.aavso.org/110-annual-meeting-oral-abstracts. Abstracts will be published in a companion publication to the *Proceedings*, no longer in *JAAVSO*. If a submitted abstract is accepted, the author will be invited— but not required—to submit a full paper to be published in the *Proceedings*. In this way, the the excellent science presented at AAVSO meetings will have a wider audience than at present: readers who are unable to attend meetings will have access to a more complete description of the research than the abstracts can convey.

The ability to publish in the *Proceedings* will provide authors with the opportunity to develop their ideas about their research results in preparation for the meeting. Interested authors will be well advised to sketch out the full article before submitting the abstract, since the deadline for the paper will be only two weeks after the abstract deadline. In doing so, they will be able to clarify and, perhaps, extend their ideas. There will be opportunities to revise both the submitted abstract and the submitted conference manuscript before publication.

Whether or not presenters choose to submit a conference paper, AAVSO meetings represent an opportunity for members to present their research results to peers/colleagues before submitting those results to *JAAVSO* for refereeing. Scientific feedback or questions from those at the meeting are likely to lead to an improved paper and a better refereeing process. Additional benefit would come from writing a conference paper, because input from the AAVSO editorial staff will enable improvements in manuscripts.

Conference presenters will be encouraged to develop their papers further for submission to peer review for *JAAVSO*. In the astronomical profession, it is not unusual to submit the same work as both a (usually curated but not refereed) conference report, published in a conference proceedings volume, and a refereed journal article. The peer-reviewed version usually has higher status. In case the conference report comes first, meeting attendees get a preview of the eventual journal article with opportunities to ask questions and comment on the research. Sometimes the conference report is a summary of an already-published paper; in this case, the author still learns from questions and comments from the audience.

Usually, the two written descriptions of the work are not identical. The refereed version contains more detail, more graphics than the limited time frame of an oral presentation would permit, and more tabular information.

We at the AAVSO are looking forward to working with our meeting attendees as they participate in this exciting experiment.

Low Resolution Spectroscopy of Miras 2—R Octantis

Bill Rea
6A Bygrave Place, Bishopdale, Christchurch 8053, New Zealand; rea.william@gmail.com

John C. Martin
Henry R. Barber Observatory, University of Illinois at Springfield

Received July 13, 2020; revised November 20, 30, 2020; accepted December 9, 2020

Abstract Low resolution spectroscopy with a filter wheel grating (R ~ 50–200) is an effective tool to monitor Mira type variables around their cycle. In early type Mira variables changes in spectral type are reflected in the depth of TiO absorption bands relative to nearby quasi-continuum points. However, those indices lose sensitivity in spectral types later/cooler than M6 or M7. Flux ratios between quasi-continuum points are better suited to monitor a cooler Mira like R Oct at low spectral resolution through its entire cycle. We identify flux ratios between quasi-continuum points in low resolution spectra that are sensitive enough to distinguish between comparison stars of different spectral types and find cycle-to-cycle differences in the behavior of R Oct around peak brightness. Those ratios are also much more sensitive than TiO to changes from mid to minimum in the cycle even when rendered less effective by lower signal to noise levels when R Oct approached minimum brightness.

1. Introduction

The long periods and large amplitudes of Mira variables make them a favorite observing target of non-professional observers using both visual and CCD photometry (Mattei1997). Those qualities also make them ideal targets for low resolution spectroscopy using filter wheel gratings spectrographs. As Wing (1997) notes: "If we think of Miras as variable stars with time-dependent spectra, it is clearly desirable to record both their spectroscopic and photometric behavior." While much of the professional focus on Mira variables has shifted to the infrared part of the spectrum, non-professionals limited by the sensitivity of silicon based CCD detectors, continue to observe mostly in the visual part of the spectrum. Readily available, low cost, filter-wheel gratings have made it easy to add routine low resolution spectroscopy to any CCD photometric observing program and the AAVSO Spectroscopic Database archives spectra of this type. Previous papers (Martin *et al.* 2016a, b; Rea 2019) addressed many issues relating both to the collection and interpretation of low resolution spectra of Miras through the use of filter wheel gratings, including problems associated with differential spectroscopy. The resolution of the spectra are very low with typical $R = \lambda / \Delta\lambda$ values from 50–200. However, even spectral resolutions this low record scientifically relevant changes in Mira variables.

The surface temperature of Mira variables change significantly over their pulsation cycle. As they fade in brightness their surface temperature cools, causing a shift in blackbody emission to longer wavelengths. Ideally that change could be measured from the peak and/or slope of the continuum flux relative to wavelength. However, in late type stars like Mira variables, strong molecular absorption features obliterate the continuum, particularly when recorded at low spectral resolution. So the presence and strength of key absorption features (mostly molecular bands) which also depend on temperature are the most reliable basis for determining temperature through spectral type (Gray and Corbally 2009). Wing (1992) proposed a narrow band photometric system to measure the spectral type for M-stars using the relative flux measured between points in the spectrum occupied by TiO molecular absorption bands and adjacent quasi-continuum. Azizi and Mirtorabi (2015) proposed refinements to that system intended for use with professional high resolution NIR spectroscopy.

The Wing ratio measures the strength of TiO absorption near 719 nm relative to quasi-continuum near 754 nm. Our investigation of the Mira variable X Oct (Rea 2019) used spectral peaks and troughs in the low resolution spectra to reproduce the diagnostic ratios for Mira variables in the Wing (1992) and Azizi and Mirtorabi (2015) systems. That work revealed as the star approached minimum brightness (its coolest temperature, about spectral type M7 for X Oct) the Wing ratio became unreliable due to interference by increasing VO molecular absorption. Azizi and Mirtorabi (2015) used a point at 704 nm to measure the continuum instead. But in the low resolution spectra of X Oct, the Azizi ratio was *less* sensitive to change in spectral type than the Wing ratio. While the Azizi ratio can work for high resolution IR spectra, that study showed it is not well suited for application with low resolution spectra.

Kirkpatrick *et al.* (1991) identified six points in M-type spectra between 630 and 900 nm that at sufficiently high spectral resolution measures the continuum free from molecular absorption (Table 1). Particularly at low spectral resolution, C2 (704 nm) corresponds to the Azizi and Mirtorabi (2015) continuum measurement and C3 (756 nm) corresponds to the Wing (1992) continuum measurement Wing B (754 nm).

Table 1. The six possible continuum points in spectral class K5 to M9 identified by Kirkpatrick *et al.* (1991).

Point	*Wavelength*
C1	653 nm
C2	704 nm
C3	756 nm
C4	813 nm
C5	884 nm
C6	904 nm

Given the 11-nm bandpass of the Wing B filter the small difference in central wavelength is not significant. At high spectral resolution, patches of continuum are clearly present around those points across most of the M-type spectral range. However, the low resolution of grating spectra only allow measurement quasi-continuum points affected by both continuum and nearby absorption.

Lower spectral resolution "blurs" the continuum with nearby absorption features. At the resolution of spectra obtained in this study one pixel on the CCD detector corresponds to more than 1 nm = 10 Å in wavelength. A single resolution unit in the spectrum (determined mostly by seeing profile in a slit-less spectrum) is several times that. The effect of absorption features on a given quasi-continuum point measured at low resolution can also change with spectral type. So at low spectral resolution each of these quasi-continuum points should be sensitive to changes in effective temperature over a fixed range of spectral types.

In this work we use the Pickles (1998) spectral library to predict the continuum points which can be used in ratios to measure the change in spectral type for stars later than M6. To test the predictions, we will focus on R Oct, which varies in spectral type from M5.3 to M8.4.

The remainder of this paper is structured as follows: section 2 describes the observing equipment, target stars, and methods; section 3 predicts which ratios of continuum points which should be most sensitive to changes in spectral type and effective temperature of Miras. Section 4 presents observations of R Oct and comparison stars, section 5 discusses how our observations of R Oct match the expectations, and section 6 explains our conclusions along with recommendations for implementing this method and direction of future work.

2. Observing equipment and methods

2.1. Observing equipment

Two telescopes were used in this study.

1. Rea operated an 80-mm f/6 Explore Scientific apochromatic refractor in Christchurch, New Zealand, with an Atik 414E Mono CCD camera using a SONY ICX424AL front-illuminated chip. The plate scale in the imaging plane was 2.77 arcseconds / pixel. Rea used a Paton Hawksley Star Analyzer 100 grating yielding a first order spectrum with a dispersion of 1.488 nm / pixel.

2. BSM_South of the AAVSOnet's Bright Star Monitors (https://www.aavso.org/bsm and https://www.aavso.org/bright-star-monitor-section). It was an AstroTech-72ED, a 72-mm, f/6 apochromatic refractor, located at Ellinbank Observatory in Victoria, Australia. At the time the data in this paper were collected it was fitted with an SBIG ST8-XME CCD camera and the filter wheel holding Astrodon high-thoughput Johnson and Cousins filters. The Johnson B, V, and I filters were used in this study.

2.2. Stars observed

Six stars were observed in this study. Basic details as well as results from this paper (discussed later) are presented in Table 2.

R Oct is a Mira variable close to the south celestial pole. The literature on R Oct is somewhat sparse owing to the difficulty of getting long-term grants of time on professional telescopes to monitor long period variables. The AAVSO International Database (AID) contains more than 6,000 visual observations of R Oct going back to 1893 (Kafka 2020). A VSTAR (Benn 2012) analysis of all the AAVSO visual photometry finds only one statistically significant period at 405.5 days photometric. A complementary analysis of a subset of the 2207 most recent visual observations using FAMIAS (Zima 2008) measures a 407-day period. Both are in good agreement with the 405- to 405.5-day periods found in the analysis of more sparsely sampled photometry by Celis (1978), deLaverny *et al.* (1997) and Serkowski and Shawl (2001).

Celis (1978), deLaverny *et al.* (1997) and Serkowski and Shawl (2001) classify R Oct as M5.5. Keenan (1966) reports spectral classification as M5.5e. Only deLaverny *et al.* (1997) gives a range: M5.3-M8.4.

2.3. Calibration and measurement of spectra

The spectra obtained with the gratings were extracted with SAOImage DS9 (https://sites.google.com/a/uis.edu/grating-spectroscopy-workshop/simple-spectrum-extraction-tutorial) and analyzed with our own code developed in R (R Core Team 2019).

The wavelength scale for the spectra was set using the dispersion per pixel and the distance of a pixel from the zero-order image. The dispersion for the SA-100 grating on the Rea 80-mm telescope was determined from spectra of planetary nebulae NGC 3132 and NGC 5315. The pixel-to-nanometer

Table 2. Target and comparison stars.

Star	*Spectral Class*	*T_{eff} (K)[b]*	*Variable Type[a]*	*Brightness Range (V mag)[a]*	*Period (days)[a]*	*C2 / C5[c]*	*Wing C3 / TiO[c]*	*Azizi C2 / TiO[c]*
R Oct	M5.3-M8.4e	2571	Mira	6.4–13.2	407	1.04 (0.43)	4.92 (0.94)	3.28 (0.57)
BQ Oct	M4III	3442	LB	6.80	—	3.36 (0.21)	2.21 (0.15)	2.05 (0.15)
CV Oct	M3	3507	LB	8.92–9.19	—	3.07 (0.39)	2.63 (0.37)	2.27 (0.25)
ε Oct	M5III	3355	SRB	4.58–5.30	55	—	4.08 (0.29)	2.81 (0.19)
CQ Oct	M4/M5III	3358	SRB	8.12–8.59	50.8	2.49 (0.20)	3.82 (0.30)	2.76 (0.19)
BW Oct	M5-M7III	2849	LB	7.90–9.10	—	1.12 (0.06)	5.85 (0.41)	3.26 (0.20)

[a] *The spectral type and variability data are taken from the AAVSO Variable Star Index (VSX). LB = slow irregular late type variables. SRB = Semi-regular type B, late type giants with poorly defined periodicity.*

[b] *The photospheric effective temperatures are taken from McDonald* et al. *(2012). R Oct is included in the McDonald* et al. *(2012) catalog under the identification HIP 25412.*

[c] *Average of ratios measured as described in section 2.2. Standard deviations given in brackets.*

conversion was averaged for the two lines (Hα and Hγ) and the two nebulae, giving a dispersion of 1.4880 nm/pixel. The OIII and Hβ lines were merged at this low resolution and were unsuitable for determining the per-pixel wavelength scale. This remained constant throughout the work as the distance between the filter wheel and the CCD was fixed.

The zero-point of a spectrum's wavelength scale is directly affected by uncertainty in the position of the center of the zero-order image for the star (often overexposed). The accuracy of the wavelength calibration is also affected by small changes in the alignment of the first order spectrum on the CCD chip (due to rotation of the grating in the filter holder) and higher order dispersion terms. These effects were sometimes noted in the spectrum but were estimated to cause systematic error no more than three pixels (less than 5 nm) at the key continuum point of 756 nm.

This level of uncertainty in wavelength scale is usual for low resolution spectra obtained through CCD imaging with filter wheel gratings. Our goal is to develop a diagnostic method which is accessible to non-professional astronomers and easily incorporated into existing and future crowd sourcing campaigns like those hosted by the AAVSO. To that end, we have consciously explored an approach which does not require accurate wavelength and/or flux calibration. The Wing (1992) filter system is our inspiration but we are *not* reproducing it by integrating the observed spectra over comparable band passes. Instead, our method relies on measuring the ratio between local flux peaks and troughs easily identified, even by visual inspection, near the central wavelengths of the Wing (1992) filters and the Kirkpatrick *et al.* (1991) quasi-continuum points. Reference to C1-C6 and the Wing A in our measurements refer to the flux of the peak or trough in the recorded flux found within about 7.5 nm of those wavelengths.

Figure 1 presents three spectra of R Oct from near maximum, mid, and minimum light with the continuum points from Table 1 marked. To minimize the impact on flux measurements from errors due to accuracy of the wavelength scale, the counts for each quasi-continuum point were measured at the local maximum within five pixels (≈ 7.5 nm) of their expected location. Each quasi-continuum point was visually inspected to verify that the pixel capturing the local maximum had been found. The depth of the TiO feature near 719 nm for the Wing A flux was determined in a similar manner using the flux from the pixel at the local *minimum*.

The signal-to-noise ratio (SNR) in the spectra decreased significantly as R Oct approached minimum brightness (see Figure 1). Both the decrease in SNR and the shifting of flux to longer wavelengths increase the uncertainty in the flux measured at the C1 quasi-continuum point and the bottom of the 719-nm TiO absorption line. Near minimum brightness, as many 16 to 25 individual images were stacked to create a spectrum with better SNR near minimum light. Despite best efforts, the influence of noise is more significant when the star is fainter than 12 magnitude. Worst case scenario, on the nights near minimum brightness with the highest sky background the SNR in the C1 and TiO measurements dipped as low as 3–4, translating into a 20–30 % error in ratios containing those measurements. Increased random noise is obvious in the ratios measured near minimum (see section 5).

Figure 2 illustrates how low spectral resolution and the growth of absorption features in later/cooler spectral types influence the measurement of the spectra. The Wing and Azizi ratios rely on the growth of the TiO absorption feature near 719 nm relative to the continuum. The overall shape of the spectra are influenced by the underlying blackbody continuum as it changes with the star's effective temperature.

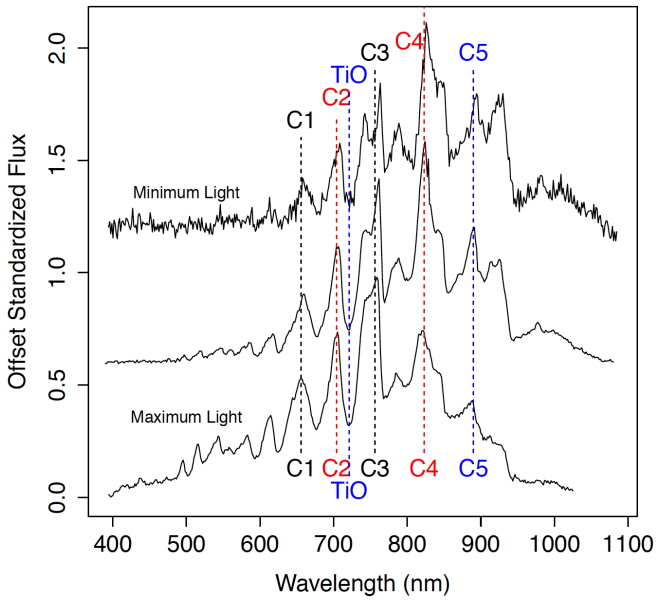

Figure 1. Spectra of R Oct at three epochs between maximum and minimum light. The quasi-continuum points C1 through C5 of Table 1 plus the TiO absorption line at 719 nm used by both the Wing A/C3 and Azizi A/C2 ratio have been labeled. Note that Wing B and C3 and the continuum point used by Aziz and C2 are equivalent as measured using the method employed at low spectral resolution.

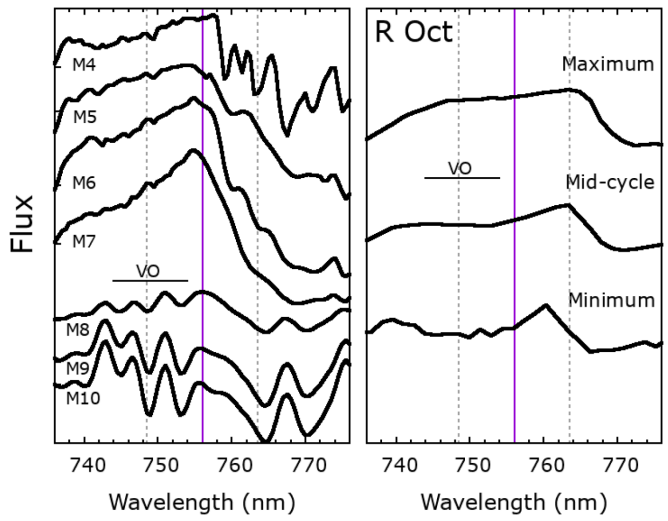

Figure 2. The left panel shows representative M type giant (luminosity class III) spectra from the Pickles (1998) spectral library covering the usual temperature range of R Oct. The right panel shows the low resolution spectra observed for R Oct at maximum brightness/hottest (2017 Feb 20), mid-cycle (2017 June 26), minimum brightness/coolest (2017 Sep 16). The position is marked for the VO absorption features which influence the measurement of C3 at later/cooler spectral types. The solid vertical line is the location of the C3, the quasi-continuum point, and the dotted vertical lines mark the ± 7.5-nm range on either side used to find the local maximum.

As reported by Azizi and Mirtorabi (2015), both the library spectra and the spectra of the target reveal the influence of VO absorption on the C3 quasi-continuum point at spectral types M8 and later. Low spectral resolution "blurs" nearby absorption features so that *none* of the Kirkpatrick *et al.* (1991) continuum points are free of absorption influence in the spectra recorded for this project. But Figure 2 shows that our method of using the local maximum to measure the low resolution spectra of R Oct best samples the quasi-continuum that is present.

In addition to changing absorption bands, Mira variables also undergo large swings in effective temperature that significantly affect the flux distribution of the spectrum over their cycle. When R Oct is spectral type M4-M5 near maximum brightness the spectrum clearly shifts toward blue/shorter wavelengths (Figure 1). When measuring the earliest spectral types (M1-M5) it is difficult to identify a local maximum to measure the flux of longest wavelength quasi-continuum points (C4 to C6). This is why the Wing and Azizi ratios, primarily developed for early spectral types, focus on the shorter wavelength end of the spectrum. Since R Oct gets much cooler than M5, focus must to shift to longer wavelengths to measure its temperature changes. A significant drop in quantum efficiency of silicon based CCD detectors at longer wavelengths also contributes to difficulty measuring flux at C4-C6 (see section 3.2).

3. Ratios from continuum points

3.1. Continuum ratios from library spectra

While the presence and strength of key absoprtion features is considered the best way to measure the spectral type, the continuum points identified by Kirkpatrick *et al.* (1991) (Table 1) should also be influenced by change in blackbody temperature. The curves plotted in Figure 3 illustrate that across spectra types M0 to M10 there is a steady change in the ratio of the flux between continuum points corresponding to the effective temperature.

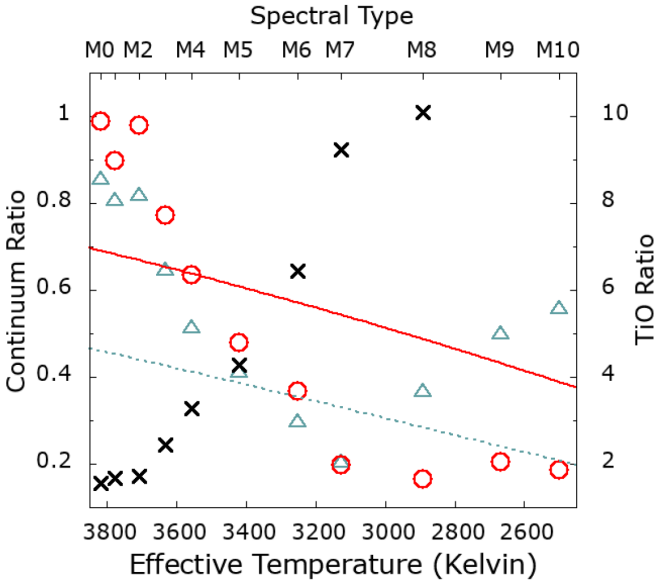

Figure 3. Ratios of the continuum points C1/C3 (triangles), C2/C5 (circles), and Wing C3/TiO ratio (X's, right y-axis) computed from library spectra (Pickles 1998) over a range of spectral types. The dashed line is the C1/C3 ratio from a pure blackbody. The solid line is the C2/C5 ratio from a pure blackbody. The quasi-continuum ratios are read off the y-axis on the left and the Wing ratio is read off the axis on the right. The ratios plotted only account for the relative flux in the library spectra and from the blackbody function. They do not account for the sensitivity of the CCD.

The flux at the Kirkpatrick *et al.* (1991) continuum points was measured in the library spectra of giants (luminosity class III) published by Pickles (1998). To reproduce what was done with the observed spectra, fluxes in the library spectra were recorded at the local maximum within ± 7.5 nm of each continuum point. The Wing TiO absorption (Wing A filter) was measured as the local minimum within ± 7.5 nm of 719 nm. The continuum point C6 was excluded from this analysis because the sensitivity of most CCDs are very low (quantum efficiency < 20%) at wavelengths greater than 900 nm.

Of the ratios investigated, the C2/C5 and C1/C3 ratios show the most pronounced and clear variation across the M spectral types for giants. As expected, the ratios measured from the Pickles (1998) library spectra differ significantly from those predicted for a pure blackbody (Figure 3). This demonstrates how the absorption features influence the "continuum" points at low spectral resolution. Careful investigation of the template spectra within 10 nm of C1 and C2 show that the general appearance of the spectrum around those points is relatively similar across all M spectral types. However within 10 nm of C3 and C5 the shape of the spectrum changes substantially by adding several significant absorption features in spectral types M9 and cooler. Regardless, each continuum point still shows a clear dependence on spectral type whether they are free from the influence of absorption or not.

As shown in previous work (Rea 2019), the Wing TiO/C3 ratio, measuring the relative depth of the 719 nm TiO absorption feature, is a reliable indicator of effective temperature in low resolution spectra of earlier spectral types. When measuring the flux at the local maximum, Wing (1992) B is equivalent to C3. The Wing TiO/C3 ratio shows clear variation in the earlier spectral types (M0-M5). In later spectra types (M6-M10) the TiO absorption near 719 nm becomes saturated and the depth of the band cannot be distinguished from a flux of zero in observed spectra.

Of the continuum ratios investigated, C2/C5 shows the most variation, decreasing in value by a factor of almost 9 between spectral types M2 and M8 (Figure 3). This behavior is comparable to performance of Wing (1992) C3/A ratio but with a steeper slope with respect to effective temperature and no limiting factor like the TiO band saturating. As a result, we predict that C2/C5 shows promise as a temperature indicator in the middle of the M spectral types. That makes it well suited to measure the effective temperature change of R Oct which varies between spectral types M5-M8. However, note that while the C2/C5 ratio shows promise in the mid-range of spectral types, it shows no significant variation in earliest (M0-M2) and latest spectra types (M8-M10).

Neither the C2/C5 or Wing (1992) C3/A ratio are sensitive to changes in temperature in the latest spectral types (M8-M10). This presents a problem for measuring variation in the coolest Mira variables. Fortunately, the C1/C3 ratio is predicted to show variation through latest spectral types (M7-M10). The trend of that ratio reverses near M7 so there is aliasing

of ratio values between late and early spectral types. In future work, that aliasing could be disentangled using other indicators to create a two dimensional index (i.e. brightness of star near minimum/coolest, Wing C3/A, or C2/C5).

3.2. Practical considerations

The approach used in this work to measure the spectra of R Oct is appealing for low resolution slit-less spectroscopy because it does *not* require accurate wavelength calibration of the spectra. Using the local maximum or minimum to measure the flux allows the method to be applied even via visual inspection.

The ratios calculated in Figure 3 do *not* include consideration of CCD efficiency or flat fielding effects on the extracted spectrum. The CCD sensitivity as a function of wavelength acts like a multiplicative factor for all ratios. Note that C1 is near the peak sensitivity of most CCDs. The Sony ICX424AL CCD used in this study has a bluer response peaking closer to 500 nm. The solid state physics of silicon dictates that the sensitivity of most CCDs decreases by more than a factor of two between C2 and C5 and they are less than 20% efficient at wavelengths longer than 900 nm. The sensitivity of most silicon detectors is much too low to effectively measure the flux of C6.

As noted in section 2.3, at low spectral resolution (R ~ 100) it becomes very difficult to accurately measure C4, C5, and C6 in early spectral types. In M3 and earlier spectral types the molecular absorption around C4-C6 decreases in strength and it is harder to distinguish absorption from continuum. That, combined with low spectral resolution, obliterates the spectral "peak" near those points and makes it difficult to accurately employ the our method to measure the spectral flux without accurate wavelength calibration.

Flat fielding effects in the images and sampling at different spectral resolutions could also influence the continuum ratios. *This implies that it is important to calibrate each telescope, grating, and camera combination with comparison stars of known spectral type.* A selection of comparison stars with spectral types covering the range of the target's pulsation should be used to calibrate the relationship between ratio value and spectral type for a given equipment setup. To avoid changes in the observed ratios due to flat fielding effects, the spectrum should always be recorded in the same part of the field. And for the highest accuracy, the sky background/illumination (i.e. the Moon, during dusk) should be monitored and subtracted from the extracted spectrum.

4. Results

4.1. The comparison stars

Spectra of five comparison stars observed between April and September 2018 were used to calibrate the spectral ratios recorded for R Oct with the Rea 80 mm telescope. Those spectra are similar to those recorded for R Oct and described in detail in Rea (2019). That work showed only BW Oct and CQ Oct exhibited any significant change in brightness over the period of observation.

The method used to measure the R Oct spectrum was also used to measure the continuum fluxes for each comparison star spectrum. The average and standard deviation of the C1/C3, C2/C5, Wing C3/TiO, and Azizi C2/TiO ratios are given in Table 2 and the results for the C2/C5 ratio are plotted as a function of photospheric effective temperature in Figure 4.

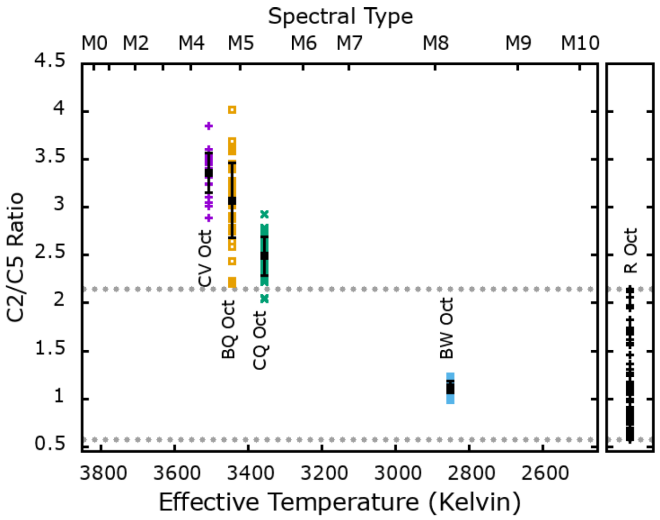

Figure 4. A plot of the C2/C5 ratio measured from the spectra of the comparison stars plotted against their surface temperature. Horizontal dotted lines mark the minimum and maximum C2/C5 ratio measured for R Oct. The distribution of ratio values measured for R Oct are shown on the right on the same y-scale in the detached panel.

Only CV Oct shows any evidence of a change in its spectral ratios over that period. The average C1/C3 and C2/C5 ratios for CV Oct were slightly lower in the first half relative to the second half of the period of observation, but not significantly so.

4.2. Results from R Oct

The period along with the range of spectral type and brightness of Mira variable R Oct are given in Table 2. In addition to being a cooler Mira variable, R Oct is desirable as a target because it is near the south celestial pole and can be observed year round from New Zealand. No part of the cycle was lost due to solar conjunction.

The 80-mm Rea telescope was used to collect 93 spectra of R Oct between 11 October 2015 and 25 September 2018, an interval that covered approximately two and a half pulsation cycles. The Bright Star Monitor South measured its brightness in Johnson B and V starting 12 November 2017. When the B magnitude dropped below about 13, the I filter was used in place of B. All the photometry obtained for this study are available for download from the AAVSO International Database (https://www.aavso.org/data-download) submitted by observer RWSA (William Rea). Prior to November 2017, the brightness of R Oct is tracked using the visual estimates of Ejii Kato (observer ID KEI) submitted to the AAVSO International Database. While there are other visual estimates for R Oct in the AAVSO International Database, we relied exclusively on Kato's observations since they were made by a single reliable observer (no concern of differences between observers) and covered the same epochs as the spectra recorded for R Oct.

Spectra were extracted and measured as outlined in section 2.3. Figure 6 shows the Wing TiO/C3 and Aziz TiO/C2

Table 3. Observed Brightness and Spectral Ratios for R Oct.

JD –2450000	Visual Mag[a]	V_{mag}	(B–V)	C1/C3	C2/C5	Wing A/B	Azizi
7306	—	—	—	0.36	0.89	4.49	2.82
7313	—	—	—	0.35	0.90	4.84	2.95
7315	10.4	—	—	0.38	0.81	4.46	2.65
7331	—	—	—	0.36	0.98	4.19	2.56
7339	—	—	—	0.34	0.97	4.67	2.87
7345	9.9	—	—	—	—	—	—
7347	—	—	—	0.37	1.13	4.52	2.70
7358	—	—	—	0.36	1.05	4.65	2.72
7370	—	—	—	0.48	1.71	4.31	3.21
7371	8.8	—	—	—	—	—	—
7381	—	—	—	0.56	1.98	3.59	2.72
7391	—	—	—	0.54	2.12	3.18	2.42
7396	—	—	—	0.58	2.15	3.16	2.47
7405	7.7	—	—	—	—	—	—
7407	—	—	—	0.59	2.06	3.30	2.55
7419	—	—	—	0.57	1.83	2.99	2.16
7427	8.4	—	—	—	—	—	—
7436	8.8	—	—	—	—	—	—
7441	—	—	—	0.46	1.46	4.03	2.65
7450	—	—	—	0.42	1.24	4.57	2.85
7457	—	—	—	0.46	1.31	4.50	2.99
7474	—	—	—	0.36	1.12	5.23	3.15
7479	9.9	—	—	—	—	—	—
7483	—	—	—	0.40	1.24	5.19	3.57
7488	—	—	—	0.34	1.27	5.84	3.37
7492	10.3	—	—	—	—	—	—
7502	10.4	—	—	—	—	—	—
7503	—	—	—	0.34	0.88	5.36	3.01
7515	—	—	—	0.31	0.82	5.70	3.14
7520	11.2	—	—	—	—	—	—
7526	—	—	—	0.40	0.90	5.99	3.86
7534	11.4	—	—	—	—	—	—
7533	—	—	—	0.34	0.77	5.52	3.34
7541	—	—	—	0.33	0.68	4.92	3.00
7548	11.6	—	—	—	—	—	—
7565	12.2	—	—	—	—	—	—
7570	—	—	—	0.40	0.63	5.73	3.30
7578	12.5	—	—	—	—	—	—
7581	—	—	—	0.35	0.63	5.47	3.55
7590	—	—	—	0.21	0.68	5.33	3.60
7599	12.9	—	—	—	—	—	—
7607	—	—	—	0.21	0.57	8.01	4.82
7622	—	—	—	0.34	0.64	4.77	2.99
7628	12.8	—	—	—	—	—	—
7629	—	—	—	0.40	0.60	4.89	3.10
7634	—	—	—	0.37	0.64	6.34	3.95
7651	12.5	—	—	—	—	—	—
7648	—	—	—	0.38	0.66	4.61	3.14
7666	—	—	—	0.41	0.73	4.77	3.45
7673	—	—	—	0.34	0.70	5.01	3.11
7680	12.2	—	—	0.34	0.65	3.61	2.18
7691	—	—	—	0.38	0.73	5.12	3.35
7697	11.6	—	—	—	—	—	—
7699	—	—	—	0.29	0.62	4.30	2.54
7703	11.2	—	—	—	—	—	—
7711	—	—	—	0.35	0.78	4.93	3.11
7719	—	—	—	0.35	0.78	4.84	3.21
7736	10.4	—	—	—	—	—	—
7741	—	—	—	0.49	1.13	4.14	3.18
7754	—	—	—	0.44	1.18	4.07	2.70
7758	9.4	—	—	—	—	—	—
7763	9.2	—	—	—	—	—	—
7765	—	—	—	0.51	1.58	3.74	2.79
7776	—	—	—	0.54	1.62	3.24	2.40
7777	8.7	—	—	—	—	—	—
7786	—	—	—	0.54	1.69	3.02	2.24
7790	8.3	—	—	—	—	—	—
7793	—	—	—	0.54	1.73	3.32	2.51
7804	—	—	—	0.54	1.73	3.75	2.72
7807	8.4	—	—	—	—	—	—
7815	—	—	—	0.50	1.67	3.84	2.67
7828	—	—	—	0.48	1.74	4.33	3.04
7829	8.4	—	—	—	—	—	—
7839	8.8	—	—	—	—	—	—
7850	8.9	—	—	—	—	—	—
7852	—	—	—	0.37	1.15	4.76	2.83
7858	—	—	—	0.41	1.27	5.43	3.44
7859	9.4	—	—	—	—	—	—
7865	—	—	—	0.37	1.17	5.53	3.35
7873	10.0	—	—	—	—	—	—
7874	—	—	—	0.38	1.10	5.81	3.56
7886	—	—	—	0.39	1.05	5.12	3.26
7890	10.5	—	—	—	—	—	—
7904	10.8	—	—	—	—	—	—
7920	11.1	—	—	—	—	—	—
7930	—	—	—	0.39	0.87	5.31	3.50
7935	11.6	—	—	—	—	—	—
7952	—	—	—	0.48	0.81	4.29	3.29
7955	11.9	—	—	—	—	—	—
7959	—	—	—	0.37	0.69	5.22	3.20
7966	12.4	—	—	—	—	—	—
7970	—	—	—	0.38	0.79	5.62	3.46
7977	12.5	—	—	—	—	—	—
7983	—	—	—	0.39	0.62	4.59	2.90
7989	—	—	—	0.34	0.59	4.44	2.95
7994	12.9	—	—	—	—	—	—
8000	—	—	—	0.35	0.67	5.82	4.56
8007	13.0	—	—	—	—	—	—
8012	—	—	—	0.43	0.60	5.51	3.93
8019	12.9	—	—	—	—	—	—
8026	—	—	—	0.36	0.58	4.94	3.80
8036	12.9	—	—	—	—	—	—
8038	—	—	—	0.42	0.90	5.11	3.84
8045	—	—	—	0.38	0.61	6.48	3.60
8056	12.8	—	—	0.32	0.62	6.33	3.84
8068	—	—	—	0.40	0.63	4.73	2.98
8069	12.4	—	—	—	—	—	—
8070	—	11.992 ± 0.038	—	—	—	—	—
8071	—	11.944 ± 0.063	2.06	—	—	—	—
8072	—	11.907 ± 0.036	—	—	—	—	—
8076	—	11.901 ± 0.048	—	—	—	—	—
8078	—	11.792 ± 0.043	—	—	—	—	—
8079	—	11.823 ± 0.044	1.885	0.35	0.63	5.04	3.23
8082	12.2	—	—	—	—	—	—
8089	—	11.615 ± 0.052	—	0.38	0.70	5.07	3.31
8093	11.9	—	—	—	—	—	—
8094	—	11.471 ± 0.043	—	—	—	—	—
8096	—	11.504 ± 0.045	2.01	—	—	—	—
8100	—	11.349 ± 0.045	2.14	—	—	—	—
8102	11.6	11.298 ± 0.064	1.986	—	—	—	—
8103	—	11.314 ± 0.027	1.699	0.29	0.61	4.68	2.72
8109	—	11.134 ± 0.024	1.981	—	—	—	—
8113	—	11.108 ± 0.039	1.85	—	—	—	—
8114	—	11.111 ± 0.032	1.812	—	—	—	—
8118	—	10.965 ± 0.04	1.198	—	—	—	—
8120	—	11.021 ± 0.056	1.25	—	—	—	—
8122	—	11.058 ± 0.039	1.775	—	—	—	—
8123	—	11.007 ± 0.05	1.777	—	—	—	—
8124	11.4	—	—	—	—	—	—
8128	—	10.958 ± 0.044	1.709	—	—	—	—
8132	—	—	—	0.45	0.86	4.82	3.63
8134	—	10.851 ± 0.032	1.75	—	—	—	—

Table continued on next page

Table 3. Observed Brightness and Spectral Ratios for R Oct, cont.

JD –2450000	Visual Mag[a]	V_{mag}	(B–V)	C1/C3	C2/C5	Wing A/B	Azizi	JD –2450000	Visual Mag[a]	V_{mag}	(B–V)	C1/C3	C2/C5	Wing A/B	Azizi
8135	—	10.812 ± 0.027	1.641	—	—	—	—	8275	10.2	—	—	—	—	—	—
8137	—	10.767 ± 0.056	1.642	—	—	—	—	8277	—	—	—	0.34	0.99	6.09	3.61
8146	—	—	—	0.41	0.86	5.36	3.46	8280	—	10.001 ± 0.021	1.621	—	—	—	—
8147	—	10.767 ± 0.056	1.642	—	—	—	—	8288	10.5	—	—	—	—	—	—
8154	—	10.527 ± 0.053	1.698	—	—	—	—	8289	—	10.277 ± 0.031	1.521	—	—	—	—
8155	11.1	—	—	—	—	—	—	8291	—	—	—	0.32	0.83	5.43	3.29
8156	—	—	—	0.39	0.86	5.45	3.38	8301	—	10.673 ± 0.041	1.491	—	—	—	—
8166	—	—	—	0.44	1.09	4.96	3.38	8302	—	—	—	0.38	0.85	6.28	3.95
8180	—	—	—	0.48	1.36	4.53	3.13	8310	10.8	—	—	—	—	—	—
8189	8.7	—	—	—	—	—	—	8311	—	—	—	0.35	0.86	6.96	4.43
8191	—	8.314 ± 0.049	1.425	—	—	—	—	8320	11.5	—	—	—	—	—	—
8195	—	—	—	0.52	1.94	4.06	3.05	8321	—	—	—	0.43	0.92	6.65	4.50
8200	—	7.787 ± 0.046	1.473	—	—	—	—	8322	—	11.149 ± 0.031	1.732	—	—	—	—
8203	8.3	—	—	—	—	—	—	8332	—	11.342 ± 0.034	—	—	—	—	—
8206	—	7.664 ± 0.039	1.499	0.51	1.96	4.03	2.85	8333	—	—	—	0.44	0.81	5.75	4.06
8212	—	7.652 ± 0.045	1.456	—	—	—	—	8336	—	11.393 ± 0.047	—	—	—	—	—
8217	8.2	—	—	—	—	—	—	8340	—	11.512 ± 0.028	—	—	—	—	—
8224	8.3	—	—	0.50	1.82	4.16	3.03	8341	—	—	—	0.39	0.83	5.09	3.50
8227	—	7.962 ± 0.031	1.528	—	—	—	—	8345	—	11.668 ± 0.02	—	—	—	—	—
8231	—	8.061 ± 0.047	1.543	—	—	—	—	8342	12.0	—	—	—	—	—	—
8233	—	—	—	0.42	1.56	4.68	3.07	8349	—	—	—	0.44	0.89	5.39	4.06
8236	8.7	—	—	—	—	—	—	8351	12.4	—	—	—	—	—	—
8239	—	8.327 ± 0.018	1.539	—	—	—	—	8356	—	—	—	0.50	0.83	6.11	4.74
8252	—	8.838 ± 0.033	1.515	—	—	—	—	8365	—	12.066 ± 0.045	—	—	—	—	—
8255	—	—	—	0.39	1.15	4.74	2.89	8368	—	—	—	0.38	0.76	5.78	3.83
8257	—	—	—	0.39	1.11	4.63	2.80	8373	—	12.261 ± 0.041	—	—	—	—	—
8259	9.5	—	—	—	—	—	—	8375	—	—	—	0.42	0.68	7.19	4.70
8264	—	9.327 ± 0.019	1.575	—	—	—	—	8381	—	12.464 ± 0.037	—	—	—	—	—
8268	—	9.52 ± 0.024	1.511	—	—	—	—	8386	—	—	—	0.45	0.69	4.48	3.40
8272	—	9.727 ± 0.051	1.51	—	—	—	—								

[a] *By Eiji Kato (Observer ID: KEI) from the AAVSO International Database (Kafka 2020).*

ratios and Figure 7 shows the C2/C5 and C1/C3 ratio measured compared with the fluctuating brightness of the target. The data in those Figures are given in Table 3.

5. Discussion

Figure 5 presents more than a century's worth of visual and, later, Johnson V band observations of R Oct. Taking only the visual observations, the brightness has ranged over eight magnitudes from 6 to 14. Note that the maxima and minima of the main 405.5-day period vary in brightness. Within any particular cycle the brightness range was typically between five and six magnitudes. These variations are sufficiently irregular that no longer term periods have been conclusively identified. Note in Figure 7 that the maximum brightness and shape of the brightness peak around each maximum varied significantly over the 2.5 cycles observed in this study but were towards the lower end of the historical range. Any spectral index that successfully measured R Oct should also capture these variations.

The Wing C3/TiO and Azizi C2/TiO ratios do not capture most of the variation in R Oct's cycle (see Figure 6). When the R Oct is hottest, near the peak of its brightness, there is some noticeable decrease in both ratios (more in Wing than in Azizi) but the remainder of the cycle both are mostly the same unvarying value. The abrupt increase ("spikes") in both observed ratios near minimum brightness are caused by the spectrum becoming faint and noisy and the depth of the TiO absorption increasing so that it approaches the zero level in the spectrum (see section 2.3).

The failure of the Wing ratio in late spectral types was expected and primarily attributed to the increase in VO absorption near C3. Azizi and Mirtorabi (2015) formulated their ratio with the intention of applying it to higher resolution spectra. Rea (2019) and this result demonstrate that the Azizi ratio is not as sensitive as the Wing ratio when using low spectral resolution.

The C2/C5 ratio followed changes in R Oct throughout the 2.5 cycles observed (Figure 7). The range of values of the C2/C5 ratio is compared to the ranges of the comparison stars in Figure 4). That Figure confirms other authorities who give R Oct's spectral type as about M5.5 at maximum light. At minimum light the C2/C5 ratio is much lower that the closest comparison star, BW Oct, which has a published spectral classification of M7.

Other ratios (C1/C4, C2/C4, and C1/C5, Figure 8) show results that are similar to C2/C5. However, C2/C5 is favored because it has the steepest predicted slope with respect to spectral type and the measurements of C2/C5 from the spectra of R Oct have a larger range of values than the other ratios. Ratios using C1 are less desirable because C1 is fainter and more uncertain due to increased noise in R Oct's spectrum near minimum brightness (section 2.3).

The differences in the three peaks of the light curve around maximum brightness (i.e. change in peak brightness, and shape

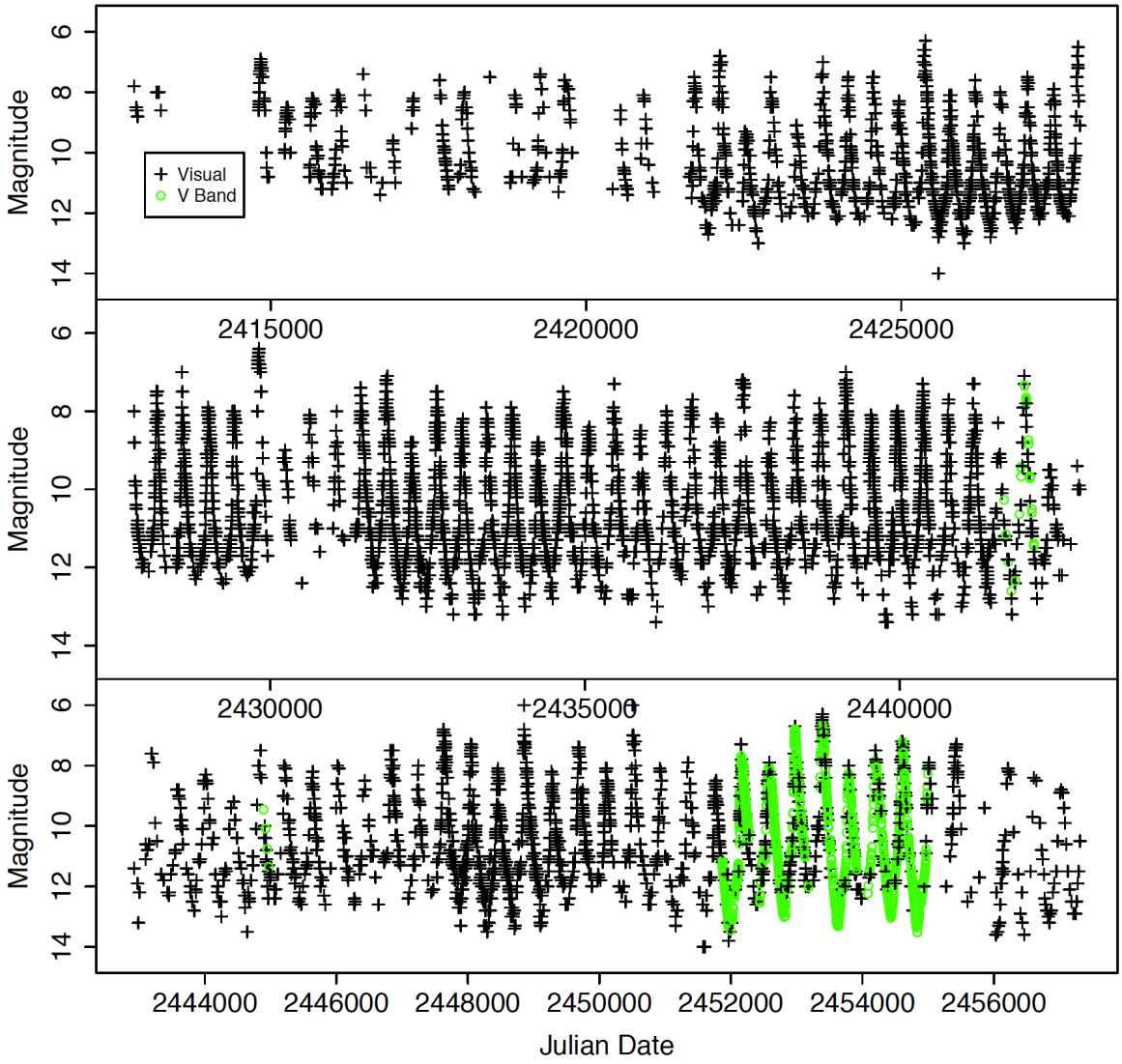

Figure 5. The visual (black) and V band (green) observations of R Oct in the AAVSO International Database up until the start of the study period. The visual estimates of the magnitude range from 6 to 14.

of light curve) are tracked closely by the C2/C5 ratio. The C2/C5 ratio clearly reveals that R Oct's surface was hotter when the maximum was brighter and that it stayed hotter longer when the maximum was broad instead of sharply peaked. It is not clear from this data if R Oct was always roughly the same spectral type at minimum brightness or if C2/C5, as predicted, becomes insensitive to changes around spectral type M7 or M8. Correlating R Oct's C2/C5 ratio with the comparison stars in Figure 4 reveals that at peak brightness R Oct had a spectral type that was similar to CQ Oct (spectral type M 5.5) and at minimum it was later in spectral type than BW Oct (spectral type M7).

Analysis in section 3 predicts that the C1/C3 ratio should be sensitive to changes in M type giants later than spectral type M7. R Oct is supposed to get as late as spectral type M8.4 (deLaverny *et al.* 1997) and comparison of R Oct's C2/C5 ratio with BW Oct implies that over the period of this study R Oct got later than M7. The C2/C3 and C1/C2 ratios are also predicted to react to changes in late spectral types in a manner similar to C1/C3. However, in R Oct's spectrum only C1/C3 showed significant correlation with the changing brightness of the star. We conclude that the spacing between adjacent continuum points is too small to be sensitive to temperature changes in these low resolution spectra.

Aside from some variation near peak brightness, Figure 7 shows no significant variation in the C1/C3 ratios measured for R Oct over 2.5 cycles. This does not support the prediction made in section 3 that the C1/C3 ratio should "rebound" and increase as R Oct reached its latest spectral type near minimum. Instead the C1/C3 variation flattens and becomes more random when R Oct's brightness dips fainter. The noise level in the spectrum only contributes significantly when R Oct gets fainter than 12.0 (section 2.3). However, note that the C1/C3 ratio flattens *before* the star's brightness drops fainter than 10.0; at about the same point the Wing ratio also loses sensitivity. Therefore we cannot exclude that this effect is influenced by additional factors like absorption features filtered through the "blurring" influence of low spectra resolution. The observational limitations of our study prevent us from reaching a clear conclusion.

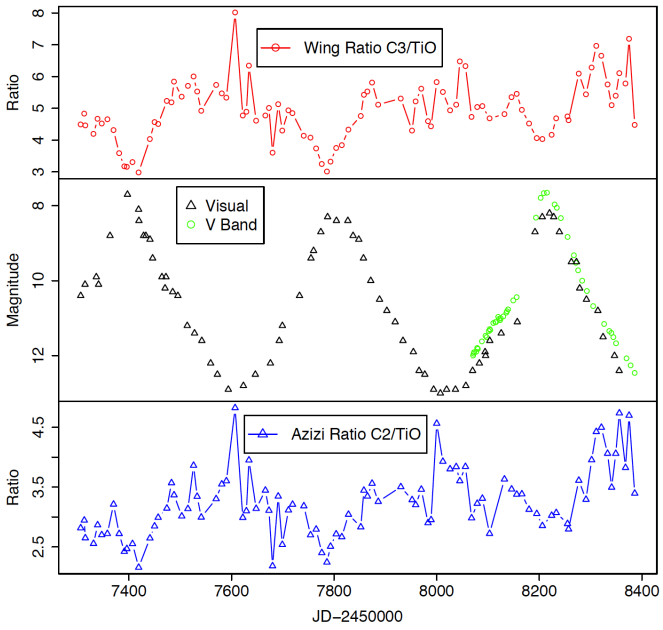

Figure 6. Wing C3 / TiO (top panel) and Azizi C2 / TiO (bottom panel) measured from spectra, and the brightness of R Oct (middle panel) over about 2.5 cycles between 11 October 2015 and 25 September 2018.

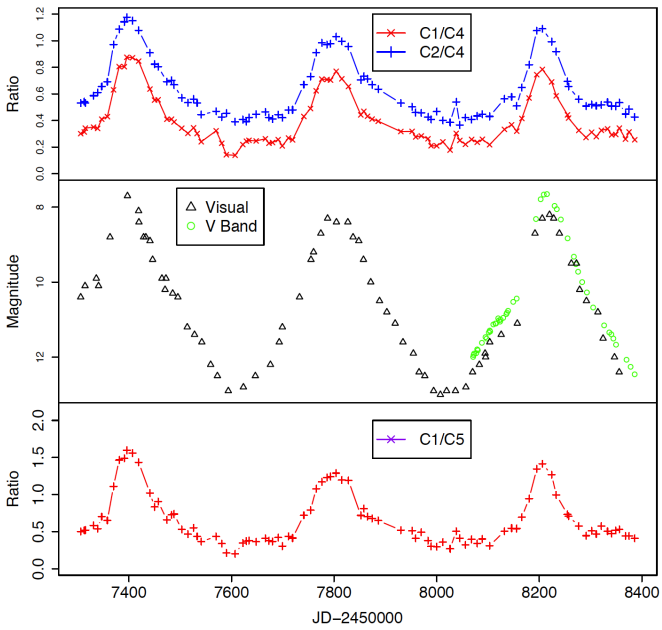

Figure 8. The C1/C4 and C2/C4 ratios (top panel) and C1/C5 ratio (bottom panel) measured from spectra, and the brightness of R Oct (middle panel) over about 2.5 cycles between 11 October 2015 and 25 September 2018.

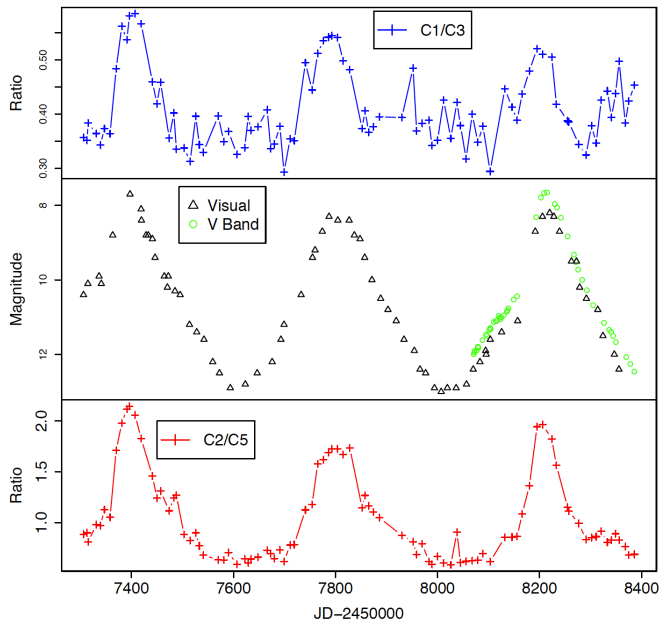

Figure 7. The C1/C3 (top panel) and C2/C5 (bottom panel) ratios measured from spectra, and the brightness of R Oct (middle panel) over about 2.5 cycles between 11 October 2015 and 25 September 2018.

6. Conclusions and future directions

R Oct and other circumpolar Miras offer excellent opportunities to include grating spectroscopy in a CCD photometric observing program. Low resolution spectral observations add scientific value beyond what can be obtained from multi-color photometry. For Miras with very long histories of visual observation, low resolution spectroscopy adds to understanding of these "legacy" stars. To maximize their contribution observers must be well aware of how to use comparison stars to calibrate their observing setup and understand how noise limits their measurements.

The measure of TiO absorption strength, which we refer to as the Wing and Azizi ratios, is ineffective for measuring the physical changes of R Oct around its cycle since its spectral type is always later than M5. The linear response of CCD chips compared to photographic emulsions allows us to transition from relying on absorption line strength and appearance to determining spectral type from continuum points that sample the shape of the underlying blackbody curve. In late type stars, spectroscopy offers an advantage over even narrow band photometry in the ability to more finely select quasi-continuum points and measure their flux, even without highly accurate wavelength calibration. The C1 / C3 ratio and the C2 / C5 ratios are the two most reliable guides to R Oct's changes in effective temperature over the course of its pulsation cycle. The C2 / C5 ratio is sensitive to all the fine details in the visible light curve around peak brightness. However, both C2 / C5 and C1 / C3 appear to become less sensitive to changes in spectral type as R Oct approaches minimum brightness, due at least in part to increased noise when R Oct was fainter than 12th magnitude. However, it is unclear if other factors may contribute.

This work is limited by having only one cool comparison star and no comparison stars cooler than spectral type M7. It is unclear if R Oct was the same temperature at each minimum or if the C2 / C5 ratio is insensitive to change below spectral type M7. Having more comparison stars and more cool comparison stars over the full expected range of the target could yield more precise results. Future work should explore if there is a low temperature failure point of C2 / C5 ratio and if C1 / C3 is sensitive to change in the coolest M type giants. However, we acknowledge that work will face significant challenges when identifying suitable M-type comparison giants of the latest types since they are rare and tend to be variable.

7. Acknowledgements

We thank Robert Wing for the email discussions about his three- and eight-filter photometry systems and the particular problems posed by the presence of the VO molecule in the coolest Miras. We thank Arne Henden, Michael Nicholas, George Silvis, and Bill Toomey of the AAVSO for their help in operating the AAVSO's Bright Star Monitor telescopes. We thank Tim Crawford of the AAVSO comparison star team for adding further suitable comparison stars to fields captured by the BSM telescopes used in this project. We thank the AAVSO observers who contributed to the observations AAVSO's International Database used in this study. Without the assistance and encouragement of these people this study would not have been possible.

References

Azizi, F., and Mirtorabi, M. T. 2015, *Astrophys. Space Sci.*, **357**, 96.

Benn, D. 2012, *J. Amer. Assoc. Var. Star Obs.*, **40**, 852.

Celis, S. L. 1978, *Astron. Astrophys.*, **63**, 53.

de Laverny, P., Geoffray, H., Jorda, L., and Kopp, M. 1997, *Astron. Astrophys., Suppl. Ser.*, **122**, 415.

Gray, R. O., and Corbally, C. J. 2009, *Stellar Spectral Classification*, Princeton University Press, Princeton, NJ.

Kafka, S. 2020, variable star observations from the AAVSO International Database (https://www.aavso.org/aavso-international-database-aid).

Keenan, P. C. 1966, *Astrophys. J., Suppl. Ser.*, **13**, 333.

Kirkpatrick, J. D., Henry, T. J, and McCarthy, D. W. 1991, *Astrophys. J., Suppl. Ser.*, **77**, 417.

Martin, J. C., Rea, B., McFarland, R., and Templeton, M. 2016a, 2016 Symposium Videos (http://socastrosci.org/Video2016.html), Society for Astronomical Sciences, Rancho Cucamonga, CA.

Martin, J. C., Rea, B., McFarland, R., and Templeton, M. 2016b, SAS Publications (http://socastrosci.org/Publications.html), Society for Astronomical Sciences, Rancho Cucamonga, CA.

Mattei, J. A. 1997, *J. Amer. Assoc. Var. Star Obs.*, **25**, 57.

McDonald, I., Zijlstra, A. A., and Boyer, M. L. 2012, *Mon. Not. Roy. Astron. Soc.*, **427**, 343.

Pickles, A. J. 1998, *Publ. Astron. Soc. Pacific*, **110**, 863.

R Core Team. 2019, R: A Language and Environment for Statistical Computing, R Foundation for Statistical Computing, Vienna, Austria (https://www.R-project.org).

Rea, B. 2019, *J. Amer. Assoc. Var. Star Obs.*, **47**, 70.

Serkowski, K., and Shawl, S. J. 2001, *Astron. J.*, **122**, 2017.

Wing, R. F. 1992, *J. Amer. Assoc. Var. Star Obs.*, **21**, 42.

Wing, R. F. 1997, *J. Amer. Assoc. Var. Star Obs.*, **25**, 63.

Zima, W. 2008, *Commun. Asteroseismology*, **155**, 17.

The Confirmation of Three Faint Variable Stars and the Observation of Eleven Others in the Vicinity of Kepler-8b by the Lookout Observatory

Neil Thomas
Margaret Paczkowski
Department of Astronautical Engineering, United States Air Force Academy, CO 80840; neil.thomas@afacademy.af.edu

Received September 16, 2020; revised November 19, December 16, 2020; accepted December 16, 2020

Abstract A commissioning survey of the Lookout Observatory has observed fourteen faint (V ~ 13 to 17) variables in the region of the exoplanet Kepler-8b. Three of these are variable star candidates discovered by the Asteroid Terrestrial-Impact Last Alert System (ATLAS) and confirmed here. The ATLAS survey identified 315,000 probable variables within its wide-field survey in 2018. The faintness (down to r ~ 18) and small amplitudes (down to 0.02 mag) included in these candidates makes external validation difficult. The confirmation of this handful of variable stars lends credibility to the ATLAS catalog. Lastly, the agreement between various surveys and this new one validates the use of this instrument for variable star and exoplanet research.

1. Introduction

The primary function of the Lookout Observatory (LO) is to observe exoplanets via the transit photometry method. It routinely attains photometric precision better than 0.002 mag (2 mmag) for bright targets. It autonomously performs photometry on all suitable stars within the field of view (FOV) in addition to the targeted exoplanet host star. It thus provides valuable observations of many variable stars during a given night.

Section 2 discusses the characteristics and expected performance of the LO in contrast to several other sources of photometry. Section 3 validates results against external data, provides light curves for 14 variable stars, and confirms the existence of three variable star candidates identified by ATLAS. Section 4 is the conclusion.

2. Instrumentation and methods

The LO is optimized to maintain the photometric precision necessary to observe exoplanet transits. Even large, short-period exoplanets generally only cause a stellar dimming of 30 mmag or less and have a duration of two to three hours. To decisively capture a transit (and a sufficient baseline before and afterwards), noise levels of less than 2 mmag are routinely maintained from dusk to dawn for 10th magnitude stars using one-minute exposures. However, the LO generally collects useful photometry down to V < 17, depending on conditions and exposure length. A single FOV is observed with dimensions: 114' × 86' or 2.7 deg^2. This allows the LO to collect photometry on 500 to 15,000 stars with a photometric cadence of 10 to 60 seconds. Optical filters are not usually used. Within the past two years the LO has successfully observed approximately 70 exoplanet transits. The results presented here are from a single night. In summary, LO provides high-cadence and nearly continuous photometry for up to 15,000 stars over the time span of a night. Appendix A provides more detailed performance characteristics.

Images are collected semi-autonomously using Maxim DL and CCDCOMMANDER. A custom-made software pipeline developed in MATLAB performs the photometry. The software is specifically designed to mitigate the impact of observing from a light-polluted site in Colorado which also typically experiences variable cloud cover each night. The site has a light pollution Bortle index of four, with sky brightness being measured at 20 mag per square arc second on moonless nights.

This paper uses photometry from several other external surveys to validate ours. The ATLAS survey is a wide-field survey with the primary purpose of detecting hazardous asteroids approaching Earth (Tonry *et al.* 2018). It has incidentally become a rich source of detections for other transient evens such as supernovae, flares, gamma-ray bursts, and variable stars down to r ~ 19. Recently, a dedicated list of new variable star candidates was released (Heinze *et al.* 2018). In contrast to the high cadence of observations collected during transit photometry, ATLAS generally makes a few photometric measurements of any given star each night. ATLAS identifies variables and catalogs them using complex frequency analysis techniques and many months of such observations. While the ATLAS archive of new variables is significant, the faintness and low amplitude of many of these variables makes verification difficult. Yet LO also identified 14 of the variables detected by ATLAS. Three of them were only previously identified by ATLAS as candidates and thus likely do not appear in the International Variable Star Index (VSX; Watson *et al.* 2014), operated by the American Association of Variable Star Observers (AAVSO) catalog for this reason.

The All-Sky Automated Survey for Supernovae (ASAS-SN) is an all-sky survey which collects photometry on stars down to V < 17 every two to three days in the search for supernovae (Jayasinghe *et al.* 2018). The survey has incidentally identified over 66,000 variable stars and made their light curves available to the public. Although the observations are often spaced days apart, short-period variables are detectable thanks to an archive of observations extending back to 2014 and frequency analysis techniques.

Unlike ATLAS and ASAS-SN, the mission of the Super Wide Angle Search for Planets (SuperWASP) project is exoplanet discovery, and as a result, it has been responsible for the discovery of nearly 200 exoplanets (Pollacco *et al.* 2006). It can survey the entire sky every 40 minutes, but at a modest accuracy of 1% (or ~ 11 mmag) for bright targets (V = 7–11.5).

Table 1. Existing characteristics of the 14 variable stars observed by LO. ID #4, 10, and 14 are ATLAS candidates confirmed in this paper.

ID	*Name*[1]	*R.A.*[2] °	*Dec.*[2] °	*Mag.*[1]	*Period*[1] *(days)*	*Range*[1]	*Type*[1]	*Discoverer*
1	ROTSE1 J184234.00+420947.9	280.6414	42.1635	13.440	0.319774	0.403	RRC	ROTSE
2	ROTSE1 J184517.00+424010.4	281.3238	42.6700	13.380	0.807725	0.277	ELL	ROTSE
3	ASASSN-V J184116.40+421342	280.3183	42.2284	13.430	0.175226	0.050	DSCT	ASAS-SN
4	2MASS 18441165+4201591	281.0486	42.0331	—	—	—	—	ATLAS candidate(dub)
5	KIC 7176440	282.5124	42.7709	14.293	0.358267	0.115	ECL	Kepler
6	KIC 7173910	281.2031	42.7461	14.360	0.402244	0.132	EW	Kepler
7	WISE J184227.5+422724	280.6149	42.4568	12.429	0.846410	0.357	EA	WISE
8	KIC 6836820	281.4374	42.3286	14.500	0.227270	—	DSCT	Kepler
9	KIC 6836140	281.0407	42.3978	14.646	0.487721	0.245	SD (EW)	Kepler
10	2MASS 18452610+4231055	281.3588	42.5181	—	—	—	—	ATLAS candidate (EW)
11	MarSEC_V13	280.2693	42.6732	15.65	0.333045	0.400	EW	Mar-SEC
12	V351 Lyr	282.3584	42.9808	15.25	0.839481	1.100	AHB1	C. Hoffmeister (1966)
13	CSS_J184816.3+414748	282.0681	41.7965	16.04	0.600642	1.190	RRAG	Catalina
14	2MASS 18465788+4156020	281.7412	41.9339	—	—	—	—	ATLAS candidate (EW)

[1] *Typically from the discovery source (magnitudes zero points can vary greatly based on the survey wavelength sensitivity).*
[2] *From Gaia, J2000 (Gaia Colalb.* et al. *2016, 2018).*

This level of accuracy is sufficient to detect large exoplanets, particularly when its long baseline of observations allows for phase-folding many periods to reduce noise.

The Kepler spacecraft collected photometry with the precision necessary to detect the transits of Earth-sized planets (Borucki *et al.* 2010). Its primary mission monitored a relatively small FOV in the region of Cygnus and Lyra. As a result, the quality of the nearly continuous photometry of stars within this region is unprecedented.

The LO observed a FOV centered on Kepler-8b (R.A. 281.2881°, Dec. 42.4511° J2000) on 7 June 2020, and the number of stars ultimately providing useful light curves was 4,508. The data pipeline flagged merely 14 stars (0.35%) as variables. This low fraction is largely attributed to the fact that LO detections are limited to variables having a period comparable to or less than the 5.3-hour observation window. Three of these variables were not identified as variables in any other survey source except as ATLAS candidates. Existing characteristics for these 14 stars are provided in Table 1. Targets 4, 10, and 14 did not appear in VSX, likely because ATLAS has been the only source to report them as candidates.

3. Results

This section seeks to validate the LO survey by comparing these results to two variables in this FOV having available photometry from several other surveys. Light curves for all 14 variables are subsequently shown, including the three ATLAS candidates that this survey confirms.

3.1. External validation

The availability of external photometry for these variables is given in Table 2. To demonstrate the validity in this survey, LO results are first compared for a known variable that has been observed by all four surveys. The star KIC 7173910 is a W Ursae Majoris-type eclipsing variable (EW) identified initially in Kepler data (Prša *et al.* 2011) and is ID # 6 in this survey. It is V = 14.36 and has a period of 0.402247 day (Prša *et al.* 2011) with an amplitude of 264 mmag. ATLAS observed this variable 151 times over several years and correctly classified it as a contact or near-contact eclipsing binary. Photometry obtained from CasJobs (see Acknowledgements) was phase-folded to the known period. Kepler and SuperWASP data were then retrieved from the NASA Exoplanet Archive (see Acknowledgements). ASAS-SN photometry was obtained directly from the survey's website (Jayasinghe *et al.* 2018). The phase-folded measurements from all these surveys are shown in Figure 1. The detections are clear and consistent among all surveys.

To ensure equity among the comparisons, each survey is binned to have the same density of data in phase space that appears in the sparsest survey, ATLAS in this case. Binning reduces the number of data points but also reduces their statistical scatter so long as the noise is Gaussian (white) as opposed to that caused by instrumental systematics (red). Kepler provides nearly 200,000 data points and is effectively noise-free once binned. Figure 2 shows these binned light curves. ASAS-SN provides 210 raw data points prior to binning, and the SuperWASP data includes 8,573 observations. The value of SuperWASP's persistence in collecting many medium-precision observations is the most evident after binning. The LO results are favorably comparable to ATLAS and ASAS-SN in quality even though LO photometry comes from a single night. Unfortunately, the LO observation duration did not allow for coverage of a full period.

The same approach is followed for the similar study of a star having the same sources of independent data. The star KIC 6836140 (ID #9) has a magnitude of V = 14.646 and is classified by Kepler as a semi-detached (SD) eclipsing binary, a subclass of EW, with a period of 0.487721 day (Prša *et al.* 2011). ATLAS and ASAS-SN both classify it as an EW with an amplitude of 270 mmag. Figure 3 shows the binned light curves of this star from various surveys. All sources agree, including LO results.

A comparison between non-binned LO and binned Kepler results is shown in Figure 4. If Kepler data are considered to be virtually noise free in this case and the two are subtracted, then we have a nearly direct measure of LO noise levels.

Table 2. Light curve availability[1].

ID	Kepler[2]	SuperWASP[2]	ASAS-SN[3]	ATLAS[4]	Notes
1	y	y	y	—	
2	y	y	y	y	
3	—	—	y	y	
4	—	—	—	y	Only identified by ATLAS
5	y	y	—	y	
6	y	y	y	y	First test case, Figures 1 and 2
7	—	—	—	y	Figure 6. STOCH detection by ATLAS of a known EA.
8	y	y	y	y	
9	y	y	y	y	Second test case, Figsures 3 and 4.
10	—	—	y	y	Only identified by ATLAS
11	—	—	y	y	
12	—	—	y	y	
13	—	—	y	y	
14	—	—	y	y	Only identified by ATLAS

[1] *Availability is only marked when the survey also identified a star as variable. Photometry may actually exist for these stars.*
[2] *https://exoplanetarchive.ipac.caltech.edu/*
[3] *https://asas-sn.osu.edu/variables*
[4] *http://mastweb.stsci.edu/*

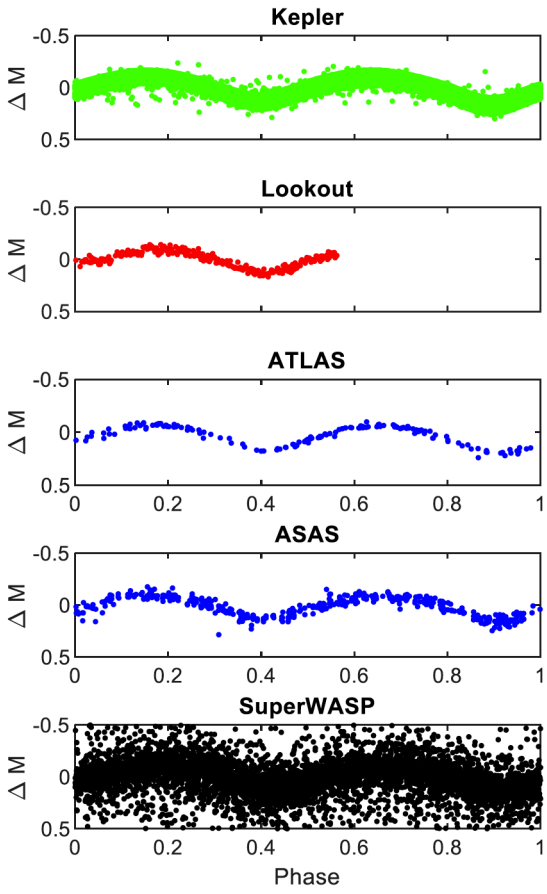

Figure 1. Phase-folded light curves for the EW variable KIC 7173910 (ID #6) from multiple surveys. This star is V = 14.36 and has a period of 0.402244 day. LO results compare well with ATLAS and ASAS-SN. Kepler and SuperWASP light curves appear deceptively noisy. But in fact, the much larger sizes of their datasets allows for greatly improved results once binned.

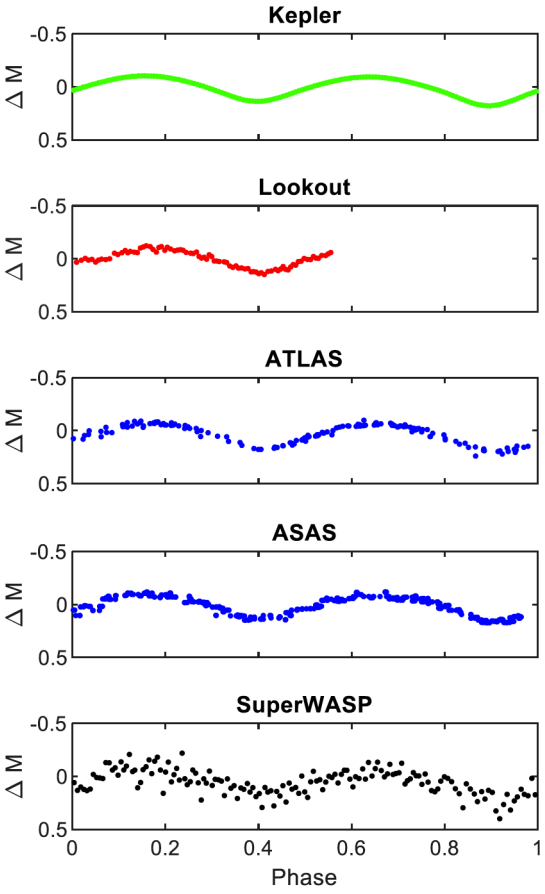

Figure 2. Phase-folded light curves for KIC 7173910 (ID #6) with data binned to a common sampling to fairly compare surveys having widely varying numbers of observations. LO results compare well with other ground-based surveys. SuperWASP noise levels are greatly reduced, and Kepler data appear free of noise after binning.

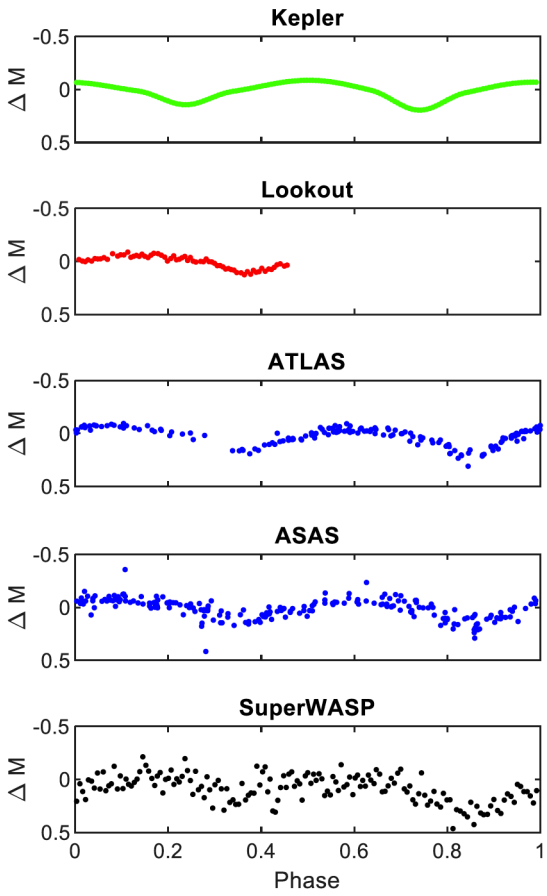

Figure 3. Phase-folded light curves for the EW KIC 6836140 (ID # 9). This star is V = 14.646 and has a period of 0.487721 day. LO results compare well with other ground-based surveys.

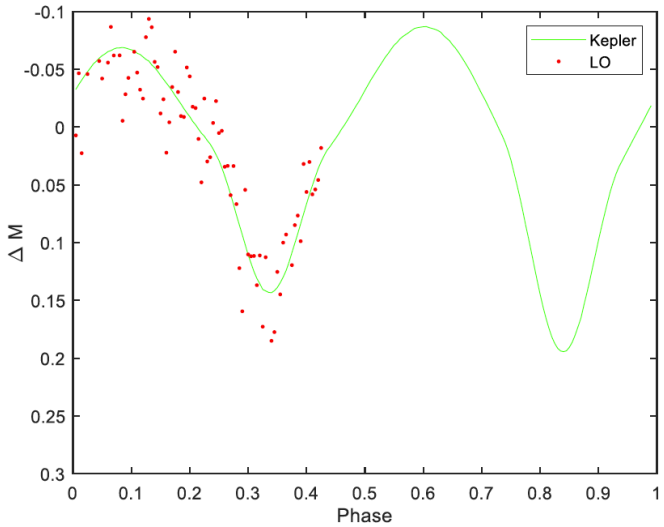

Figure 4. Non-binned LO data (dots) compared to binned Kepler data (solid). Kepler results are practically noise free at this scale and the deviation in LO data from Kepler can be used to measure our noise at 28.4 mmag for this V = 14.6 star.

Doing so yields an RMS of 28.4 mmag, which is consistent with our design goals for a star of this magnitude (see Appendix B).

3.2. Photometric results

Having confidence in the LO light curves, Figure 5 presents the light curves and results for all 14 variable stars detected in this survey. Table 3 provides characteristics derived from this work, when possible.

3.3. ATLAS candidate confirmations

This survey has confirmed three candidate variables previously only identified by ATLAS. They range in magnitude from V = 14.15 to 16.08. ID #4 (2MASS 18441165+4201591) is an ATLAS candidate classified as dubious by their survey. This survey, however, confirms a significant variability. The observation window range is too limited to characterize it completely, but it seems to be a transient event such as an EA eclipsing binary. ID #10 (2MASS 18452610+4231055) clearly shows sinusoid variability, in agreement with the ATLAS classification as an EW. The results for ID #14 (2MASS 18465788+4156020) do not show a significant portion of the period but the LO light curve is consistent with the ATLAS identification as an EW.

We also match a star classified by ATLAS as STOCH to the known EA WISE J184227.5+422724 (Chen *et al.* 2018). The STOCH classification implies "variables that do not fit into any coherent periodic class" (Heinze *et al.* 2018). The inability of ATLAS to classify this variable (ID #7 in our survey) is likely due to the inherent difficulty in the detection of transient events using traditional frequency analysis, which favors sinusoidal patterns (Kovacs *et al.* 2002). Figure 6 shows the light curves from several surveys. The WISE detection clearly shows the primary and secondary eclipses. The ATLAS photometry demonstrates the eclipsing nature of this system once phase-folded to the period established by WISE. For this variable, ASAS-SN observations were poorly sampled during the phase of the transit. Their results are consistent with an EA but would not have been expected to lead to a detection due to their sampling. The LO results clearly show a portion of the primary eclipse.

4. Conclusion

The Lookout Observatory has finished its commissioning phase and demonstrated its photometric goals by automatically identifying short-period variables at a quality that is comparable to other ground-based programs. The data were collected in a single night rather than the years required by the low-cadence surveys (ATLAS and ASAS-SN), for which this is not their primary goal. Of the 14 stars examined here, three ATLAS candidates were confirmed. ATLAS, ASAS-SN, and LO also successfully observed an EA discovered by WISE. The LO has observed many FOVs over the past two years, often multiple times. This survey will continue to focus on exoplanet observation, but variable star data will be released as they become available.

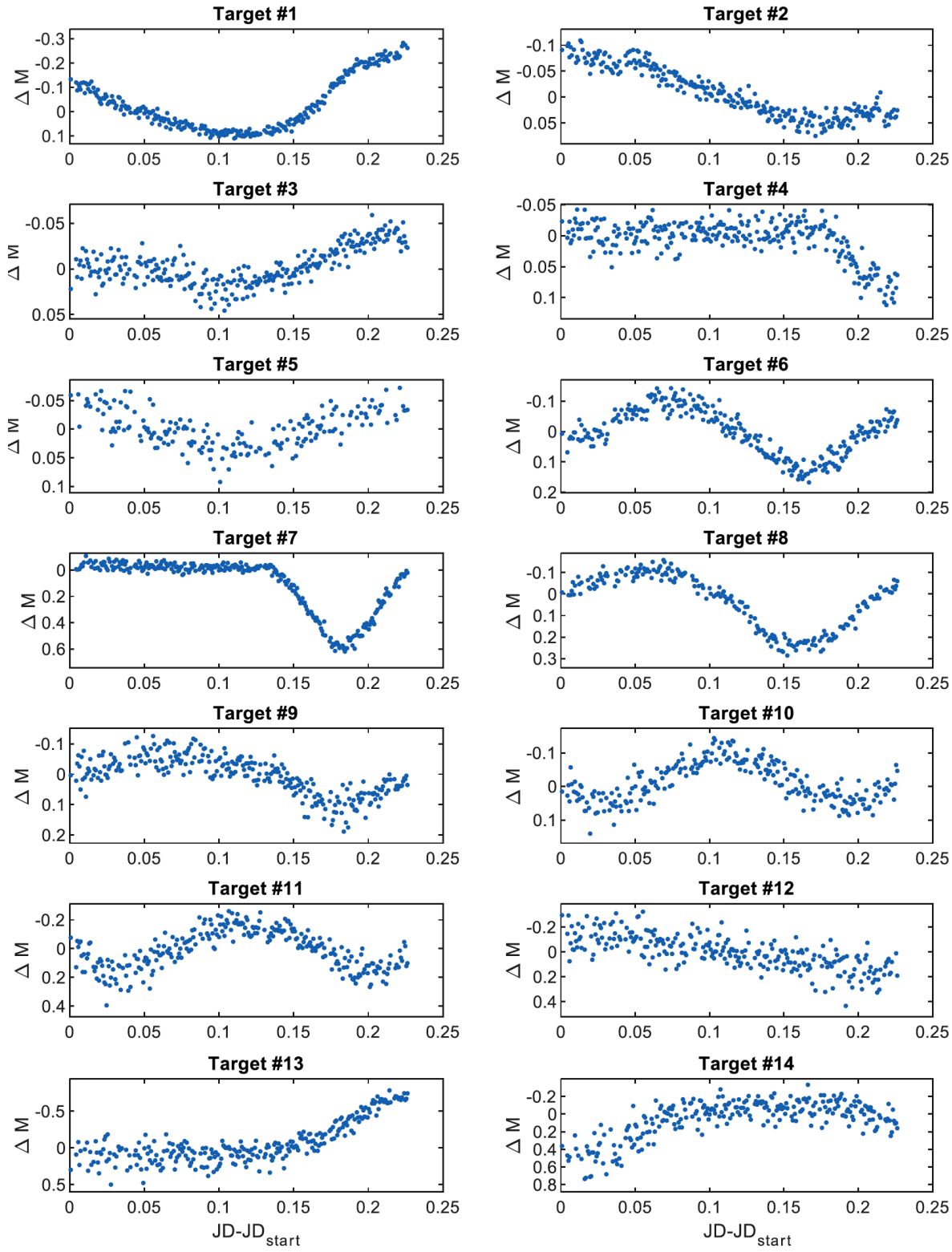

Figure 5. The LO light curves of the 14 variables automatically detected by our software. Targets 4, 10, and 14 do not appear in VSX, likely because they have only been previously reported as ATLAS candidates.

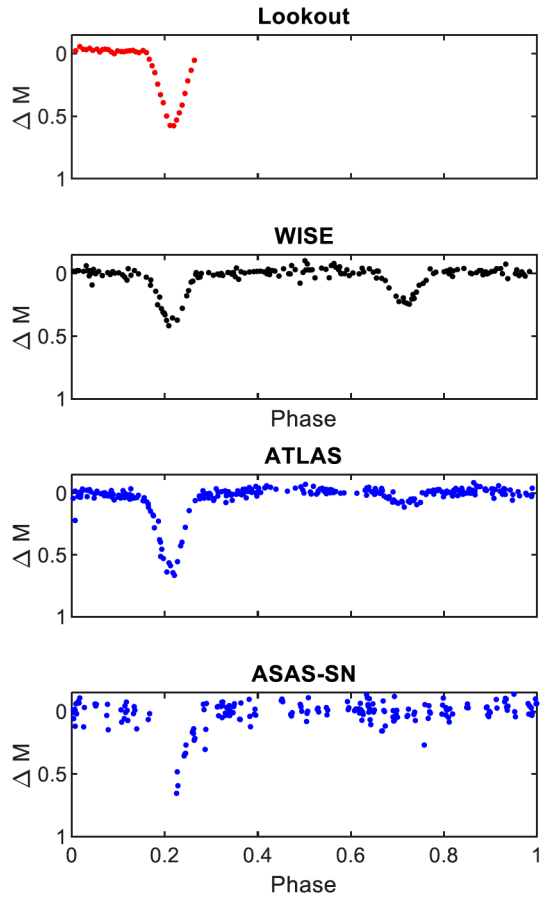

Figure 6. The light curves of variable star ID #7, an EA type binary discovered by WISE. ATLAS and ASAS-SN photometry agree, although those surveys did not initially classify its type.

5. Acknowledgements

In addition to the support of the Astronautical Engineering Department at the U. S. Air Force Academy, the authors would like to thank the LO construction team, Savannah Jane and P. P., as well as Kyle Ziegler, who was instrumental during the proofing process.

CasJobs was used in retrieving ATLAS light curves as authored by the JHU/SDSS team (http://casjobs.sdss.org/CasJobs).

This research has made use of the NASA Exoplanet Archive, which is operated by the California Institute of Technology, under contract with the National Aeronautics and Space Administration under the Exoplanet Exploration Program.

This paper makes use of data from the first public release of the WASP dataset provided by the WASP consortium and services at the NASA Exoplanet Archive, which is operated by the California Institute of Technology, under contract with the National Aeronautics and Space Administration under the Exoplanet Exploration Program.

We acknowledge with thanks the variable star observations from the AAVSO International Database contributed by observers worldwide and used in this research.

PA#: USAFA-DF-2020-337

References

Borucki, W., *et al.* 2010, *Science*, **327**, 977.

Chen, X., Wang, S., Deng, L., de Grijs, R., and Yang, M. 2018, *Astrophys. J., Suppl. Ser.*, **237**, 28.

Gaia Collaboration, et al. 2016, *Astron. Astrophys.*, **595A**, 1.

Gaia Collaboration, et al. 2018, *Astron. Astrophys.*, **616A**, 1.

Heinze, A., *et al.* 2018, *Astron. J.*, **156**, 241.

Hoffmeister, C. 1966, *Astron. Nachr.*, **289**, 139.

Jayasinghe, T., *et al.* 2018, *Mon. Not. Roy. Astron. Soc.*, **477**, 3145.

Kovács, G., Zucker, S, and Mazeh, T. 2002, Astron. Astrophys., **391**, 369.

Pollacco, D., *et al.* 2006, *Publ. Astron. Soc. Pacific*, **118**, 1407.

Prša, A., *et al.* 2011, *Astron. J.*, **141**, 83.

Tonry, J., *et al.* 2018, *Publ. Astron. Soc. Pacific*, **130**, 064505.

Watson, C., Henden, A. A., and Price, C. A. 2014, AAVSO International Variable Star Index VSX (Watson+, 2005–2020; https://www.aavso.org/vsx).

Appendix A: Performance characteristics of the Lookout Observatory

The Lookout Observatory consists of an 11-inch Celestron telescope modified to f/1.9 with a HyperStar. Imaging is done with a ZWO ASI 1600 CMOS camera. LO was constructed by faculty and students of the Astronautical Engineering Department at the U. S. Air Force Academy and focused on consumer grade instruments (entire observatory less than $10,000 USD). It first successfully observed an exoplanet transit in May of 2019. Although it is at an altitude of 7,000 feet, it suffers from suburban light pollution and variable weather. About 20% of nights have long enough periods of clarity to allow for observations.

This team developed a custom data pipeline to allow flexibility in dealing with poor sky conditions as well as issues common to small observatories such as errors in tracking, focus, and mirror flop. It also allows for automated processing of all reasonable stars without user input for targeting, calibration star choice, or photometric aperture selections. Light curves lasting 5.4 hours were produced for 4,508 stars ranging 12–17th magnitude, at a 60-second cadence. The standard deviation of the photometry for each star observed this night is plotted against magnitude in Figure A1. Since most stars are stable, the data create a clear function of expected performance versus magnitude. Photon shot noise is also calculated using the flux of each star and the excess observed noise is used to model scintillation noise and red noise. The standard deviation in magnitude for stable stars of 13th magnitude is approximately 10 mmag and is primarily photon limited. The red noise was calculated to be 0.61 mmag and indicates the ultimate precision possible of any star in this survey, regardless of brightness.

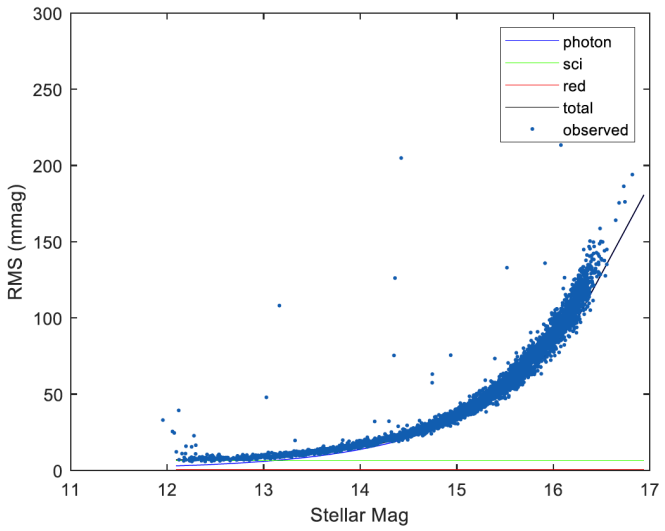

Figure A1. The performance of the LO survey on this night. The precision of the data degrades as expected with increasing magnitude. The standard deviation of the photometry for each of these mostly stable stars creates a curve very much in accordance with the calculated photon limits. Quality is slightly worse because of atmospheric scintillation and the red noise caused by imperfect instrumentation and programming. The instrumental noise is below 10 mmag for V < 13.

Appendix B: Design goals for the Lookout Observatory

Our primary design goal is maintaining noise levels of less than 2 mmag from dusk to dawn for 10th magnitude stars and one-minute exposures. Most stars in this survey are fainter than this. So, we must have a way of scaling results for fainter stars to judge performance.

The photon-limited shot noise, σ, is the square root of the measured flux, F, as seen in Equation 1, where both are measured in photons.

$$\sigma = \sqrt{F} \tag{1}$$

A brighter star will have greater flux and while its noise will increase, the fraction of noise in the overall signal will decrease. The fraction of the signal that is noise will be given by Equation 2.

$$\text{noise fraction} = \frac{\sqrt{F}}{F} = \frac{1}{\sqrt{F}} \tag{2}$$

If we compare two stars of different brightness we can estimate the ratio of precisions with Equation 3. If flux is increased four times, then the relative error will be cut in half.

$$\frac{\sigma_1}{\sigma_2} = \sqrt{\frac{F_2}{F_1}} \tag{3}$$

The ratio of fluxes between a notional V = 10 star, F_{10}, can be related to the flux of target star, F_T, of known magnitude by Equation 4.

$$\frac{F_{10}}{F_T} = 10^{-0.4(M_{10} - M_T)} \tag{4}$$

We have been using the logarithmic magnitude scale to measure our noise, not flux. While the same relationship between brightness and relative noise does not strictly apply when speaking in magnitudes, it is very close so long as the flux values are large, which is the case here. When we combine Equations 3 and 4, we can estimate the RMS (in units of magnitude) for a V = 10 star based on observed error in a target star using Equation 5. This equation also includes the fact that flux is linearly dependent on exposure time, t.

$$RMS_{10} = RMS_T \sqrt{\left(\frac{t}{60}\right) 10^{0.4(M_{10} - M_T)}} \tag{5}$$

For the example in section 3.1, we have a V = 14.75 star demonstrating an RMS of 28.4 mmag using 60-second exposures. Equation 5 yields an equivalent RMS for a V = 10 star under these same conditions of 3.18 mmag.

While this performance is slightly poorer than the design objective, it is comparable. Also, this is an analysis of only one star and not a statistical study of all stars in the FOV. A more comprehensive approach is to note in Figure A1 that the body of data for all stars indicates a noise level of approximately 10.3 mmag at V = 13. Using Equation 5 with this relationship yields an estimated error at V = 10 of 2.58 mmag. Considering that this is based on a single and unremarkable night, we consider this a successful demonstration of our design goals.

An Update on the Periods and Period Changes of the Blazhko RR Lyrae Star XZ Cygni

Dylan Kaneshiro
'Iolani School, 563 Kamoku Street, Honolulu, HI 96826; dtk2101@iolani.org

Horace A. Smith
Department of Physics and Astronomy, Michigan State University, East Lansing, MI 48824; smithhh@msu.edu

Gerard Samolyk
P. O. Box 20677, Greenfield, WI 53220; gsamolyk@wi.rr.com

Received October 15, 2020; revised December 8, 15, 2020; accepted December 17, 2020

Abstract XZ Cygni is an RR Lyrae variable that underwent relatively large changes in its primary and Blazhko periods during the 20th century. Here we use AAVSO photometry obtained between 2001 and 2019 to extend previous studies of this star. Whereas XZ Cygni's fundamental mode and Blazhko periods changed dramatically between 1965 and 1979, those periods have been more stable since the 1980s, although the fundamental period has not been entirely constant. We compare the period change behavior of XZ Cygni with theoretical predictions of period change.

1. Introduction

XZ Cygni (HD 239124, BD +56 2257) was discovered in 1905 and found to be an ab-type RR Lyrae variable (RR0 star) with a period near 0.467 day. It exhibits the Blazhko effect, a periodic modulation in the shape of its light curve. The Blazhko effect is now known to be common among ab-type RR Lyrae stars, and less frequent but not rare among c-type (RR1) RR Lyrae stars (Smolec 2016; Skarka *et al.* 2020; Arellano Ferro *et al.* 2012).

The long term behavior of XZ Cyg was studied by Klepikova (1958), Baldwin (1973), Smith (1975), Pop (1975), Taylor (1975), Bezdenezhny (1988), Baldwin and Samolyk (2003), and LaCluyzé *et al.* (2004). These studies found that the fundamental mode period of XZ Cyg declined slowly in the first half of the 20th century falling from 0.4665878 d at its discovery to 0.4665790 d in 1964. Beginning in 1965, the decline in period became steeper, dropping in steps to reach a minimum of 0.4664464 d between 1974 and 1978 (Baldwin and Samolyk 2003). The direction of period change then suddenly reversed, with the period jumping upward in 1979 to a value near 0.4666938 d, before dropping once again to 0.46659934 d at the close of the 20th century.

As the primary (fundamental mode) period of XZ Cyg changed, so did its Blazhko period. Before 1965, the Blazhko period was about 57.4 days. When the primary period fell to its minimum, the Blazhko period increased to about 58.5 d. Following the 1979 increase in primary period, there was an interval when the Blazhko effect was weak. When it resumed, the Blazhko period was once more near 57.5 d.

Thus, between 1965 and 1979, there appear to have been changes in the structure of XZ Cyg that resulted in relatively large changes in both its fundamental mode and Blazhko periods. In this paper, we investigate the period behavior of XZ Cyg between 2001 and 2019. Has there been any repeat of the large period jumps seen half a century ago, or has XZ Cyg maintained a more sedate rate of period change? How do the period changes of XZ Cyg match theoretical predictions?

2. Observations

During the interval spanned by this study, visual observations of XZ Cyg were supplanted by CCD photometry. Between 2001 and 2019, the AAVSO RR Lyrae star Legacy program received 911 visual observations of XZ Cyg and 86,926 CCD observations in the V band. These observations were downloaded from the AAVSO International Database (AID; Kafka 2020) for our investigation. Because about 98% of the CCD observations contributed to the AID were made with a Johnson V filter, only the V band CCD data were used in this study. These observations were reduced using multiple comparison stars (referred to as ensemble photometry). The comparison stars were chosen using the AAVSO Variable Star Plotter (VSP). The 100 (mag 10.005 V) and 106 (mag 10.579 V) were typically used and the 103 (mag 10.347 V) comparison star was also used when it fit into the field of view. The telescopes used ranged from 20 to 61 cm in aperture.

3. Changes in the primary period

The O–C diagram in Figure 1 indicates that XZ Cyg has not undergone any large change in its primary (fundamental mode) period since 2001. However, a closer look at the O–C diagram for the interval 2003–2019 indicates that a small change in period did occur around 2012 (Figure 2). Linear least squares fits to the O–C values yielded periods of 0.46659846 d ± 0.00000038 d for the interval JD 2452771–2456062, and 0.46659753 d ± 0.00000019 d for the interval JD 2456431–2458825. Figure 2 shows that a parabola also provides a satisfactory fit to the 2003–2019 observations. A parabola implies a constant rate of period change. Because the period change is small in this case, it is difficult to distinguish between

the shallow curve of the second order fit and the fit with two distinct but similar periods. In our Fourier analyses, we adopt the two-line model as a guide to how to divide the observations.

The Period04 Fourier analysis program (Lenz and Breger 2005) was used to validate the fundamental periods within these two intervals. Using Period04 we found the fundamental period in the first interval (9,443 CCD points) to be 0.4665976 ± 0.0000002 d, close to, but slightly smaller than, the result from the O–C diagram. In the second interval (77,483 points) Period04 yielded a period of 0.4665973 ± 0.0000001 d, consistent with the O–C result to within the uncertainties.

4. The Blazhko effect

As noted above, XZ Cyg has long been known to exhibit the Blazhko effect. The recent continuation of this phenomenon is illustrated in Figure 3, which plots data from the AID for 2015. To further investigate the Blazhko effect in XZ Cyg, we used Period04 to pre-whiten the two CCD photometric datasets to remove the fundamental frequency and its six higher harmonics (f0, 2f0, 3f0, … 7f0). In doing this, we divided the data into the two time intervals noted above, 2003 to 2012, and 2012 to 2019. Period04 was then employed to conduct a Fourier analysis of the residuals for each of these two time intervals. In such an analysis the Blazhko effect shows itself as peaks on one or both sides of the fundamental frequency and its lower harmonics (e.g. LaCluyzé *et al.* 2004). Those side-peak frequencies are equal to the fundamental frequency or the harmonic frequency plus or minus the frequency of the Blazhko effect (fBl). We found this pattern of side-peaks to be present in the analyses of the XZ Cyg data, permitting us to determine the length of the Blazhko period. These side-peaks are shown in Figure 4 for the earlier and smaller dataset and in Figures 5 and 6 for the later and larger dataset.

Table 1 shows the strongest side-peak frequencies for JD 2452771–2456062 after removing the primary frequency f0 = 2.1431745 and its harmonics. For the smaller of our two photometric datasets we list only the stronger peaks on the long frequency sides of f0 and 2f0. Table 2 shows similar results for data in the interval JD 2456431–2458825, after removal of f0 = 2.1431756 and its harmonics. In this case, the Fourier diagram was less noisy and both higher and lower side-peak frequencies are listed.

For JD 2452771–2456062, we determined an average Blazhko period of 57.85 days. The formal uncertainties for the two side-peak frequencies are correlated so that the agreement of the two Blazhko periods likely underestimates the actual uncertainty. An uncertainty of about 0.2 d for the Blazhko period is probably more realistic. For JD 2456431–2458825, we determined an average Blazhko period of 57.55 ± 0.03, where the uncertainty is the standard deviation of the mean. An uncertainty of 0.1 d may be more realistic. The difference in the two Blazhko periods, while possibly real, is not highly significant.

Some previous studies of XZ Cyg found evidence for a second Blazhko period, which we call the tertiary period. Muller (1953) found a tertiary period of either 41.7 or 44 days. LaCluyzé *et al.* (2004) found a tertiary period of 41.6 days.

Table 1. Period04 results for the JD 2452771–2456062 data.

Frequency (1/days)	*Notation*	*Blazhko Period (days)*
2.160446	f0 + fBl	57.9
4.303648	2f0 + fBl	57.8

Table 2. Period04 results for the JD 2456431–2458825 data.

Frequency (1/days)	*Notation*	*Blazhko Period (days)*
2.16052541	f0 + fBl	57.64
2.12577107	f0 – fBl	57.46
4.26897525	2f0 – fBl	57.55
6.44687866	3f0 + fBl	57.63
6.41212833	3f0 – fBl	57.48

Table 3. Frequencies found in the search for a tertiary period.

Frequency (1/days)	*Notation*	*Tertiary Period (days)*
2.16717158	f0 + fter	41.67
2.11915428	f0 - fter	41.63
4.31037577	2f0 + fter	41.62
4.26230936	2f0 - fter	41.59
6.45353686	3f0 + fter	41.65
6.40549183	3f0 - fter	41.61

Only our larger JD 2456431–2458825 dataset is adequate for searching for the tertiary period. To search for a tertiary period, we removed not only f0, 2f0, … 7f0 but also the fBl side-frequencies, assuming a Blazhko period of 57.55 d. We did indeed find evidence for a tertiary period, with a value of 41.63 ± 0.01 d, where again the standard deviation of the mean underestimates the true uncertainty (see Figure 7). The beat period of a 41.63- and a 57.55-day period is about 150 days. The annual intervals of observation of XZ Cyg are typically longer than this, but there is usually some annual gap in the observations. Observations extending over as much of the year as possible will help the study of these two periods.

After removing the main frequency, its harmonics, and the side-peaks of the 41.63- and 57.55-day periods, the Fourier spectrum of the residuals shows no clear evidence of an additional period (Figure 8).

5. Conclusions

In the four decades since 1979, changes in both the primary and Blazhko periods of XZ Cyg have been relatively small. There has been no repeat of the episode of large period changes following 1965. In addition to the 57.5-day Blazhko period, the 41.6-day tertiary period found in some previous studies is still present in recent photometry. Interestingly, XZ Cyg showed a slow period decline before the acceleration of that decline in 1965. Since 1979, XZ Cyg has resumed a slow decrease in period. Nonetheless, the recent period of XZ Cyg, 0.4665974 d, is slightly greater than Klepikova's (1958) value for the early 20th century. Thus, despite decades of slow period decrease,

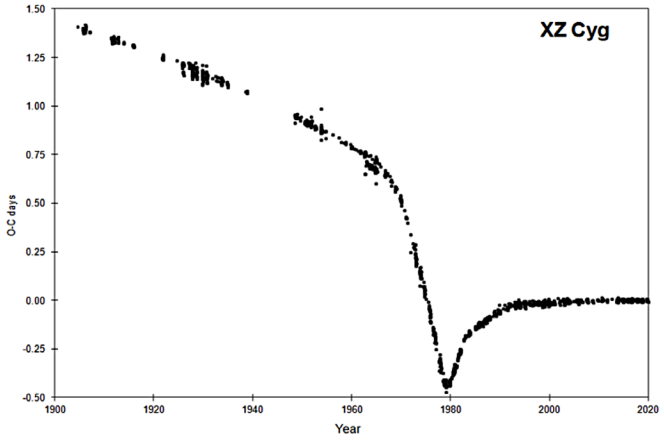

Figure 1. O–C diagram for XZ Cyg for times of maxima from 1900 to 2020. This plot is based on the period of 0.46659753 day. In addition to the AAVSO data, this plot includes times of maxima from the GEOS database.

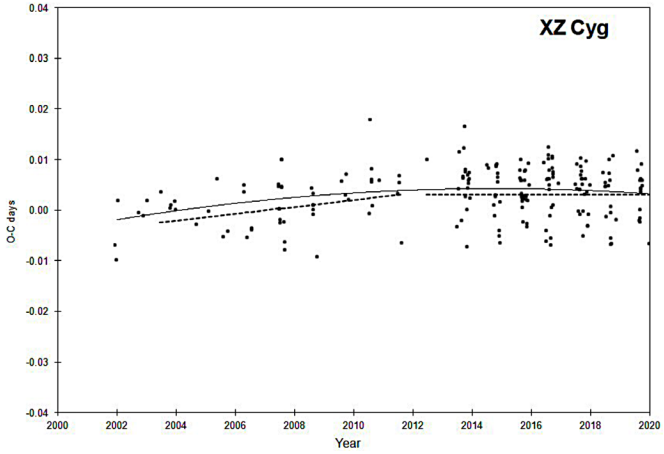

Figure 2. O–C diagram for XZ Cyg for times of maxima from 2002 to 2019. The left dashed line is based on the period of 0.46659846 day. The right dashed line is based on the period of 0.46659753 day. The solid line is a parabolic fit to the 2002–2019 O–C data.

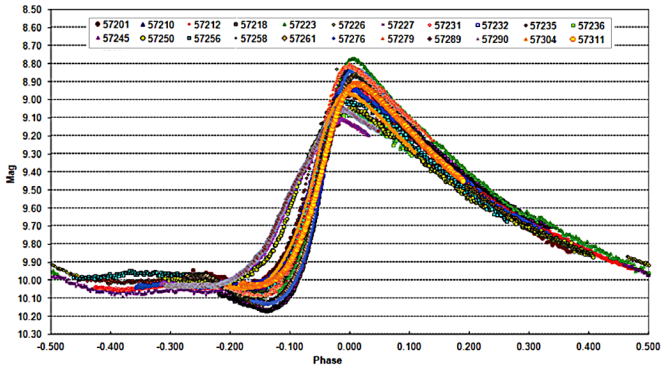

Figure 3. A phase plot of V-band observations made during the 2015 observing season. This plot is based on a period of 0.4665992 d.

the large increase in period around 1979 leaves the period today higher than it was soon after the discovery of XZ Cygni.

Are these period changes consistent with those expected from stellar evolution theory? Periods of pulsating stars obey the pulsation equation $P\sqrt{\rho} = Q$, where P is the pulsation period, ρ is the density of the star, and Q is the pulsation constant. In the long term we expect the observed rate of period change to reflect the slow changes in the size and structure of the star as nuclear burning on the horizontal branch moves the star through the H-R diagram. However, the existence of erratic period changes in some RR Lyrae stars has long been known (e.g. Sweigart and Renzini 1979). Le Borgne *et al.* (2007) investigated the period changes of a large number of field RRab stars using the GEOS database (GEOS 2000–2017). They concluded that, while many RR Lyrae variables showed small rates of period change consistent with the predictions of stellar evolution, others showed large period changes and complicated O–C diagrams requiring other phenomena to be at work.

XZ Cyg clearly falls into the group of RR Lyrae variables with large and erratic period changes. Sweigart and Renzini (1979) proposed that discrete mixing events in the semi-convective zone within RR Lyrae stars could produce abrupt period changes, which could both increase and decrease the period of an RR Lyrae depending upon the exact nature of the mixing. Possibly, mixing events associated with instabilities in the semi-convective zone of XZ Cyg produced the large period changes of 1965–1979.

Taken at face value, the increase in the period of XZ Cyg between 1905 and 2019 implies that its density has decreased. That would be consistent with redward evolution in the H-R diagram, assuming an unchanged pulsation constant. However, the slow period decline over much of that timespan indicates long intervals of increasing density. That would be consistent with blueward evolution. Thus, after more than a century of observation, it is not clear which direction nuclear burning is carrying XZ Cyg through the H-R diagram.

As noted by LaCluyzé *et al.* (2004), the observed changes in the Blazhko period of XZ Cyg argue against any theory which requires that the Blazhko period be exactly equal to, or directly proportional to, the rotation period of the star. To conserve angular momentum, a longer Blazhko period would require a bigger stellar radius, were the Blazhko period directly correlated with the rotation period. However, a larger radius would mean a lower stellar density and a longer fundamental period by the pulsation equation. That is not what has been seen in XZ Cyg.

Finally, we note that Gaia has found evidence that XZ Cyg is a member of a binary star system, though it is not a tight binary (Kervella *et al.* 2019). The orbital period of XZ Cyg is not well-defined, but, if XZ Cyg and its companion are indeed bound, any period is likely in the hundreds or thousands of years (Table A.6 of Kervella *et al.*). It cannot yet be excluded that changing light travel time because of an orbit could produce a very small apparent change in the primary period of XZ Cyg. Any such change would not, however, produce the large and abrupt period changes of the 1960s–1970s.

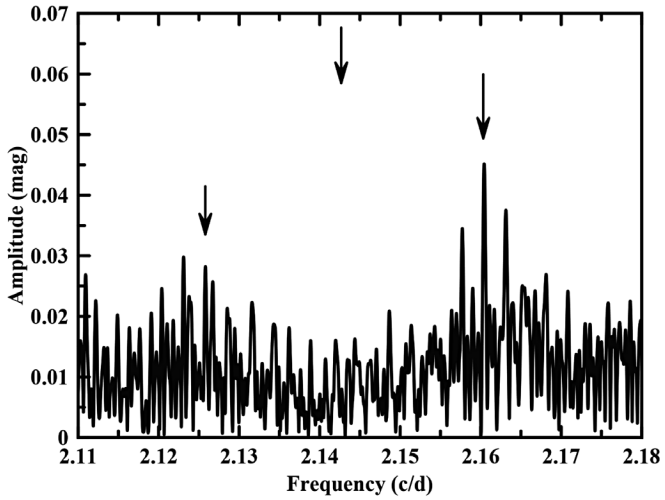

Figure 4. A portion of the Fourier spectrum of XZ Cyg based on the JD 2452771–2456062 photometry, after removal of the main frequency and its harmonics. Peaks due to the 57.85-day Blazhko effect are marked, though only the peak on the long frequency side is strongly significant. Annual alias peaks of these frequencies are also present. The location of the subtracted frequency f0 is also indicated.

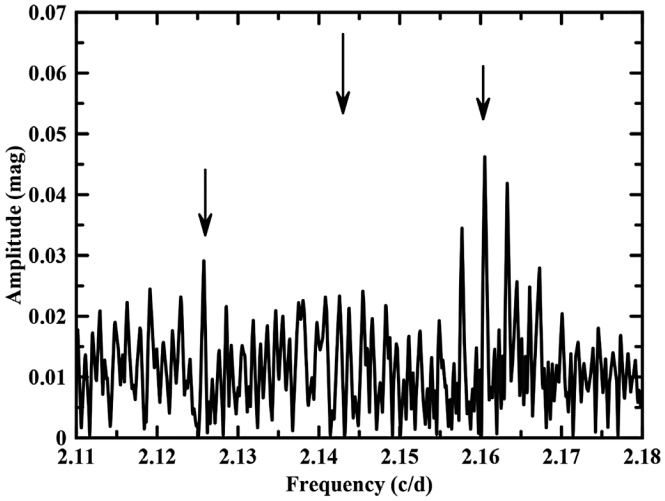

Figure 5. This figure is similar to Figure 4, but is based on photometry from JD 2456431–2458825. In this larger dataset, side-peaks both higher and lower than f0 reveal the presence of a 57.55-day Blazhko period. Annual alias peaks are also present.

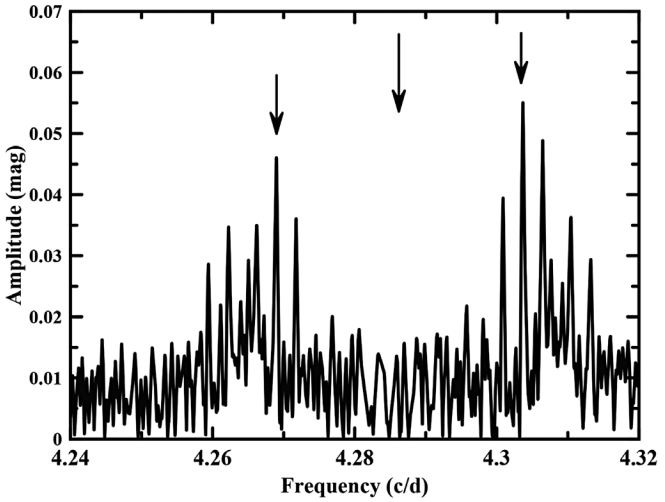

Figure 6. This figure is similar to Figure 5, but for the vicinity of 2f0. Side-peaks due to the 57.55-day Blazhko period are marked, as is the subtracted 2f0 frequency. One cycle per year annual aliases of the Blazhko peaks are evident.

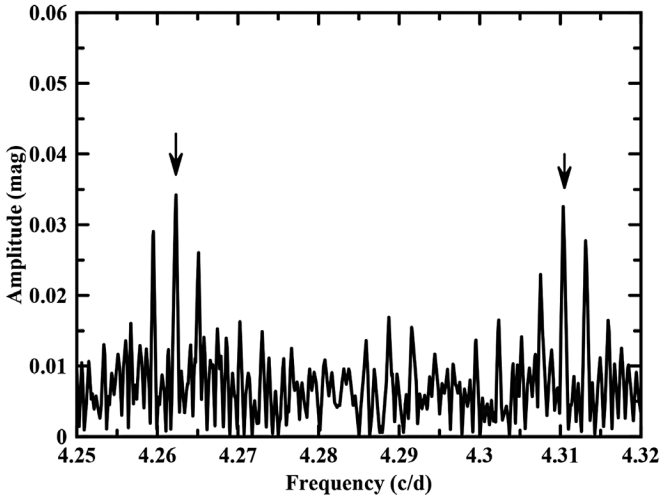

Figure 7. After subtraction of f0, harmonics of f0, and the side-peaks of the 57.55-day Blazhko period, the side-peaks of the 41.63-day period are revealed. Their annual alias peaks are also present. Here we show the peaks around the 2f0 frequency.

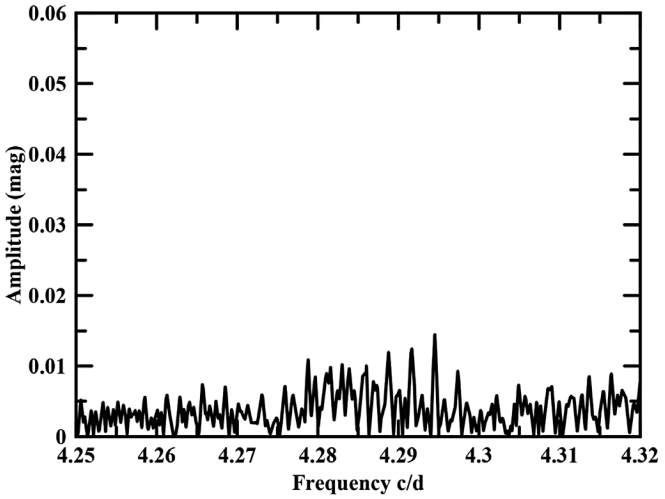

Figure 8. The Fourier spectrum around 2f0 after removal of the main frequency, its harmonics, and the 41.63- and 57.55-day side-peak frequencies. Based on photometry from JD 2456431 to 2458825.

6. Acknowledgements

We acknowledge with thanks the variable star observations from the AAVSO International Database contributed by observers worldwide and used in this research.

We also thank Dr. Yvonne Chan from the Science and iDepartment of ʻIolani School for facilitating this project and guiding Dylan through the research process. We thank the referee for several helpful comments which improved this paper.

References

Arellano Ferro, A., Bramich, D. M., Figuera Jaimes, R., Giridhar, S., and Kuppuswamy, K. 2012, *Mon. Not. Roy. Astron. Soc.*, **420**, 1333.

Baldwin, M. E. 1973, *J. Amer. Assoc. Var. Star Obs.*, **2**, 14.

Baldwin, M. E., and Samolyk, G. 2003, *Observed Maxima Timings of RR Lyr Stars, No. 1*, AAVSO, Cambridge, MA.

Bezdenezhnyi, V. P. 1988, *Inf. Bull. Var. Stars*, No. 3141, 1.

Groupe Européen d'Observation Stellaire (GEOS) 2000–2017, GEOS RR Lyr Database (http://rr-lyr.irap.omp.eu/dbrr/index.php).

Kafka, S. 2020, variable star observations from the AAVSO International Database (https://www.aavso.org/aavso-international-database-aid).

Kervella, P., *et al.* 2019, *Astron. Astrophys.*, **623A**, 117.

Klepikova, L. A. 1958, *Perem. Zvezdy*, **12**, 164.

LaCluyzé, A., *et al.* 2004, *Astron. J.*, **127** 1653.

Le Borgne, J. F., *et al.* 2007, *Astron. Astrophys*., **476**, 307.

Lenz, P., and Breger, M. 2005. *Commun. Asteroseismology*, **146**, 53 (http://www.univie.ac.at/tops/Period04/).

Muller, A. B. 1953, *Bull. Astron. Inst. Netherlands*, **12**, 11.

Pop, V. 1975, *Inf. Bull. Var. Stars*, No. 990, 1.

Skarka, M., Prudil, Z., and Jurcsik, J. 2020, *Mon. Not. Roy. Astron. Soc.*, **494**, 1237.

Smith, H. A. 1975, *Publ. Astron. Soc. Pacific*, **87**, 465.

Smolec, R. 2016, in *37th Meeting of the Polish Astronomical Society, held 7-10 September, 2015 at Adam Mickiewicz University in Poznań, Poland*, eds. A. Różańska, M. Bejger, *Proc. Polish Astron. Soc.*, **3**, 22.

Sweigart, A. V., and Renzini, A. 1979, *Astron. Astrophys.*, **71**, 66.

Taylor, M. 1975, *J. Amer. Assoc. Var. Star Obs.*, **4**, 1, 25.

Four New Variable Stars in the Field of KELT-16

Daniel J. Brossard
Department of Physics and Astronomy, Ball State University, 2000 West University Avenue, Muncie, IN 47306; DBrossard25@gmail.com

Ronald H. Kaitchuck
Department of Physics and Astronomy, Ball State University, 2000 West University Avenue, Muncie, IN 47306; rkaitchu@bsu.edu

Received October 27, 2020; revised December 8, 15, 2020; accepted December 17, 2020

Abstract We present three new variable stars in the field around the star KELT-16, and new period estimates for four previously known contact binary systems in this field, ASASSN-V J205658.12+314215.9, ASASSN-V J205552.88+314615.9, ZTF J205733.78+314612.6, and ZTF J205627.42+315322.4. Due to the short periods of these three new variable stars, and the shape of the light curves, we believe they are contact binary systems. In addition, we have found that the star Gaia DR2 1864883699097368448 is an additional variable star candidate and possibly an eclipsing binary eclipse candidate star.

1. Introduction

Binary systems are a common type of external variable star which can provide a great source of information about the stars in the pairing. Detached binary systems can provide mass and inclination estimates for the pair, while contact binary stars can provide a means to estimate the distance to the system (Rucinski 1994; Chen *et al.* 2018) along with being potential precursors to Type IIb Supernovae (Sravan *et al.* 2019).

Exoplanet transits are another type of external variable. Over 4,000 exoplanets have been found to date, with new discoveries being made every day. Based on recent transit occurrence rate studies that planets could potentially be common enough that there could be up to 0.18 habitable-zone planets per Sun-like star (Kunimoto and Matthews 2020), it's clear that there are many more planets left to be found.

Here we examine two previously known variable stars, ASASSN-V J205658.12+314215.9 and ASASSN-V J205552.88+314615.9, referred to as V1 and V2 respectively, discovered during the All-Sky Automated Survey for Supernovae (Shappee *et al.* 2014). Both stars are listed in the ASAS-SN Catalog of Variable Stars: VI (Jayasinghe *et al.* 2018, 2019).

In addition to these two ASAS-SN variables in this field, there are two other variable stars, ZTF J205733.78+314612.6 and ZTF J205627.42+315322.4, referred to as V5 and V6 respectively, that were announced in July as part of the Zwicky Transient Facility survey (ZTF) (Chen *et al.* 2020). We also discovered three new variable star candidates, labeled as V3, V4, and V7 in this paper. All three of these stars have Gaia and 2-MASS designations and but do not appear to have been the focus of any prior studies. Additional information on the new variable candidates is available in Table 4.

During our observations we detected one star that might have undergone a stellar or exoplanet transit of some kind. As with the variable star candidates it has Gaia and 2-MASS designations but again this star does not appear to have been the focus of any prior studies. Additional information is available in Table 6.

Table 1. Observation dates, filter used, and locations of our observations.

Observation Date (UT)	*Filter*	*Exposure Length (sec.)*	*Images Taken*	*Telescope*
2019-06-06	Cousins R	20	504	SARA-RM
2019-07-03	Cousins R	75	86	BSUO
2019-07-04	Cousins R	75	171	BSUO
2019-07-05	Cousins R	75	26	BSUO
2019-08-03	Cousins R	75	158	BSUO
2019-08-04	Cousins R	75	206	BSUO

2. Observations

Our observations of the region around the known planet hosting star KELT-16 (Oberst *et al.* 2017) were made using two different telescopes, the 0.5-meter at Ball State University Observatory (BSUO) in Muncie, Indiana, and the 1-meter at Observatorio del Roque de los Muchachos (SARA-RM) Observatory on La Palma in the Canary Islands. We obtained a total of 647 images using the FLI camera, cooled to between –28°C and –32°C and mounted on the BSUO telescope. A total of 504 images were taken with the Andor Ikon-L Camera, cooled to –49°C, mounted on the SARA-RM telescope. Between the two locations we had a total of 1,151 images (Table 1).

SARA-RM has a field of view of 11.62' (Keel *et al.* 2016), while the BSUO telescope has a field of view of 30.74'. Because of its large field of view several of the variable star candidates are only visible with the BSUO telescope. Additionally, only two potential comparison stars with known R-band photometry are visible in either of these fields. Unfortunately, the brighter of the two comparison stars was saturated in all of our images, leaving us with one usable comparison star.

Additionally, we used observations listed in the ASAS-SN database for stars V1 and V2. The survey had relatively few images of each field in the same night, leading to potential aliasing in the period estimates. Both stars have period estimates obtained using V-band images from the ASAS-SN survey, which has amassed at least 100 epochs for each field as of 2018. Additional information about these stars is available in Table 2. V1 had 173 magnitude measurements while V2 had 158 measurements listed in the ASAS-SN database as of the time of this paper. Because of the relatively few samples the periods of each should be examined further.

Table 2. Relevant information for the four known variable stars.[1]

Star	*R.A.* °	*Dec.* °	*Designation*	*ASAS-SN V-Mag.*	*ZTF. R-Mag.*	*Period (days)*	*Type*
ASASSN-VJ205658.12+314215.9	314.242	31.704	V1	14.62	—	0.7543	EW
ASASSN-VJ205552.88+314615.9	313.970	31.771	V2	14.29	—	0.6002	EW
ZTF J205733.78+314612.6	314.391	31.770	V5	—	16.35	0.4251	EW
ZTF J205627.42+315322.4	314.114	31.890	V6	—	16.93	0.2925	EW

[1] *Listed in the ASAS-SN catalog and the ZTF catalog. Additional information was from the Gaia mission via the NASA/IPAC Infrared Science Archive (IRSA, Jayasinghe* et al. *2018, 2019; Masci* et al. *2019; Chen* et al. *2020). It should be noted that neither the ASAS-SN nor the ZTF survey had errors assigned to their period estimates.*

Table 3. Information on the reference star.[1]

Comparison Star	*R.A.* *h m s*	*Dec.* ° ′ ″	*R mag*
TYC 2688-139-1	20 57 03.06	+31 42 43.3	12.03 ± 0.03

[1] *Listed in UCAC3 (Zacharias* et al. *2010).*

For V5 and V6 there were 69 G-band images and 68 Sloan R-band images listed in the ZTF Catalog of Periodic Variable Stars (Chen *et al.* 2020). Additional information about both of these stars is available in Table 2.

3. Analysis

3.1. Methodology

3.1.1. Initial image processing

The initial image processing was done using the CCDRED package of IRAF (Valdes 1988) to subtract the master bias, master dark, and the flat field correction. IRAF's SetJD tool was used to add the HJD date of the observations.

3.1.2. Variable detection

After the initial image processing was completed, we performed differential photometry with two different programs, AstroImageJ (AIJ) (Collins *et al.* 2017), and Variability Search Toolkit (VaST) (Sokolovsky and Lebedev 2017).

VaST is a program which specializes in finding objects undergoing brightness variations over the course of a set of observations. VaST operates by creating a source list and then does aperture photometry using the SExtractor program. VaST creates several variability indices for each source and compares it to other sources of similar brightness in order to flag potential variable candidates. VaST then generates a plot comparing the various variability indexes of each set of data. Candidate variable stars have a much higher variability index value than stars of similar instrumental magnitude. This plot feature also allows the user to examine the Individual light curves for any of the stars on the image. Additional information includes the location of the target in the image (Sokolovsky and Lebedev 2017).

AstroImageJ is a program that specializes in performing time-series differential photometry on specific targets. One of the main ways that AIJ differs from VaST is that the user selects the primary targets and the comparison stars to be used instead of every star in the field being compared to one another. This allows for shorter run times for creating the light curves (Collins *et al.* 2017). We had one usable R-band reference star Table 3), so AIJ provided a means to obtain standardized magnitude estimates for each of the stars of interest in the field.

3.1.3. Period determinations

Period estimates for each of the variable stars observed were found using the light curve and period analysis software Peranso 2.0 (Vanmunster 2006). Peranso contains several period analysis methods broadly broken into two categories: Fourier methods which attempt to fit the data to trigonometric functions, or statistical methods which compare individual points to one another. Our data were examined using a variety of methods to find the best-fit period for each variable star.

FALC (Fourier Analysis of Light Curves) (Harris *et al.* 1989) is a Fourier method used for both asteroid and variable star light curve analysis. It operates by breaking the light curve into segments and fitting them using Fourier analysis to fit a set of observations to a period (or phase) of the object's variations (Paunzen and Vanmunster 2016).

ANOVA (Schwarzenberg-Czerny 1996) Is a statistical method that uses orthogonal polynomials to analyze a set of observations. It uses multiple Fourier series to approximate the observation set (Paunzen and Vanmunster 2016; Vanmunster 2006).

PDM (Phase Dispersion Minimization) (Stellingwerf 1978) works by comparing the data to a series of trial frequencies which are then divided into bins. A variance is then calculated for each trial frequency and compared to the original data set (Paunzen and Vanmunster 2016; Vanmunster 2006).

3.2. Known variables in field

Prior to our observations four variable stars had been reported in the wider BSUO field. Two of the variable stars were found in 2018, with one of the two falling within the smaller SARA-RM field. Both are reported as being roughly 14th magnitude (V-band), and as contact binary systems (EW) (ASAS-SN; Jayasinghe *et al.* 2018). The other two previously known variable stars were 16th and 17th R-band magnitude, respectively, were found as part of the ZTF survey, and again are believed to be contact binary stars (Chen *et al.* 2020) (see Table 2).

The locations of the four previously discovered variable stars and the R-band reference star TYC 2688-139-1 are indicated in Figure 1.

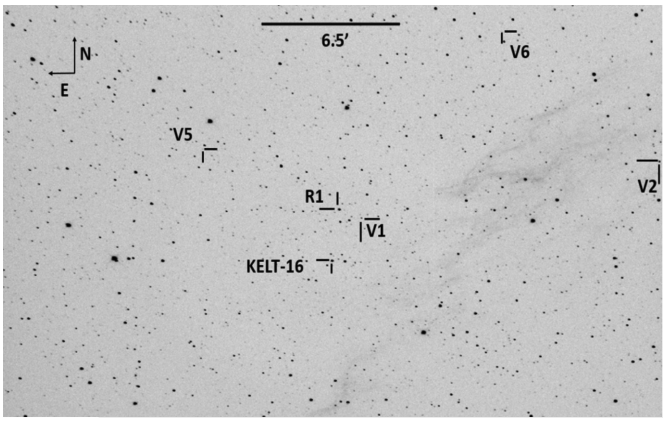

Figure 1. Finding chart for the four known variables in the field. They are labeled V1 (ASASSN-V J205658.12+314215.9), V2 (ASASSN-V J205552.88+314615.9), V5 (ZTF J205733.78+314612.6), and V6 (ZTF J205627.42+315322.4). The magnitude reference star TYC 2688-139-1 is marked as R1 on the image.

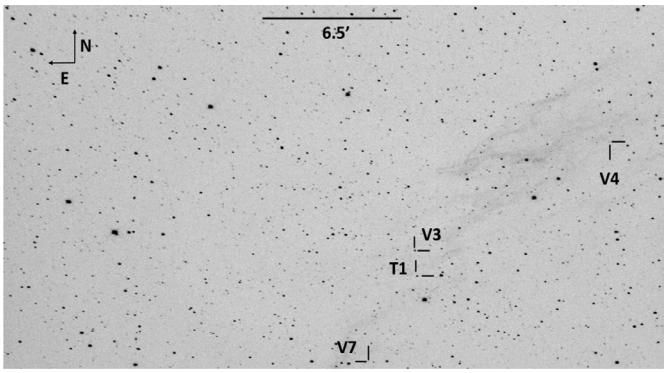

Figure 2. Finding chart for the four new variable star candidates. The image was taken on the night of 4 August 2019. 2MASS J20564622+3138394 is marked as V3, 2MASS J20560314+3145505 is marked as V4, and 2MASS J20565617+3131253 is marked as V7. The potential eclipsing binary candidate Gaia DR2 1864883699097368448 is marked as T1.

Table 4. Information for the three new variable star candidates.

Star	*Designation*	*R.A.*[1] °	*Dec.*[1] °
2MASS J20564622+3138394	V3	314.192	31.644
2MASS J20560314+3145505	V4	314.014	31.764
2MASS J20565617+3131253	V7	314.234	31.524

[1] *From Gaia Collaboration* et al. *(2016, 2018), NASA/IPAC (2020).*

3.3. Variable star candidates

Three new variable star candidates were found using VaST and then confirmed with AstroImageJ. The locations and other known information from the Gaia mission are presented in Table 4. The locations of the three candidate variable stars can be found in Figure 2.

3.4. Period estimates

3.4.1. V1 analysis

V1 refers to the known variable star ASASSN-V J205658.12+314215.9 in this paper. Analysis was done using our R-band images and V-band data taken from the ASAS-SN database.

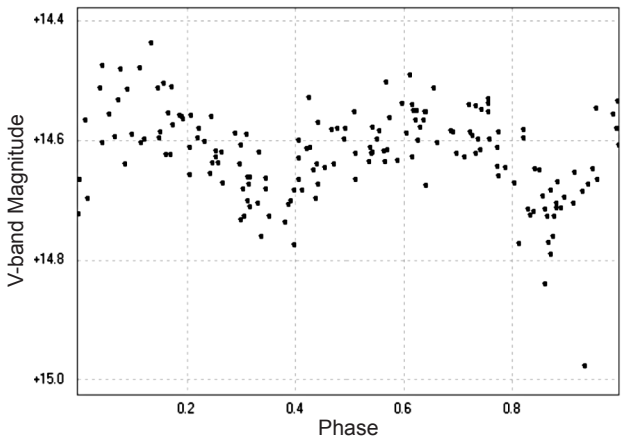

Figure 3a. V-band magnitude-phase plot for V1, showing the ASAS-SN data with the 0.7544 ± 0.0002-day period estimate from the FALC method.

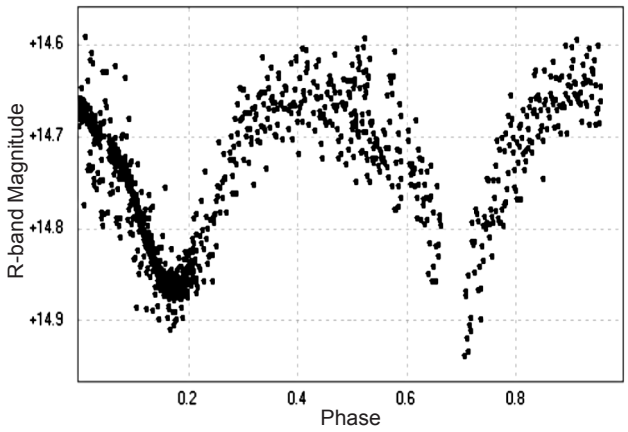

Figure 3b. R-band magnitude-phase plot for V1, showing the 0.7643 ± 0.0009-day period using the ANOVA method.

For the V-band analysis 173 images were used. The FALC method gave a period estimate of 0.7544 ± 0.0002 day (Figure 3a). This matches well the ASAS-SN period estimate of 0.7543 day.

For the R-band analysis a total of 1,110 images were used from the SARA-RM and the BSUO telescopes. From these measurements a mean apparent R-magnitude was determined to be 14.76 ± 0.02.

The Peranso R-band analysis of V1 yielded a period estimate of 0.7643±0.0009 day, found using the ANOVA method. This period can be seen in the magnitude-phase plot in Figure 3b. This is very close to the ASAS-SN period estimate and our estimate of 0.7544 day from the re-analysis of the V-band ASAS-SN data. Because the difference between the V-band and R-band analysis is larger than the error associated with our R-band measurements, there must be an additional reason for the difference. Based on the total number of images taken in each set, and the fact that the V-band data weren't taken using consecutive images but instead a single image per night over a long series of nights, we believe that correct period is closer to the R-band period.

It should be noted in Figure 3b that the more condensed grouping of data seen in the first minimum is due to those observations coming from SARA-RM, which had a much better signal-to-noise ratio than the observations obtained using BSUO.

3.4.2. V2 analysis

With V2, we were again able to do V-band and R-band analysis. Our V-band analysis using the ASAS-SN data found a best fit period of 0.8576 ± 0.0004 day using the PDM method.

Because of its smaller field of view the SARA-RM images of the KELT-16 did not include V2. The analysis was based on the 594 R-band images obtained with BSUO. From our measurements the mean R-magnitude was 14.08 ± 0.02.

Using the ANOVA method from Peranso gave a period estimate of 0.4388 ± 0.0005 day. This period estimate is fairly far from both the 0.600-day period from ASAS-SN and the 0.859-day estimate found in our reanalysis of the V-band photometry listed in the ASAS-SN database. We believe our R-band estimate is closer to the true period based on the larger data set used in the analysis. Additionally, unlike with our reanalyzed V-band ASAS-SN data, our R-band observations have a more noticeable difference in the sizes of the primary and secondary minima, as seen in Figure 4b.

3.4.3. V3 analysis

2MASS J20564622+3138394, now called V3, was near enough to KELT-16 that it was visible in the observations from both SARA-RM and the BSUO telescope, putting the number of R-band measurements available for its analysis at 1110. From these measurements we found that the mean apparent R-magnitude of V3 is 14.0 ± 0.02.

Using the ANOVA method, we arrive at a period estimate of 0.3465 ± 0.0005 day, as seen in Figure 5.

3.4.4. V4 analysis

The remaining four variable star candidates are located outside the field of the SARA-RM images. As such, 2MASS J20560314+3145505, now called V4, only appeared in the larger field of view offered by the BSUO telescope, leaving us with 594 R-band images. This star was much fainter than the previous three stars discussed, having a R-band magnitude estimate of 17.1 ± 0.02.

Because the star is so faint the analysis was done using a flux-phase plot instead of magnitude-phase. Because this star is much fainter the overall pattern showed up much better using flux-phase instead of with the magnitude-phase used for the three brighter stars. Figure 6 shows this data set for the best period found using the ANOVA method of 0.3022 ± 0.0006 day.

3.4.5. V5 analysis

As with V4, our only observations for ZTF J205733.78+314612.6, now called V5, were made at BSUO. The star's mean R-magnitude over the course of our observations was found to be 16.4 ± 0.02, which closely matches the magnitude listed for this star in the ZTF catalog of 16.347 (Chen *et al.* 2020).

We were able to confirm the variability of this star with our data and that it appears to be a contact binary as well. The analysis of our R-band images reveals a period estimate of 0.4282 ± 0.0007 day using the ANOVA method, which closely matches the ZTF survey period of 0.4251 day, as seen in Figure 7. Again, our result is close to the previously reported period estimate but they are outside of the error range. In this case we again believe our estimate is closer to the true period of this system because the number of observations used in our analysis was nearly ten times higher than those used in the ZTF survey's analysis, and because ours included more consecutive measurements as opposed to just a few images per night.

3.4.6. V6 analysis

We estimated that ZTF J205627.42+315322.4, now called V6, has a mean R-magnitude 16.9 ± 0.02. Again, our results closely matched those determined in (Chen *et al.* 2020), with their R-magnitude estimate listed at 16.926. Our analysis yields a period estimate of 0.2981 ± 0.0004 day using the PDM method as seen in Figure 8. This estimate closely matches up well with the period estimate obtained by the ZTF of 0.2925 day. As with the previous cases this estimate closely matches the period estimate made by the prior survey but is still outside of the error estimate. As with previous cases we again believe our estimate is closer to the true period of the system because of the larger amount of data used and because our data are made of consecutive images while it appears the ZTF data are not.

3.4.7. V7 analysis

We estimated 2MASS J20565617+3131253, now called V7, has a mean apparent R-magnitude of 17.7 ± 0.02, which makes it the faintest variable star candidate we've found in this search by over half a magnitude. Because it is so faint, we are only able to determine that V7 is likely a variable star, though we are less certain of its variability type. Figure 9 shows a sinusoidal pattern similar to the other candidate variable stars, though with a much lower signal to noise. It is possible that this is another contact binary star.

We used 582 R-band images to obtain our period estimate. The flux-magnitude plot can be seen in Figure 9. From the Peranso analysis we estimate this variable's period to be 0.2963 ± 0.0005 day using the ANOVA method.

3.4.8. Combined results

Table 5 contains the compiled period and magnitude estimates for each of the variable stars in the field. The R-band images for this analysis come from our own observations, while the V-band analysis was done using data listed in the ASAS-SN database.

3.5. Variable star candidate

In addition to the new variable star candidates listed in Table 5, there was one additional object of interest found. On the night of 6 June 2019 (UT) one other star in the field near Kelt-16 exhibited a variation in brightness. The location of this star, Gaia DR2 1864883699097368448, is marked in Figure 2. Following the same method as the other stars we calculated its R-band magnitude as 13.6 ± 0.02. Table 6 contains some of the previously known information about the star, mostly from the Gaia catalog.

Upon discovering this variation in our SARA-RM observations, we examined our five nights of observations from BSUO, but out of all of our observations the only ones to exhibit this change are our SARA-RM observations.

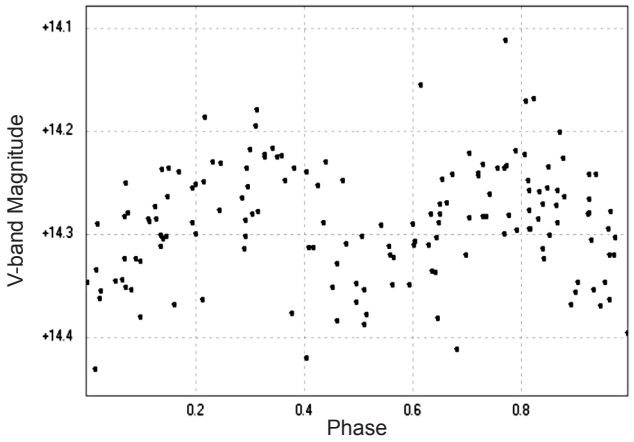

Figure 4a. V-band magnitude-phase plot for V2, showing the ASAS-SN data with the best fit period of 0.8576 ± 0.0004 day using the PDM method.

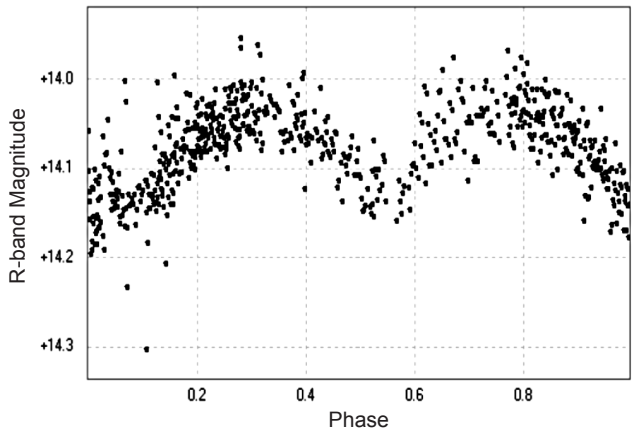

Figure 4b. R-band magnitude-phase plot for V2, showing the ANOVA method magnitude-phase plot of the period 0.4388 ± 0.0005 day.

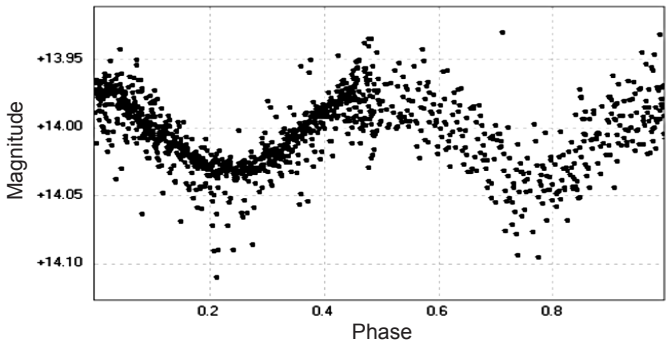

Figure 5. R-band magnitude-phase plot for V3, a period of 0.3465 ± 0.0005 day found using the ANOVA method. As noted in Figure 3b, the darker region in the first minimum is due to SARA-RM observations having a better SNR and so a smaller scatter in the data points.

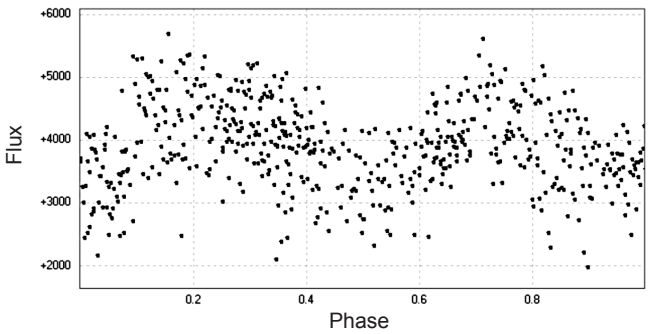

Figure 6. R-band flux-phase plot for V4 showing a period of 0.3022 ± 0.0006 day found using the ANOVA method.

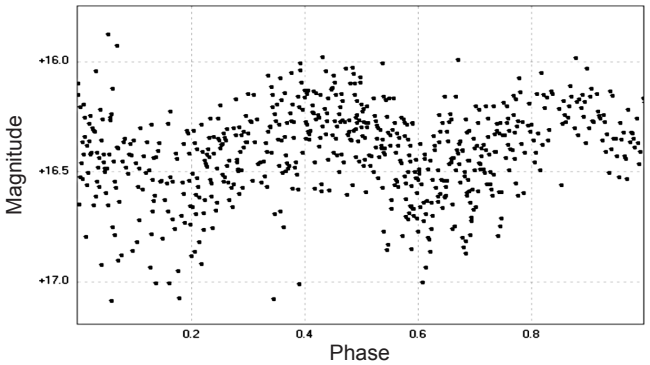

Figure 7. R-band magnitude-phase plot for V5. The flux-phase plot of our R-band data of V5 is for a period of 0.4282 ± 0.0007 day found using the ANOVA method.

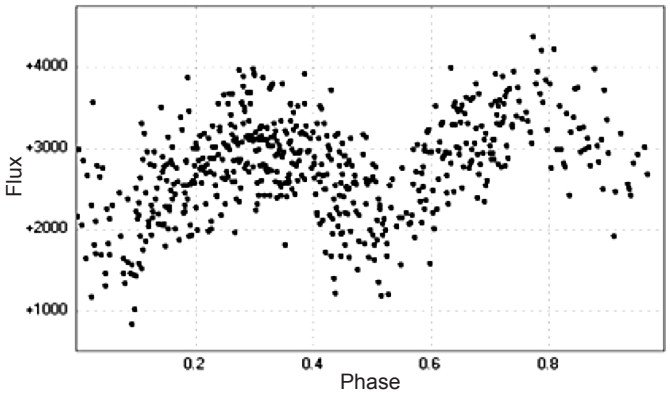

Figure 8: R-band flux-phase plot for V6, showing a period of 0.2981 ± 0.0004 day found using the ANOVA method.

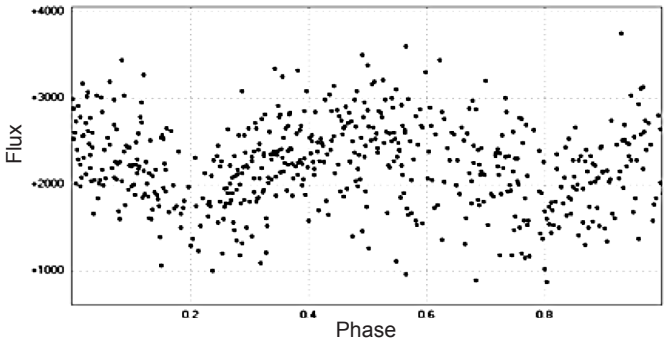

Figure 9. R-band folded flux-phase plot for V7, showing a period of 0.2963 ± 0.0005 day found using the ANOVA method.

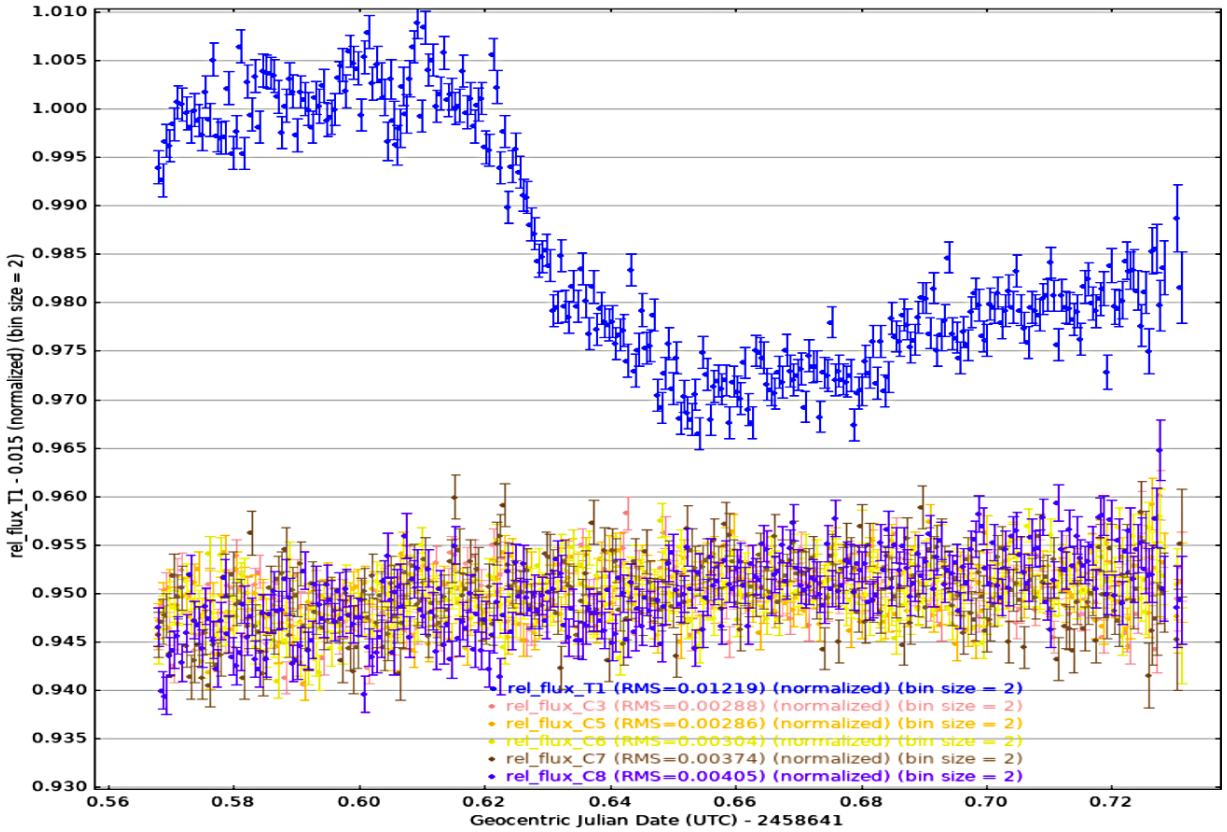

Figure 10a. Comparison of the light curve from Gaia DR2 1864883699097368448 and the first 6 of the 21 comparison stars used to obtain these light curves. Binning is set to 2 on AIJ for this plot. As can be seen there is a clear linear trend to all of the stars in this image, which was removed to measure the depth seen in the target star's light curve.

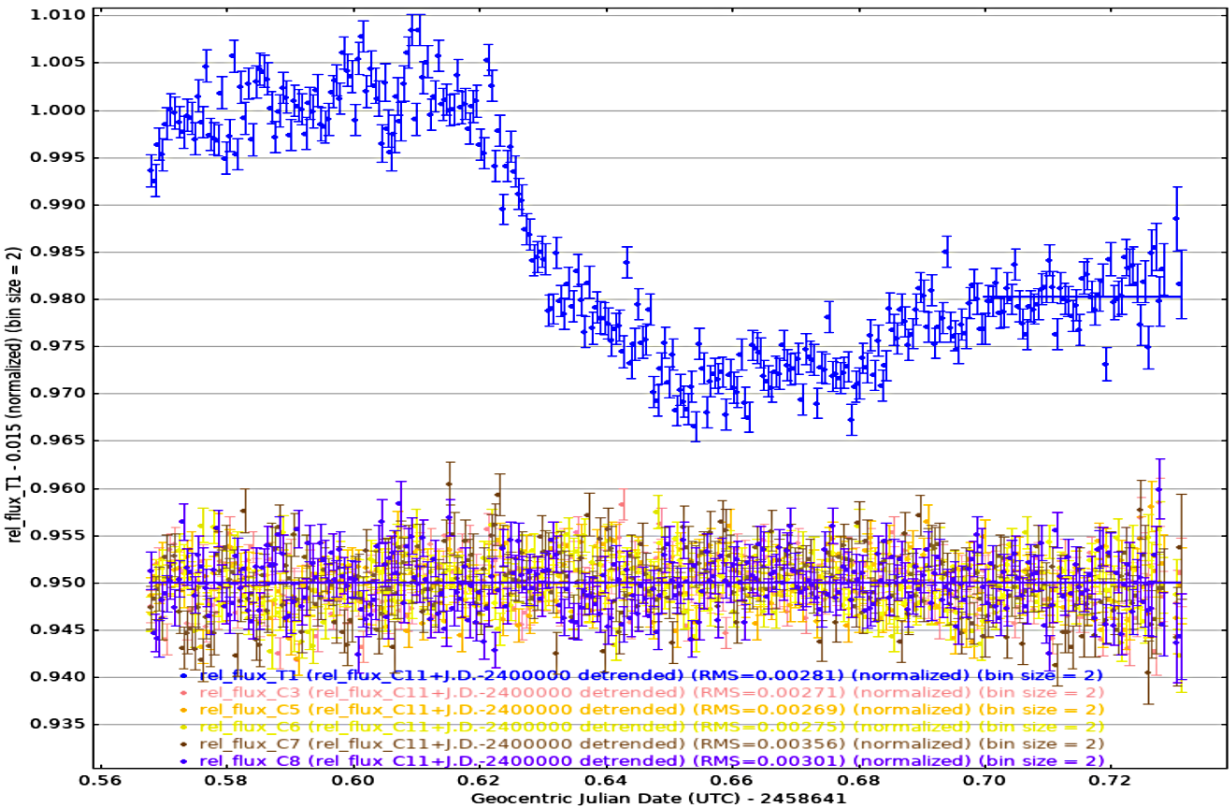

Figure 10b. Detrended Gaia DR2 1864883699097368448 and comparison star light curves, detrended using AIJ.

Table 5. Variable candidate periods and magnitude estimates.

Designation	*Star*	*R-Band Apparent Mag.*	*ASAS-SN/ZTF Survey Period (days)*	*Reanalysis of ASAS-SN V-band Period (days)*	*Our R-band Period (days)*	*Classification*
V1	ASASSN-V J205658.12 +314215.9	14.8 ± 0.02	0.7543	0.7544 ± 0.0002	0.7643 ± 0.0009	EW
V2	ASASSN-V J205552.88 +314615.9	14.1 ± 0.02	0.6002	0.8586 ± 0.0071	0.4388 ± 0.0005	EW
V3	2MASS J20564622+3138394	14.0 ± 0.02	—	—	0.3465 ± 0.0005	EW
V4	2MASS J20560314+3145505	17.1 ± 0.02	—	—	0.3021 ± 0.0006	EW
V5	ZTF J205733.78+314612.6	16.4 ± 0.02	0.4251	—	0.4282 ± 0.0007	EW
V6	ZTF J205627.42+315322.4	16.9 ± 0.02	0.2925	—	0.2981 ± 0.0004	EW
V7	2MASS J20562743+3153225	17.7 ± 0.04	—	—	0.2963 ± 0.0005	Possible EW

Note: As mentioned before, error estimates were not provided for the ASAS-SN and the ZTF survey periods. (Jayasinghe et al. *2018, 2019; Masci* et al. *2019; Chen* et al. *2020).*

Table 6. Gaia information on the possible transit star.[1]

Gaia Designation	*R.A.* °	*Dec.* °	*Parallax (mas)*	*Distance (pc)*	*Temperature K*	*Radius ($R_\odot$)*	*Luminosity ($L_\odot$)*
DR2 1864883699097368448	314.190	31.617	0.965 ± 0.018	$1036.4^{+19.3}_{-18.6}$	6224^{+63}_{-233}	$1.480^{+0.117}_{-0.030}$	2.962 ± 0.153

[1] *From Gaia Collaboration* et al. *(2016, 2018), NASA/IPAC (2020).*

As with the other variable star candidates discussed in the previous sections, we examined the region on the charge-coupled device (CCD) near the star's position, and were able to rule out bad columns or other CCD artifacts affecting the light curve.

The shape of the light curve seen in Figures 10a and 10b, suggests an eclipsing binary system or exoplanet transit. If this is indeed the case, these observations span the ingress phase and an addition 100 minutes until terminated by the approaching dawn. No egress was seen.

As can be seen in Figures 10a and 10b there appears to be a linear trend to not only the target star but the comparison stars as well. After correcting for this trend, the overall depth of the minima is 4.1% of the total flux of the star.

Based on the stellar radius estimate from the Gaia database, listed in Table 6, this star is larger than the sun. If we assume this variation is indeed caused by a transit, we can estimate the planet's radius to be:

$$R_p = 2.98^{+0.35}_{-0.09} R_{Jupiter}$$

Because of the overall depth of the variation, it appears to be more likely to be an eclipsing binary system than an exoplanet transit, although such size is not without precedent for planets, as the directly imaged exoplanet GQ Lupi b was estimated to be 3 Jupiter radii (Neuhäuser *et al.* 2008).

4. Conclusions

In this paper we presented evidence for three new variable stars in the field around the star KELT-16. We provided period estimates for each of these three newly detected variable stars. Based on these periods and their light curves we classified them as likely contact binary stars. Each of the periods for these three stars were less than a day, with the periods ranging from 0.3 to 0.5 day. Additionally, we provided photometry and period analysis of four previously known variable stars in this field.

Finally, on one night, another field star showed a dimming similar to an eclipsing binary system or an exoplanet transit. Either additional observations of this star or a search through archival observations of this region will be necessary to confirm both the existence of this object and whether it is planetary or stellar in nature.

5. Acknowledgements

We thank Ball State University and the SARA consortium for providing the observatories and the observing time used in this search without which this research would not have been possible.

Additionally, this work made use of public data provided by both the ASAS-SN survey and the ZTF survey during our V-band analysis and as a check for our R-band analysis, respectively.

Finally, thank you to the anonymous referee for their valuable comments during the referee process.

References

Chen, X., Deng, L., de Grijs, R., Wang, S., and Feng, Y. 2018, *Astrophys. J.*, **859**, 140.

Chen, X., Wang, S., Deng, L., de Grijs, R., Yang, M., and Tian, H. 2020, *Astrophys. J., Suppl. Ser.*, **249**, 18.

Collins, K. A., Kielkopf, J. F., Stassun, K. G., and Hessman, F. V. 2017, *Astron. J.*, **153**, 77 (arXiv:1701.04817v1).

Gaia Collaboration, *et al.* 2016, *Astron. Astrophys.*, **595A**, 1.

Gaia Collaboration, *et al.* 2018, *Astron. Astrophys.*, **616A**, 1.

Harris, A. W., *et al.* 1989, *Icarus*, **77**, 171.

Henden, A. A., and Kaitchuck, R. H. 1990, *Astronomical Photometry: A Text and Handbook for the Advanced Amateur and Professional Astronomer*, Willmann-Bell, Richmond, VA.

Jayasinghe, T., *et al.* 2018, *Mon. Not. Roy. Astron. Soc.*, **477**, 3145.

Jayasinghe, T., *et al.* 2019, The ASAS-SN Catalog of Variable Stars VI (arXiv:1910.14187v1), (https://asas-sn.osu.edu/variables/AP10960259), (https://asas-sn.osu.edu/variables/AP10971522).

Keel, W. C., *et al.* 2016, "The Remote Observatories of the Southeastern Association for Research in Astronomy (SARA)", (arXiv:1608.06245).

Kunimoto, M., and Matthews, J. M. 2020, *Astron. J.*, **159**, 248.

Masci, F. J., *et al.* 2019, *Publ. Astron. Soc. Pacific*, **131**, 018003.

NASA/IPAC Infrared Science Archive (IRSA). 2020 (https://irsa.ipac.caltech.edu).

Neuhäuser, R., Mugrauer, M., Seifahrt, A., Schmidt, T. O. B., and Vogt, N. 2008, *Astron. Astrophys.*, **484**, 281.

Oberst, T. E., *et. al.* 2017, *Astron. J.*, **153**, 97.

Paunzen, E., and Vanmunster, T. 2016, *Astron. Nachr.*, **337**, 239 (arXiv:1602.05329).

Rucinski, S. M. 1994, *Publ. Astron. Soc. Pacific*, **106**, 462.

Schwarzenberg-Czerny, A. 1996, *Astrophys. J., Lett.*, **460**, L107.

Shappee, B. J., *et al.* 2014, *Astrophys. J.*, **788**, 48.

Sokolovsky, K. V., and Lebedev A. A. 2017, VaST: Variability Search Toolkit, Astrophysics Source Code Library, record ascl:1704.005.

Sravan, N., Marchant, P., and Kalogera, V. 2019, "Progenitors of Type IIb Supernovae: I. Evolutionary Pathways and Rates" (arXiv:1808.07580v2).

Stellingwerf, R. F. 1978, *Astrophys. J.*, **224**, 953.

Valdes, F. 1988, in *Instrumentation for Ground-Based Optical Astronomy: Present and Future—The 9th Santa Cruz Summer Workshop in Astronomy and Astrophysics, July 13–July 24, 1987, Lick Observatory,* ed. L. B. Robinson, Springer-Verlag, New York, 417.

Vanmunster, T. 2006, light curve and period analysis software, peranso v.2.0 (http://www.cbabelgium.com/peranso).

Zacharias, N., *et al.* 2010, *Astron. J.*, **139**, 2184.

A Spectroscopic Study of the Variable Star T Centauri Over a 91-day Cycle, and the Effects of Titanium Oxide on Its Atmosphere

Julian F. West
Astronomical Association of Queensland (AAQ), P. O. Box 6101, St. Lucia, Queensland 4067, Australia; spectroscopy@aaq.org.au

Benedict Pace
54 Bowley Street, Hendra, Queensland 4011, Australia; ben_penny1@bigpond.com

Received November 9, 2020; revised March 7, 2021; accepted March 15, 2021

Abstract We observed spectra of the large amplitude semiregular variable T Centauri during a complete 91-day period, which were subsequently combined with contemporaneous photometric data from the AAVSO International Database. The analysis of these data, together with other reference material, has enabled us to estimate a mean photospheric radius of T Centauri at ~94 $R_\odot$, and to develop a simple model reflecting the effects of the formation of titanium oxide in the star's atmosphere as it cools through minimum brightness. Our model incorporated the variation in atmospheric opacity due to TiO and, in comparison with the observed magnitudes, indicated an increase of 20–40% in the apparent stellar radius, as observed in the visual and near-infrared bands as the star cooled mid-phase.

1. Introduction

Miras and other large amplitude semiregular variables have long periods of between 100 and 1,000 days, and visual amplitudes of at least 2.5 magnitudes, but in some cases up to 10 magnitudes (Percy 2007). They are enormous stars, with radii often extending to ~2 AU, or several hundred solar radii. They are also cool, generally of spectral type M, and metals in their extended atmospheres can form molecules such as titanium oxide (TiO) and vanadium oxide (VO) as they cool towards minimum light. This has been described as creating a "visual surface" far above the true stellar surface—the photosphere—if the optical depth is sufficiently great and can therefore affect the apparent radius of the star (Reid and Goldston 2002a, b). Our paper explores these issues for T Centauri based on extensive captured spectra, together with photometric data from the AAVSO's International Database of variable stars (Kafka 2020). These data have been used to estimate a mean photospheric radius of the star for the purposes of calculation (but for which little information was readily available), and to develop a simple model of the behavior of the complex atmosphere and the increase in the apparent "effective radius" related to the formation of atmospheric TiO.

Our broader project involves the examination of a number of southern Mira variable stars—which may not have been well studied by northern hemisphere astronomers—with a particular focus on their spectral variation and the effects of metallic oxides in their atmospheres. Ten Miras were selected with a broad range of period, magnitude, and spectral type, well spread out in Right Ascension, to permit observations throughout the year. Each candidate star was allocated a reference star, to enable an accurate determination of, and correction for, instrument response. T Cen was included as a candidate in this project as it is indicated as a Mira variable in the SIMBAD database (Wenger *et al.* 2000), although in the wider literature it is more commonly listed as a large amplitude semiregular variable, of type SRa (Lebzelter *et al.* 2005; Lançon and Mouhcine 2002); it is also listed by the AAVSO as a form of RV Tauri semiregular variable. Nevertheless, its visual amplitude regularly exceeds the 2.5-magnitude threshold specified by the *General Catalogue of Variable Stars* (GCVS; Samus *et al.* 2017) for inclusion as a Mira. Its amplitude in spectral type is similar to that of other Miras, such as S Car, X Men, and SW Hya, whereas its spectroscopic behavior beyond 1μm reinforces the SRa classification (Lançon and Wood 2000). These potentially mixed characteristics leave T Cen as an interesting object whose behavior we have tried to model within the scope of our available data, and which may in turn facilitate interesting comparisons with other Mira variables within our study.

2. Observations

2.1. Spectra

The spectra of T Cen were captured at the Hendra, Queensland, observatory located at latitude 27.42° S and longitude 153.06° E, at an altitude of 26 m. The instruments used were a Takahashi 180ED telescope on an EM200 mount, equipped with a 2× Barlow and a Spectra 200 Littrow slit spectrograph manufactured by JTW Astronomy. The spectrograph was equipped with a grating of 600 lines/mm, giving R ~ 2000. Spectra were recorded on an Atik 383L+ monochrome CCD camera, cooled to –10° C. The grating was set to record a wavelength range of λλ 6400–7600, with multiple 10-minute subframes captured to ensure a signal to noise ratio of at least 50 when the star was at minimum. Wavelength calibration spectra were captured using an integrated neon source, and corresponding spectra were also recorded for the nearby designated reference star, ι Cen (A2 V), at each observing session.

The captured spectrograms were processed using the software program ISIS: Integrated Spectrographic Innovative Software, developed and supported by Christian Buil (Buil 2019). This program simplifies the processing of spectra, and applies flat fields, master bias, dark, and "hot pixel" frames and takes account of tilt and slant occurring in the recorded

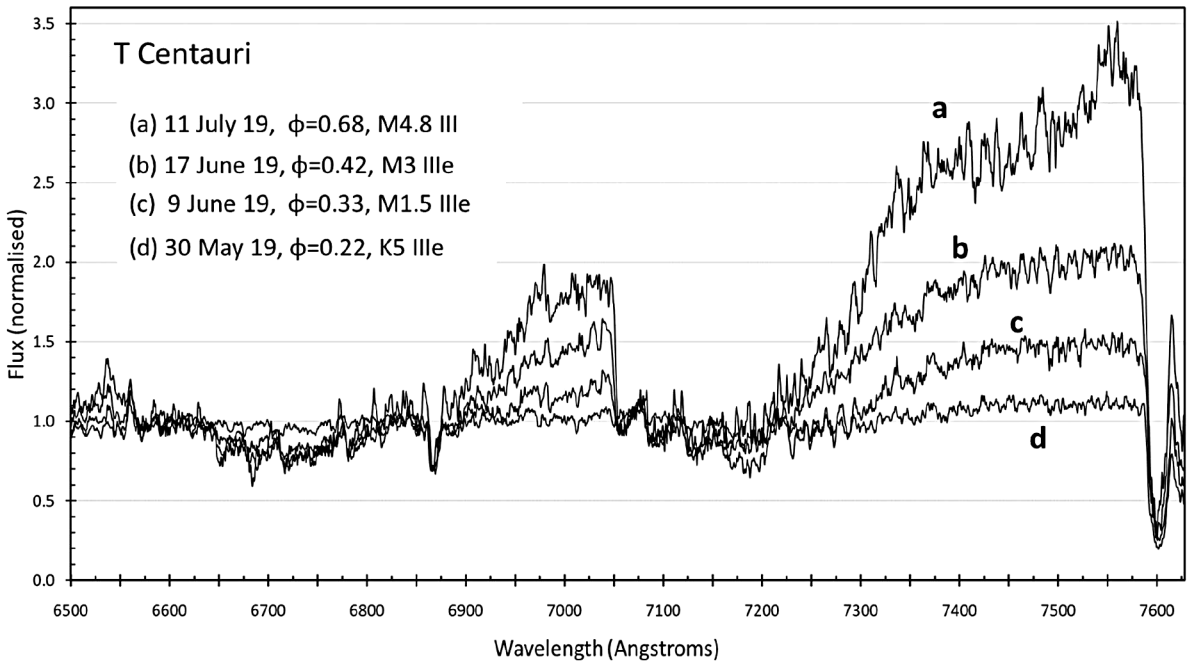

Figure 1. Example captured spectra, normalized at λ6610; the legend shows phase and spectral type, illustrating both maximum light in May 2019 and minimum light in July 2019.

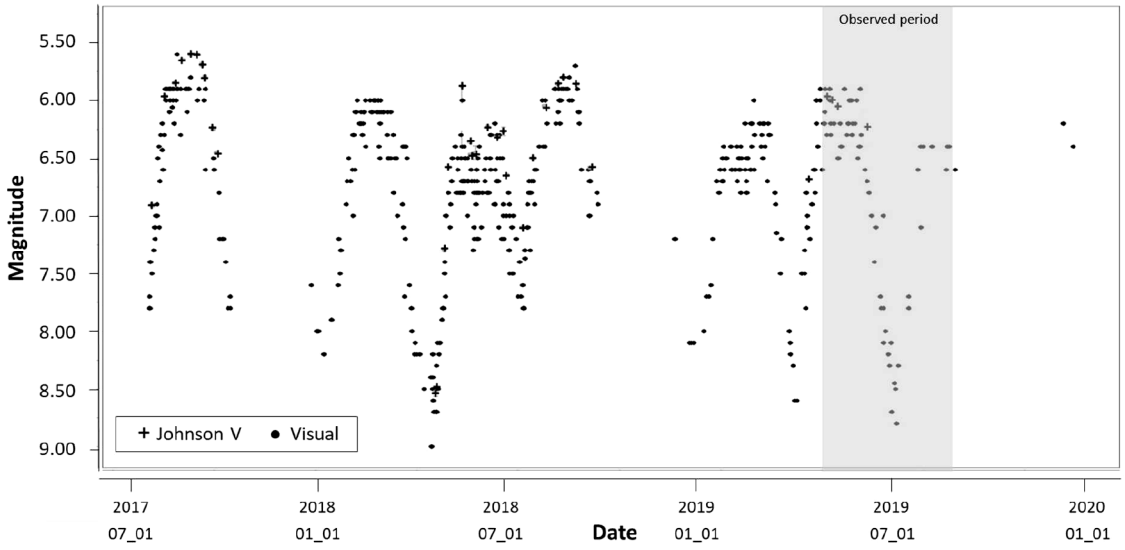

Figure 2. Observed apparent magnitude m_v of T Cen from July 2017 to the end of 2019; the shaded section is the period of observations used in this paper (from the AAVSO International Database, Kafka 2020).

spectrograms. It also applies the instrument response correction derived from the reference star and normalizes the target spectra at the specified λ6610. Examples of the captured spectra are compared in Figure 1, and profiles of all spectra referenced in the tables are also shown in the Appendix. In addition, original copies of these spectra in .fit format may be accessed through the AAVSO ftp site at

ftp://ftp.aavso.org/public/datasets/west491-fitsspectra.zip.

We classified the spectra visually using the XCLASSMIRA program, adapted from the XCLASS and MKCLASS programs of Professor R. O. Gray (Gray and Corbally 2014). XCLASSMIRA provides classification capabilities at the red end of the visual spectrum (as opposed to the more conventional blue end used by XCLASS), better suited to cooler stars, and uses a library of reference spectra developed at the Astronomical Association of Queensland (AAQ) for that purpose.

2.2. Photometric data

We did not observe T Cen photometrically during the spectroscopy observations. We therefore referred to the extensive resource provided by the American Association of Variable Star Observers (AAVSO), which offers a long historical record of apparent magnitudes of variable stars including T Cen. However, these observations are mostly visual and commonly vary by ±0.25 mag (or more) so some interpretation was required. The AAVSO record of observed m_v for T Cen over

an extended period is shown in Figure 2, illustrating a regular amplitude in m_v of well over 2.5 magnitudes, and its regular period of 90.7 days (Kafka 2020).

The apparent visual magnitude data available from the AAVSO has been used in section 3.3 to develop a set of bolometric magnitudes and luminosity values to compare with those calculated directly from the spectra themselves.

3. Analysis and results

By themselves, neither the captured spectra nor the observed magnitudes provided by the AAVSO gave a complete picture of the behavior of T Cen and its atmosphere throughout its period. Our analysis of the captured spectra, together with readily available reference data, was conducted in two stages: first, the expected luminosities and magnitudes were calculated, as outlined in section 3.1, for comparison with the observed magnitudes from the AAVSO. Second, the 18 key spectra represented in the tables and figures were rectified, setting the continuum at unity, to enable the absorption of light by the atmospheric TiO to be measured by wavelength across the cycle (section 3.2), to indicate the atmospheric optical depth.

The calculated (expected) magnitudes from section 3.1 were then compared with the magnitudes and luminosities derived from the AAVSO's corresponding T Cen observations (section 3.3) to enable disparities to be identified. The reconciliation of these differences is discussed in section 3.4, together with an interpretation of the results, including estimates of the apparent "effective radius" of T Cen when affected by TiO during minimum light. The optical depth of the stellar atmosphere, derived from the absorption measurements, is also considered in this context and in the Discussion (section 4).

3.1. Captured spectra: calculation of magnitudes

Following data reduction of the captured spectra, 53 in total, 33 were selected to provide a thorough coverage of the spectral variations across the complete period, without undue repetition. These were then visually classified by spectral type using the XCLASSMIRA application and the AAQ's library of Mira reference spectra. In addition, the phase was calculated from the observation date, using ephemerides from the AAVSO, with the peak of the light curve on 2019 May 10 defined as phase zero and a period of 90.7 days. The standard effective temperature indicated by each spectrum was then sourced from "Appendix B: Calibrations of the MK System" (Gray and Corbally 2009). To enable a comparison with the photometric observations of the AAVSO, the spectral classifications and their corresponding MK temperatures (for giant stars) were used to calculate the expected luminosity and bolometric magnitude of T Cen for each spectrum, from which were derived absolute and apparent visual magnitudes. The classified spectral types, temperatures, and results are shown in Table 1, and an explanation of the calculations and assumptions follows. The results are plotted by phase in Figure 6 (in section 3.3), which also illustrates both the values observed by the AAVSO contributors and the revised calculated magnitudes resulting from the comparison.

Luminosity was calculated using the Stefan-Boltzmann formula:

$$L = 4\pi R^2 \sigma T^4 \quad (1)$$

where R is the stellar radius (m), T the temperature (K), and σ is the Stefan-Boltzmann constant ($5.67 \times 10^{-8}\ W \cdot m^{-2} \cdot K^{-4}$).

Little information was readily available on the radius of T Cen; a value of 4.5×10^{10} m was adopted as a starting point, being $\sim 65\ R_\odot$, obtained from Universe Guide (2020). The radius of a Mira has been shown to vary, and interferometric measurements at 11 μm of Mira (o Ceti) itself have indicated variations with phase of perhaps 10% (Weiner *et al.* 2003a, Figure 5). Measurements of the radial velocity of T Cen (Lebzelter *et al.* 2005) show variations from 24 km s^{-1} to 36 km s^{-1}, an amplitude of ± 6 km s^{-1}, inferring significant pulsation with the mean radius occurring at phase ~0.8.

Luminosity is more dependent on temperature (at the fourth power), so the radius of the photosphere was assumed to be constant for the purposes of these initial calculations.

Luminosity L (in Watts) may be converted into an absolute bolometric magnitude using the following equation:

$$M_{Bol} = -2.5 \log (L / L_0) \quad (2)$$

where L_0 is the zero point of the absolute bolometric magnitude scale and is defined as the following value:

$L_0 = 3.0128 \times 10^{28}$ W (Mamajek *et al.* 2015).

Bolometric conversion factors (Kaler 1989), BC_v, which are dependent on stellar temperature, were subtracted to convert bolometric magnitudes to absolute visual magnitudes, M_v. Then, applying the distance modulus:

$$m_v = M_v - 5 + 5 \log (d) \quad (3)$$

for 430 pc (parallax of 2.3248 milliarcseconds) gave the anticipated apparent magnitude (m_v) for each of the captured spectra.

These magnitudes are compared with their corresponding observed values in section 3.3.

3.2. Captured spectra: measurement of TiO transmittance and optical depth

To estimate the direct effects of atmospheric TiO in the range covered by our captured spectra, the levels of absorption across the specific TiO absorption bands in those spectra were examined. However, the level of the continuum in cool stars increases rapidly with increasing wavelength, especially so in the later M spectral classes; the required interpolation makes the measurement of depth across broad absorption bands difficult. A feature of XCLASS, included in its XMK25 display routine and therefore implemented in the modified version XCLASSMIRA, is the ability to "rectify" the spectra; that is, to convert a flux-normalized spectrum to a spectrum with a fixed continuum set at unity, with the absorption value below the continuum for each wavelength correctly scaled in proportion. If the spectra are presented in an Excel spreadsheet as a list of each sampled wavelength and its corresponding amplitude, an individual wavelength or a wavelength group—such as a TiO band—may readily be selected for analysis. Thus, the absorption effects

Table 1. Luminosity and magnitudes calculated from spectra.

Obs. Date	*Phase*	*Spectral Class*	*MK Temp. K*	*Luminosity W*	*M (bol)*	*Bol Conv.*	*M (v)*	*m (v)*
07-May-19	0.97	M0 IIIe	3845	3.15E+29	–2.55	–1.25	–1.30	6.87
26-May-19	0.18	K7 IIIe	3910	3.37E+29	–2.62	–1.09	–1.53	6.64
30-May-19	0.22	K5 IIIe	3955	3.53E+29	–2.67	–1.00	–1.67	6.50
03-Jun-19	0.26	K8 IIIe	3890	3.30E+29	–2.60	–1.13	–1.47	6.70
09-Jun-19	0.33	M1.5 IIIe	3700	2.70E+29	–2.38	–1.64	–0.74	7.43
13-Jun-19	0.37	M2.2 IIIe	3635	2.52E+29	–2.31	–1.81	–0.50	7.67
17-Jun-19	0.42	M3 IIIe	3560	2.32E+29	–2.22	–2.00	–0.22	7.95
22-Jun-19	0.47	M4 IIIe	3460	2.07E+29	–2.09	–2.24	0.15	8.32
02-Jul-19	0.58	M4.5 III	3408	1.95E+29	–2.03	–2.36	0.33	8.50
11-Jul-19	0.68	M4.8 III	3382	1.89E+29	–1.99	–2.40	0.41	8.58
15-Jul-19	0.73	M4.6 III	3397	1.92E+29	–2.01	–2.38	0.37	8.54
20-Jul-19	0.78	M4.5 III	3408	1.95E+29	–2.03	–2.36	0.33	8.50
23-Jul-19	0.82	M4.2 IIIe	3439	2.02E+29	–2.06	–2.30	0.24	8.40
26-Jul-19	0.85	M3.2 IIIe	3540	2.27E+29	–2.19	–2.05	–0.14	8.03
29-Jul-19	0.88	M2.5 IIIe	3610	2.45E+29	–2.28	–1.88	–0.40	7.77
02-Aug-19	0.93	M2.2 IIIe	3635	2.52E+29	–2.31	–1.81	–0.50	7.67
05-Aug-19	0.96	M2.1 IIIe	3645	2.55E+29	–2.32	–1.78	–0.54	7.63
12-Aug-19	0.04	M2 IIIe	3655	2.57E+29	–2.33	–1.76	–0.57	7.60

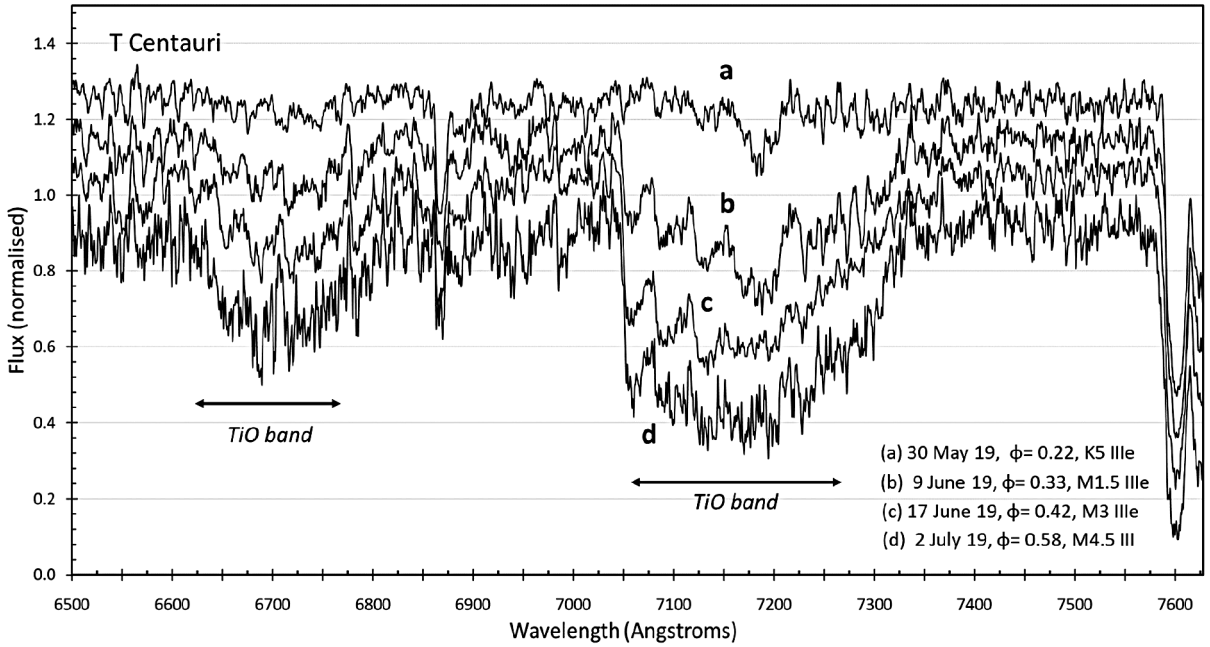

Figure 3. Example rectified spectra used for the measurement of the effect of TiO on atmospheric transmittance (with each continuum separated by 0.1 for clarity). The legend indicates phase and spectral type.

may be measured by selecting a wavelength range and taking the mean of those amplitudes relative to the continuum. The 18 spectra referenced in the tables were rectified, representing the entire period of T Cen under study; examples of those rectified spectra are presented in Figure 3.

As will be noted, the absorption by TiO occurs in clearly defined bands; these exist over much of the visual range, from λ4750 onwards. The transmittance (defined as radiant flux transmitted/incident radiant flux) of the major TiO absorption band covering the wavelength range λλ 7054–7300 was measured, wavelength by wavelength, over T Cen's period from the Excel spreadsheet. Also measured was the transmittance of the wider wavelength range of λλ 6500–7500, covering the majority of the recorded spectrum whilst avoiding the telluric O2 absorption at λ 7605.

Also calculated was the optical depth of the absorption band, from:

$$\tau = -\ln T \quad (4)$$

where T is the Transmittance. Transmittance and optical depth are shown together in Figure 4 for both cases.

Optical depth reached a maximum of around 0.7 in the λλ 7054–7300 TiO band at minimum light, confirming a

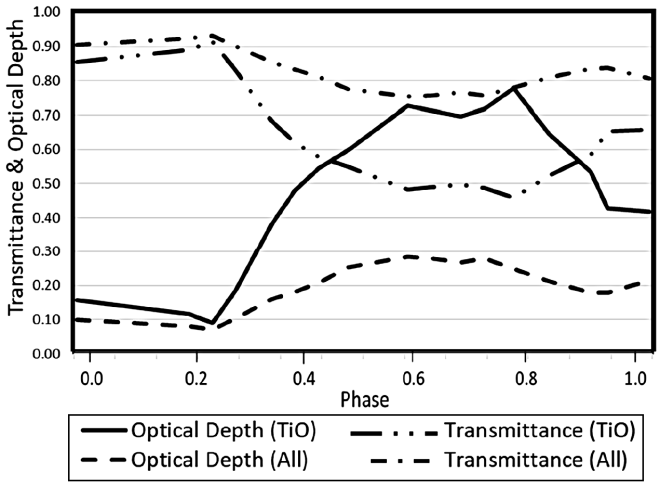

Figure 4. Transmittance and optical depth as measured from the rectified spectra. The plots designated "TiO" are for the absorption band λλ 7054–7300; those designated "All" are for the wider spectral range, λλ 6500–7500.

significant absorption of visible light within that band. This will also have occurred to a varying degree across the visible spectrum, as indicated by the curve for the wider wavelength range. Reid and Goldston (2002a, b) and Wing (1980) have adopted $\tau \geq 1$ as the requirement for atmospheric TiO to have formed a real "visual surface" above the true stellar surface represented by the photosphere. In the case of T Cen, this requirement was not met in full; nevertheless, the presence of significant quantities of molecular TiO in the extended atmosphere must create a structure—potentially complex—absorbing some of the emitted visual radiation and re-emitting it at longer wavelengths beyond the visual. If this structure—of layers, perhaps—is distant from the true stellar surface, it could well appear as a detectable increase in the effective stellar radius, together with a reduction in observed temperature and luminosity in the visual wavelength range. This potential increase in the apparent stellar radius, and its sensitivity to wavelength, is considered in section 3.4 and in section 4.

Table 2. Magnitudes of T Cen derived from AAVSO observations.

Obs. Date	*Phase*	*Observed m (v)*	*Observed M (v)*	*Bol Conv.*	*M (bol)*	*Luminosity W*
07-May-19	0.97	6.30	–1.87	–1.25	–3.12	5.32E+29
26-May-19	0.18	6.20	–1.97	–1.09	–3.06	5.04E+29
30-May-19	0.22	6.25	–1.92	–1.00	–2.92	4.43E+29
03-Jun-19	0.26	6.30	–1.87	–1.13	–3.00	4.77E+29
09-Jun-19	0.33	6.55	–1.62	–1.64	–3.26	6.06E+29
13-Jun-19	0.37	7.00	–1.17	–1.81	–2.98	4.68E+29
17-Jun-19	0.42	7.20	–0.97	–2.00	–2.97	4.64E+29
22-Jun-19	0.47	7.60	–0.57	–2.24	–2.81	4.00E+29
02-Jul-19	0.58	8.10	–0.07	–2.36	–2.43	2.82E+29
11-Jul-19	0.68	8.45	0.28	–2.40	–2.12	2.12E+29
15-Jul-19	0.73	8.20	0.03	–2.38	–2.35	2.62E+29
20-Jul-19	0.78	7.75	–0.42	–2.36	–2.78	3.89E+29
23-Jul-19	0.82	7.45	–0.72	–2.30	–3.02	4.86E+29
26-Jul-19	0.85	7.05	–1.12	–2.05	–3.17	5.57E+29
29-Jul-19	0.88	6.85	–1.32	–1.88	–3.20	5.73E+29
02-Aug-19	0.93	6.55	–1.62	–1.81	–3.43	7.08E+29
05-Aug-19	0.96	6.45	–1.72	–1.78	–3.50	7.55E+29
12-Aug-19	0.04	6.45	–1.72	–1.76	–3.48	7.42E+29

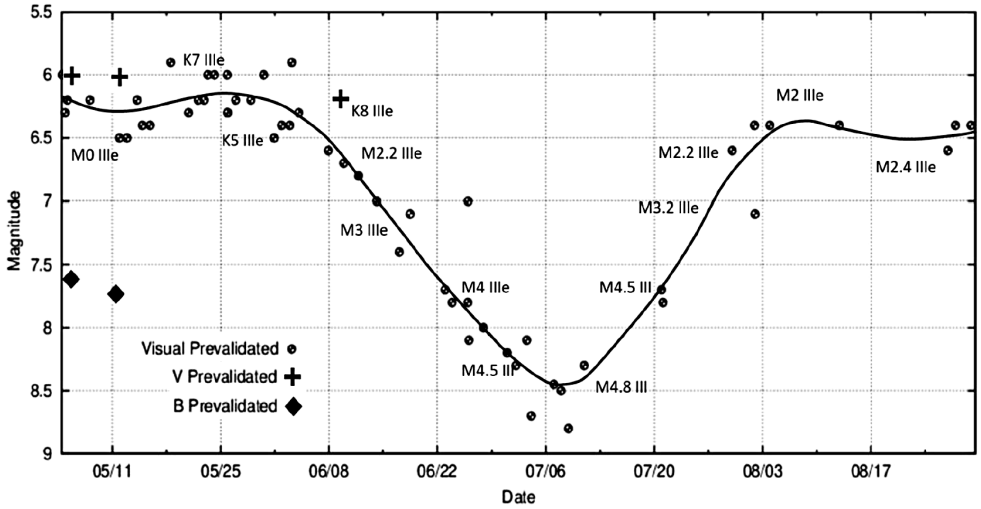

Figure 5. T Cen interpolated light curve (from a 12th order polynomial fit) with spectral classifications from XCLASSMIRA, covering the period studied (AAVSO data).

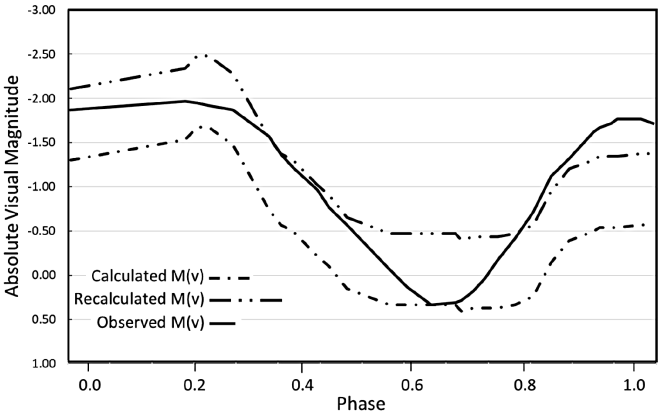

Figure 6. Original and recalculated absolute visual magnitudes from spectral data, compared with the observed values provided by the AAVSO. The recalculated values of M_v are based on the increased stellar radius of 94 $R_\odot$.

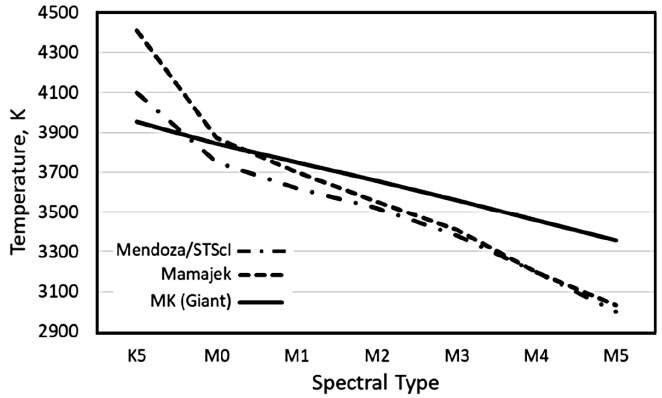

Figure 7. Comparison of (V–R) effective temperatures as compiled by Mamajek (2019) and Mendoza (1969)/STScI (2002), shown together with the MK standard effective temperatures for giant stars.

3.3. Derivation of photometric magnitudes

The next step was to compare the magnitudes derived from spectra with the observed magnitudes as published by the AAVSO.

The apparent visual magnitudes (m_v) of T Cen are shown in Figure 5, interpolated across the visual records using a 12th order polynomial fit to the purely visual measurements (using the AAVSO's VSTAR application (Benn 2013)). The figure has been annotated with the spectral classes identified for those dates, as determined in section 2.1.

To enable a thorough comparison with the luminosities and magnitudes calculated from the spectra, the observed apparent magnitudes were converted, using the same parameters as in section 3.1, to their absolute and bolometric magnitudes, and finally to luminosity, where:

$$L = L_0 \times 10^{-M_{Bol}/2.51} \quad (5)$$

Again, $L_0 = 3.0128 \times 10^{28}$ W (Mamajek *et al.* 2015).

Table 2 shows the AAVSO observed values of m_v for T Cen, together with their converted magnitudes and luminosities.

3.4. Reconciliation of calculated (from spectra) and observed magnitudes

Significant differences were apparent between the magnitudes calculated from the spectra and the AAVSO-observed magnitudes, which required explanation and resolution. The absolute visual magnitudes initially calculated from the spectral type (using the parameters outlined previously) and their AAVSO-observed counterparts are illustrated in Figure 6.

Despite having a similar shape, the curves only intersect at minimum brightness; it was considered, however, that the observed magnitudes were simply brighter than their calculated equivalents. To compare the behavior of T Cen from both the spectroscopic and photometric perspectives, it was necessary to bring the curves into much better alignment, to identify the key areas of difference. This entailed adjusting only the calculated values based on the spectra, as the observed absolute visual magnitudes were derived from many separate observations and were independent of any assumptions made or data used in the calculations. Both the assumed effective temperature and the effective stellar radius were reviewed to this end.

The effective temperatures used in calculating luminosity were the standard MK reference temperatures, as noted in section 3.1 (Gray and Corbally 2009), determined by spectral type. These are effectively the observed temperature of the stellar surface and may be more applicable to main sequence stars than to Miras and SRa stars on the Asymptotic Giant Branch. As the atmospheres of stars such as T Cen become obscured by molecules such as TiO as they cool, their observed temperatures may therefore be significantly lower than those prescribed by the MK model. Using the temperature to lift the calculated M_v curve into better alignment would have required increasing the temperatures above the MK giant values and would conflict with the overall structure of the MK temperature model. However, varying the radius alone would shift the calculated M_v curve without distorting it; this was preferred as the mechanism to improve the initial alignment of the two curves. A 45% increase, from the initial 65 $R_\odot$ (4.5×10^{10} m) to 94 $R_\odot$ (6.53×10^{10} m), was found to achieve the best fit, giving a revised stellar radius of ~0.44 AU, a not unreasonable size for a Mira variable (or similar) with a short period.

The revised calculated values of absolute visual magnitude, in comparison with the original and the observed values, are shown in Figure 6.

The improved alignment was not perfect, however, and differences persisted both in the early phases and around minimum light. The lower magnitudes observed by AAVSO contributors early in the period might have been due to molecular TiO, formed far from the true stellar surface, remaining in the atmosphere until dissociated either by the radiation from the star at its hottest spectral type or by shock waves induced by pulsation; following this, the magnitudes would be expected to converge as shown (Wing 1980). Alternatively, as the star pulsates, with its minimum photospheric radius estimated to occur at $\varphi \sim 0.8$, it may be that the expansion prior to $\varphi = 0$ reduced the temperature, and hence the luminosity. These issues are considered further in section 4.

At minimum light ($\varphi \sim 0.63$), a full magnitude difference remained between the values of M_v derived from AAVSO observations and those recalculated based on spectral type and

the larger radius. At this stage in the period, TiO is expected to increase towards its maximum in the atmosphere, absorbing radiation within its absorption bands, and reducing T Cen's visual brightness and observed temperature. As noted in section 3.2, the TiO absorption evident in our captured spectra confirmed significant levels of absorption in these bands around minimum light. giving rise to these lower observed magnitudes, and potentially increasing its apparent radius.

It was suspected, therefore, that in mid-phase the MK standard temperatures, although falling mid-period according to spectral type, did not accurately represent the external appearance of the complex atmosphere of a pulsating giant star such as a Mira (or similar). The atmosphere is not only enormous but may have widely different structure and temperatures at different depths (Hinkle and Barnes 1979, cited by Wing 1980); hence, whilst the MK temperatures may be appropriate for the photosphere itself, other methods—such as the well-established use of color indices—may give a better indication of the cooler conditions farther out, which affect the visual magnitudes. The B–V color index-temperature relationship appeared to be of lesser value for cool stars, given that much of the radiation is in the infra-red, and varies significantly with spectral type. The use of the V–R color index to refine the effective temperature of T Cen was therefore investigated and two relationships were found between effective temperature and the V–R color index. First, a comprehensive table of spectral types, temperatures, and a wide range of color indices compiled by Mamajek (2019) offered a set of spectral types and associated effective temperatures that could be applied in this model, although the data relate to dwarf stars.

Second, a paper by Mendoza (1969) linked V–R indices (originally $(V–R)_J$) to effective temperature based on observations of stars with a range of luminosities, including several giants; applying these $(V–R)_J$ indices to the extensive table linking color indices and spectral types published by the Space Telescope Science Institute (2002), gave another set of spectral types and corresponding effective temperatures.

The two sets of data, plotted in Figure 7, showed considerable similarity, especially at minimum light, but diverge towards spectral type K5. For the transition M0 to K5, Mamajek's temperatures show a significantly greater increase than the Mendoza/STScI interpretation.

Also shown in Figure 7 is the MK temperature sequence for giant stars of luminosity type III (Gray and Corbally 2009), which remains above both the (V–R) curves from M0 to M5 as the atmosphere cools and becomes obscured by TiO. Between K5 and M0, however, the MK temperature for giants remains below both (V–R) projections; this is consistent with the MK effective temperature calibration for late-type stars (Gray and Corbally 2009), in which giants of type G and K are shown to be significantly cooler than their dwarf counterparts. The rapid rise in temperature in the Mamajek study plainly follows the behavior of dwarf stars once the atmosphere is clear of molecules such as TiO; the lesser rise in the Mendoza/STScI temperatures, extending almost as far as M2, is probably attributable to Mendoza's inclusion of giant stars (Mendoza 1969).

Gray and Corbally refer specifically to this spectroscopic transition in their discussion of the classification of M-type stars

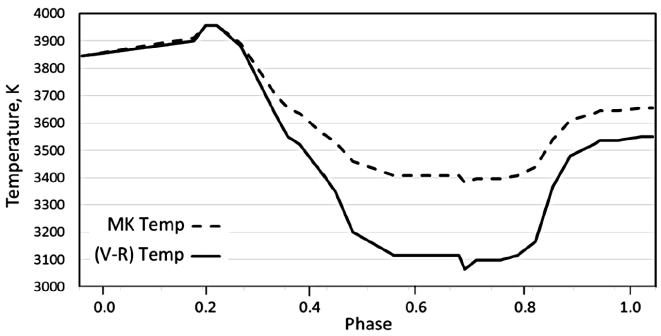

Figure 8. Combined MK and Mamajek (V–R) temperatures compared to the MK standard values for giant stars (applied to the spectral classifications across the period).

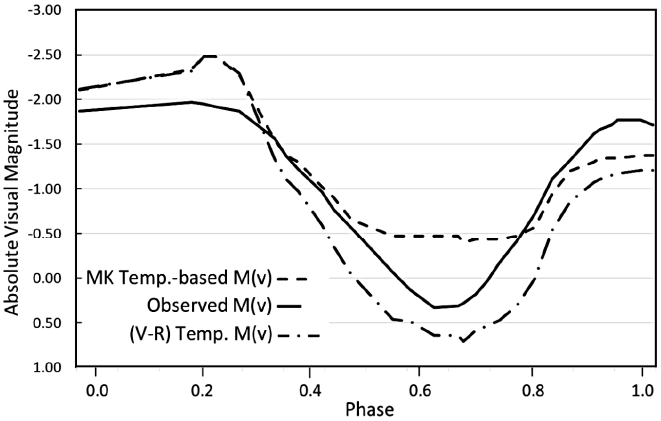

Figure 9. Comparison of the absolute visual magnitudes: Observed values are the AAVSO observed values; MK Temp.-based magnitudes are those derived from spectral data (using MK standard temperatures and the increased radius of 94 $R_\odot$); (V–R) Temp. magnitudes are based on the combination of both the MK-based standard temperatures and the (V–R)-derived (Mamajek) temperatures of Table 3 and Figure 9, also with the increased radius of 94 $R_\odot$.

(Gray and Corbally 2009, sec. 8.2.2 and their footnote No. 1), and state that "in terms of effective temperature, the jump from K5 to M0 is small, and is comparable to that between M0 and M1." The K5–M0 region is when T Cen is brightest and its atmosphere is least obscured, based on the absence of TiO in the spectra; it may be assumed that the effective temperature should then be closest to the MK standard for giant stars. In developing our simplified model of T Cen's behavior, those MK (giant) temperatures were adopted for spectral types from K5 to M0, and Mamajek's more recent temperatures were applied thereafter; these are listed in Table 3 and are shown in

Table 3.Spectral type and effective temperature (based on MK temperatures for giant stars and Mamajek's (2019) color index data).

Spectral Class	*Effective Temp. K*
K5	3955
M0	3845
M1	3700
M2	3550
M3	3410
M4	3200
M5	3030

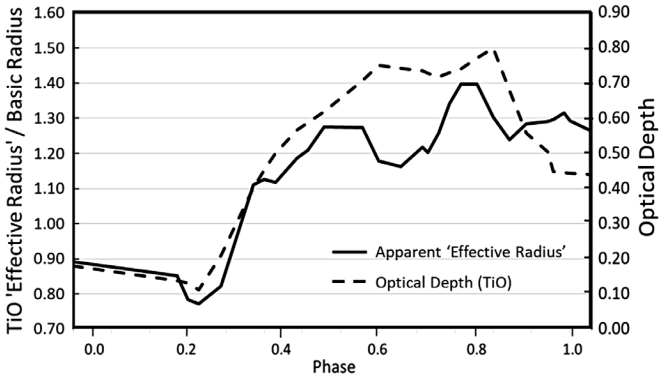

Figure 10. Estimated ratio of the "effective radius" of T Cen, increased due to atmospheric TiO, relative to the assumed "basic radius" of 94 $R_\odot$ (left axis); also illustrated is the optical depth of the TiO absorption band λλ 7054–7300 (right axis).

Figure 8 as they apply to the spectral types across the period; the temperatures were interpolated linearly for intermediate spectral types. The corresponding MK standard temperatures for giant stars are also shown in Figure 8.

These (V-R) temperatures were then applied in the standard Stefan-Boltzmann formula (Equation 1), using the previously increased assumed stellar radius of 94 $R_\odot$, to recalculate revised luminosities and bolometric magnitudes. Prior to determining the visual magnitudes, the bolometric conversion factors were plotted and corrected to match the effective temperatures now being applied. The results are shown in Table 4 and in Figure 9; for clarity, "(V–R)" precedes references to the applied temperatures, and to other values dependent on them.

The values for M_v based on the combined temperature sequence (incorporating both MK standard and Mamajek (V–R) values) were largely as expected, with the temperatures in the early and late phases not unlike those previously calculated. Toward minimum light, however, the values are fainter than the AAVSO observed values, as expected for a cool outer atmosphere significantly obscured by TiO, but where the expected increase in the apparent "effective radius" due to the atmospheric TiO has not yet been incorporated into the calculation of luminosity. These differences in magnitude now offered an opportunity to assess the apparent increase of the TiO "surface" and how it varied during T Cen's cycle, as a form of proxy for the undoubted complexity of the real atmospheric structure, in which the observed "disk radius" is itself wavelength-dependent.

The scale of this increase in apparent "effective radius" may be approximated by calculating the ratio of the radii from the Stefan-Boltzmann formula (Equation 1), using the absolute visual magnitude as representing the luminosity in the visual range. If the effective temperatures, for both the observed and (V–R) cases, are assumed to be the same, the ratio of the radii may be calculated as follows:

$$R_{(V-R)} / R_{(Observed)} = (2.51^{\Delta M})^{1/2} \quad (6)$$

where

$$\Delta M = M_{V(V-R)} - M_{V(Observed)} \quad (7)$$

Applying this to the magnitudes quoted in Table 4 gives the curve shown in Figure 10.

Based on this modelling, the apparent "effective radius" of T Cen increased by between 20–30%, with a brief maximum of 40% above the (previously enlarged) radius assumed for the photosphere (94 $R_\odot$). The rise commenced at $\varphi \sim 0.25$ and decreased again after $\varphi \sim 0.8$. The general shape of the variation in apparent radius is consistent with the increase in optical depth, also shown in Figure 10, inferring a clear relationship with the appearance and increase of TiO in T Cen's atmosphere. The apparent radius measurements also show similar characteristics to those taken for Mira (o Ceti) itself, including the significant dip at around $\varphi \sim 0.6$, although Mira's variation was significantly greater (Mahler *et al.* 1997). The values of less than one occurring up to $\varphi \sim 0.3$ result from the

Table 4. Luminosities and magnitudes based on the (V–R) temperatures.

Obs. Date	*Phase Class*	*Spectral K*	*(V–R) Temp. W*	*(V–R) Lum. M(bol)*	*(V–R)*	*Bol Conv. M(v)*	*(V–R) M(v)*	*(V–R)*
07-May-19	0.97	M0 IIIe	3845	6.63E+29	–3.36	–1.50	–1.86	6.31
26-May-19	0.18	K7 IIIe	3900	7.02E+29	–3.42	–1.35	–2.07	6.10
30-May-19	0.22	K5 IIIe	3955	7.42E+29	–3.48	–1.10	–2.38	5.79
03-Jun-19	0.26	K8 IIIe	3880	6.88E+29	–3.40	–1.45	–1.95	6.22
09-Jun-19	0.33	M1.5 IIIe	3625	5.24E+29	–3.10	–1.90	–1.20	6.97
13-Jun-19	0.37	M2.2 IIIe	3522	4.67E+29	–2.98	–2.10	–0.88	7.29
17-Jun-19	0.42	M3 IIIe	3410	4.10E+29	–2.84	–2.40	–0.44	7.73
22-Jun-19	0.47	M4 IIIe	3200	3.18E+29	–2.56	–2.55	–0.01	8.16
02-Jul-19	0.58	M4.5 III	3115	2.86E+29	–2.44	–3.00	0.56	8.73
11-Jul-19	0.68	M4.8 III	3064	2.67E+29	–2.37	–3.20	0.83	9.00
15-Jul-19	0.73	M4.6 III	3098	2.79E+29	–2.42	–3.05	0.63	8.80
20-Jul-19	0.78	M4.5 III	3115	2.86E+29	–2.44	–3.00	0.56	8.73
23-Jul-19	0.82	M4.2 IIIe	3166	3.05E+29	–2.51	–2.80	0.29	8.46
26-Jul-19	0.85	M3.2 IIIe	3368	3.90E+29	–2.78	–2.25	–0.53	7.64
29-Jul-19	0.88	M2.5 IIIe	3480	4.45E+29	–2.92	–2.20	–0.72	7.44
02-Aug-19	0.93	M2.2 IIIe	3522	4.67E+29	–2.98	–2.10	–0.88	7.29
05-Aug-19	0.96	M2.1 IIIe	3536	4.74E+29	–2.99	–2.03	–0.96	7.21
12-Aug-19	0.04	M2 IIIe	3550	4.82E+29	–3.01	–2.06	–0.95	7.22

lower observed values of M_V relative to those calculated based on spectral type; this was noted earlier and is considered in more detail in section 4, as is the residual expansion remaining after $\varphi \sim 0.9$.

The effective temperatures based on (V–R) data are essentially approximations linked to spectral type and were not otherwise derived from our observations; the estimated variations in effective radius should, therefore, only be considered as a simple model representation. T Cen has a relatively short period and a limited visual amplitude that does not extend as deeply into the M spectral types as do longer period Miras; nevertheless, the presence of an expanded apparent radius due to atmospheric TiO is clearly shown, and has a significant effect on the star's behavior, especially in the visual range.

4. Discussion

4.1. Radius considerations

The dimensions of cool giant stars such as Miras are generally difficult to determine, especially during the cooler phases of their periods, when the atmosphere forms substantial amounts of metallic oxides such as TiO, VO, and others (Wing 1980). The obscuring effects of these oxides, which are themselves wavelength-dependent, have been described as both reducing the apparent temperature as viewed by an observer and increasing the apparent stellar radius (Reid and Goldston 2002a, b). Under such circumstances, however, a true stellar radius is not clearly visible, at least at most visual wavelengths, although interferometry is feasible in the infra-red (Weiner *et al.* 2003b; van Belle *et al.* 2002). The atmosphere itself is probably layered and subject to the effects of shock waves resulting from pulsation, both creating and eliminating molecules such as TiO, in addition to the effects of changing temperature (Höfner and Olofsson 2018). The concept here of an "effective radius" for T Cen is therefore a representation of the overall impact of TiO on the atmosphere for the purposes of developing what is sometimes referred to as an "embedded toy model" (Reutlinger *et al.* 2016), rather than an attempt to describe the physics in detail. Such a model may, however, potentially enable interesting comparisons to be made with the other Miras included in our wider study.

4.2. Estimation of basic stellar radius

At maximum brightness, T Cen exhibits as spectral type K5-K8 IIIe, with no spectroscopic indication of significant quantities of TiO in its atmosphere. With the photosphere clearly visible to an observer, its effective temperature was expected to be reasonably consistent with the MK standards for those spectral types. Thus, around maximum brightness, the luminosities and absolute visual magnitudes calculated using an assumed stellar radius should have approached those derived from the visual observations drawn from the records of the AAVSO. They did not, however, and varying the previously adopted stellar radius and recalculating the spectrum-based luminosities and magnitudes across the entire period, as described in Section 3.3, enabled the calculated and observed absolute visual magnitudes to be brought into significantly better alignment. A 45% increase, from 65 $R_\odot$ to 94 $R_\odot$, was determined to give the best fit, giving a revised mean stellar radius of ~0.44 AU.

The period of a Mira variable has been described as primarily dependent upon its radius, and secondarily upon its mass (Percy 2007); indeed, Percy notes that that the average radius of a Mira, in solar units, is approximately equal to its period in days so a radius of 94 $R_\odot$ may be considered reasonable in this simple model for T Cen with its period of 91 days. However, the measured radii of Miras (and SRa stars) are dependent on wavelength, especially in the visual range when the atmosphere contains molecules such as TiO or VO. Interferometric measurements in the infrared have also given widely differing values for even the most extensively studied Miras, with the radius of Mira itself (o Ceti, period 332 days) being quoted as ~350 $R_\odot$ (Woodruff *et al.* 2004) and ~475 $R_\odot$ (van Belle *et al.* 2002). Other Miras have been given similarly broad estimates, so while our estimate of the mean radius of T Cen may pleasingly fit this assumption it must remain as an approximation for the purposes of our model, especially as T Cen appears only marginally to be a true Mira variable.

4.3. Consideration of Effective Temperature and radius variation

The anomaly created by the fainter observed magnitudes, and therefore lower effective temperatures (as opposed to the MK standard values) early in the cycle, up to $\varphi \sim 0.25$ as illustrated in Figure 6, was considered to be due to either of two potential causes (or possibly a combination of both):

1. TiO formed far from the true stellar surface but remaining in the atmosphere until finally dissociated by the radiation from the star at its hottest spectral types, at which point the magnitudes would again converge. Wing (1980) indicates that this situation can occur and can last for a month or two after the photospheric temperature starts to approach maximum, which is reasonably consistent with this case. Had this been so, the observed magnitudes should have been brightening until $\varphi \sim 0.2$ or even later, whereas having been relatively stable, they were now becoming steadily fainter. The absence of spectra between 2019 May 7–26 left an area of uncertainty in these early phases but from May 26 to June 3 the spectra showed no significant TiO absorption bands, so this interpretation was discounted at this stage.

2. Alternatively, it is probable that the star pulsates significantly, its radius changing by perhaps ± 10% (Weiner *et al.* 2003a), with a noticeable effect on luminosity, although in the absence of information confirming the nature of pulsation by T Cen, this was ignored in our initial estimate of T Cen's radius. As the star pulsates, its minimum photospheric radius probably occurs around $\varphi \sim 0.8$, as indicated by the onset of emission at Hα due to the likely development of outward shockwaves as expansion commences, and the radial velocity variations shown by Lebzelter *et al.* (2005). It was possible, therefore, that the actual effective temperature differed from the MK standard, which we presumed related to stars in a steady state. As pulsating stars should cool as they expand (albeit

with a small delay between minimum radius and maximum brightness), it was thought possible that the star might be somewhat cooler by the time the phase reached $\varphi \sim 0$. However, to investigate the timing and degree of pulsation requires spectra capable of yielding radial velocities and is therefore beyond the scope of this paper.

The potential that the MK standard temperatures might not apply directly to a pulsating star, together with the difference of a full magnitude between the calculated and observed M_V values at minimum brightness, raised the possibility that a different method should be applied to determine the effective temperature, at least around minimum light. Color indices are commonly used to estimate stellar temperatures and, as has been described in section 3.3, the V–R relationship appeared to be more suitable for cool stars, given that much of the radiation is in the infra-red and varies significantly in the later M spectral classifications. The identification of a range of temperatures to be incorporated into our simplified model of T Cen's behavior has been described in section 3.3; the MK (giant) temperatures were adopted for spectral types from K5 to M0, and Mamajek's sequence of temperatures was applied thereafter into the M classifications.

This sequence of effective temperatures yielded calculated magnitudes much better aligned to those observed for T Cen, especially mid-period, and enabled an estimate to be made of the degree of apparent expansion of T Cen's radius related to the TiO in its atmosphere. As noted above, this apparent "effective radius" is intended solely as a representation of the overall effect of TiO in T Cen's atmosphere; further, as these temperatures were based on externally sourced data not captured directly from our own observations of T Cen, the derived variations in effective radius should only be considered as approximate. As described in section 3.3, the estimated increase in the "effective radius" was of the order of 20–30%, commencing at $\varphi \sim 0.25$, and peaking at 40% above the estimated photospheric radius of 94 $R_\odot$. T Cen has a relatively short period compared with most Miras or SRa stars; it also descends appreciably less into the later M spectral classes than true Miras. The opacity of the atmospheric TiO may, therefore, be expected to be less than that for longer period Miras, in which the apparent radius may double (or more). Nevertheless, it is clear that T Cen does develop some form of exterior "visual surface" in mid-period, although its true structure may well be complex and a limited study such as this cannot determine it. The presence of an expanded apparent "effective radius" due to molecular TiO is clearly shown, however, and has a significant effect on the star's behavior, especially in the visual range.

During the later phases of the cycle, the captured spectra clearly showed that the atmosphere of T Cen retains some TiO, at least in this cycle; its spectral type stabilized at around M2 IIIe rather than rising to the previous K5-K8 IIIe, and its optical depth remained at $\tau \sim 0.44$. As pulsation may vary from cycle to cycle, a reduced incidence of shockwaves in the case under study may have led to TiO remaining in the atmosphere for longer than in other cycles, whereas a more vigorous pulsation may accelerate the dissociation of TiO and T Cen's return to spectral type K. A review of T Cen's light curve across several 91-day cycles (Figure 2) shows a considerable variation in peak brightness and in amplitude, leading to the conclusion that this situation is not unusual. It may be, therefore, that the fundamental period of T Cen is longer—181 days is commonly suggested—but with a first overtone perhaps governing much of its behavior. Determination of this would require detailed analysis over a much longer period and has not been considered here.

Note: Original copies of these spectra in .fit format may be accessed through the AAVSO ftp site at

ftp://ftp.aavso.org/public/datasets/west491-fitsspectra.zip.

5. Acknowledgements

We acknowledge with thanks the variable star observations for T Cen from the AAVSO International Database, contributed by observers worldwide and used in this research.

We thank Prof. Richard O. Gray (Appalachian State University, NC) for providing the XCLASS program and its standard databases, and in addition we express our appreciation to both him and Dr. Christopher Corbally S. J. (Vatican Observatory), for their kind support in its use. We also thank fellow members of the Astronomical Association of Queensland for their contributions in reviewing and advising on the content of this paper. We further thank both the editorial staff at JAAVSO for their support, and the anonymous referee who provided a careful review and valuable recommendations for this paper.

We acknowledge with thanks a grant from the Edward Corbould Research Fund, of the Astronomical Association of Queensland, for the purchase of a spectrograph, gratings, and CCD camera.

References

Benn, D. 2013, VSTAR data analysis software (https://www.aavso.org/vstar-overview).

Buil, C. 2019, ISIS: Integrated Spectrographic Innovative Software (http://www.astrosurf.com/buil/isis-software.html).

Gray, R. O., and Corbally, C. J. 2009, *Stellar Spectral Classification*, Princeton Univ. Press, Princeton, NJ.

Gray, R. O., and Corbally, C. J. 2014, *Astron. J.*, **147**, 80.

Hinkle, K. H. and Barnes, T. G. 1979, *Astrophys. J.*, **227**, 923.

Höfner, S., and Olofsson, H. 2018, *Astron. Astrophys. Rev.*, **26**, 1 (https://doi.org/10.1007/s00159-017-0106-5).

Kafka, S. 2020, variable star observations from the AAVSO International Database (https://www.aavso.org/aavso-international-database-aid).

Kaler, J. B. 1989, *Stars and their Spectra: An Introduction to the Spectral Sequence*, Cambridge Univ. Press, Cambridge, 263.

Lançon, A., and Mouhcine, M. 2002, *Astron. Astrophys.*, **393**, 167.

Lançon, A., and Wood P. R. 2000, *Astron. Astrophys., Suppl. Ser.*, **146**, 217.

Lebzelter, T., Hinkle K. H., Wood P. R., Joyce R. R., and Fekel F. C. 2005, *Astron. Astrophys.*, **431**, 623.

Mahler, T. A., Wasatonic, R., and Guinan, E. F. 1997, *Inf. Bull. Var. Stars*, No. 4500, 1.

Mamajek, E. 2019, "A Modern Mean Dwarf Stellar Color and Effective Temperature Sequence" (2019.03.22 version used; http://www.pas.rochester.edu/~emamajek/EEM_dwarf_UBVIJHK_colors_Teff.txt (2021.0302 version)).

Mamajek, E. E., *et al.* 2015, "IAU 2015 Resolution B2 on Recommended Zero Points for the Absolute and Apparent Bolometric Magnitude Scales," XXIXth IAU General Assembly in Honolulu, 13 August 2015 (https://www.iau.org/administration/resolutions/).

Mendoza v., E. E. 1969, in *Proceedings of the 3rd Harvard-Smithsonian Conference on Stellar Atmospheres*, ed. O. Gingerich, Massachusetts Institute of Technology, Cambridge, MA, 27.

Percy, J. R. 2007, *Understanding Variable Stars*, Cambridge University Press, Cambridge, 209–.

Reid, M. J., and Goldston, J. E. 2002a, *Astrophys. J.*, **568**, 931.

Reid, M. J., and Goldston, J. E. 2002b, *Astrophys. J.*, **572**, 694 (erratum).

Reutlinger, A., Hangleiter, D, and Hartmann, S. 2018, *Br. J. Philos. Sci.*, **69**, 1069.

Samus, N. N., Kazarovets, E. V., Durlevich, O. V., Kireeva, N. N., and Pastukhova, E. N. 2017, *Astron. Rep.*, **61**, 80, *General Catalogue of Variable Stars: Version GCVS 5.1* (http://www.sai.msu.su/gcvs/gcvs/index.htm).

Space Telescope Science Institute. 2002, "Intrinsic Colours as a Function of Spectral Type" (https://www.stsci.edu/~inr/intrins.html).

Universe Guide. 2020, T Cen (https://www.universeguide.com/star/66825/tcentauri).

van Belle, G. T., Thompson, R. R., and Creech-Eakman, M. J. 2002, *Astron. J.*, **124**, 1706.

Weiner, J, Hale, D. D. S., and Townes, C. H. 2003a, *Astrophys. J.*, **588**, 1064.

Weiner, J, Hale, D. D. S., and Townes, C. H. 2003b, *Astrophys. J.*, **589**, 976.

Wenger, M., *et al.* 2000, *Astron. Astrophys., Suppl. Ser.*, **143**, 9. (http://simbad.u-strasbg.fr/simbad).

Wing, R. F. 1980, in *NASA. Goddard Space Flight Center Current Problems in Stellar Pulsation Instabilities*, 533 (https://core.ac.uk/reader/42864826).

Woodruff, H. C., *et al.* 2004, *Astron. Astrophys.*, **421**, 703.

Appendix: Spectra used in this paper

These spectra in .fit format may be accessed through the AAVSO ftp site at ftp://ftp.aavso.org/public/datasets/west491-fitsspectra.zip.

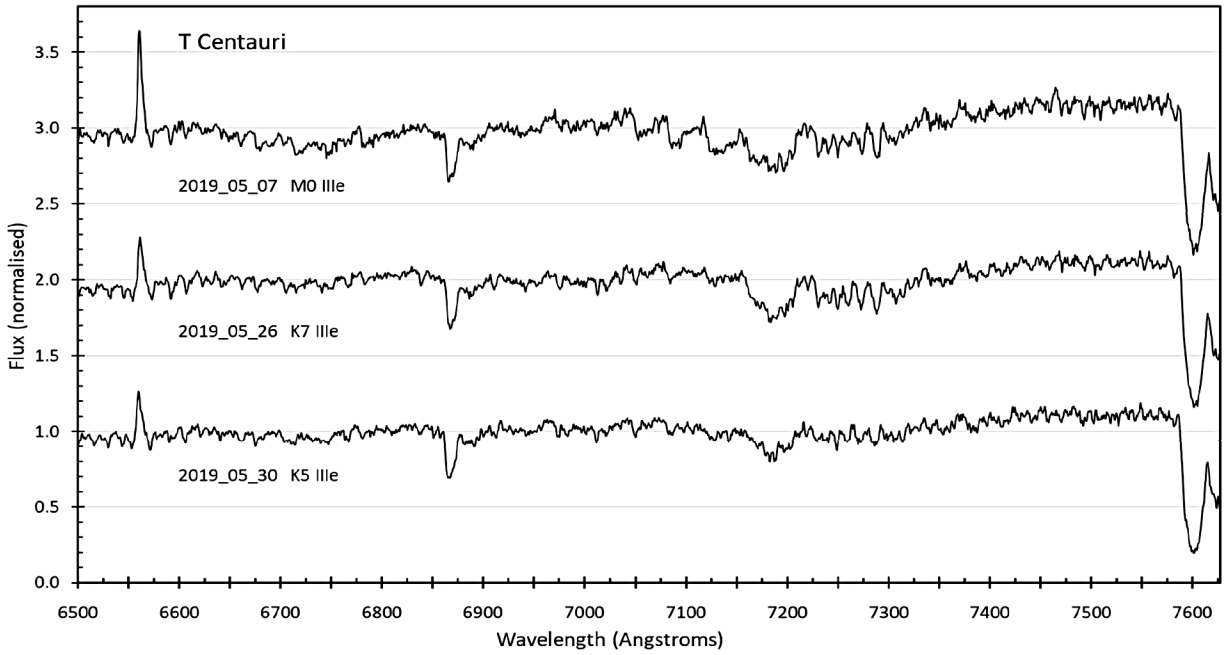

Figure A1. Spectra of λλ 6500–7630, from the dates shown and at phases 0.97 (–0.03 of the studied period), 0.18, and 0.22 respectively, normalized at λ 6610; the profiles are separated by amplitude 1.0 for clarity.

Figure A2. Spectra of λλ 6500–7630, from the dates shown and at phases 0.26, 0.33, and 0.37 respectively, normalized at λ 6610; the profiles are separated by amplitude 1.0 for clarity.

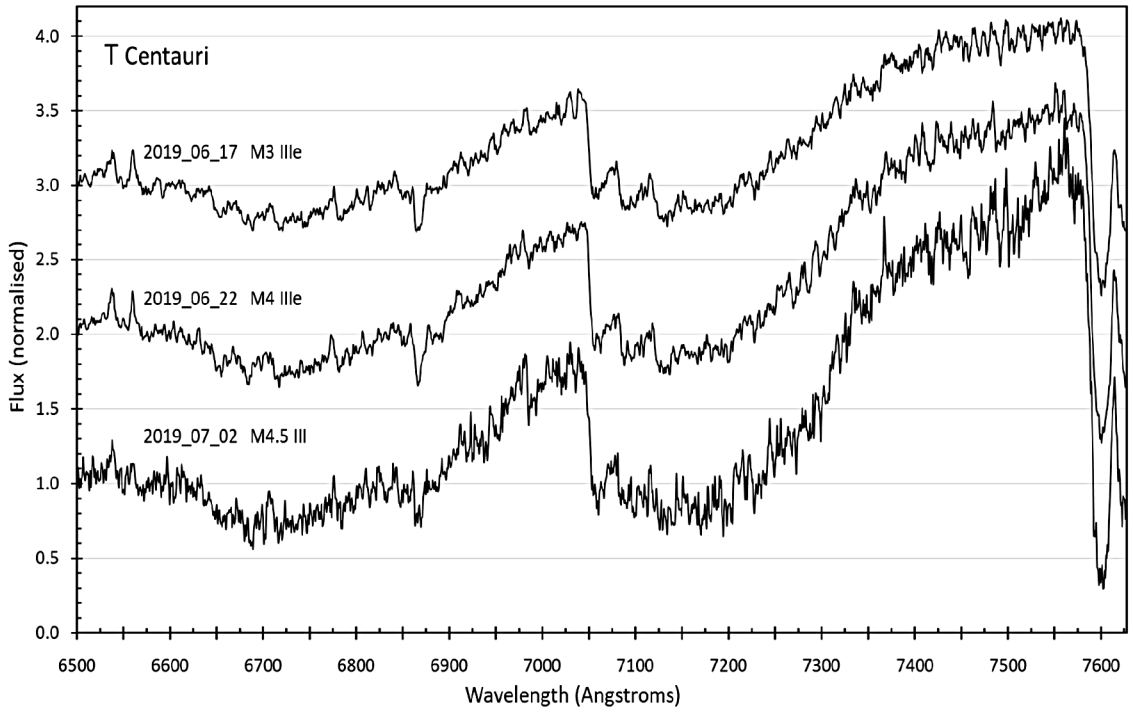

Figure A3. Spectra of λλ6500–7630, from the dates shown and at phases 0.42, 0.47, and 0.58 respectively, normalized at λ6610; the profiles are separated by amplitude 1.0 for clarity.

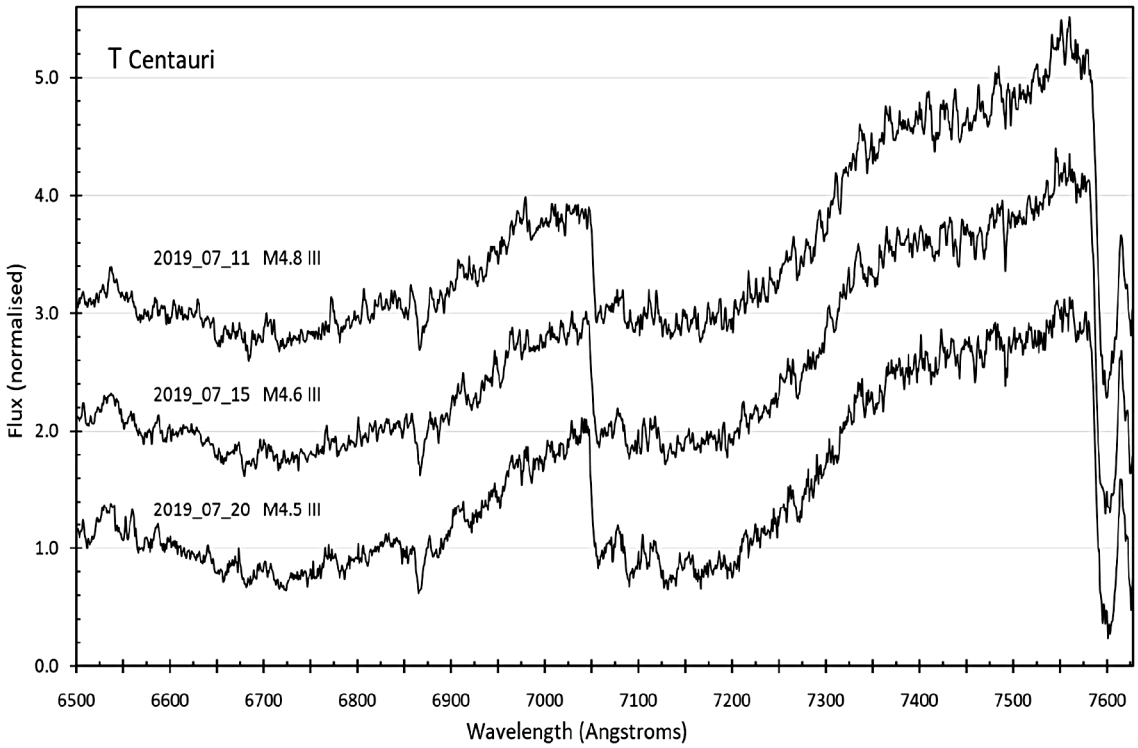

Figure A4. Spectra of λλ6500–7630, from the dates shown and at phases 0.68, 0.73, and 0.78 respectively, normalized at λ6610; the profiles are separated by amplitude 1.0 for clarity.

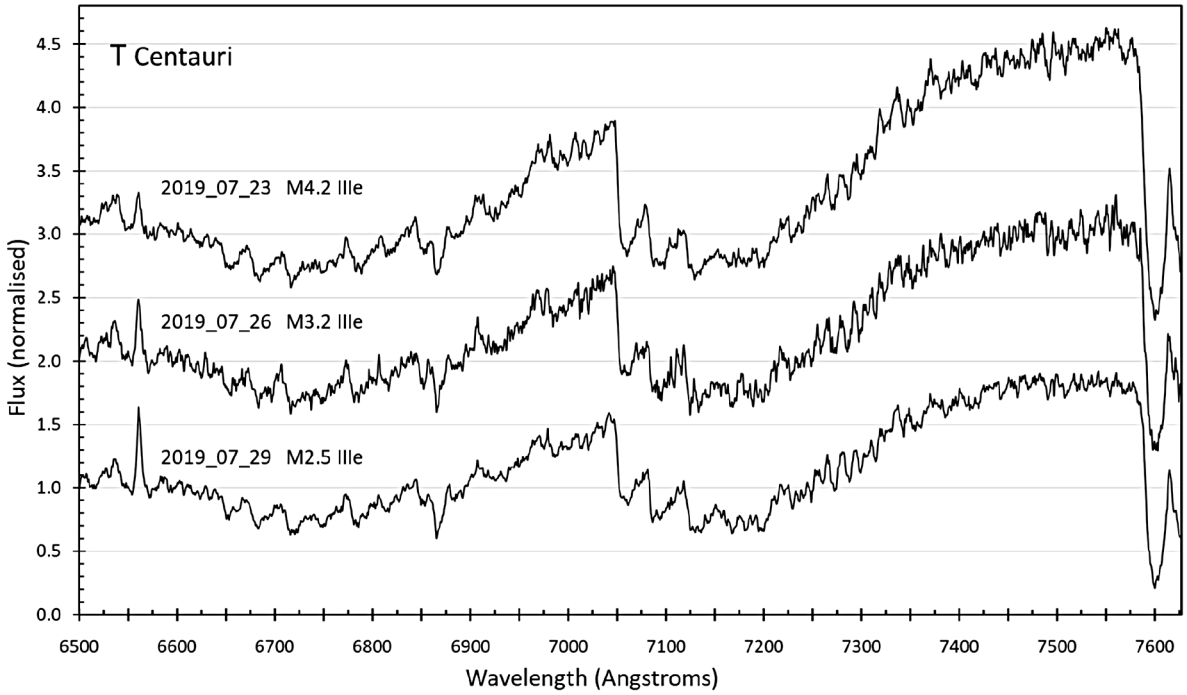

Figure A5. Spectra of λλ 6500–7630, from the dates shown and at phases 0.82, 0.85, and 0.88 respectively, normalized at λ 6610; the profiles are separated by amplitude 1.0 for clarity.

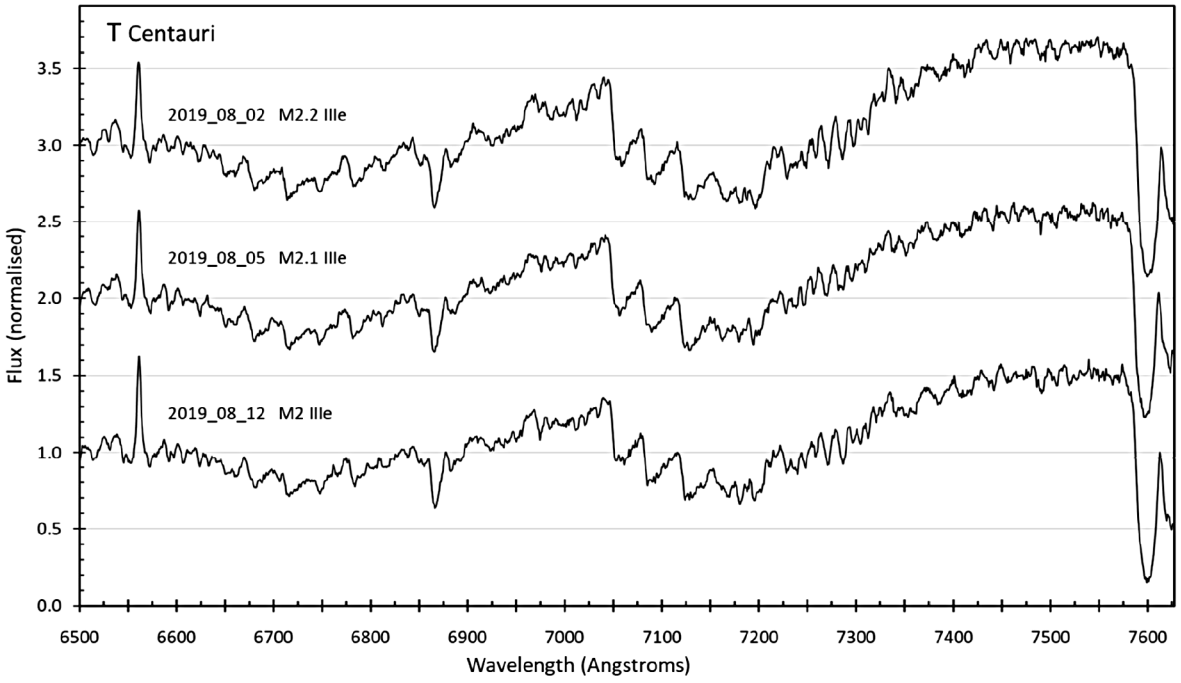

Figure A6. Spectra of λλ 6500–7630, from the dates shown and at phases 0.93, 0.96, and 0.04 (1.04 in the following period) respectively, normalized at λ 6610; the profiles are separated by amplitude 1.0 for clarity.

RU Cam: The Reluctant Cepheid Revisited

John R. Percy
Department of Astronomy and Astrophysics, and Dunlap Institute for Astronomy and Astrophysics, University of Toronto, 50 St. George Street, Toronto, ON M5S 3H4, Canada; john.percy@utoronto.ca

Received November 24, 2020; revised January 16, 2021; accepted January 25, 2021

Abstract Skilled amateur astronomers can still make significant contributions to variable star research, even in this age of massive automated sky surveys. Among other things, they can identify and/or observe stars with unusual properties or behavior. RU Cam, a 22-day carbon-rich Population II Cepheid (CW variable), is one such star. In 1965, Serge Demers and Don Fernie discovered that it had abruptly decreased in full amplitude from 1.0 to 0.1 magnitude. It was subsequently observed intensively until the 1990s, especially at the Konkoly Observatory, and this enabled theoretical discussions about the possible nature of the star's pulsation. The cause of the amplitude decrease was and still is not clear. Observations have been more sporadic since the 1990s. There is some AAVSO V photometry, and sparse AAVSO visual photometry from before the amplitude decrease to the present. More recently, RU Cam was observed by the All-Sky Automated Survey for Supernovae (ASAS-SN) from 2014 to 2018, and by the Transiting Exoplanet Survey Satellite (TESS) over two pulsation cycles. In this paper, I analyze the ASAS-SN data and the AAVSO data for possible changes in the period and the amplitude. The period has remained more-or-less stable at 22 ± 1 days and, since 1965, the full amplitude has continued to vary from less than 0.1 to about 0.3 on a time scale of hundreds of days (tens of pulsation periods), reminiscent of the variability of red SR variables. An attempt to follow the period changes using the (O–C) method was unsuccessful because of the sparseness of the data. I therefore suggest that this star should be monitored systematically, preferably in UBV. It is well-placed for northern observers.

1. Introduction

RU Cam is a 9th magnitude, carbon-rich 22-day Population II Cepheid (W Virginis or CW) pulsating variable star. In 1965–1966, it abruptly decreased in V full amplitude from 1 to 0.1 magnitude (Demers and Fernie 1966). This generated much interest and many papers. In a comprehensive paper, Szeidl *et al.* (1992) published photometry of RU Cam on 1,343 nights between 1966 and 1982, and discussed the long-term changes in the star's period and amplitude. After 1965–1966, RU Cam continued to vary with a period of about 22 days, with a small and variable amplitude. Figure 1 shows the changing amplitude with time, based on AAVSO visual data and wavelet analysis.

Kolláth and Szeidl (1993) discussed possible explanations for the star's behavior. They concluded that the regular part of the star's pulsation disappeared in 1965, leaving only an erratic or irregular component. They found no evidence for multiperiodicity, or low-dimensional chaos, but did not rule out higher-dimension chaos, or other stochastic effect—possibly caused by dynamical processes in the star's atmosphere. For a general understanding of CW variables, and related objects, the review by George Wallerstein (2002) is still useful.

Prior to 1965, the period of RU Cam was about 22.16 days, and the (O–C) diagram subsequently showed a constant linear decrease to about 21.75 days, plus wave-like fluctuations (Szeidl *et al.* 1992; Percy and Hale 1998). These fluctuations can be modelled as random cycle-to-cycle fluctuations, similar to those which occur in Mira stars (Percy and Hale 1998).

What has happened to RU Cam since then? In this paper, I use data from the AAVSO International Database (Kafka 2020), the All-Sky Automated Search for Supernovae (ASAS-SN: Jayasinghe *et al.* 2018, 2019), and some limited data from the Transiting Exoplanet Survey Satellite (TESS; STScI 2020) to study the period and amplitude of the star. The visual observations were quite numerous after 1965, but have become increasingly sparse. Some AAVSO photoelectric observations were obtained over the years. There are five seasons of data from ASAS-SN, but only two pulsation cycles from TESS.

2. Data and analysis

In order to study the changing period and amplitude of RU Cam, the ASAS-SN data and the AAVSO visual observations were analyzed using the Fourier and wavelet analysis routines in the AAVSO time-series analysis package VStar (Benn 2013). The TESS data were too limited for time-series analysis. Note: in the literature, the term "amplitude" is generally used to indicate the peak-to-peak range, whereas VStar gives, as amplitude, the coefficient of the sine curve representing the period. I will use the term "full amplitude" for the former, and "semi-amplitude" for the latter.

3. Results

The period of RU Cam, prior to 1965, was 22.16 days, and was decreasing (Szeidl *et al.* 1992, Figure 3). After 1965, it was fluctuating around 21.75 days (Szeidl *et al.* 1992, Figure 5). The fluctuations appear to be cyclic (but not periodic), with a typical length of 600 days, or 25 periods. The authors do not mention this, but it is relevant because of its similarity to the behavior of other pulsating variables such as SR stars. Percy and Hale (1998) showed that the fluctuations could be modelled by random cycle-to-cycle fluctuations, but there was also a weak time scale of about 20 periods (their Figures 1 and 2).

The periods which we obtained from Fourier analysis, and their sources, are listed in Table 1. Figure 2 shows the Fourier spectrum of the ASAS-SN observations, determined using VStar.

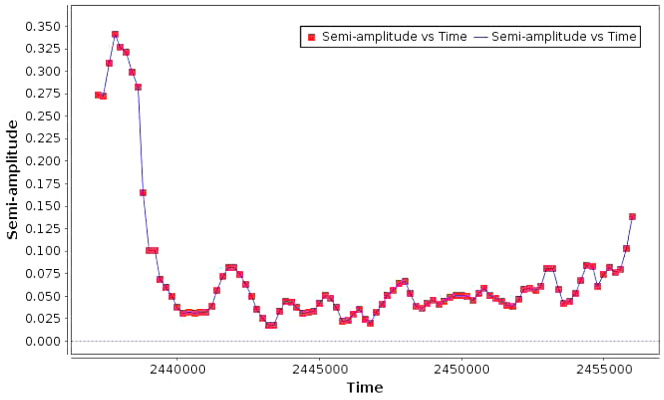

Figure 1. The change in the semi-amplitude of pulsation of RU Cam with time, using AAVSO visual data and the wavelet routine in the AAVSO VStar time-series analysis package. The final increase is spurious, and depends on a very few observations. This is an example of how the sparseness of recent data negatively affects the analysis.

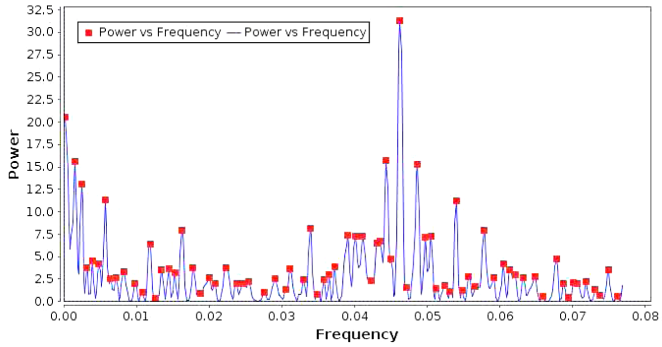

Figure 2. The Fourier spectrum of the ASAS-SN observations of RU Cam, as determined with VStar. The period of 21.62 days is consistent with that determined by Szeidl *et al.* (1992) from earlier data.

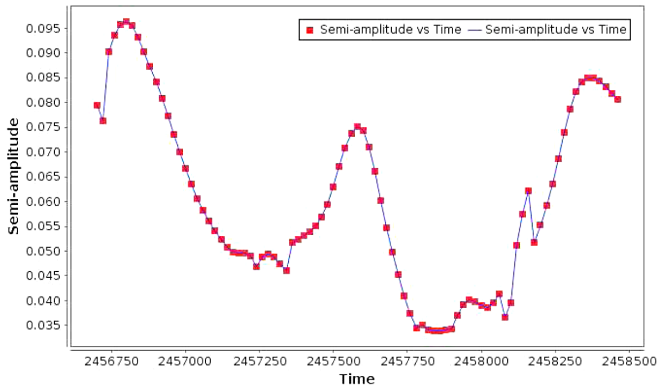

Figure 3. The variations of the semi-amplitude of RU Cam, derived by wavelet analysis from ASAS-SN data. The amplitude variation is consistent with that observed by Szeidl *et al.* (1992).

These are the mean periods and semi-amplitudes for the datasets; they will be affected by the slow fluctuations in both the period and the semi-amplitude. The uncertainties in the periods in Table 1, typically one day, are such that the periods are not significantly different. In particular, the period from the recent ASAS-SN data is the same as that before 1965.

The TESS data covered two cycles of variability: JD 2458842.5–2458867.5, and 2459010.0–2459035.0, in each case with a two-day gap in the middle. The semi-amplitudes of the two cycles were 0.01 and 0.045, respectively, showing the time variation of the pulsation amplitude.

Table 1. Periods and semi-amplitudes determined from Fourier analysis.

P (days)	*A* (mag.)	*Source*
21.45	0.04	AAVSO since 2450000 (Kafka 2020)
23.30	0.06	AAVSO visual 2450000–51000 (Kafka 2020)
20.17	0.05	AAVSO visual 2451000–52000 (Kafka 2020)
21.90	0.06	AAVSO visual 2452000–53000 (Kafka 2020)
21.41	0.06	AAVSO PEP (Kafka 2020)
21.62	0.04	ASAS-SN (Jayasinghe *et al.* 2018, 2019)
22.28	0.06	Hipparcos/Tycho (Perryman *et al.* 1997)

Table 2. Times of minimum, cycle numbers, (O–C) values, sources.

JD (min.)	*N*	*(O–C) (days)*	*Source*
2445254	284	–2.6	Szeidl *et al.* (1992)
2449628	485	–15.4	Berdnikov (2008)
2450195	511	1.6	AAVSO vis (Kafka 2020)
2450377	519	10	AAVSO V (Kafka 2020)
2450418	521	6.6	AAVSO V (Kafka 2020)
2450541	527	–1.4	AAVSO vis (Kafka 2020)
2450543	527	1.5	AAVSO V (Kafka 2020)
2451490	571	–9.0*	AAVSO vis phased (Kafka 2020)
2451552	573	9.2*	AAVSO vis phased (Kafka 2020)
2452432	614	–2.5*	AAVSO vis phased (Kafka 2020)
2452947	638	–9.4*	AAVSO vis phased (Kafka 2020)
2452718	627	1.1	AAVSO V (Kafka 2020)
2453124	646	–6.1	AAVSO V (Kafka 2020)
2453147	647	–4.9	AAVSO V (Kafka 2020)
2456932	821	–4.0	ASAS–SN (Jayasinghe *et al.* 2018, 2019)
2457371	841	–0.5	ASAS–SN (Jayasinghe *et al.* 2018, 2019)
2458061	873	–6.4	ASAS–SN (Jayasinghe *et al.* 2018, 2019)
2458857	909	+6.6:	TESS (STScI 2020)
2459024.5	917	+0.1	TESS (STScI 2020)

I then used (O–C) analysis to attempt to follow changes in the period since the work of Szeidl *et al.* (1992). Table 2 lists times of pulsation minimum, cycle numbers, (O–C) values in days, and their sources. The TESS data yielded two times of minimum, but the first is highly uncertain because of the small amplitude, and the noise in the data. Following Szeidl *et al.* (1992), I used times of pulsation minimum, because they were considered better-defined. I also used the same ephemeris for the C values, namely C = JD 2439079.6 + 21.75N. Unfortunately, for much of the time interval, the data are too sparse to yield times of minimum. This is especially true between JD 2450000 and 2453000. Table 2 includes four times (marked with asterisks) that were derived by phasing together observations within 500-day intervals, but these do not yield a consistent pattern; it is unclear how many cycles are contained between JD 2450000 and 2453000. An (O–C) diagram has therefore not been plotted.

The amplitude of RU Cam varies slowly. This can be seen in Figure 1 of Kolláth and Szeidl (1993), which is based on the data in Szeidl *et al.* (1992). Specifically, the amplitude rises and falls on a time scale of about 430 days, on average, or about 20 pulsation periods, judging from that Figure. The variation is certainly not periodic. Figure 3 shows the semi-amplitude

variation in the ASAS-SN data. It varies from 0.035 to 0.095 on a time scale of roughly 800 days, or about 35 pulsation periods.

4. Discussion

The mean period of RU Cam has not undergone long-term systematic change since 1965, but has fluctuated around the value of 21.75 days, obtained by Szeidl *et al.* (1992). The fluctuations can be modelled as random, cycle-to-cycle fluctuations, such as occur in Mira stars. Mira stars are strongly affected by convection—much more so than in a warmer star like RU Cam. So the cause of RU Cam's fluctuations is unclear.

The amplitude variation in RU Cam is rather similar to that in red semiregular (SR) variables, whose amplitudes vary by up to a factor of 10 on a time scale of 20–40 pulsation periods (Percy and Abachi 2013). It might be useful to study other small-amplitude yellow pulsating variables. Small-amplitude CW stars are, unfortunately, very rare.

Why did RU Cam stop pulsating—almost? The usual answer is that it had evolved out of the instability strip. Its physical properties were no longer such that it was unstable to radial pulsation. But that's just a hypothesis. The constancy of the period, over the past 50 years, places some limits on the rate of evolution of the star (see below).

And what is the nature of its present pulsation, with a wandering period and a variable amplitude—much like the SR variables? Can we really attribute it to stochastic or atmospheric effects? The latter question might be solved through more systematic observation.

Fortunately, there are some very recent theoretical studies which may help to answer some of these questions (Bono *et al.* 2020; Fadeyev 2020). Fadeyev (2020) concludes that W Virginis stars are low-mass post-AGB (asymptotic giant branch) stars that are experiencing the final helium flash. His Figures 4 and 5 shows predicted rates of period change, as a function of period, after the second crossing of the blue edge of the pulsation instability strip. His units are seconds per year. The rate of period change in RU Cam appears to be no greater than 0.5 day in 60 years, or 720 seconds per year—within the range of the models which are plotted in Fadeyev's (2020) Figures 4 and 5. Further comparison with the models is beyond the scope of this paper.

5. Conclusions

For over half a century, the variability of RU Cam has been consistent: a period of about 21.75 days, about which there are slow fluctuations, and a full V amplitude which varies between 0.00 and 0.30 on time scales of 20 to 40 pulsation periods. Perhaps this is the "new normal" for this star. But will it continue?

RU Cam deserves to be monitored systematically, preferably in UBV filters. Its amplitude decrease was highly unusual. Its period and amplitude variations continue, and they may tell us about the evolution and the stochastic processes in this and other types of pulsating stars.

6. Acknowledgements

I thank the ASAS-SN team for making their data and results publicly available. I also thank the AAVSO observers and staff for making and archiving the AAVSO data, and the developers of VStar for creating this very useful resource. This paper also made use of data from the Hipparcos and TESS missions. I thank Drs. Scott Fleming and Rebekah Hounsell, of the TESS team, for their assistance in accessing TESS data. This project also made use of the SIMBAD database maintained in Strasbourg, France. The Dunlap Institute is funded through an endowment established by the David Dunlap family, and the University of Toronto.

References

Benn, D. 2013, VStar data analysis software (https://www.aavso.org/vstar-overview).

Berdnikov, L. N. 2008, VizieR Online Data Catalog: Photoelectric Observations of Cepheids in UBV(RI)$_c$.

Bono, G., *et al.* 2020, *Astron. Astrophys.*, **644A**, 96.

Demers, S., and Fernie, J. D. 1966, *Astrophys. J.*, **144**, 440.

Fadeyev, Yu. A. 2020, arXiv:2011.09313.

Jayasinghe, T., *et al.* 2018, *Mon. Not. Roy. Astron. Soc.*, **477**, 3145.

Jayasinghe, T., *et al.* 2019, *Mon. Not. Roy. Astron. Soc.*, **486**, 1907.

Kafka, S. 2020, variable star observations from the AAVSO International database (https://www.aavso.org/aavso-international-database-aid).

Kochanek, C. S., *et al.* 2017, *Publ. Astron. Soc. Pacific*, **129**, 104502.

Kolláth, Z., and Szeidl, B. 1993, *Astron. Astrophys.*, **277**, 62.

Percy, J. R., and Abachi, R. 2013, *J. Amer. Assoc. Var. Star Obs.*, **41**, 193.

Percy, J. R., and Hale, J. 1998, *Publ. Astron. Soc. Pacific*, **110**, 1428.

Perryman, M. A. C., European Space Agency Space Science Department, and the Hipparcos Science Team. 1997, The Hipparcos and Tycho Catalogues, ESA SP-1200 (VizieR On-line Data Catalog: I/239), ESA Publications Division, Noordwijk, The Netherlands.

Shappee, B. J., *et al.* 2014, *Astrophys. J.*, **788**, 48.

Space Telescope Science Institute. 2020, Transiting Exoplanet Survey Satellite (TESS), Missions and Data (https://archive.stsci.edu/missions-and-data/transiting-exoplanet-survey-satellite-tess).

Szeidl, B., Olah, K., Szabados, L., Barlai, K., and Patkos, L. 1992, *Commun. Konkoly Obs.*, No. 97, 245.

Wallerstein, G. 2002, *Publ. Astron. Soc. Pacific*, **114**, 689.

Light Curve Analysis of 185 YSOs: New Periods Discovered for 9 Stars

Joshua R. Hamilton
Citizen Scientist, Disk Detective Project (NASA); Lansing, MI 48912; joshuahamiltonmi@gmail.com

Received November 30, 2020; revised May 27, 2021; accepted June 2, 2021

Abstract Using AAVSO's VSTAR software, all 185 YSOs listed in the AAVSO's Target Tool were analyzed using the Date Compensated Discrete Fourier Transform (DCDFT) algorithm, searching for periodicity. Light curves created from the AID (AAVSO International Database) data and ASAS-SN data were used for this analysis. Of the 185 YSO candidates analyzed, new semiregular periods were discovered for nine stars. The remaining 176 YSO candidates analyzed did not show significant semiregular periodicity, were unable to be analyzed due to the lack of enough usable data, or already had periods listed in VSX or ASAS-SN.

1. Introduction

The AAVSO Target Tool lists 185 YSO (Young Stellar Objects) candidates. YSOs are stars in their earliest stages of development. As these stars age, there are many physical processes both internally and externally that impact their variability. Regular observation and analysis of YSOs is key in better understanding stellar evolution from protostar to main sequence. YSOs are highly variable, and their variability is often irregular.

Using the most recent data from AID (Kafka 2021) and ASAS-SN (Shappee *et al.* 2014; Kochanek *et al.* 2017) on these 185 YSO candidates, periods have been discovered for nine stars.

2. Light curve analysis using DC DFT algorithm

2.1. Methods

From the list of 185 YSO candidates in AAVSO's Target Tool (https://www.aavso.org/aavso-target-tool), a DC DFT algorithm (Ferraz-Mello 1981) in the AAVSO's software VSTAR (Benn 2012) was used to look for periodicity in the light curves of any YSO candidates as long as the star had at least 100 Johnson V-band observations in the AID.

If a YSO candidate met these two criteria, its AAVSO light curve data set was downloaded into VSTAR, where a DC DFT algorithm was used to look for any periodicity in the Johnson V-band. The Johnson V-band was chosen because most stars in the AID have primarily Visual and Johnson V-band data, with other light bands being sporadic and therefore not useful in this analysis.

Each star was then run through the ASAS-SN database (Shappee *et al.* 2014; Kochanek *et al.* 2017). The ASAS-SN data were downloaded into VSTAR and combined with the AID data. DC DFT was used for various bands / means to search for any regular periodicity.

2.2. Results

Most of the YSO candidates analyzed were listed as irregular variables of various types (UXOR, IS, INS, CTTS, etc.) and as expected, a DC DFT analysis of their data was unable to find any significant periodicity (i.e. confirming their classification as irregular variables). Of the 185 YSO candidates:

- 73 stars did not have enough data to provide a useful analysis (i.e. they had less than 100 Johnson V-band observations in the AID).
- 95 of the stars showed no significant periodicity.
- Due to the AID and ASAS-SN data spacing, low periods (less than 30 days) are difficult to detect with these data sets and a DCDFT analysis alone.
- 17 of those 95 stars had previously recorded periods in VSX (Watson *et al.* 2006–2014). Those periods in VSX ranged from 2.09 d to 18.58 d.
- 13 of those 95 stars had previously recorded periods in ASAS-SN. Those periods ranged from 0.5d to 27.0d.
- 8 stars showed periods consistent with those already reported in ASAS-SN or other literature. Periods ranged from 62 d to 1297 d.
- 9 stars showed new periods (Table 1).

The list of the 176 YSO candidates without new periods are not listed here; however, they are available upon request or by using the AAVSO Target Tool.

2.3. Notes and discussion

The nine stars showing new periods were queued in SIMBAD to look for previous literature references and in VIZIER for data and references to their spectral type, variation type, and Gaia data (Table 2).

CT Vul DC DFT analysis in VSTAR created a periodogram which indicated a power of 100.33 for the frequency 0.002588, which correlated to a period of 386 days (Figure 1). The period model of 386 days shown in red within the light curve from VSTAR (Figure 2) shows that the model period is a close fit to the actual observations. While CT Vul appears to follow the 386-day period regularly, there are fluctuations in the range of these semi-regular variations. At JD 2456750, JD 2458250, and JD 2458750 (Figure 2), CT Vul moves to various faint magnitudes, reaching as low as magnitude 16.7 in the V-band at JD 2458250, while at other faint sections, the star appears to remain brighter than magnitude 15.

Schaefer (1986) and others have labeled CT Vul as a R CrB star. R CrB stars are a rare class of variable stars in which they remain at a fairly stable maximum brightness until occasionally their brightness abruptly drops by a large but variable amount for an indeterminate length of time before brightening back to the previous maximum. This variable drop in brightness is believed to be caused when a stream of matter is ejected out of the star, and some of the metals condense, obscuring the star. These ejections are related to semiregular pulsations that R CrB stars undergo (Trimble 1972). The light curve developed

Table 1. New semi-regular periodicity of YSO candidates.

Star	*GCVS Type*	*Number of Data Points*	*Time Period of Data*	*Period (days)*	*Johnson V Range (mag)*
CT Vul	IS	648	Mar. 2014–Aug. 2019	386	2.7
FY Lac	I	936	June 2013–Nov. 2020	279	1.1
MY Lup	TTS	11711	Mar. 2016–Sep. 2018	2.63	1.0
SV Cep	UXOR	2432	Sep. 2005–Nov. 2020	975	1.2
V0369 Per	IS	1084	Dec. 2011–Oct. 2020	212	1.8
V0561 Cyg	ISB	1547	July 2011–Nov. 2020	101	1.1
V1331 Cyg	INST	2244	June 2011–May 2021	449	1.1
V1515 Cyg	FUOR	2407	Sep. 2001–Nov. 2020	341	1.5
WW Vul	UXOR	6627	Sep. 2000–May 2021	69	2.0

Table 2. Gaia DR2 Data (Gaia Collaboration *et al.* 2018) on stars with new periods discovered.

Star	*R.A. (J2000) h m s*	*Dec. (J2000) ° ‘ “*	*Distance (pc)*	*Effective Temo. (K)*	*Radius (solRad)*	*Luminosity (solLum)*
CT Vul	19 47 32.57	+20 54 17.79	1121	5068	1.95	2.27
FY Lac	22 32 35.51	+45 31 46.27	1050	3306	102.14	1123.14
MY Lup	16 00 44.52	–41 55 30.93	156	4412	1.60	0.88
SV Cep	22 21 33.22	+73 40 27.10	344	6395	2.04	6.25
V0369 Per	02 51 17.20	+38 14 40.77	11494	3771	—	—
V0561 Cyg	20 25 58.22	+52 08 41.19	2458	3306	91.76	906.21
V1331 Cyg	21 01 09.21	+50 21 44.80	596	4403	4.97	8.36
V1515 Cyg	20 23 48.02	+42 12 25.78	1008	3595	9.59	13.85
WW Vul	19 25 58.75	+21 12 31.33	504	6634	2.69	12.62

here could be consistent with the behavior of an R CrB star. Though holding to a fairly consistent maximum brightness between 14.0 and 14.3 (V band), CT Vul dramatically drops in brightness to as low as magnitude 16.7 before returning to its maximum. This cyclic pulsation occurs approximately every 386 days.

FY Lac DC DFT analysis in VSTAR shows semiregular periodicity at 279 days (Figure 3). FY Lac is listed in Gaia DR2 (Gaia Collaboration 2018) collection of Long Period Variable candidates (LPVc). It is an M6 star (Lee *et al.* 1947). FY Lac is likely a semiregular pulsating red giant. The title of long period variable would also fit this star, as it does not show the regularity or large brightness variations of a Cepheid or a Mira variable but it does show semiregular variability.

MY Lup Due to an abundance of AID data for this star, a highly frequent period of 2.63 days was discovered (Figure 4). MY Lup is a K0 star (Alcalá *et al.* 2017), categorized as a T Tau star in VSX and most literature. T Tau stars are quick-rotating young stars on their way to the main sequence. The cause of this short-period variation shown here in this analysis is difficult to pinpoint. Some T Tau stars are known to contain large sunspots, which could diminish the brightness of MY Lup during each short rotation. T Tau stars are also known to have powerful stellar winds and/or mass ejections of materials through jets at their poles. T Tau variation is often attributed to unevenly distributed dust and debris in the disk surrounding the star. More research is needed to find the cause of this 2.63-day cyclic drop of ~1 magnitude.

SV Cep DC DFT analysis in VSTAR shows semiregular periodicity at 975 days (Figure 5). It is listed as a Herbig Ae/Be star in Simbad and in most literature. SV Cep is 2.5 $M_{\odot}$, which puts it on the smaller end of Herbig Ae/Be stars (typically 2–8$M_{\odot}$). This star is known to have a circumstellar disk, and this disk is extremely well studied. Many have theorized that SV Cep's disk is not homogenized, but rather contains populations of dust varying in size, density, and material make-up. Using infrared observations during different periods of SV Cep's brightness variation, Friedemann *et al.* (1992) were able to determine that at least three different grain populations exist within SV Cep's circumstellar disk. Since SV Cep is listed in VSX as a UXOR or UX Ori star, the long-period semiregular variation seen in this analysis would be consistent with variability in other UXOR stars (most of which are Herbig Ae/Be stars). VSX defines a UXOR as a star with "irregular variations on time-scales of days around a mean brightness level that changes on a much longer time-scale (typically years), sometimes in a quasi-cyclic fashion...." The variation over 975 days could account for the quasi-cyclic mean brightness levels that change, while the star's brightness varies greatly on a shorter time scale (Figure 6).

V369 Per DC DFT analysis shows a semiregular period of 212 days for V369 Per (Figure 7). The data cover 2,655 days between July 7, 2013, and October 14, 2020. This star is not particularly well studied, but is among the large catalogue of LPVc from Gaia DR2 (Gaia Collaboration 2018). Gaia DR2 also classifies V369 Per as a Mira variable with a period estimate of ~282 days. Skiff (2009) classifies this star as a M5 star, and with its distance (11,494 pc) and low proper motion in Gaia DR2, it is likely a pulsating semiregular red giant. Combined with the light curve and model of a 212-day period (Figure 7), this analysis appears to confirm the Gaia DR2 classification of V369 Per as a Mira variable.

V561 Cyg DC DFT analysis shows a semiregular period of 101 days for V561 Cyg (Figure 9). It appears in Gaia DR2 (Gaia Collaboration 2018) as a Mira and is listed with a spectrum of G-K (Samus *et al.* 2007–2017). It is an extremely luminous star, recorded at 906 times as luminous as the sun. This fact, combined with the Mira-like variation, low proper motion, and distance, makes this star a likely candidate for a pulsating giant (G or K giant). An analysis of the 101-day period model overlaid on the light curve in VStar (Figure 10) does show some Mira-like variation. A lack of frequent enough measurement makes this evidence suggestive at best, and more data at a higher cadence are needed to confirm this period and V561 Cyg's potential classification as a Mira variable.

V1331 Cyg DC DFT analysis shows a semiregular period of 449 days for V1331 Cyg (Figure 11). There is some variation in classification of this star's spectral type, but F0/F4-G5 (Gramajo *et al.* 2014) seems to be the most commonly referenced spectral type. It is also listed as a T Tau star in the pre-FUOR stage (FU Ori star—when a star experiences a large change in brightness and spectral type), though this is highly debated in a number of papers. Quanz *et al.* (2007) suggest that V1331 Cyg does not meet the behavioral requirements to be labeled as a pre-FUOR or FUOR star. A FUOR eruption in the past may have shaped some of the disc and dust around V1331 Cyg, including the large outer ring that surrounds V1331 Cyg. It is unclear what internal or external processes may be causing this semiregular variation at ~449 days.

V1515 Cyg DC DFT analysis shows a semiregular period of 341 days for V1515 Cyg (Figure 12). This star has a spectrum G0/G2Ib (Skiff 2009), and is labeled as a FUOR. It is listed among Gaia DR2's LPVc as a Mira variable (Gaia Collaboration 2018). The light curve from VStar (Figure 13) also shows an overall decrease in brightness, even while lesser cycles of brightening and darkening occurred around every 341 days. In October 2004, the mean of the Johnson V measurements at maximum was 12.7, and by July of 2020, the mean at maximum was 13.9. This is consistent with a star post-FUOR episode or ejection, as many stars darken by one or two magnitudes in the months and years after a FUOR ejection or episode. A portion of the light curve from JD 2456020 to 2459177 includes enough data and a high enough cadance to compare the 341-day period model to the actual measurements. Though there are some semiregular variations similar to a Mira variable, more data and closer intervals are needed to confirm or deny Gaia DR2's categorization as a Mira. Since the star otherwise shows signs of being a T Tau star and an FUOR (designations of pre-main sequence stars), it would be unlikely that this star was a Mira (designation of a star in the late stages of stellar evolution).

WW Vul DC DFT analysis in VStar shows semiregular periodicity at 69 days for WW Vul (Figure 14). WW Vul is a well-studied star with a spectrum of A2IVe (Mora *et al.* 2001) and is labeled as a UXOR. As defined for SV Cep above, these stars show variation on a short time-scale, while displaying an overall shift in brightness over longer time-scales, sometimes in a cyclic or quasi-cyclic manner. The AID data and ASAS-SN data are too sporadic to compare the model period at 69 days to the light curve in order to determine what kind of variation might be happening. Consistent with UXOR stars, the variation appears cyclic overall, with lots of micro-variations on short time scales. The amount of darkening and brightening also varies within each cycle. In some cycles, WW Vul darkens by as much as 1.75 magnitude in the Johnson V-band, while in other cycles, a variation of 0.5 magnitude is observed. There also appears to be a large brightening event culminating at a maximum magnitude (V-band) of 9.99 at JD 2456549. More data and high frequency intervals are needed to continue to learn about WW Vul and seek to explain the internal and/or external causes of its semiregular variations.

3. Conclusions

Nine variable stars have been shown to have new semiregular periods. Continued monitoring of these nine variable stars is necessary to confirm these newly discovered periods and to understand the physical processes that cause this semiregular periodicity in these stellar systems. Understanding the various processes at work in stellar systems as they evolve from protostar to the main sequence and beyond is essential in understanding the evolution of our own solar system, and all stellar systems.

As shown in Table 1, CT Vul shows a period of 386 days and the findings here appear to confirm the theory of Schaefer (1986) that CT Vul is an R CrB-type star. FY Lac shows semiregular variability at around 279 days. Gaia DR2 (Gaia Collaboration 2018) lists this star at a LPVc and the findings here of periodicity at 279 days confirms that categorization. MY Lup showed a very short period of 2.63 days. It is listed as a T Tau-type star, but it is difficult to pinpoint the exact internal or external causes of this strong and frequent periodicity. SV Cep shows a period of 975 days. It is listed as a Herbig Ae/Be star and an UXOR, and the light curve and periodicity appear to confirm its categorization as an UXOR. V369 Per shows a periodicity of 212 days. The light curve shows Mira-like variation at this periodicity, and confirms its previous categorization by Gaia DR2 as a Mira-type star. V561 Cyg shows a period of 101 days. It is listed in Gaia DR2 as a Mira-type star (Gaia Collaboration 2018). Due to AID and ASAS-SN data for this star being sporadic, there is not enough of a complete light curve here to confirm this categorization, though some Mira-like motion can be seen in the light curve. More research and smaller-interval data measurements are needed. V1331 Cyg shows a period of 449 days. Some literature list this star as an FUOR, though other papers indicate there may not be enough evidence to accurately list it as an FUOR. The light curve with data from AID and ASAS-SN does not give conclusive evidence as to this categorization, and therefore more research is needed to confirm or disprove its categorization as an FUOR and to explain this 449-day periodicity. V1515 Cyg shows a period of 341 days. It is listed as an FUOR in Simbad, though Gaia DR2 lists it as a Mira-type star. The light curve generated from AID and ASAS-SN data shows some signs that the star may be in a post-FUOR period as the overall brightness decreased steadily over time, even while the semi-cyclic variations appeared every 341 days. More data are needed to accurately categorize this star properly and to explain the periodicity discovered here. WW Vul shows a period of 69 days. It is categorized as an

UXOR, and the light curve overall appears consistent with this designation (cyclic overall, with micro-variations on shorter time scales of days to weeks). Further and more frequent observations are needed to better understand the type of variability WW Vul is experiencing, and the cause(s) of that variation.

Of the 176 remaining YSOc from the AAVSO Target Tool list, 73 stars did not have enough data to provide a useful analysis, and 95 of the stars showed no significant periodicity (though due to the AID and ASAS-SN data spacing, low periods (less than 30 days) are difficult to detect with these data sets and a DCDFT analysis alone). 17 of those 95 stars had previously recorded periods in VSX; those periods in VSX ranged from 2.09 to 18.58 days. 13 of those 95 stars had previously recorded periods in ASAS-SN; those periods ranged from 0.5 to 27.0 days. Eight of those 95 stars showed periods consistent with those already reported in ASAS-SN or other literature; those periods ranged from 62 to 1,297 days.

4. Acknowledgements

I want to acknowledge the variable star observations from the AAVSO International Database contributed by observers around the world and used in this research. There are too many observers to list by name, but without their observations, this type of data analysis would not be possible. Thanks to the developers of the VStar data analysis and visualization software package, which allowed for the analysis of AID data using the DC DFT algorithm. This research paper has also made use of the SIMBAD and Vizier databases. The International Variable Star Index (VSX) database, operated at AAVSO, Cambridge, Massachusetts, was also very helpful in completing this research. Special thanks also to the developers of the DC DFT algorithm, which allowed this analysis to take place.

References

Alcalá, J. M., *et al.* 2017, *Astron. Astrophys.*, **600A**, 20.
Benn, D. 2012, *J. Amer. Assoc. Var. Star Obs.*, **40**, 852.
Ferraz-Mello, S. 1981, *Astron. J.*, **86**, 619.
Friedemann, C., Reimann, H.-G., and Guertler, J. 1992, *Astron. Astrophys.*, **255**, 246.
Gaia Collaboration, et al. 2018, *Astron. Astrophys.*, **616A**, 1.
Gramajo, L. V., Rodón, J. A., and Gómez, M. 2014, *Astron. J.*, **147**, 140.
Kafka, S. 2021, Observations from the AAVSO International Database (https://www.aavso.org).
Kochanek, C. S., et al. 2017, *Publ. Astron. Soc. Pacific*, **129**, 104502.
Lee, O. J., Baldwin, R. J., Hamlin, D. W., Bartlett, T. J., Gore, G. D., and Baldwin, T. J. 1943, *Ann. Dearborn Obs.*, **5, 1.**
Mora, A., *et al.* 2001, *Astron. Astrophys.*, **378**, 116.
Quanz, S. P., Apai, D., and Henning, Th. 2007, *Astrophys. J.*, **656**, 287.
Samus, N. N., *et al.* 2007–2013, *General Catalogue of Variable Stars*, VizieR On-line Data Catalog (http://cdsarc.u-strasbg.fr/viz-bin/Cat?B/gcvs).
Schaefer, B. E. 1986, *Astrophys. J.*, **307**, 644.
Shappee, B. J., *et al.* 2014, *Astrophys. J.*, **788**, 48.
Skiff, B. A. 2009, *VizieR Online Data Catalog: Catalogue of Stellar Spectral Classifications* (https://ui.adsabs.harvard.edu/abs/2014yCat....1.2023S).
Trimble, V. 1972, Mon. Not. Roy. Astron. Soc., **156**, 411.
Watson, C., Henden, A. A., and Price, C. A. 2014, AAVSO International Variable Star Index VSX (Watson+, 2006–2014; https://www.aavso.org/vsx).

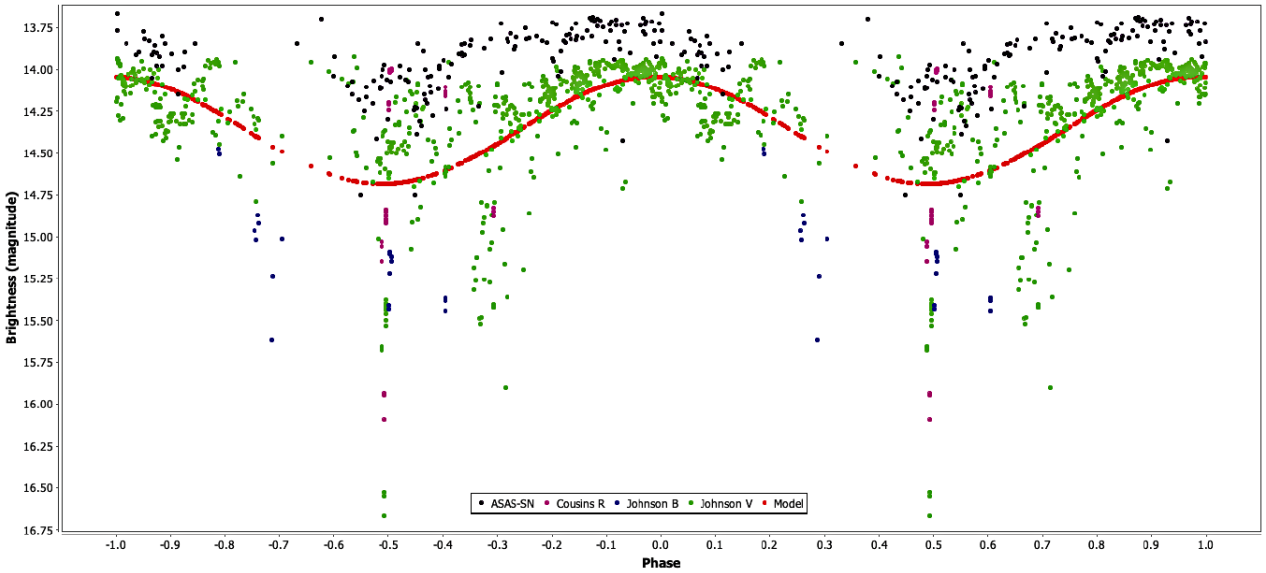

Figure 1. Phase plot for CT Vul (period 386 d, epoch 2456891) including AID and ASAS-SN data.

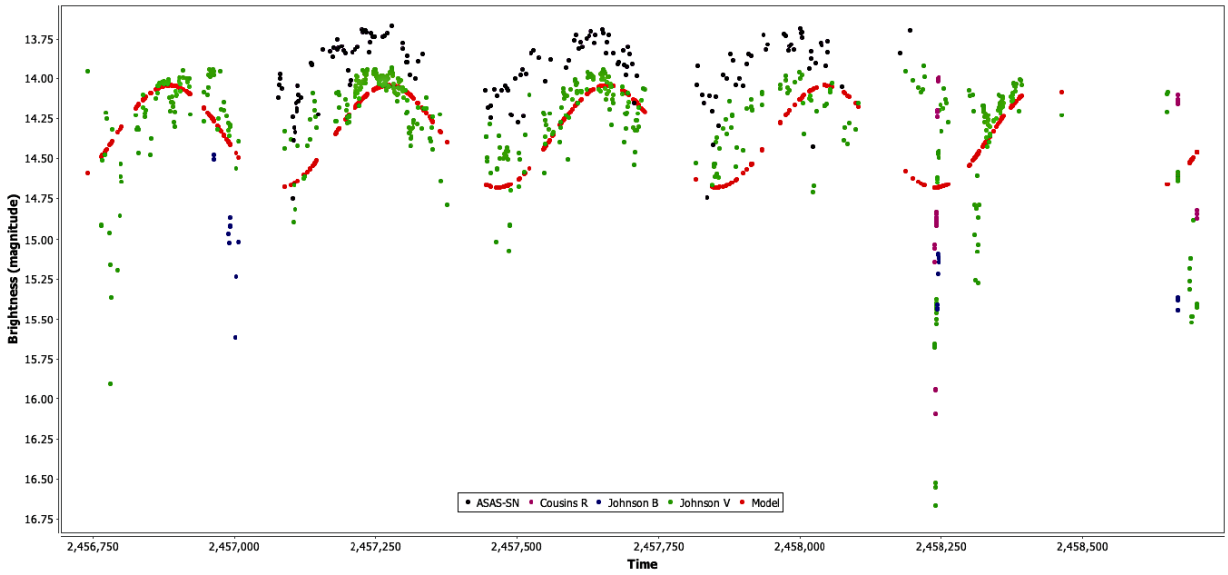

Figure 2. Light curve for CT Vul including AID and ASAS-SN data.

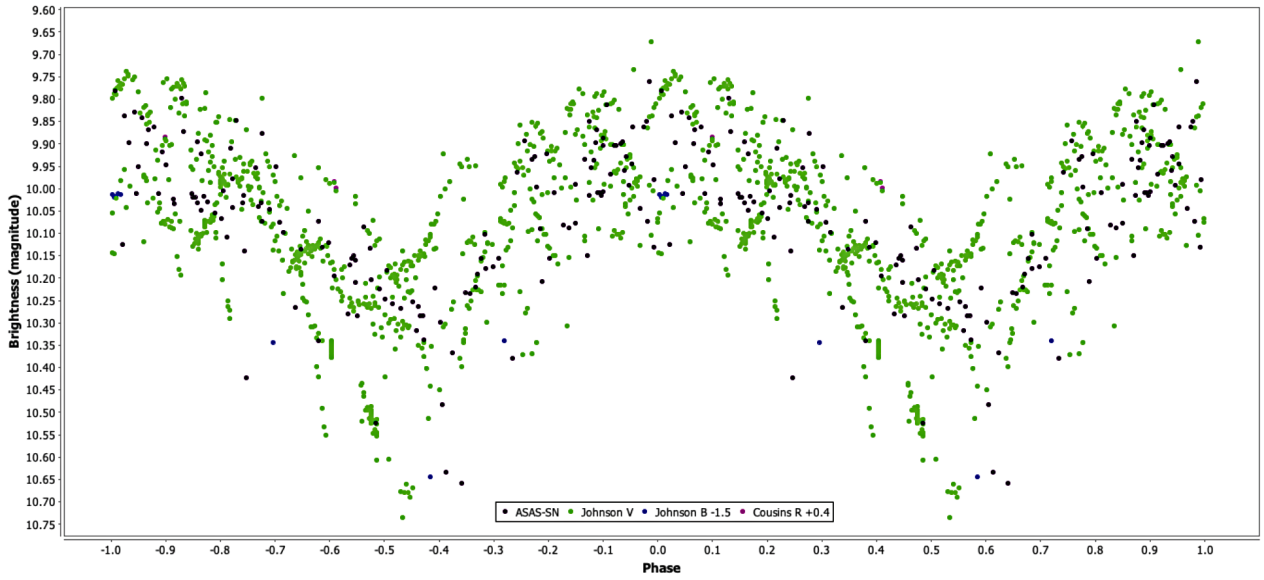

Figure 3. Phase plot for FY Lac (period 279 d, epoch 2456608) including AID and ASAS-SN data.

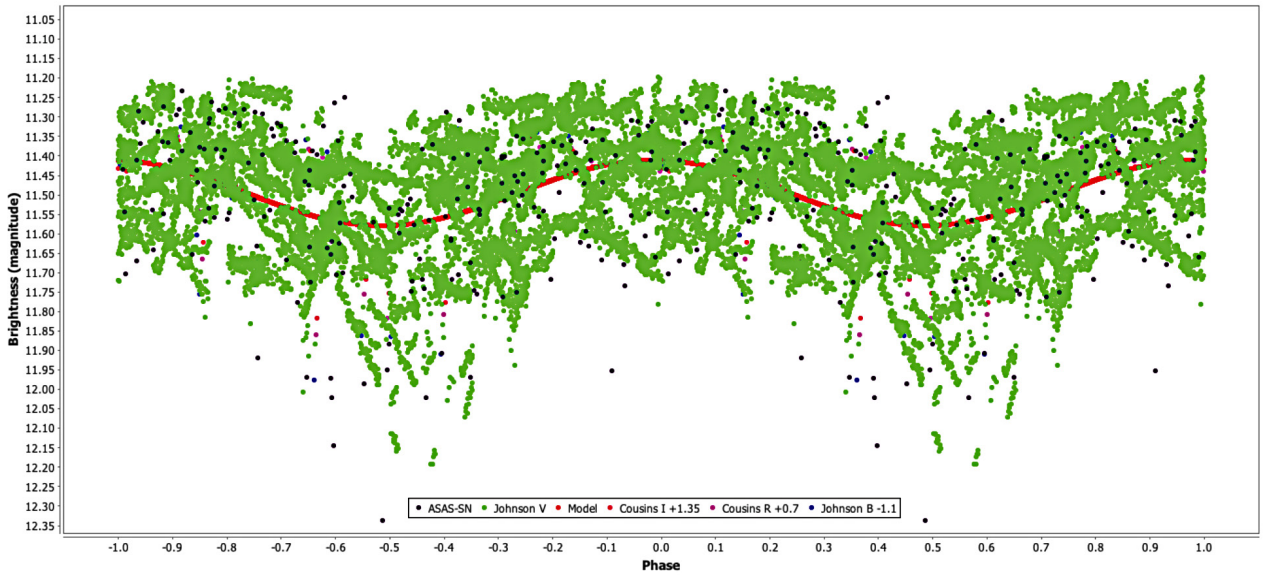

Figure 4. Phase plot for MY Lup (period 2.629 d, epoch 2457877.1) including AID and ASAS-SN data.

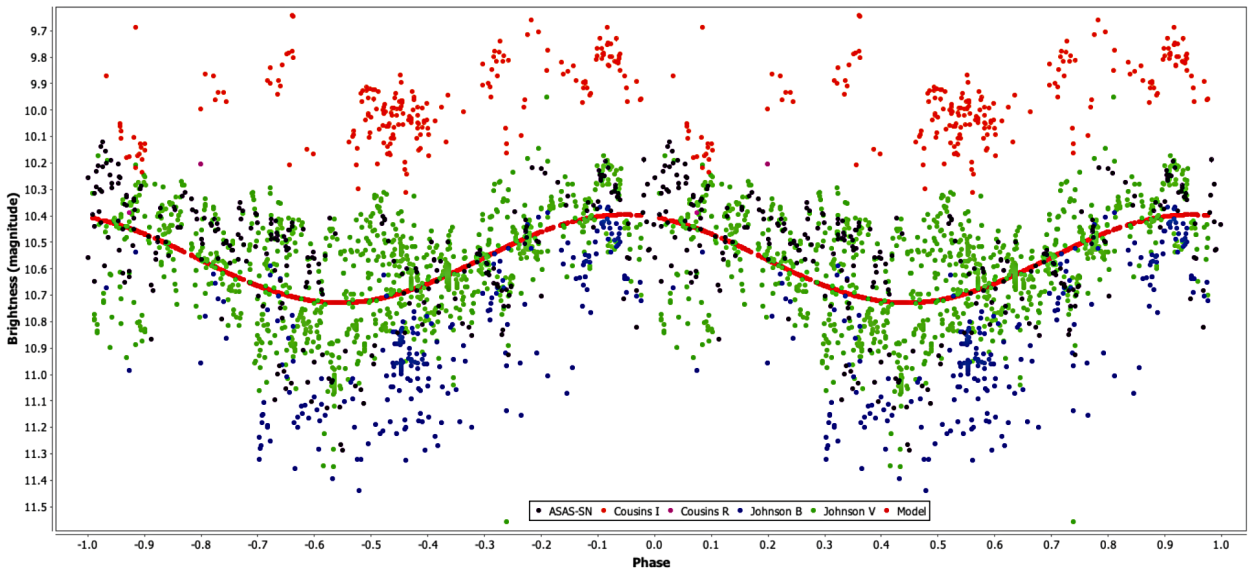

Figure 5. Phase plot for SV Cep (period 975 d, epoch 2455033) including AID and ASAS-SN data.

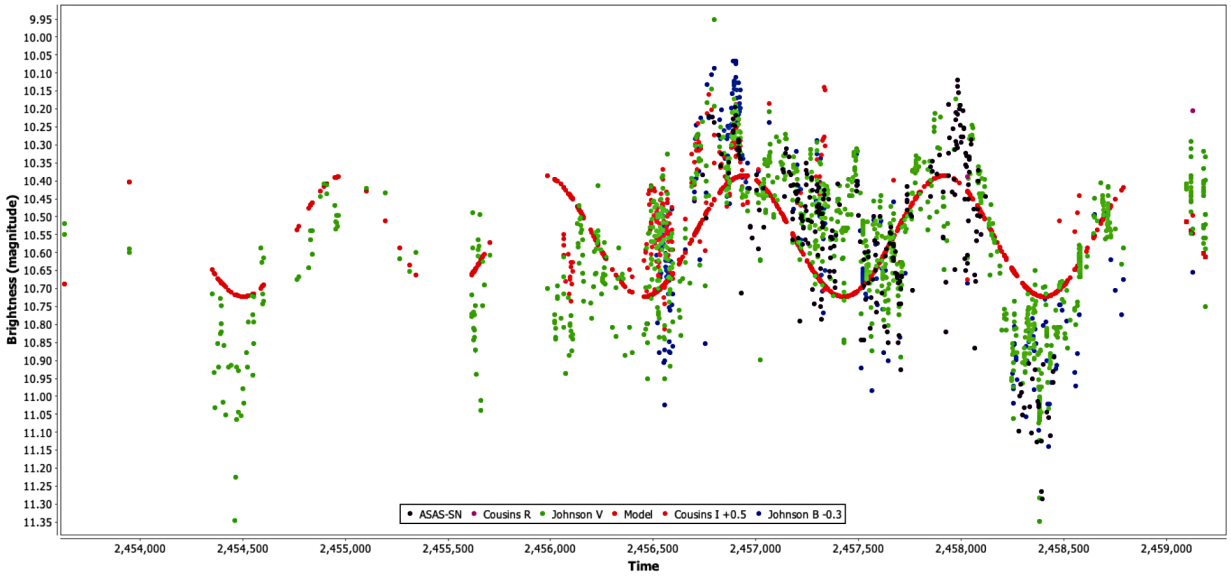

Figure 6. Light curve for SV Cep including AID and ASAS-SN data.

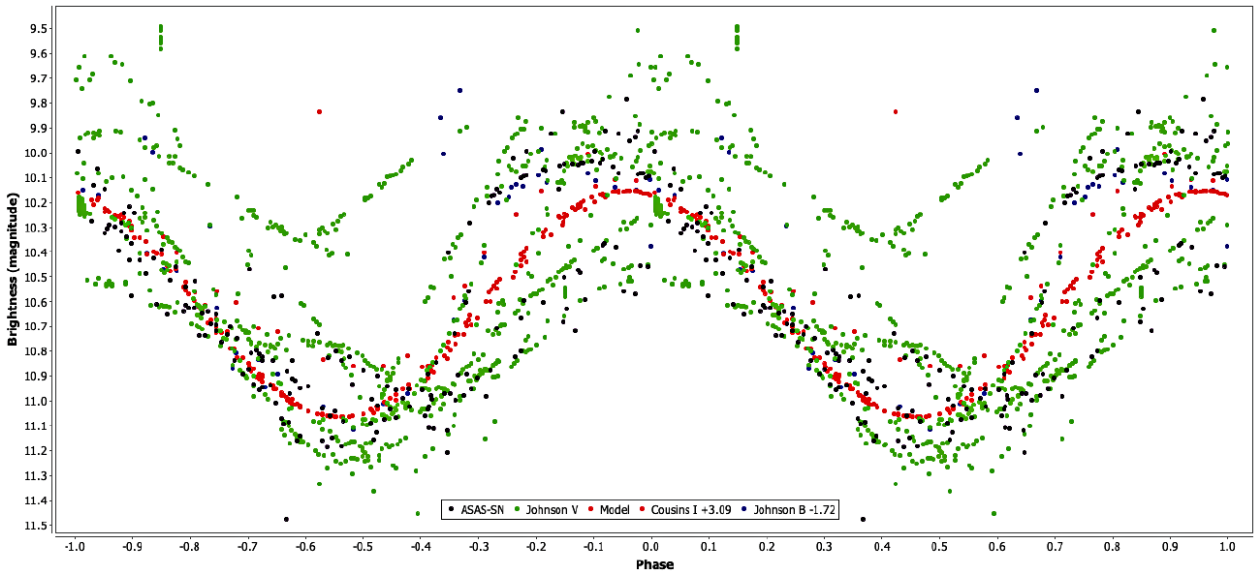

Figure 7. Phase plot for V369 Per (period 212 d, epoch 2456922) including AID and ASAS-SN data.

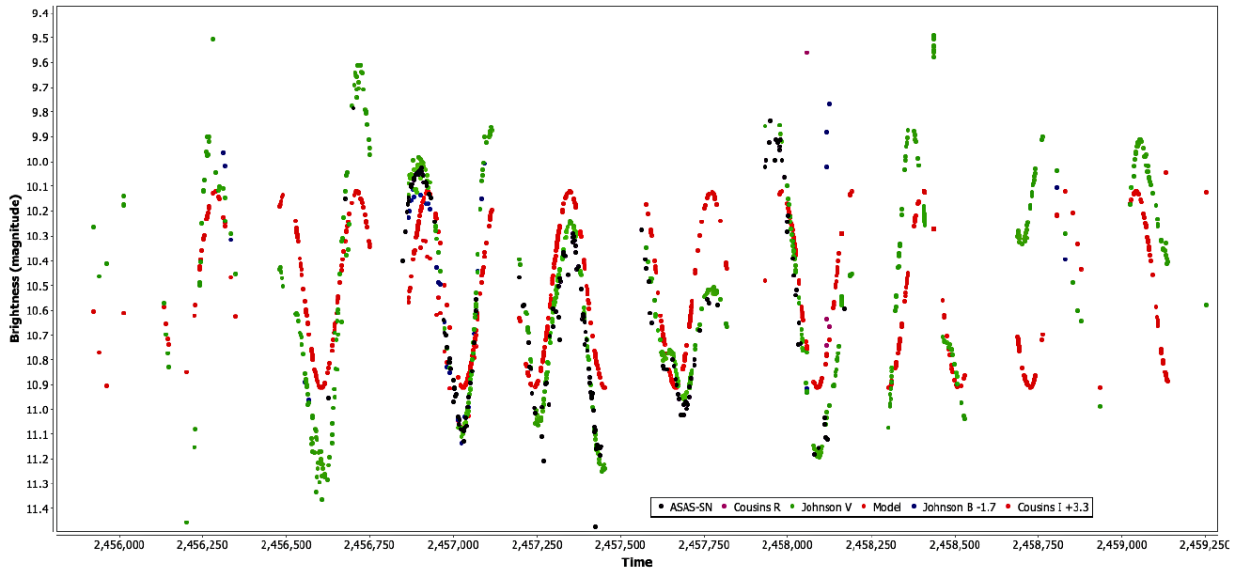

Figure 8. Light curve for V369 Per including AID and ASAS-SN data.

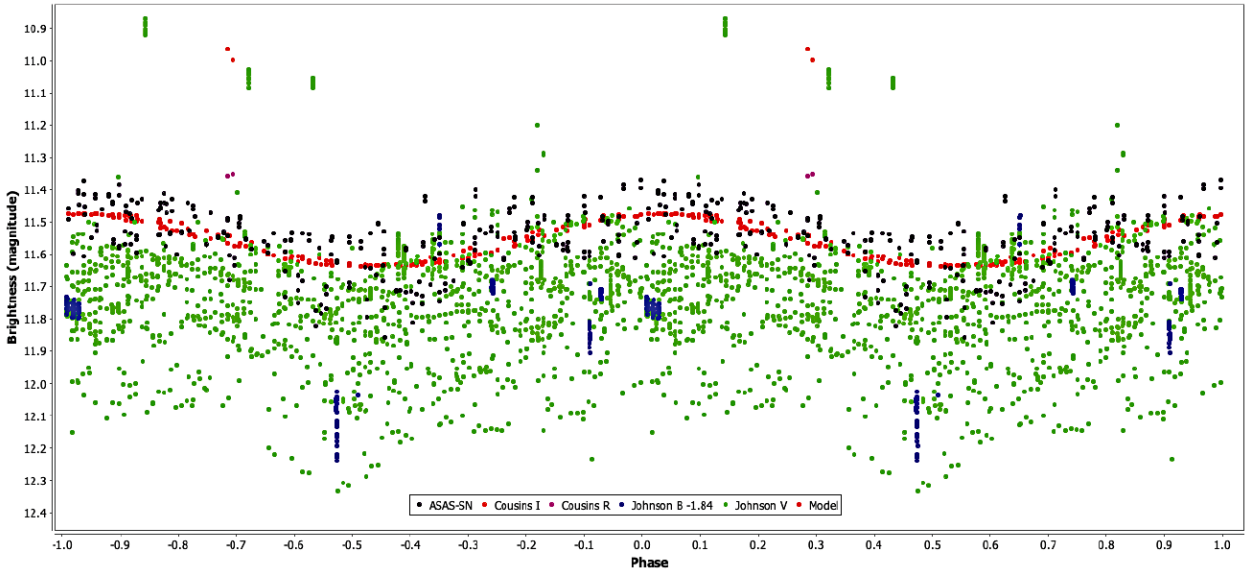

Figure 9. Phase plot for V561 Cyg (period 101 d, epoch 2457193) including AID and ASAS-SN data.

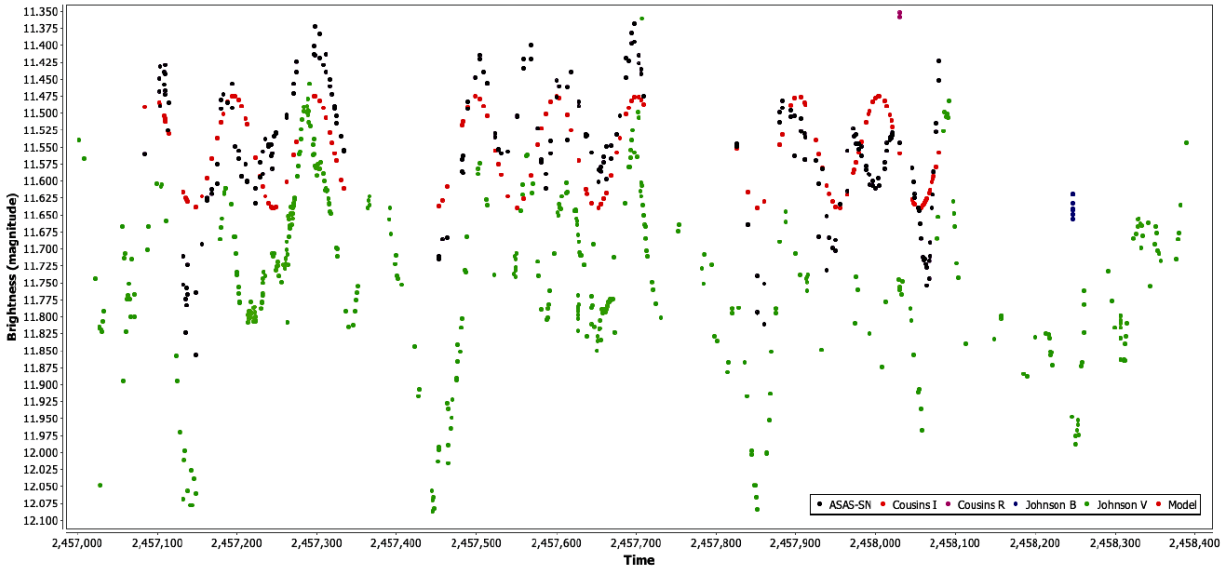

Figure 10. Light curve for V561 Cyg including AID and ASAS-SN data.

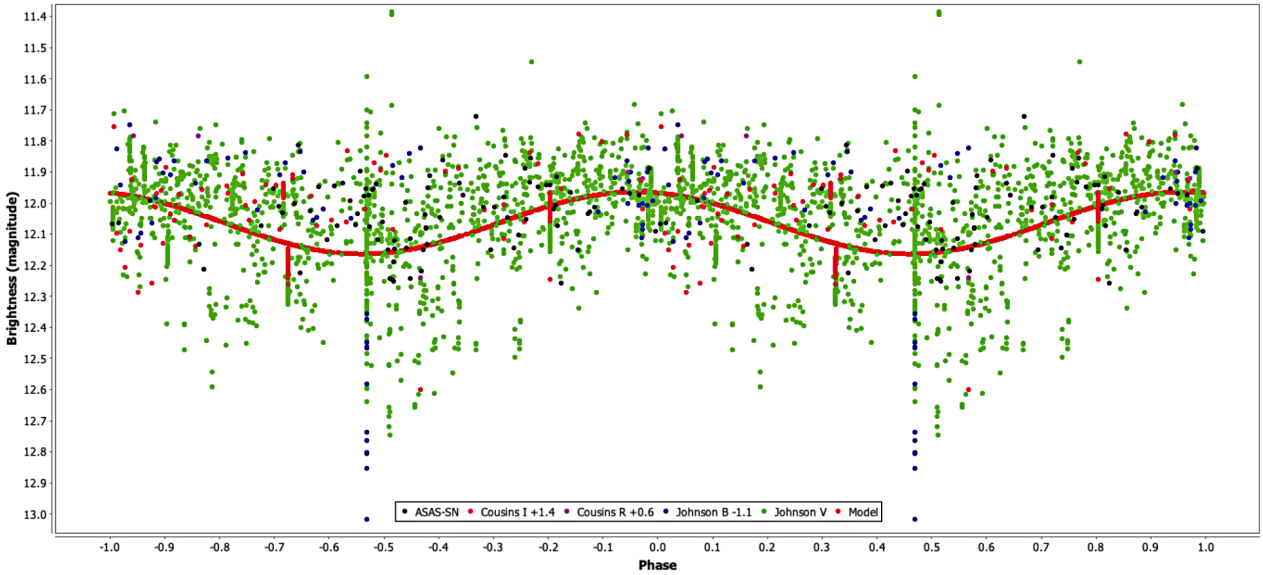

Figure 11. Phase plot for V1331 Cyg (period 449 d, epoch 2456878) including AID and ASAS-SN data.

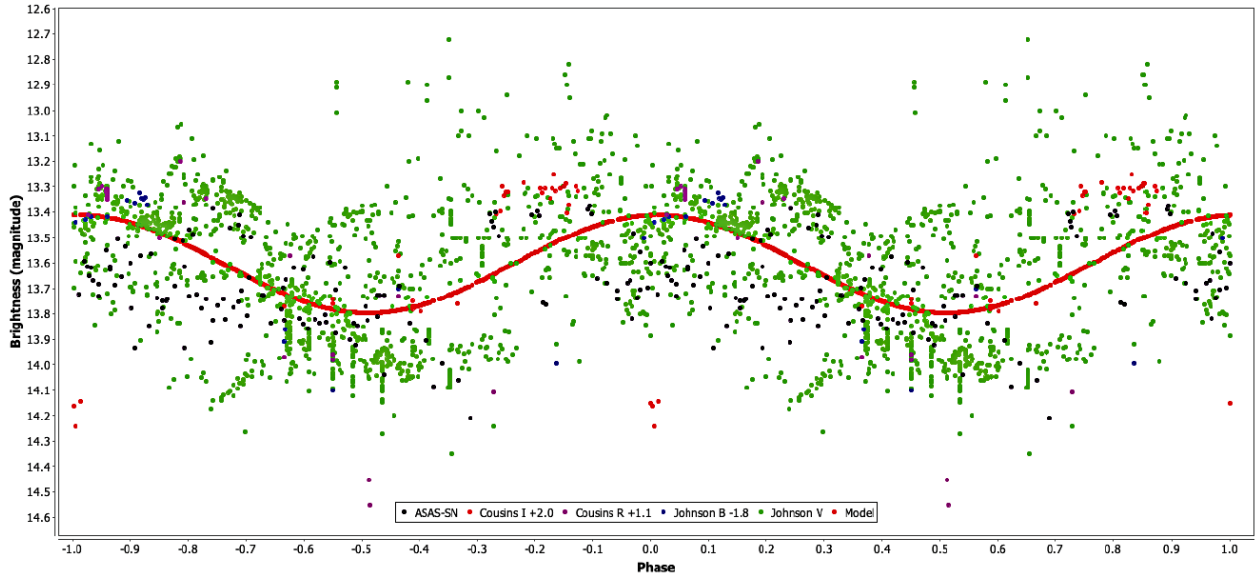

Figure 12. Phase plot for V1515 Cyg (period 341 d, epoch 2455468) including AID and ASAS-SN data.

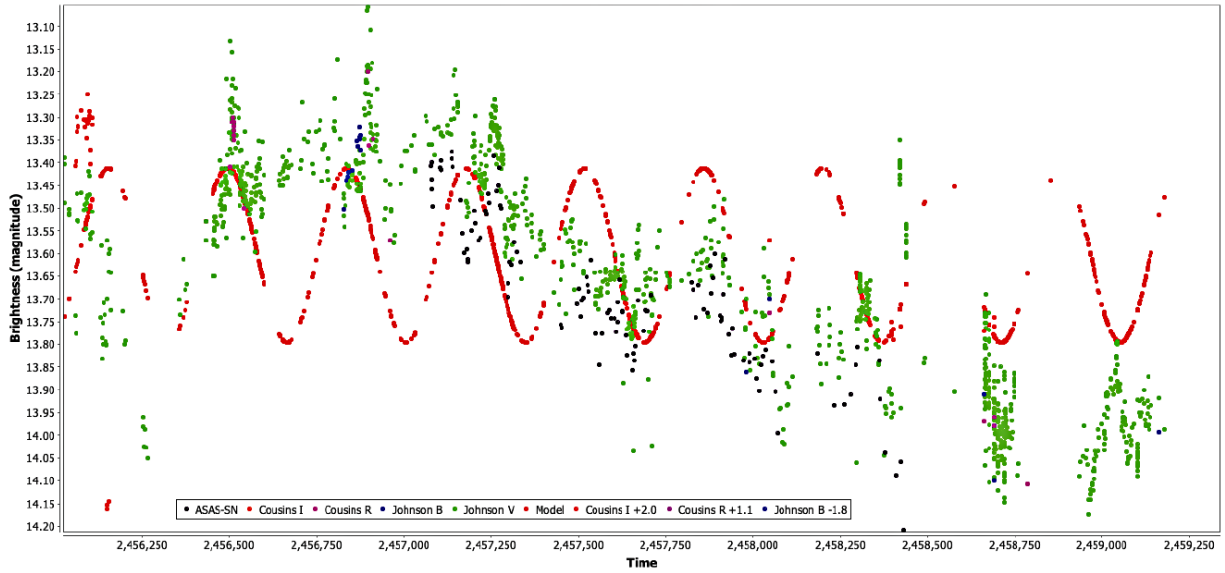

Figure 13. Light curve for V1515 Cyg including AID and ASAS-SN data.

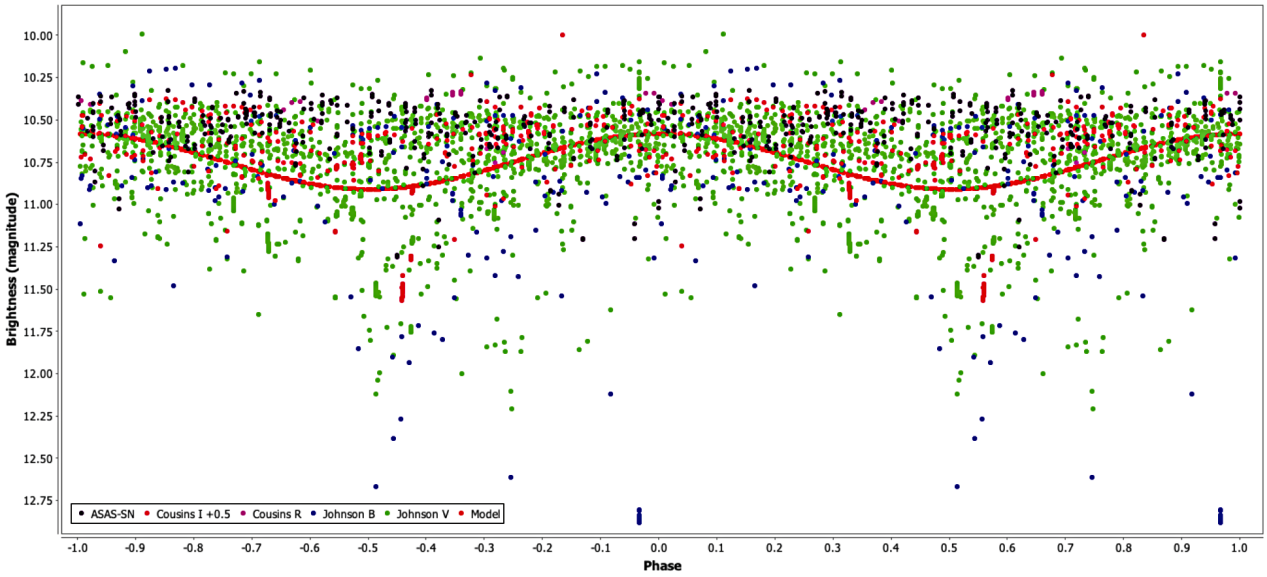

Figure 14. Phase plot for WW Vul (period 69 d, epoch 2452816) including AID and ASAS-SN data.

Refining Ephemeris and Estimating Period Change Rate for V965 Cephei

Maksym Pyatnytskyy
Dzhona Makkeina 37, apt. 6, Kyiv, 01042, Ukraine; mpyat2@gmail.com

Received December 13, 2020; revised February 2, March 19, 2021; accepted March 30, 2021

Abstract Using observations from the AAVSO International Database, data from the literature, and new photometry from the current investigation, the author has produced an O–C diagram for the HADS star V965 Cephei for the time interval September 2011 through December 2020. Analysis of the O–C diagram revealed that V965 Cep has been increasing its period at a constant rate $(1/P)(dP/dt)$ of $1.02(8)\times10^{-6}$ yr^{-1}. A refined ephemeris for the star: $T_{max}(HJD) = 2457504.8963(2) + 0.085067421(9)\,E + 1.01(8)\times10^{-11}\,E^2$.

1. Introduction

The variable star NSVS 304708 (later named V965 Cephei) appeared in a table entry from the Northern Sky Variability Survey by J. Scott Shaw and collaborators (provided by Wozniak *et al.* 2004). The star was originally classified as a W Ursae Majoris-type (EW) eclipsing variable. Based on the shape of its light curve and period that is shorter than typical periods of eclipsing EW-type stars, Sokolovsky (2009) reclassified it as a High Amplitude δ Scuti (HADS) pulsating star with one dominant pulsation with a period of 0.0850695 (0.000002) d. At the time of writing, the AAVSO VSX database (Watson *et al.* 2014) showed this period for V965 Cep.

Analyzing his observational data along with data from the AAVSO International Database, the author found that the folded light curve built using the period from the VSX looked "messy." This indicated that the VSX period was not consistent with the observations during September 2011–December 2020, either due to the period's inaccuracy or because the period has changed over time.

Many HADS stars (including their superclass, δ Scuti stars) exhibit period changes. These changes could be caused by stellar evolution, the presence of an undiscovered companion, i. e., light-time effect, secular changes in the chemical structure, nonlinear interactions between pulsation modes (Breger and Pamyatnykh 1998; Templeton 2005; Sterken 2005; Neilson and Percy 2016). This paper investigates the behavior of the HADS V965 Cephei during the past decade.

2. Methods

An effective commonly used method for diagnostic variation of the period is analyzing a dependency of observed minus calculated (O–C) times of maxima on a number of a variability cycle (Sterken 2005). An O–C diagram was utilized in the current work to analyze the suspected period change.

The analysis drew on published times of maxima for V965 Cep (Wills *et al.* 2012, 2013, 2014, 2015) and an ample number of V965 Cep observations available through the AAVSO International Database for September 2011–November 2020.

The author also observed V965 Cep during two nights in December 2020 using a 6-inch f/5 Newtonian with ZWO ASI120MM-S CMOS camera with a photometric V filter. The observational site was in a relatively highly light-polluted urban area (Osokorky neighborhood, Kyiv, Ukraine). The author used his toolkit (Pyatnytskyy 2018–2020) to calibrate images. The differential aperture photometry was performed with AstroImageJ (Collins *et al.* 2017). Table 1 lists comparison and check stars from a standard AAVSO sequence. Standardized magnitudes were transformed using one-band transformation with the Tv_b-v transformation coefficient obtained from photometry of the AAVSO Standard Field for M67 and with the target's (B–V) index (0.44) from the VSX. The Tv_b-v value turned out to be relatively small (0.0086 (0.0042)); therefore, the transformation introduced a minor correction to the data. The observations can be found in the AAVSO database by observer code PMAK.

The initial analysis of the light curve was carried out with VStar software (Benn 2013). The Date Compensated Discrete Fourier Transform (DC DFT) was performed on data in the Johnson V filter available from the AAVSO International Database and data from The All-Sky Automated Survey for Supernovae (ASAS-SN) (Kochanek *et al.* 2017). The power spectrum of the light curve for V965 Cep showed only one dominant frequency corresponding to a period of 0.0850674 d (Figure 1). Other prominent peaks seen in the plot in Figure 1 are alias frequencies separated by a 1-day interval. The peak at a frequency of 1 day^{-1} is a "phantom" caused by gaps in the source data; the rightmost peak with a period of 0.0425337 d corresponds to the second harmonic.

Knowing the period's crude value, we can determine exact times of maxima in the AAVSO data using an approach described by Wils *et al.* (2009). Since only one dominant frequency exists, the light curve shape should reoccur in each pulsation cycle; thus, we can create an average light curve

Table 1. Comparison and check stars.

AAVSO UID	*Type*	*R.A. (2000)* *h m s*	*Dec. (2000)* *° ′ ″*	*B*	*V*	*B-V*
000-BMX-931	Comparison	00 08 27.43	80 20 25.3	13.986	13.038	0.948
000-BMX-933	Check	00 12 28.41	80 14 29.5	14.495	13.783	0.712

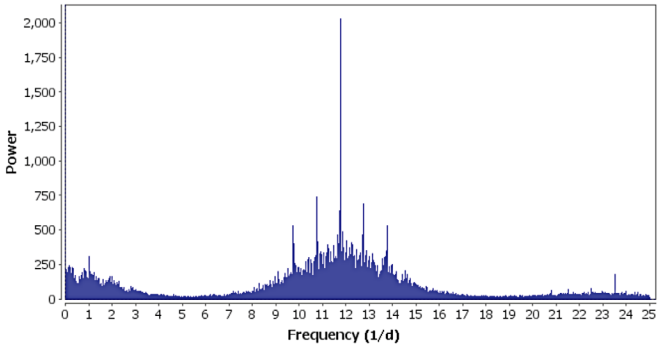

Figure 1. Power spectrum of the light curve for V965 Cep in the V band. The light curve includes data from the AAVSO International Database (September 2011–November 2020), the author's observations (December 2020), and ASAS-SN data (January 2014–November 2018). The primary peak corresponds to a period of 0.0850674 d.

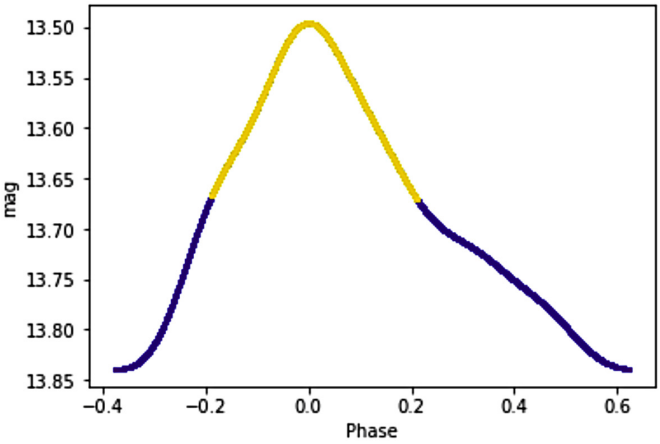

Figure 2. The average cycle profile for V965 Cep. The part of the profile used for light curve matching to determine times of maximum light is shown in the lighter color.

profile for a cycle. Shifting this average profile along the time and magnitude axes near a particular maximum (shift along magnitude axis is required to compensate systematic magnitude offsets for different observers), matches with the observed light curve can then be found, with the best match corresponding to the precise time of maximum.

To create the average cycle profile, a VSTAR-built Fourier model was used, i. e., approximation of the light curve (observations from AAVSO) with a trigonometric polynomial composed of the primary frequency and its harmonics (up to the 6th harmonic). Figure 2 shows the resulting average cycle profile.

For practical purposes, the upper part of this model profile was taken, from the highest point (maximum) to half-height (see Figure 2). Shifting this partial profile by time and magnitude around the selected maximum and applying the least-squares procedure to the measured and calculated magnitudes, a required value of time of the maximum was obtained; the procedure was repeated for each maximum seen in the data. Figure 3 shows typical results of light curve matching. Even when the observations were incomplete, a position of the maximum was estimated well.

Measurement uncertainty of a particular time of maximum was estimated by calculating a square root of the average

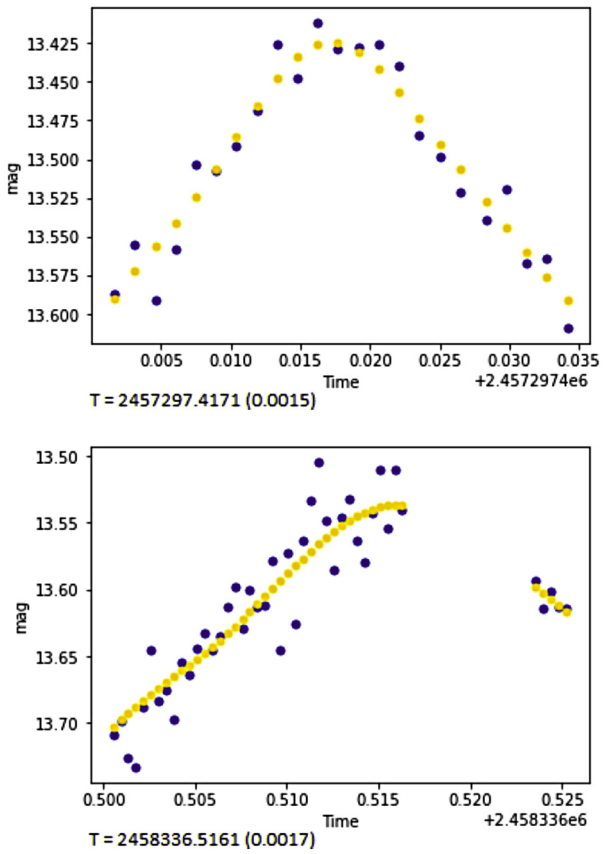

Figure 3. Examples of light curve matching. Observed values are indicated by the dark points and the modeled light curve is shown in a lighter color.

squared difference in time between observations and the matched profile (according to Wils *et al.* 2009). The light curve matching was performed using a PYTHON tool developed by the author.

3. Results and discussion

Table 2 lists the times of maxima. Most maxima found in the literature (Wills *et al.* 2012, 2013, 2014, 2015) could also be derived from the AAVSO data; those maxima were associated with the same observers as in the mentioned papers. For maxima from the AAVSO dataset, the author used his estimations for maxima times rather than those available in other sources. Figure 4 presents the O–C diagram built based on times of maxima listed in Table 2.

Zero epoch (zero cycle) was chosen as a mean time between the first and the last times of maxima available. The zero epoch period P_0 was initially set to the value obtained by DC DFT and improved at the next step (see below). The O–C diagram shows that the period does change over time. Assuming that the change rate is constant, we can approximate the points by the quadratic function:

$$O–C = T_{max} – (T_0 + P_0 E) = \alpha E + 0.5 \beta E^2 + const \quad (1)$$

where T_{max} is the observed time of a maximum, E is its epoch (the cycle number of this maximum), T_0 is the time of the zero epoch, and β is a period change rate. The value of P_0 was

Table 2. Times of maxima, epochs, and O-C values.

Maximum	*Time of Maximum (HJD)*	*Uncertainty (d)*	*Epoch (Cycle Number)*	*O–C (d)*	*Source*	*AAVSO Observer Code*
1	2455836.3027	0.0019	–19615	0.0038	Wils *et al.* 2012	—
2	2455836.3869	0.0010	–19614	0.0030	Wils *et al.* 2012	—
3	2456886.3727	0.0019	–7271	0.0016	Wils *et al.* 2015	—
4	2455818.3536	0.0040	–19826	0.0040	AAVSO	VMAE
5	2455818.4396	0.0026	–19825	0.0049	AAVSO	VMAE
6	2456110.4736	0.0025	–16392	0.0024	AAVSO	VMAE
7	2456110.5591	0.0027	–16391	0.0029	AAVSO	VMAE
8	2456134.4620	0.0015	–16110	0.0018	AAVSO	VMAE
9	2456134.5485	0.0013	–16109	0.0032	AAVSO	VMAE
10	2456135.3988	0.0025	–16099	0.0029	AAVSO	VMAE
11	2456135.4826	0.0030	–16098	0.0017	AAVSO	VMAE
12	2456223.3587	0.0022	–15065	0.0030	AAVSO	VMAE
13	2456496.4227	0.0021	–11855	0.0006	AAVSO	VMAE
14	2456628.4463	0.0017	–10303	–0.0004	AAVSO	PNQ
15	2456628.5335	0.0022	–10302	0.0017	AAVSO	PNQ
16	2456733.3361	0.0017	–9070	0.0013	AAVSO	VWS
17	2456853.5379	0.0026	–7657	0.0029	AAVSO	VMAE
18	2456855.4921	0.0029	–7634	0.0005	AAVSO	VMAE
19	2456913.3383	0.0021	–6954	0.0008	AAVSO	VMAE
20	2456913.4237	0.0027	–6953	0.0012	AAVSO	VMAE
21	2456913.5079	0.0022	–6952	0.0003	AAVSO	VMAE
22	2457283.3794	0.0019	–2604	–0.0013	AAVSO	VMAE
23	2457283.4643	0.0018	–2603	–0.0015	AAVSO	VMAE
24	2457297.3316	0.0012	–2440	–0.0002	AAVSO	VMAE
25	2457297.4171	0.0015	–2439	0.0002	AAVSO	VMAE
26	2457614.4633	0.0014	1288	0.0001	AAVSO	VWS
27	2457618.3761	0.0009	1334	–0.0002	AAVSO	VMAE
28	2457618.4615	0.0009	1335	0.0002	AAVSO	VMAE
29	2457618.5472	0.0012	1336	0.0008	AAVSO	VMAE
30	2457623.3959	0.0007	1393	0.0006	AAVSO	VMAE
31	2457623.4809	0.0008	1394	0.0005	AAVSO	VMAE
32	2457623.5649	0.0009	1395	–0.0004	AAVSO	VMAE
33	2457633.3479	0.0007	1510	–0.0003	AAVSO	VMAE
34	2457633.4326	0.0008	1511	–0.0006	AAVSO	VMAE
35	2457633.5191	0.0014	1512	0.0009	AAVSO	VMAE
36	2457641.4288	0.0015	1605	–0.0007	AAVSO	VWS
37	2458020.3191	0.0007	6059	–0.0007	AAVSO	VMAE
38	2458020.4054	0.0008	6060	0.0005	AAVSO	VMAE
39	2458020.4903	0.0014	6061	0.0004	AAVSO	VMAE
40	2458336.4302	0.0026	9775	–0.0002	AAVSO	VWS
41	2458336.5161	0.0017	9776	0.0007	AAVSO	VWS
42	2458390.6204	0.0012	10412	0.0021	AAVSO	DFS
43	2458390.7055	0.0016	10413	0.0021	AAVSO	DFS
44	2458541.3605	0.0013	12184	0.0027	AAVSO	SDWA
45	2458541.4447	0.0011	12185	0.0018	AAVSO	SDWA
46	2458541.5289	0.0014	12186	0.0010	AAVSO	SDWA
47	2458646.5029	0.0013	13420	0.0018	AAVSO	DFS
48	2458680.5294	0.0014	13820	0.0013	AAVSO	DFS
49	2458680.6145	0.0012	13821	0.0014	AAVSO	DFS
50	2458716.4278	0.0015	14242	0.0012	AAVSO	VWS
51	2458734.6334	0.0009	14456	0.0025	AAVSO	DFS
52	2458764.5771	0.0010	14808	0.0024	AAVSO	DFS
53	2458764.6624	0.0017	14809	0.0026	AAVSO	DFS
54	2458877.2900	0.0010	16133	0.0009	AAVSO	SDWA
55	2458877.3756	0.0010	16134	0.0015	AAVSO	SDWA
56	2459036.5411	0.0024	18005	0.0058	AAVSO	DFS
57	2459036.6250	0.0019	18006	0.0047	AAVSO	DFS
58	2459066.5693	0.0016	18358	0.0053	AAVSO	DFS
59	2459156.4002	0.0015	19414	0.0050	AAVSO	SDWA
60	2459156.4835	0.0019	19415	0.0032	AAVSO	SDWA
61	2459190.2551	0.0021	19812	0.0030	AAVSO	PMAK
62	2459190.3397	0.0022	19813	0.0026	AAVSO	PMAK
63	2459191.1924	0.0022	19823	0.0045	AAVSO	PMAK
64	2459191.2757	0.0024	19824	0.0029	AAVSO	PMAK
65	2459191.3616	0.0032	19825	0.0037	AAVSO	PMAK

chosen so that the minimum of the approximating parabola coincides with zero epoch (i.e., α becomes null). The fitting of the quadratic function to O–C data and tuning of P_0 was performed using LibreOffice Calc. The best fit delivered the following equation for the ephemeris:

$$T_{max}\,(HJD) = 2457504.8963(2) + 0.085067421(9)\,E + 1.01(8)\times 10^{-11}\,E^2 \qquad (2)$$

The period change rate is $2.03(17)\times 10^{-11}$ days/cycle, which corresponds to the rate of $(1/P)(dP/dt)\ 1.02(8)\times 10^{-6}\,yr^{-1}$.

Figure 5 shows the folded light curve with AAVSO and ASAS-SN data in V-filter built using the obtained period and epoch. For AAVSO data, zero magnitude levels for each cycle were adjusted based on the profile fitting outcomes.

The obtained value of $1.02(8)\times 10^{-6}\,y^{-1}$ for $(1/P)(dP/dt)$ is relatively high. Breger and Pamyatnykh (1998) give a characteristic value of $(1/P)(dP/dt)$ for δ Scuti stars around 10^{-7} year^{-1} (with equal distribution between positive and negative values); they hold that even such values cannot be fully explained by stellar evolution. In their sample, only stars with nonradial pulsations have absolute values of $(1/P)(dP/dt)$ that are close to or greater than $1\times 10^{-6}\,yr^{-1}$. For such multiperiodic stars, a cause of period change might be nonlinear mode-coupling (Breger and Pamyatnykh 1998; Templeton 2005). However, V965 Cep is a high amplitude δ Scuti star that oscillates at one frequency (see Figure 1); therefore, it looks like a radial-mode pulsator (Templeton 2005). Another possible cause of the period change is a light-time effect in binary systems (Sterken 2005; Templeton 2005). However, there is no evidence that V965 Cep belongs to such a system (Liakos and Niarchos 2017).

To prove the effect and rule out any observation bias, an independent set of observations was used, namely, a quite long yet sparse ASAS-SN series (Kochanek *et al.* 2017). Two intervals were taken: from JD 2456681 to JD 2458028 (data in V band) and from JD 2458033 to JD 2459167 (data in g band). DC DFT performed on each subset returned a period of 0.08506731 d for the first subset (V band, mean JD = 2457241) and 0.08506771 d for the second subset (g band, mean JD = 2458612). A difference in periods for these two intervals is 4×10^{-7} d, and a difference in mean epochs is 1,372 days. From those values, we can derive a crude estimation of the period change rate as $\sim 1.3\times 10^{-6}\,yr^{-1}$, which is consistent with the value of $(1/P)(dP/dt)$ obtained from O–C diagram. Its unusually high rate of period change makes V965 Cep an interesting object that deserves continuing observations.

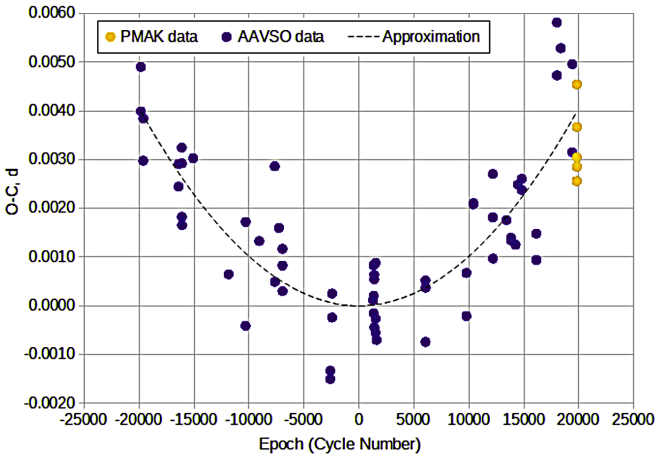

Figure 4. O–C diagram for V956 Cep (T_0 = HJD 2457504.8963, P_0 = 0.085067421 d). Maxima derived from the author's observations (observer code PMAK in Table 2) are indicated by the lighter points. The dashed line is the approximating quadratic function.

4. Conclusions

Analysis of the O–C diagram for a high amplitude delta Scuti star V965 Cep showed that the star exhibits period change for the past decade. From September 2011 to December 2020, its period has been growing with a constant rate of $2.03\,(17)\times 10^{-11}$ days/cycle, which corresponds to $(1/P)(dP/dt)$ of $1.02(8)\times 10^{-6}\,yr^{-1}$. The period for the epoch HJD 2457504.8963 was 0.085067421 d.

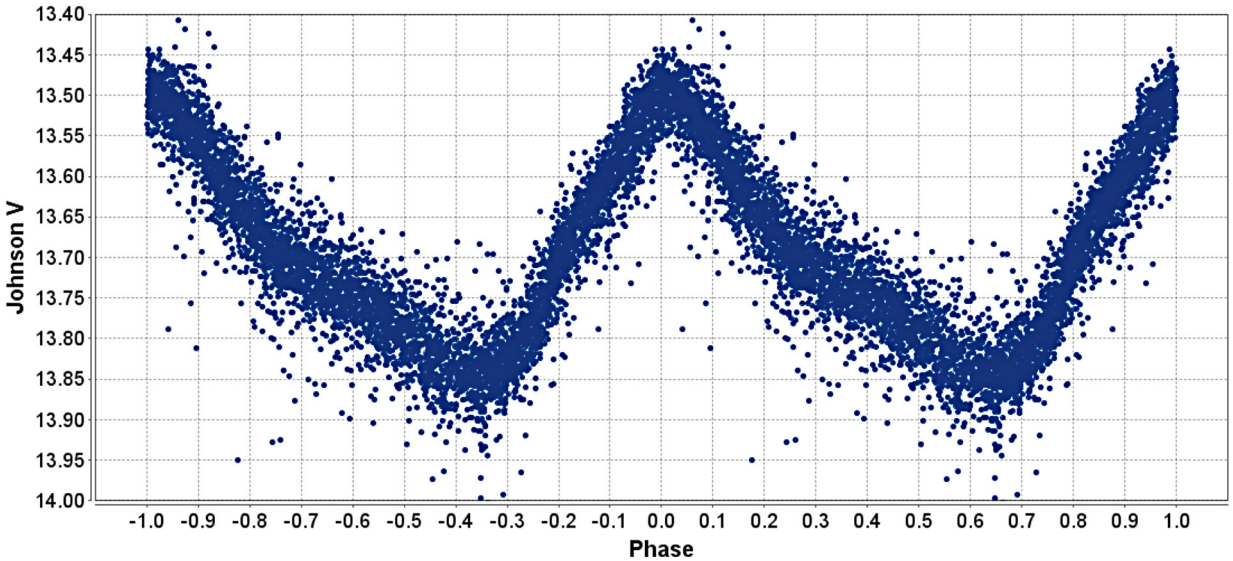

Figure 5. The folded light curve with AAVSO and ASAS-SN data. Magnitude zero levels for AAVSO data corrected for each cycle.

5. Acknowledgements

This research was made possible through the use of variable star observations from the AAVSO International Database (AAVSO 2013) and respective valuable contributions by observers DFS, PNQ, SDWA, VMAE, VWS. It also benefitted from the use of the International Variable Star Index (VSX) database operated at AAVSO, Cambridge, Massachusetts, USA.

References

AAVSO. 2013, Observations from the AAVSO International Database (http://www.aavso.org).

Benn, D. 2013, VStar data analysis software (https://www.aavso.org/vstar-overview).

Breger, M, and Pamyatnykh, A. A. 1998, *Astron. Astrophys.*, **332**, 958.

Collins, K. A., Kielkopf, J. F., Stassun, K. G., and Hessman, F. V. 2017, *Astron. J.*, **153**, 77.

Kochanek, C. S., *et al.* 2017, *Publ. Astron. Soc. Pacific*, **129**, 104502.

Liakos, A., and Niarchos, P. 2017, *Mon. Not. Roy. Astron. Soc.*, **465**, 1181.

Neilson, R. N., and Percy J. R. 2016, *J Amer. Assoc. Var. Star Obs.*, **44**, 179.

Pyatnytskyy, M. Yu. 2018–2020, FITS Command-line Utilities (http://fits-command-line-utilities.sourceforge.net).

Sokolovsky, K. V., 2009, *Perem. Zvezdy Prilozh.*, **9**, 30.

Sterken, C., ed. 2005, The Light-Time Effect in Astrophysics: Causes and Cures of the O–C Diagram, ASP Conf. Ser., 335, Astronomical Society of the Pacific, San Francisco.

Templeton, M. R. 2005, *J Amer. Assoc. Var. Star Obs.*, **34**, 1

Watson, C., Henden, A. A., and Price, C. A. 2014, AAVSO International Variable Star Index (VSX, Watson+, 2005-2014, https://www.aavso.org/vsx).

Wils P., *et al.* 2009, *Inf. Bur. Var. Stars*, No. 5878, 1.

Wils P., *et al.* 2012, *Inf. Bur. Var. Stars*, No. 6015, 1.

Wils P., *et al.* 2013, *Inf. Bur. Var. Stars*, No. 6049, 1.

Wils P., *et al.* 2014, *Inf. Bur. Var. Stars*, No. 6122, 1.

Wils P., *et al.* 2015, *Inf. Bur. Var. Stars*, No. 6150, 1.

Woźniak, P. R., *et al.* 2004, *Astron. J.*, 127, 2436 (https://www.physast.uga.edu/~jss/nsvs/).

V350 Muscae: RR Lyrae Star Distance Estimate and RRab Reclassification

Demetris Nicolaides
Natural Science and Mathematics, Bloomfield College, 467 Franklin Street, Bloomfield, NJ 07003; demetris_nicolaides@bloomfield.edu

Destiny L. King
Bloomfield College, 467 Franklin Street, Bloomfield, NJ 07003

Sandra Moreno Cristobal
Gardner-Webb University, 110 S. Main Street, Boiling Springs, NC 28017

Received December 15, 2020; revised January 15, 27, 2021; accepted February 15, 2021

Abstract V350 Mus was observed in the B, V, and, for the first time, the i and z bands, for a total of eighteen days. The telescope images were processed through aperture photometry. The star's light curves reclassified it as an RRab type from its previous RRc or EW (eclipsing variable) classification. Its pulsation period was 0.3705 ± 0.0012 day. Three theoretical period-luminosity-metallicity relations of RR Lyrae stars (M_V, M_i, and M_z), were shown to collectively work quite well with the corresponding observed apparent magnitudes of V350 Mus in matching its Gaia reported distance of (165.34 ± 1) parsecs. Specifically, the distance estimates (in parsecs) for the V, i, and z filters were 145.70 ± 11, 172.14 ± 7, and 176.70 ± 7, respectively, with their average being 164.85 ± 5, a mere 0.30% difference from the Gaia value. The calculation of the three-filter average distance was optimum when A, the extinction factor due to galactic reddening, was calibrated by implementing a simple new formula that considers the amount of each wavelength's extinction proportionally, by balancing it with respect to the extinction of an average wavelength (instead of, say with respect to the extinction of only the V wavelength). The type of average wavelength that worked best was the weighted mean of the wavelengths that have a period-luminosity-metallicity relation (in our study, the V, i, and z wavelengths), and where the weight of a particular band wavelength was its ratio to an arbitrary reference wavelength.

1. Introduction

We measured the time variation of the apparent magnitude of V350 Mus, its period of pulsation, and constructed its light curves for the B, V, i, and z bands. These data were then inserted in three theoretical RR Lyrae period-luminosity-metallicity relations, the M_V (Catelan *et al.* 2004), and the M_i and M_z (Cáceres and Catelan 2008) in order to calculate the star's absolute magnitudes for each band and in turn estimate the corresponding distances. If verified, these relations can be used to calculate absolute magnitudes, thus providing an additional method in the determination of distances for RR Lyrae stars, and consequently enriching the cosmic distance ladder methodology of astronomy. Alternatively, these period-luminosity-metallicity relations may be used in "reverse": from an RR Lyrae star's known distance, apparent magnitude, and period, these relations can be applied to generate such star's extinction factor, A, and reddening value, E(B–V).

Pulsating stars have interesting and unique properties (Catelan and Smith 2014). In 1908, astronomer Henrietta Leavitt (Leavitt 1908) discovered the first period-luminosity relation of pulsating stars, the Cepheids in particular, which allowed for a new and improved method for measuring cosmic distances. Her work was seminal. Not only it is the basis of this paper and of an immense number of other ones that deal with variable stars—including Gaia Collab. *et al.* (2017)—it was also crucial in the work of Edwin Hubble (Hubble 1929) when he measured distances and recession velocities of distant galaxies and confirmed the expansion of the universe that was previously predicted theoretically by the field equations of Einstein's general relativity.

V350 Mus (Figure 1) is a relatively nearby object, in the Milky Way's disk. The star hasn't been studied in the i and z filters previously. Table 1 lists its basic properties.

Table 1. Basic Properties of V350 Mus.

R.A. (°)	203.105
Dec. (°)	–74.61
Plx (mas)	6.0193
Glon (°)	305.698
Glat (°)	–11.959
pmRA (mas/yr)	–5.59
pmDE (mas/yr)	23.337
T_{eff} (K)	6356.19
distance[1] (parsec)	165.34 ± 1
[Fe/H][2] (dex)	0.14
Flux B[3] (mag)	8.70 ± 0.02
Flux V[3] (mag)	8.23 ± 0.01
VarType*	RRc[4]/EW[5]
P[6] (d)	0.73811
P[7] (d)	0.36905
SpecType[8]	F2IV

** Our study reclassified V350 Mus as an RRab. Note: the properties without a superscript are from (Gaia* et al. *2018). [1]Bailer-Jones* et al. *2018. [2]Ammons et al. 2006; the Ammons paper estimated the value of 0.14 from polynomials of broadband photometry (although the authors wrote their code to derive [Fe/H] values using dwarf stars, not RR Lyrae); the 1σ error in this value is σ[Fe=H] = +0.15 / –0.16 dex (found in the VizieR Online Data Catalog: T_{eff} and metallicities for Tycho-2 stars (Ammons* et al. *2006)). [3]Høg* et al. *2000. [4]Watson* et al. *2006; Kazarovets* et al. *2011; Samus* et al. *2017. [5]Watson* et al. *2014; Astraatmadja and Bailer-Jones 2016. [6]Astraatmadja and Bailer-Jones 2016; the reference that reports this period classifies the star as EW. [7]Watson* et al. *2006; the reference that reports this period classifies the star as RRc. [8]Schlafly* et al. *2019.*

2. Observations and methods

The observations of V350 Mus were completed at the Siding Spring Observatory (New South Wales, Australia) and at the South African Astronomical Observatory (Sutherland, South Africa), by three 0.4-meter SBIG robotic telescopes. The observatories are part of a global network with its Headquarters at Las Cumbres Observatory (LCO). The CCD camera of such a telescope (Brown *et al.* 2013) has 2048 × 3072 pixels, each of which has a 0.57-arcsecond square view of the sky, resulting in a total Field of View (FoV) of 19 × 29 arcminutes.

These observations lasted a total of 18 days in June and July 2020. The June 12–16 observations were adjusted for a simple period cadence with period = 4.5 h and jitter = 4.5 h; for June 16–24, period = 2.9 h, jitter = 2.9 h; and July 1–5, period = 1.9 h, jitter = 1.9 h. The observations were done in the Bessel-B, Bessel-V, SDSS-i, and PANSTARRS-z filters, with wavelength center (Å) 4361, 5448, 7545, and 8700, respectively. The exposure times of each filter were: 8 sec for B; 3 sec for V; 3 sec for i; and 12 sec for z. These values were calculated based on a test observation with exposure times 12 sec for B, V, and i, and 30 sec for z. The adjusted exposure times aimed for 300,000 counts (photoelectrons) of apparent magnitude and were achieved by using the software AstroImageJ (Collins *et al.* 2017). Figure 1 shows a typical colorized image of the star field with V350 Mus in the center. Since a star's position changes with time, the most up-to-date coordinates of V350 Mus (R.A. = 203.10438°, Dec. = –74.60996°) were obtained with the use of one such image and the software Aladin (Bonnarel *et al.* 2000): we zoomed into the star, visually centered the cursor in the star image, and read off its coordinates. We used these coordinates for our analysis.

The images from the observatories were transmitted to Las Cumbres' Our Solar Siblings for processing by its data pipeline (Fitzgerald 2018). In addition to the fits files, the pipeline also generated the following two types of files: phototif (digital-camera-like images) and phot (the apt, sek, sex, dao, dop, and psx photometric procedures). These files were then forwarded to the google drives of the research team.

First, we visually inspected the phototif images of each filter and noted the unsuccessful ones—observations that occurred during a cloudy or windy night, or during excess light from the presence of the moon, or generally overexposed images with visible diffraction imperfections. We then eliminated all such images from each phot file. We cleaned further the phot images by also eliminating those with the smallest size (initially the ones up to 3 KB) as these were the images with the least number of stars detected in the specified field of view. (A good image is generally one that contains many stars for comparison purposes with catalogued stars and a target star.) The light curves of each filter in each of the six photometric analyses were constructed by running astrosource (in Spyder/Anaconda). To calibrate the comparison stars for the B and V observations, astrosource uses the APASS catalogue (Henden *et al.* 2016), but for the i and z observations (and since V350 Mus is in the southern hemisphere), astrosource used the Skymapper DR1.1 catalogue (Wolf *et al.* 2018).

The images of V350 Mus (see, for example, Figure 1) showed a rather isolated star and so we expected any of the aperture photometry procedures (apt, sek, sex files) to produce more reliable results compared to any of the point spread function (PSF) photometry procedures (dop, dao, psx), which are more appropriate for images with many and overlapping stars. The sek (Source Extractor Kron) procedure (Bertin and Arnouts 1996) provided the best light curves. The cleaned sek images were cleaned even further as follows: in the B filter we kept images of 5 KB and up; in the i, 11 KB and up; in the V, 8 KB and up; and in the z, 9 KB and up. This additional cleaning provided consistency in the shape of the light curves of each band (Figures 2–5)—showing a rather steep ascent with a more gradual descent, a characteristic of RRab Lyrae stars—as well as consistency in the values of the most likely periods in the brightness variation. This cleaning, however, also produced a bit of inaccuracy in the values of the amplitudes (Table 2)—these are usually expected to decrease with increasing wavelength. Gaps in the light curves (from the cleaning process) can generate biased amplitudes.

The periods were calculated from two methods, the PDM (phase dispersion minimization) and the string method. The astrosource routine, in search of the most probable period for each filter and for each method, was written by Altunin *et al.* (2020) by basing their work on the PDM method, first developed by Stellingwerf (1978), and on the string method, first developed by Dworetsky (1983). In the PDM method, for each probable period, the points of the corresponding potential light curve are imagined grouped in vertical bins. Each such bin choice contains, therefore, its own unique set of dispersed points. The most probable period (and thus best light curve) is produced when the dispersion of the points in each bin is minimal. In the string method, for each probable period, the points of the corresponding potential light curve are imagined connected sequentially with a string. The most probable period generates the smallest total string length and the best light curve.

3. Results and calculations

3.1. Measurements

The star's light curves, particularly that in the V filter, (Figures 2–5) reclassified it as an RRab type from its previous RRc (Watson *et al.* 2006; Kazarovets *et al.* 2011; Samus *et al.* 2017), or EW (eclipsing variable) classification (Watson *et al.* 2014; Astraatmadja and Bailer-Jones 2016). Table 2 includes the amplitude of each light curve and the most probable periods for each wavelength (from the string and PDM methods), as well as the average of these periods. All eight most likely periods were within each other's uncertainty. This table has also the mid-range value of the measured apparent magnitude, m, which is decreasing from the shorter wavelength, B, to the longer, i, (as expected, for example, by Rayleigh scattering, according to which more "blue" than "red" scatters off the main beam of the star and thus doesn't reach the telescope), although not from i to z. Amplitudes are relatively low in all filters, and we note that we do not see the usual decrease in amplitude in going from B to i. While such an effect can sometimes arise when an RR Lyrae star image is blended with that of a nonvariable star, we do not see evidence of such a blend in our images.

Figure 1. V350 Mus (enclosed by the red circle) is the brightest star in the middle of this RGB image processed from one representative image from each filter used. North is left; east is down.

Table 2. Apparent magnitudes, periods, and amplitudes of V350 Mus.

	Band			
	B	*V*	*i*	*z*
λ-ctr (Å)	4361	5448	7545	8700
m[a] (mag)	8.300	7.927	7.838	7.869
errm (mag)	0.035	0.015	0.010	0.012
P[b] (d)	0.3699	0.3715	0.3706	0.3708
errP[b] (d)	0.0044	0.0044	0.0046	0.0033
P[c] (d)	0.3695	0.3716	0.3702	0.3702
errP[c] (d)	0.0032	0.0036	0.0016	0.0029
P-avg ≡ P(d)		0.3705 ± 0.0012		
Amp[d] (mag)	0.336	0.324	0.413	0.374

[a]$m = (m_{max} + m_{min})/2$. [b]*Using the string method.* [c]*Using the PDM method.* [d]$Amp = (m_{max} - m_{min})$.

3.2. Preliminary calculations

The theoretical period-luminosity-metallicity relations that are being tested in this paper, as to whether they generate the right distance of V350 Mus, are:

$$M_V = 2.288 + 0.882 \log Z + 0.108 (\log Z)^2 \quad (1)$$

$$M_i = \begin{cases} 0.908 - 1.035 \log P + 0.220 \log Z, \text{if RRab} \\ 0.908 - 1.035 (\log P + 0.128) + 0.220 \log Z, \text{if RRc} \end{cases} \quad (2)$$

$$M_z = \begin{cases} 0.839 - 1.295 \log P + 0.211 \log Z, \text{if RRab} \\ 0.839 - 1.295 (\log P + 0.128) + 0.211 \log Z, \text{if RRc} \end{cases} \quad (3)$$

The M_V is by Catelan *et al.* (2004), and the M_i and M_z are by Cáceres and Catelan (2008). The $\log Z$ is a term related to a star's metallicity

$$\log Z = [M/H] - 1.765 \quad (4)$$

found by Catelan *et al.* (2004) and Cáceres and Catelan (2008), with

$$[M/H] = [Fe/H] + \log (0.638 \times 10^{0.3} + 0.362) \quad (5)$$

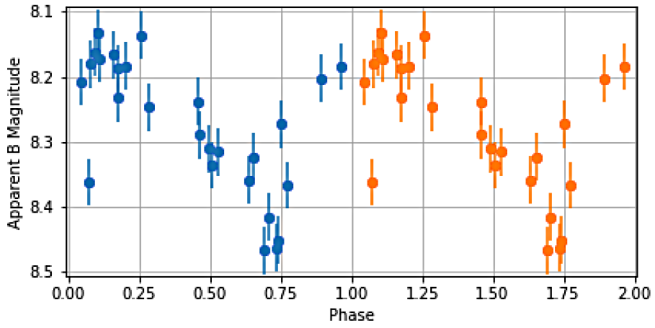

Figure 2. B light curve phase-plotted over two cycles and for the average period of 0.3705 day.

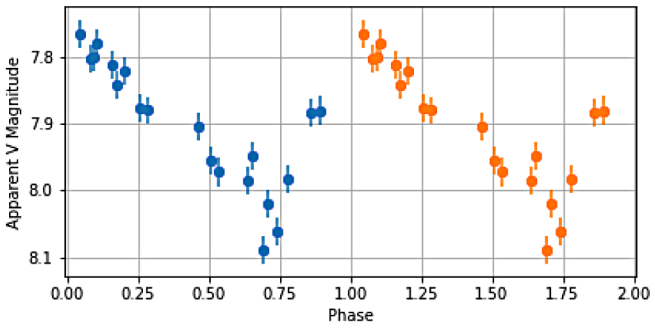

Figure 3. V light curve phase-plotted over two cycles and for the average period of 0.3705 day.

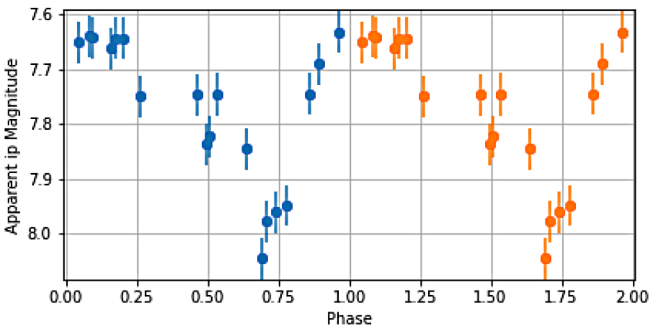

Figure 4. i light curve phase-plotted over two cycles and for the average period of 0.3705 day.

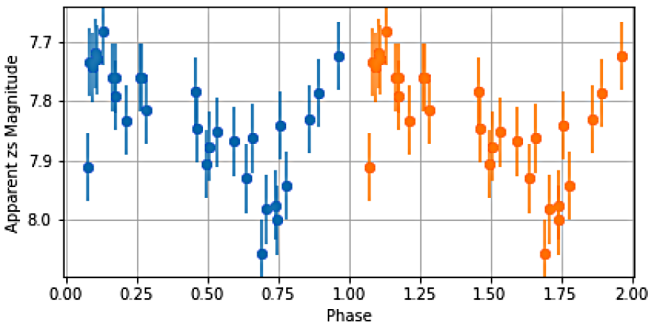

Figure 5. z light curve phase-plotted over two cycles and for the average period of 0.3705 day.

obtained by Salaris *et al.* (1993) and Cáceres and Catelan (2008). The goal is to calculate the star's absolute magnitudes and from them its distance. V350 Mus is a relatively metal-rich star, $10^{0.14} = 1.38$ times more metallic than the sun. With its metallicity being $[Fe/H] = 0.14$ (Table 1), Equation 5 gives $[M/H] = 0.354$ and Equation 4, $\log Z = -1.411 \pm 0.155$. Using the

average period P = (0.3705 ± 0.0012) d, (Table 2), and that V350 Mus is an RRab, Equations 1, 2, and 3 are easily calculated, thus: $M_V = (1.258 \pm 0.142)$ mag, $M_i = (1.044 \pm 0.078)$ mag, and $M_z = (1.100 \pm 0.068)$ mag.

These absolute magnitudes, together with the apparent magnitudes m (from Table 2), will lead us to the star's distance,

$$d = 10^{(m - M - A + 5)/5} \tag{6}$$

provided that we first adjust the measured apparent magnitudes of each passband by the extinction factor A in order to account for interstellar reddening. A, in essence, puts the scattered starlight back into the apparent magnitude m—or equivalently, reduces the absolute magnitude M, in order to balance it with the observed m. The visual extinction to reddening ratio is

$$R_V \equiv \frac{A_v}{E(B-V)} \tag{7}$$

and the usually assumed standard value for the Milky Way is $R_V = 3.1$. Furthermore, the mean reddening E(B − V), from the galactic dust within a radius of 5 arcmin in the vicinity of V350 Mus (although not exactly along the line of sight to the star), is reported by the Schegel Dust Map service (NASA/IPAC 2020) to be (0.1738 ± 0.0032) mag. With these data we proceeded to calculate the star's distance for the V-, i-, and z-bands and then find the three-band average (d-viz-avg) based on five different calibration methods of A (see the subsection below). For each calibration method the d-viz-avg was optimum (compared to the Gaia number of 165.34 parsecs) when E(B − V) = 0.200 mag, a number we chose for being the approximate upper bound of 0.1738 mag, thus justifying reasonably the optimization of our result as we arrived at it within the context of the Schegel Dust Map measured value. By the way, ASAS-SN catalogues (Jayasinghe *et al.* 2019; Shappee *et al.* 2014) list E(B–V) = 0.202 mag for V350 Mus, information which strengthens our own approximation choice of 0.200 mag.

3.3. The A factor calibration

The final step in calculating the distance (Equation 6) is the calibration of A. It attempts to restore each filter's m by putting a proportional amount of A back into it. That is (and having in mind, say, general solid particle scattering), more "blue" than "red" wavelengths must be restored, thus a calibrated value of A has to be bigger for the shorter wavelengths.

To calibrate A we first write its un-calibrated expression and value:

$$A_{-un-cal} = R_V \times E(B-V) = 3.100 \times 0.200\,\text{mag} \tag{8}$$

We propose to first calibrate A with a new extinction model, as follows:

$$A_{cal} = R_V \; E(B-V) \times \frac{\lambda_{cal}}{\lambda_b} \tag{9}$$

where λ_{cal} is a calibration wavelength (to be chosen below) and λ_b is the telescope's band wavelength center (the λ-ctr in Table 2) for the V-, i-, and z-bands. So, parenthetically, if λ_b is the λ_V, λ_i, or λ_z, the exact notation of A_{cal} is really A_V, A_i, or A_z. Note that A_{cal} is chosen to be inversely proportional to λ_b in order to ensure that the "bluer" the wavelength is, the bigger A_{cal} is. This means that the amount of "blue" (short wavelength) which is restored in a corresponding blue apparent magnitude is more than the amount of "red" (long wavelength) which is restored in a corresponding red apparent magnitude, a restoration process which is reasonable since, generally, more blue than red scatters off the main beam of starlight on its way to the telescopes. Thus, Equation 9 attempts to restore a truer (more accurate) value of m for each wavelength and consequently a more precise value of distance.

Our proposed extinction model (Equation 9) will be implemented in four calibration methods and its results will then be compared to a fifth calibration method of another model which uses an actual interstellar extinction relation, one developed by Cardelli *et al.* (1989). Specifically, Tables 3.1, 3.2, 3.3, 3.4, and 3.5 show the distance results when reddening and extinction are taken into consideration for each of the following five calibration methods of A_{cal} (each of which has a unique λ_{cal}), respectively:

(1) $\lambda_{cal} = \lambda_V$ where $\lambda_V = 5448$ Å. The results are in Table 3.1.

(2) $\lambda_{cal} = \lambda_{mean}$ where

$$\lambda_{mean} = (\lambda_V + \lambda_i + \lambda_z)/3 = (5448 + 7545 + 8700)/3 = 7231\ \text{Å}.$$

The results are in Table 3.2.

(3) $\lambda_{cal} = \lambda_{weighted-mean} \equiv \lambda_{w-mean}$ where

$$\lambda_{w-mean} = \frac{\sum_b^{V,i,z} w_b \lambda_b}{\sum_b^{V,i,z} w_b} = \frac{w_V \lambda_V + w_i \lambda_i + w_z \lambda_z}{w_V + w_i + w_z} \tag{10}$$

with weight coefficients (of each band wavelength)

$$w_b \equiv \frac{\lambda_b}{\lambda_{ref}} \tag{11}$$

and where λ_{ref} is an arbitrary reference wavelength that cancels out in the determination of λ_{w-mean}. That is, using Equation 11, Equation 10 becomes

$$\lambda_{w-mean} = \frac{\lambda_V^2 + \lambda_i^2 + \lambda_z^2}{\lambda_V + \lambda_i + \lambda_z} \tag{12}$$

Then, using each band's wavelength center, $\lambda_V = 5448$ Å, $\lambda_i = 7545$ Å, and $\lambda_z = 8700$ Å, Equation 12 yields $\lambda_{w-mean} = 7482$ Å. Thus for method (3) $\lambda_{cal} = 7482$ Å, and the consequent results are shown in Table 3.3.

(4) For calibration method (4) the weight coefficients, Equation 11, are

$$w_b \equiv \frac{I(\lambda_b)}{I(\lambda_{ref})} \tag{13}$$

Table 3.1. Distance based on reddening E(B–V) = 0.200 mag and A calibration $\lambda_{cal} = \lambda_V = 5448$ Å.

	Band		
	V	*i*	*z*
A_{cal} (mag)	0.620	0.448	0.388
d (parsec)	162.09	185.91	188.90
errd (parsec)	12	8	7
d-viz-avg (parsec)		178.97 ± 5	
% diff[G]		8.24	

[G]*Between d-viz-avg and Gaia's 165.34 parsecs.*

Table 3.2. Distance based on reddening E(B–V) = 0.200 mag and A calibration $\lambda_{cal} = \lambda_{mean} = 7231$ Å.

	Band		
	V	*i*	*z*
A_{cal} (mag)	0.823	0.594	0.515
d (parsec)	147.63	173.79	178.17
errd (parsec)	11	7	7
d-viz-avg (parsec)		166.53 ± 5	
% diff[G]		0.72	

[G]*Between d-viz-avg and Gaia's 165.34 parsecs.*

Table 3.3. Distance based on reddening E(B–V) = 0.200 mag and A calibration $\lambda_{cal} = \lambda_{w-mean-method-3} = 7482$ Å.

	Band		
	V	*i*	*z*
A_{cal} (mag)	0.851	0.615	0.533
d (parsec)	145.70	172.14	176.70
errd (parsec)	11	7	7
d-viz-avg (parsec)		164.85 ± 5	
% diff[G]		0.30[a]	

[G]*Between d-viz-avg and Gaia's 165.34 parsecs.* [a]*or 0.01% when E(B–V) = 0.198. Incidentally, when $\lambda_{cal} = \lambda_i = 7545$ Å and E(B–V) = 0.196 mag, the percent difference of the d-viz-avg (from the Gaia distance) is also low, 0.05%, but we think this is so because λ_i happens to accidentally be approximately equal to $\lambda_{w-mean} = 7482$ Å.*

Table 3.4. Distance based on reddening E(B–V) = 0.200 mag and A calibration $\lambda_{cal} = \lambda_{w-mean-method-4} = 6686$ Å.

	Band		
	V	*i*	*z*
A_{cal} (mag)	0.761	0.549	0.476
d (parsec)	151.91	177.40	181.38
errd (parsec)	11	7	7
d-viz-avg (parsec)		170.23 ± 5	
% diff[G]		2.96	

[G]*Between d-viz-avg and Gaia's 165.34 parsecs.*

Table 3.5. Distance based on reddening E(B–V) = 0.200 mag and A calibration method (5) (Cardelli *et al.* 1989).

	Band		
	V	*i*	*z*
A_{cal} (mag)	0.620	0.424	0.305
d (parsec)	162.09	187.95	196.28
errd (parsec)	12	8	7
d-viz-avg (parsec)		182.11 ± 5	
% diff[G]		10.14	

[G]*Between d-viz-avg and Gaia's 165.34 parsecs.*

where

$$I(\lambda) = \frac{2hc}{\lambda^3} \quad \frac{1}{e^{hc/\lambda kT} - 1} \tag{14}$$

is the star's black-body radiation intensity. For method (4) Equation 10 becomes

$$\lambda_{w-mean} = \frac{I(\lambda_V)\lambda_V + I(\lambda_i)\lambda_i + I(\lambda_z)\lambda_z}{I(\lambda_V) + I(\lambda_i) + I(\lambda_z)} \tag{15}$$

With $T = T_{eff} = 6356.19$ K (Table 1), Equation 15 gives $\lambda_{w-mean} = 6686$ Å. Thus $\lambda_{cal} = 6686$ Å, and the corresponding results are shown in Table 3.4.

Note that λ_{mean} (from method 2) and λ_{w-mean} (from methods 3 and 4) were calculated using only the V-, i-, and z-bands (but not the B), as only these bands have a formula for M (and thus indirectly distance), their results of which can be compared against each other (as well as against the Gaia distance) in order to determine the effectiveness of each calibration method.

(5) Lastly, calibration method (5), developed by Cardelli *et al.* (1989), yields the results of Table 3.5. For calibration (5), Equation 9 is replaced by

$$A_{cal} = R_V \times E\,(B–V) \times f \tag{16}$$

where the factor f is obtained when Equations 2 and 3 from Cardelli *et al.* (1989) are used for the V, i, and z wavelengths.

3.4. Distance results

Tables 3.1, 3.2, 3.3, 3.4, and 3.5 include the distance results with reddening and A calibration via methods (1), (2), (3), (4), and (5), respectively. The best d-viz-avg result, having only a 0.30% difference from the Gaia distance (Table 3.3), was obtained by method (3), a weighted-mean calibration of A.

4. Discussion

The main goal of the paper was to test the validity of three period-luminosity-metallicity relations (Equations 1, 2, 3) against observational data obtained from a single star, V350 Mus. The formulas performed quite well since, collectively, they generated a three-filter average distance that, within the margin of error, agrees with the Gaia distance (see Table 3.3, or Table 4 which summarizes the main results). The individual distances from the data of the i and z filters were

within each other's margin of error but not with the distance value from the V filter. Also, the M_i and M_z formulas performed better than the M_V (in matching the Gaia distance)—probably an indication that the M_V formula needs further refinement. These results are expected within the context of Catelan *et al.* (2004), where the period-luminosity graph in the i filter shows a narrower spread of points (a sharper line with less noise, thus a more accurate M_i expression), but a rather scattered spread of points in the V filter (thus a less accurate M_V expression)—V350 Mus might be an example of the scattered V points. (That paper does not include a z filter graph.)

Using the Sloan Digital Sky Survey (SDSS) photometric system, Cáceres and Catelan (2008), too, has a low noise graph in the i filter, but also in the z filter (meaning that, the M_i and M_z formulas are generally expected to outperform the M_V formula, as verified by our study). Recall, Equation 1 is from Catelan *et al.* (2004) and Equations 2 and 3 are from Cáceres and Catelan (2008). Hence our distance results confirm rather well the theoretical predictions of those papers.

If these formulas are verified further by similar research involving many other stars, they could be used in "reverse": for example, from the known distance and metallicity of an RR Lyrae star and by measuring its period and m, we can calculate A using

$$M = m - A + 5 - 5 \log d \qquad (17)$$

and thus determine a star's reddening value E(B−V). That is important as the reddening values reported by the Schegel Dust Map are generally approximations in the general vicinity of a star. Or, in another example for these formulas' usage, we could determine a star's metallicity if we knew its reddening and distance, and measured its m and period.

Interestingly, our simple calibration formula, Equation 9, implemented in methods 1-4, produced better distance results in every case (as seen in Tables 3.1, 3.2, 3.3, and 3.4), compared to the more complex calibration method (5) found in Cardelli *et al.* (1989) (as seen in Table 3.5). The reason for this might be that, in the accounting of the phenomenon of extinction, our approach considers the amount of each wavelength's extinction proportionally, by balancing it with respect to the extinction of an average wavelength (as seen specifically in Tables 3.2, 3.3, and 3.4), whereas the paper by Cardelli *et al.* (1989) arrives at its extinction formulas by calibrating a wavelength's extinction with respect to the extinction of only the V wavelength. The hypothesis that such a simple calibration formula, Equation 9, can produce good distance results (via methods 1-4) is worth testing further.

Based on the results of Tables 3.1, 3.2, 3.3, 3.4, and 3.5 we propose that the best calibration method for the extinction factor A is Equation 9 implemented via method (3), Equation 10, the weighted-mean of the wavelengths that have a period-luminosity-metallicity relation (and are used in the observations), along with Equation 11. Recall that in that case (Table 3.3 or 4), the percent difference between the Gaia value of distance and our value was only 0.30% when E(B−V) = 0.200 (or 0.01% when E(B−V) = 0.198). This hypothesis can be tested by imaging a star in as many wavelengths as possible, as long as each of these wavelengths has also a corresponding period-luminosity-metallicity relation.

Table 4. V350 Mus Summary of Main Results: E(B–V) = 0.200 mag; A is calibrated with $\lambda_{cal} = \lambda_{w-mean-method-3} = 7482$ Å.

	Band		
	V	*i*	*z*
d (parsec)	145.70	172.14	176.70
errd (parsec)	11	7	7
d-viz-avg (parsec)		164.85 ± 5	
d-Gaia (parsec)		165.34 ± 1	
% diff[G]		0.30[a]	
P (d)		0.3705 ± 0.0012	
V350 Mus		RRab (reclassified)	

[G] Between d-viz-avg and the Gaia distance. [a]or 0.01% when E(B–V) = 0.198.

Lastly, we discovered that V350 Mus is an RRab type. Prior to this research the star was classified as either an RRc (Watson *et al.* 2006; Kazarovets *et al.* 2011; Samus *et al.* 2017), or an eclipsing variable (EW) (Watson *et al.* 2014; Astraatmadja and Bailer-Jones 2016). The calculated amplitudes (Table 2) were not clearly telling of the type of RR Lyrae star V350 Mus is, as these values were roughly between those typical of an RRc type (which are usually of lower amplitudes) and those typical of an RRab type (which are usually of higher amplitudes). However, the four light curves (Figures 2–5) clearly reclassified V350 Mus as an RRab: one can see a sharper ascent with a more gradual descent in the luminosity cycle, characteristic of RRab stars. An additional piece of evidence that reinforces the star's reclassification is this: when the period-luminosity-metallicity relations (Equations 1, 2, 3) are evaluated by assuming an RRc type star then all distance results—i. e., what Tables 3.1, 3.2, 3.3, 3.4, and 3.5 would be like in such case—are worse compared to the only reported star distance, that of Gaia.

The period we measured, 0.3705 d (Table 2), is in quite good agreement with one of the reported periods, 0.36905 d (Table 1), its reference of which had classified the star as an RR Lyrae star (although of type RRc). However, our study's period doesn't agree with the other reported period, 0.73811 d (Table 1), its reference of which had classified the star as an EW type. Thus, the period analysis is additional evidence that V350 Mus is an RR Lyrae type star, and not an EW. Moreover, V350 Mus's reclassification to RRab is supported by yet more evidence related to the star's short period and relatively high metallicity, because short period and high metallicity are general characteristics of RRab variables, not of RRc. RRc variables with metallicity as high as that of V350 Mus are considered rare.

Another general characteristic, typical of an RR Lyrae star light curve, is a bump along the descent of the curve. Although not very clear, a tiny bump does exist in the descent of at least some of the light curves in our study. This feature together with the period agreement (mentioned above) solidify the star's reclassification as an RR Lyrae variable instead of an eclipsing variable (from a previous classification).

5. Conclusion

We measured the period and apparent magnitude of V350 Mus. We inserted the period and the star's metallicity

in three theoretical period-luminosity-metallicity relations (M_V, M_i, and M_z) in order to calculate the star's absolute magnitude in the corresponding filters. We then adjusted the apparent magnitude of each filter by adding to it an extinction factor, calculated each filter's distance, and, by comparing the results with one another, as well as comparing the three-filter average distance with the Gaia distance, we were able to check the validity of the theoretical period-luminosity-metallicity relations. Collectively, the relations performed quite well in the case study of a single star, V350 Mus.

The distances (in parsecs) were estimated to be: 145.70 ± 11 in the V filter; 172.14 ± 7 in i; and 176.70 ± 7 in z. The three-filter average distance is 164.85 ± 5, only 0.30% difference from the Gaia value of 165.34 ± 1. The pulsation period was 0.3705 ± 0.0012 day.

The average distance was optimum when the extinction factor was calibrated using a new simpler method, which involved the weighted mean of the band wavelengths that had a period-luminosity-metallicity relation (the V, i, and z wavelengths in our case), and where the weight of a particular band wavelength was its ratio to an arbitrary reference wavelength. This method did better compared to the older method by Cardelli *et al.* (1989). We hope to test the effectiveness of the new calibration method further in a future study. The present research reclassified V350 Mus as an RRab Lyrae type.

6. Acknowledgements

We are grateful to Dr. Michael Fitzgerald for his continuous support and valuable advice during every step of this project. We also thank Dr. Brian Uzpen for connecting us to MF. We are also indebted to both the JAAVSO editor and the anonymous referee whose comments and suggestions have undoubtedly improved the quality of the manuscript.

DN thanks Bloomfield College's PBI office for funding. DN and DK thank Bloomfield College's McNair Program office for funding.

References

Altunin, I., Caputo, R., and Tock, K. 2020, *Astron. Theory, Obs.*, Methods, **1**, 1.

Ammons, S. M., Robinson, S. E., Strader, J., Laughlin, G., Fischer, D., and Wolf, A. 2006, *Astrophys. J.*, **638**, 1004.

Astraatmadja, Tri L., and Bailer-Jones, C. A. L. 2016, *Astrophys. J.*, **833**, 119.

Bailer-Jones, C. A. L., Rybizki, J., Fouesneau, M., Mantelet, G., and Andrae, R. 2018, *Astron. J.*, **156**, 58.

Bertin, E., and Arnouts, S. 1996, *Astron. Astrophys., Suppl. Ser.*, **117**, 393.

Bonnarel, F., *et al.* 2000, *Astron. Astrophys., Suppl. Ser.*, **143**, 33.

Brown, T., *et al.* 2013, *Publ. Astron. Soc. Pacific*, **125**, 1031.

Cáceres, C., and Catelan, M. 2008, *Astrophys. J., Suppl. Ser.*, **179**, 242.

Cardelli, J. A., Clayton, G. C., and Mathis, J. S. 1989, *Astrophys. J.*, **345**, 245.

Catelan, M., Pritzl, B. J., and Smith, H. A. 2004, *Astrophys. J., Suppl. Ser.*, **154**, 633.

Catelan, M., and Smith, H. A. 2014, *Pulsating stars*, John Wiley and Sons, Hoboken, NJ.

Collins, K. A., Kielkopf, J. F., Stassun, K. G., and Hessman, F. V. 2017, *Astron. J.*, **153**, 77.

Dworetsky, M. 1983, *Mon. Not. Roy. Astron. Soc.*, **203**, 917.

Fitzgerald, M. 2018, in *Robotic Telescope, Student Research and Education Proceedings, Vol. 1, No. 1*, RTSRE, San Diego, CA, 347.

Gaia Collaboration, Brown, A., *et al.* 2018, *Astron. Astrophys.*, **616A**, 1.

Gaia Collaboration, Clementini, G., *et al*. 2017, Astron. Astrophys., **605A**, 79.

Henden, A. A., Templeton, M., Terrell, D., Smith, T. C., Levine, S., and Welch, D. 2016, VizieR Online Data Catalog: AAVSO Photometric All Sky Survey (APASS) DR9, II/336.

Høg, E., *et al.* 2000, *The Tycho-2 Catalogue of the 2.5 Million Brightest Stars*, *Astron. Astrophys.*, **355**, L27.

Hubble, E. 1929, *Proc. Natl. Acad. Sci. USA*, **15**, 168.

Jayasinghe, T., *et al.* 2019, *Mon. Not. Roy. Astron. Soc.*, **485**, 961.

Kazarovets, E. V., Samus, N. N., Durlevich, O. V., Kireeva, N. N., and Pastukhova, E. N. 2011, *Inf. Bull. Var. Stars*, No. 6008, 1.

Leavitt, H. S. 1908, *Ann. Harvard Coll. Obs.*, **60**, 87.

NASA/IPAC Infrared Science Archive (IRSA). 2020, Galactic Dust Reddening and Extinction (https://irsa.ipac.caltech.edu/applications/DUST).

Salaris, M., Chieffi, A., and Straniero, O. 1993, *Astrophys. J.*, 414, 580.

Samus, N. N., Kazarovets, E. V., Durlevich, O. V. , Kireeva, N. N., and Pastukhova, E. N. 2017, *Astron. Rep.*, **61**, 80. Schlafly, E. F., Meisner, A. M., and Green, G. M. 2019, *Astrophys. J., Suppl. Ser.*, **240**, 30.

Shappee, B. J., *et al.* 2014, *Astrophys. J.*, **788**, 48.

Stellingwerf, R. F. 1978, *Astrophys. J.*, **224**, 953.

Watson, C. L., Henden, A. A., and Price, A. 2006, in *The Society for Astronomical Sciences 25th Annual Symposium on Telescope Science*, Society for Astronomical Sciences, Rancho Cucamonga, CA, 47.

Watson, C., Henden, A. A., and Price, C. A. 2014, AAVSO International Variable Star Index VSX (Watson+, 2005–2020; https://www.aavso.org/vsx).

Wolf, C., *et al.* 2018, *Publ. Astron. Soc. Australia*, **35**, 10.

Period Determination and Classification Analysis of 25 Pulsating Red Giants

Anshita Saini
5246 145th Place SE, Bellevue, WA 98006; anshitasaini@gmail.com

Nicholas Walker
9808 Hillgreen Place, Beverly Hills, CA 90212; nickwalker106@gmail.com

Received February 6, 2021; revised February 28, March 5, 2021; accepted March 5, 2021

Abstract In this paper we present our updates and findings surrounding both period and classification analysis of 21 Miras and 4 semiregular variable stars. Our primary methods for confirming pulsation period include both qualitative and quantitative examination of time series plots and light curves, along with cross-confirmation using publicly-accessible databases with over a hundred years of published data. Using the visual observations and the Johnson V data from the AAVSO, and with the help of the AAVSO's VStar software, we arrived at refined period values to confirm data published by the VSX. Somewhat substantial updates are recommended for T UMi, from a period of 115.7 days to a primary and secondary period of 237.5 and 247.6 days, though no other variables merited such sizable adjustments. Finally, the application of self-correlation analysis provided further insight into the cycle-to-cycle changes in period and magnitude of semiregular variables.

1. Introduction

Pulsating red giants (PRGs) are radially-pulsating variable stars that occupy the ascending portion of the giant branch, along with the asymptotic giant branch (AGB), of the Hertzsprung-Russell Diagram. Stellar pulsation is typically caused by the expansion and contraction of the outer layers of such stars. Variables are classified according to factors like magnitude change and regularity of periodicity, the latter being the primary determinant of the *General Catalogue of Variable Stars* (GCVS; Samus *et al.* 2017) variability type. Mira variables, which have stellar features like those of the prototype Mira, o Ceti, have well-defined periods of around 100 to several hundred or up to 1,000 days. These periods may "wander" over time, a behavior studied in depth by Percy and Qiu (2019), Percy and Fenaux (2019), and Blackham (2020), though most Miras have regular fundamental pulsation modes. Their magnitudes vary by 2.5 to 11 magnitudes in the visual waveband.

Semiregular (SR) variable stars display periodicity, but differ from Miras due to often ill-defined periods and characteristic irregularities. The periods of semiregular variable stars can range from 20 to over 2,000 days, nearly twice those of longer-period Mira stars. Light amplitudes of semiregular stars vary as well, ranging from several hundredths to several magnitudes (GCVS). The SR stars presented in this paper exhibit increasing or decreasing trends in light amplitude over time scales of several thousand Julian days.

Semiregular variable giants are additionally subdivided into subclasses of SRA, SRB, SRC, SRD, and SRS. SRA stars similarly demonstrate periodicity and changing amplitudes and often exhibit light curves similar to Miras. However, SRA stars have smaller light amplitudes with more consistent magnitudes—generally below 2.5 magnitudes in V. Ranging from 25 to 1,200 days, the periods of SRA stars align more closely to the range of Mira periods than to the full range of SR periods.

SRB stars display poorly-defined periodicity and irregularities, distinguishing them from SR and SRA variable stars. The GCVS assigns each SRB a mean period, though these stars often have two or more pulsating modes. The mean period range is similar to that of semiregular stars and ranges from 20 to 2,300 days.

This study aims to confirm the periods and classifications of several SR variable stars and Mira variables through various methods of analysis on visual observations. The 25 variables in our study were chosen primarily due to their location in constellations near the North Celestial Pole in order to limit seasonal gaps in their light curves. Beyond that rationale, the stars were chosen semi-arbitrarily, though the SR variables within some of these constellations were selected due to their relative abundance of photometric data. Quantitative analysis of periodicity is presented through Fourier analysis and the Analysis of Variance algorithm. The classification of these stars was confirmed through qualitative analysis of light curves and self-correlation plots.

2. Resources

2.1. Variable Star Index (VSX)

The International Variable Star Index (VSX), developed for working groups of the American Association of Variable Star Observers (AAVSO), currently catalogs around 2 million variable stars (Watson *et al.* 2014). Each star in the catalog is updated with peer-reviewed information on its position, aliases, variability type, spectral type, magnitude range, and period, as well as links to relevant academic references. Many of the stars discussed in this paper may warrant updates in the VSX, while others in the index have been recently revised.

2.2. AAVSO International Database (AID)

The American Association of Variable Star Observers' International Database (AAVSO's AID) contains nearly 50 million variable stars observations, including data points from over 100 years ago. The open-source database provided the visual and Johnson V band observational data used to analyze both semi-regular and Mira stars. As the largest and

most comprehensive variable star database of its kind, the AID contains thousands of thoroughly reviewed observations contributed by various organizations and amateur astronomers around the world (Kafka 2021).

2.3. VSTAR

The AAVSO's VSTAR data visualization tool was used for period and magnitude analysis of the 25 chosen variable stars. The open-source application allows the user to generate light curves using data queried from AAVSO AID, as well as data from a variety of file types. VSTAR additionally offers the option of generating phase plots based on a user-inputted period (Benn 2013). In addition to such plots, VSTAR offers multiple implementations of Discrete Fourier Transform analysis, including a "Standard Scan" or relying on a frequency or period range as provided by the user. Applying one of these three Fourier analysis options results in a "top hits" table, as well as a power spectrum (AAVSO 2018). VSTAR also provides an implementation of the Analysis of Variance (AoV) algorithm, with an accompanying "top hits" table and periodogram.

3. Methods

3.1. DC DFT

We applied the Date-Compensated Discrete Fourier Transform (DC DFT) algorithm (Ferraz-Mello 1981) in VSTAR to determine the periods of the variable stars presented in this paper. The DC DFT finds the Fourier coefficients assuming that a periodic model fits the light curve. VSTAR's date-compensated algorithm ensures that gaps in the data are accounted for, yielding accurate analysis on both well-sampled and poorly-observed stars.

The DC DFT also determines the power, or statistical significance, associated with the Fourier coefficients. The highest power levels indicate that the corresponding frequency is a likely candidate for the fundamental frequency of the data. These values are represented in the power spectra in Figures 1 and 2, with the x-axis as Frequency (Hertz) and the y-axis as the power of each frequency.

Figure 1 depicts the DC DFT plot of T UMi with two peaks of comparable powers. The secondary peak of 0.004039 Hz corresponds to a candidate secondary pulsation mode, present in many of the DC DFT plots of semiregular variables. The plots of most Mira stars were similar to the power spectrum of X Cep in Figure 2, although this plot also shows evident harmonic peaks at frequency intervals of 0.001850 Hz. This curve, along with those in Figures 2–4, was generated for the purpose of our analysis, though we include them here as examples of VSTAR's capabilities.

3.2. AoV

A second tool—Analysis of Variance (AoV)—was applied to confirm the period(s) found by DC DFT. Unlike Fourier analysis, this method relies on the One-way Analysis of Variance (ANOVA) algorithm to extract candidate periods. Upon inputting a period range based upon the DC DFT and the VSX periods, VSTAR's AoV algorithm computes an "F-statistic," a measure of statistical significance similar to the DC DFT power level for each candidate period.

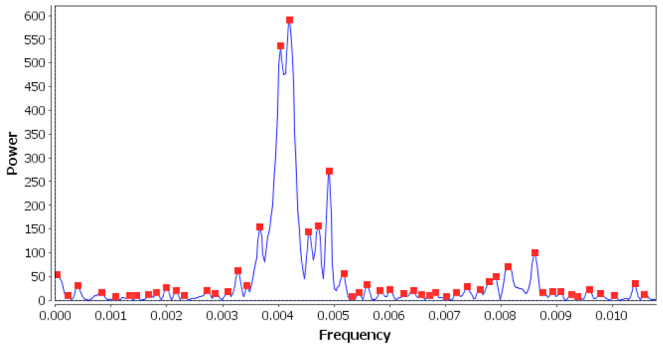

Figure 1. A power spectrum, or DC DFT plot, for SR variable T UMi (JD 2450000–JD 2459200).

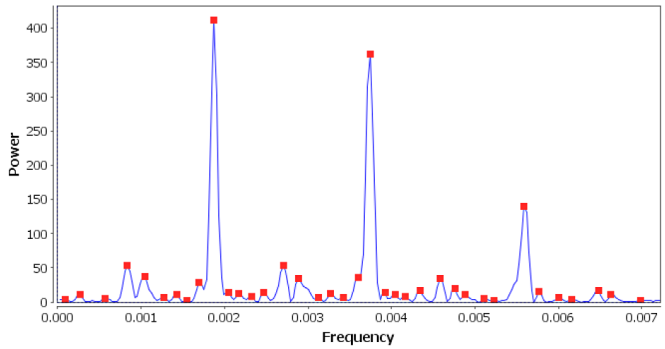

Figure 2. DC DFT plot for Mira X Cep (JD 2450000–JD 2459200).

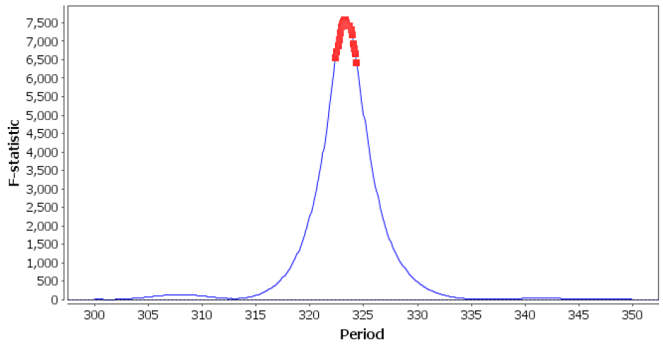

Figure 3. AoV Periodogram for S UMi (JD 2450000–JD 2459200).

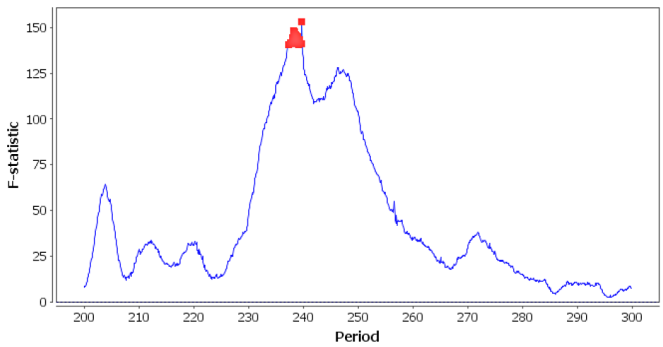

Figure 4. AoV Periodogram for T UMi (JD 2450000–JD 2459200).

A concentration of high F-statistic points, as depicted in Figure 3, indicates that the star is well-sampled, and that there is only one strong candidate period. Figure 4 depicts a periodogram with more noise, characteristic of semiregular stars. In these cases, the peak of the plot was confirmed by finding the period through the application of self-correlation studies, introduced in section 3.3. For example, the peak period in Figure 4 at approximately 240 days coincides with the period in the self-correlation plot of T UMi (Figure 5).

3.3. Self-correlation

To verify or suggest corrections and/or updates to the variability types of our subject stars (and as a tertiary form of period analysis), we developed a self-correlation algorithm, following the intuition of Percy and Kojar (2013), Percy and Mohammed (2004), and Percy and Ralli (1993). For all pairs of measurements in a given range of Julian Days, which total to $\binom{N}{2}$ pairs of (JD, magnitude in V), where N is the number of observations, we calculate Δt and |Δmagnitude| (Δmag), appending these $\binom{N}{2}/2$ values to arrays of Δts and Δmags. After deciding on an optimal "bin width" for each data set, which we found to be 10 days, all Δts that fall within that range are averaged, along with the corresponding Δmag values. We plot these averaged (Δt, Δmag) pairs in a self-correlation diagram.

Numerous changes in the period or shifts in amplitude of a subject star result in a self-correlation diagram with a non-constant amplitude. Rather than inspecting the light curves of such stars, we conduct a visual analysis of their self-correlation plots, as shown in Figures 5–7 and 13–14. A range of average Δt = 0 to average Δt = 1,000 is sufficient to detect trends in self-correlation amplitudes. As discussed in reference to our specific plots, the behavior of the plot changes noticeably when selecting different time periods with the same JD range and bin width.

The relative minima of self-correlation diagrams, in most cases, reflect primary pulsation periods for Mira stars, and often for SR variables as well, although such minima tend to be changing in average Δmag. We quantitatively confirmed the periods of the majority of our subject stars, with the exception of AU Cam, which we will discuss in section 4.4.

In some of our self-correlation diagrams, the final few peaks seem to exhibit irregular behavior. This trend is not due to intrinsic properties of the subject star, but is rather an artifact of running the algorithm; the frequency of Δt values decreases as Δt increases, and as such, Δmags are more sparse on the plots.

4. Results

All systems studied are listed in Table 1 with their GCVS variable type, most recently revised period and magnitude range listed in the VSX, periods determined through DC DFT and AoV analysis, and the magnitude range obtained from the light curve plots of the stars. Although the majority of our analyses provided confirmations of the VSX values in Table 1, we encountered numerous subject stars that exhibited deviations from the VSX data—particularly differences in period. We also make note of several trends or irregularities that we observed.

The stars with asterisked DC DFT periods exhibit one or more harmonic periods that are unit fractions of the fundamental period. RW And, TX Cam, and Y Cep have respective harmonic periods of 215.6, 279.9, and 166.9 days. X Cep has a harmonic of 267.0 days and a third harmonic of 178.9 days. These harmonics are not caused by actual pulsations of the star, but are rather high-frequency artifacts (Percy and Golaszewska 2020) due to the asymmetry of the light curve shape.

X UMi, although it has more than 2,000 visual and Johnson V band observations, has poorly dispersed data, as observations are clustered together, resulting in a light curve that lacks periodicity and consistency. However, after running both DC DFT and AoV analyses for different JD ranges, we arrived at period values consistent enough to suggest an update to X UMi's period in the VSX, from 388 days to 339 days.

Finally, T UMi, which we soon discuss in more depth, exhibited a period of approximately 237.5 days and a secondary pulsation mode with period 247.6 days, a substantial change from the period of 115.7 days listed in the VSX. Our period was confirmed by both the Fourier routine and AoV.

4.1. T UMi

Here we demonstrate the "optimal" self-correlation diagram of a well-observed SR variable—that is, almost perfectly periodic and having a steadily changing amplitude—T UMi. Corresponding with the decreasing magnitude in T UMi's light curve (Figure 8), the amplitude of the self-correlation plot in Figure 5 exhibits a decreasing trend, hinting at typical semiregular behavior. However, a decreasing self-correlation amplitude is not the sole indication of semiregularity. As we will discuss with regard to other SR-type stars, abnormal correlation diagrams—whether defined by a lack of periodicity or a changing amplitude—may also suggest semiregularity.

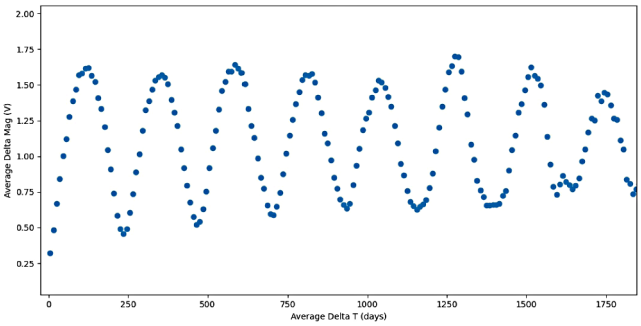

Figure 5. Self-correlation plot for T UMi (JD 2452000–JD 2454000).

4.2. R UMi

Figures 6 and 7 reflect the changing behavior of R UMi across varying Julian Day time scales. Such irregular periodicity, as is evident in R UMi's light curve in Figure 10, is characteristic of a semiregular variable star, confirming the VSX variability type of a general SR. In addition, the magnitude range decreases from 0.3–0.9 V to 0.3–0.65 V. Plots of additional Julian Day time shifts have been omitted for brevity, but generally confirm a decreasing average magnitude for R UMi. Though the upper plot reflects a clear primary period, confirmed by a brief glance at the star's light curve in Figure 10, the peaks in the lower plot suggest the potential presence of two pulsation modes.

However, both the primary and secondary periods are larger than the typical periods of Cep(B) or RR(B) stars, further confirming that the variability type of SR is the most likely classification.

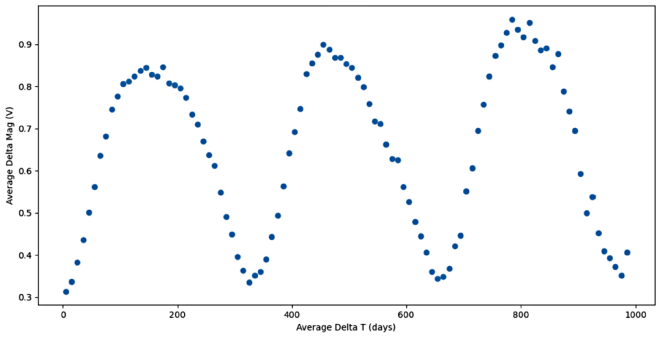

Figure 6. Self-correlation plot for R UMi (JD 2451000–JD 2452000).

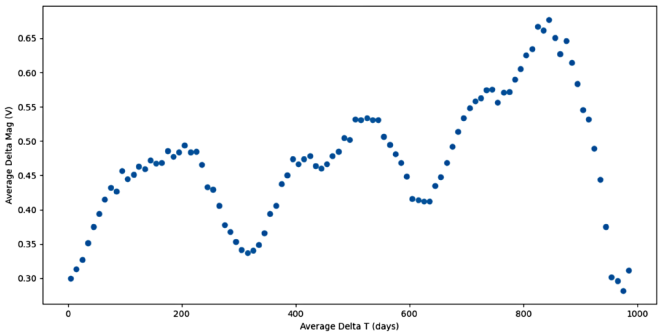

Figure 7. Shifted self-correlation plot for R UMi (JD 2452000–JD 2453000).

Table 1. Stars discussed in this study.

Name	*GCVS Type*	*VSX Period (days)*	*VSX Mag Range (V)*	*DC DFT Period (days)*	*AoV Period (days)*	*Mag Range (V)*
R And	M	409.2	5.8–15.2	407.4	409.4	5.7–15.4
RW And	M	430.0	7.9–15.7	431.1*	431.5	7.7–17.4
V And	M	256.4	9.0–15.2	257.3	258.2	15.4–18.4
AU Cam	SRA	366.0	10.0–10.7	363.5	363.7	9.0–11.4
R Cam	M	270.22	6.97–14.4	270.1	269.6	7.8–14.2
T Cam	M	369.3	7.2–14.4	375.9	375.8	7.3–14.4
TX Cam	M	558.7	7.8–16.9	559.8*	555.7	7.7–15.8
R Cas	M	430.5	4.7–13.5	435.3	433.2	3.7–14.2
S Cas	M	608.2	7.9–17.3	613.6	611.3	8.0–17.5
T Cas	M	440.0	6.9–13.0	444.1	442.5	7.3–12.3
W Cas	M	407.9	8.2–13.0	406.4	405.1	8.1–13.3
S Cep	M	484.4	6.6–12.5	482.3	482.0	6.1–11.5
T Cep	M	388.1	5.2–11.3	385.9	384.6	5.0–11.5
Y Cep	M	332.6	8.1–16.0	332.0*	333.6	8.0–15.5
X Cep	M	535.2	8.1–17.5	533.9	533.7	8.0–15.6
R Dra	M	245.6	6.7–13.2	247.5	247.5	5.9–14.0
RY Dra	SRA	300.0:	5.88–8.0	276.8	276.7	5.7–8.4
T Dra	M	422.2	7.2–13.5	420.5	422.5	8.4–14.0
U Dra	M	316.1	9.1–14.6	318.7	319.0	8.8–14.6
W Dra	M	278.6	8.9–15.4	286.6	287.0	9.0–15.8
R UMi	SR	325.7	8.5–11.5	324.3	324.4	8.2–11.5
S UMi	M	331.0	7.5–<13.2	323.9	323.3	7.4–13.0
T UMi	SR	115.7	7.8–15.0	237.5, 247.6	239.7	9.1–14.2
U UMi	M	330.9	7.1–13.0	324.1	323.9	7.4–12.5
X UMi	M	388.0	12.5–18.4**	339.2	338.8	11.5–16.1

Note: A single asterisk (*) denotes the presence of a harmonic period. Double asterisks (**) designate a magnitude range under photographic passband. The colon (:) is a symbol used by the VSX to indicate an uncertain value.

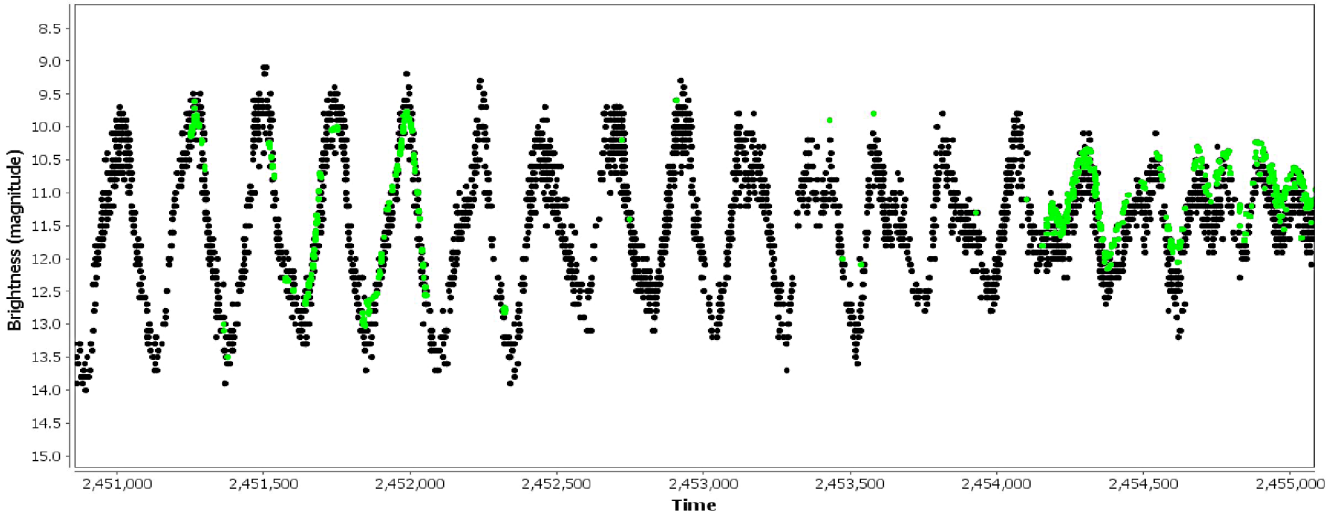

Figure 8. Light curve of T UMi generated from vstar, JD 2451000–JD 2455000.

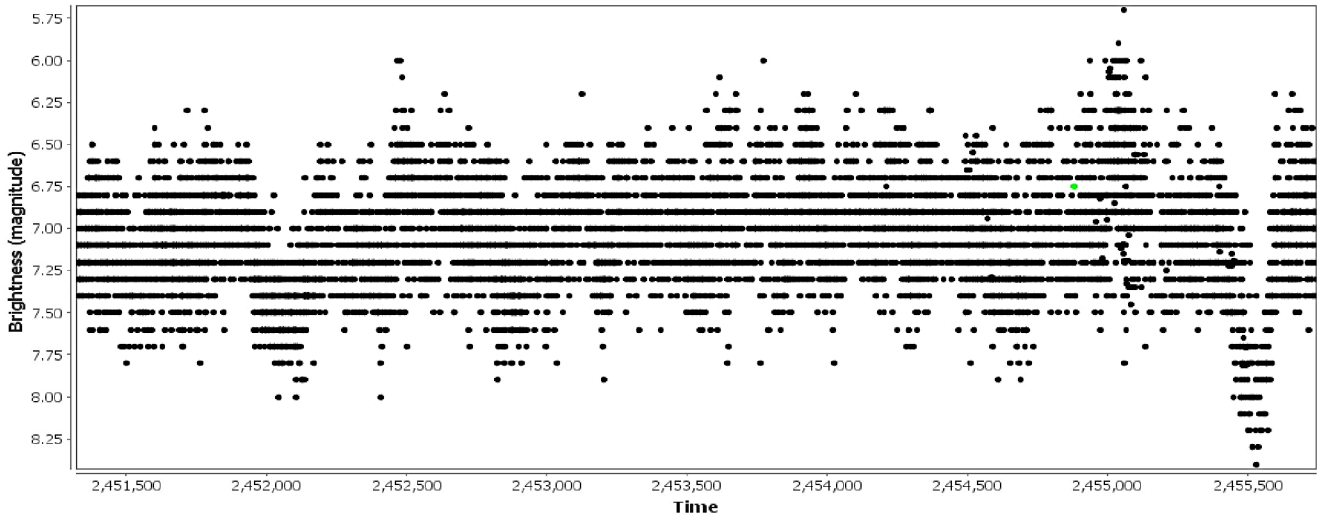

Figure 9. Light curve of RY Dra generated from vstar, JD 2451500–JD 2455500.

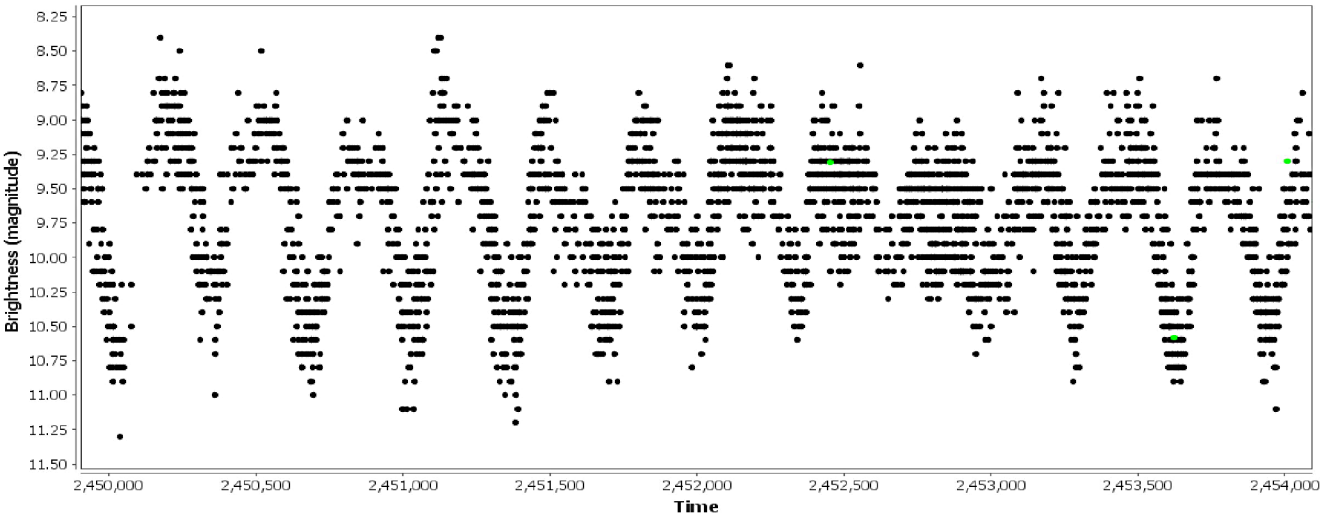

Figure 10. Light curve of R UMi generated from vstar, JD 2450000–JD 2454000.

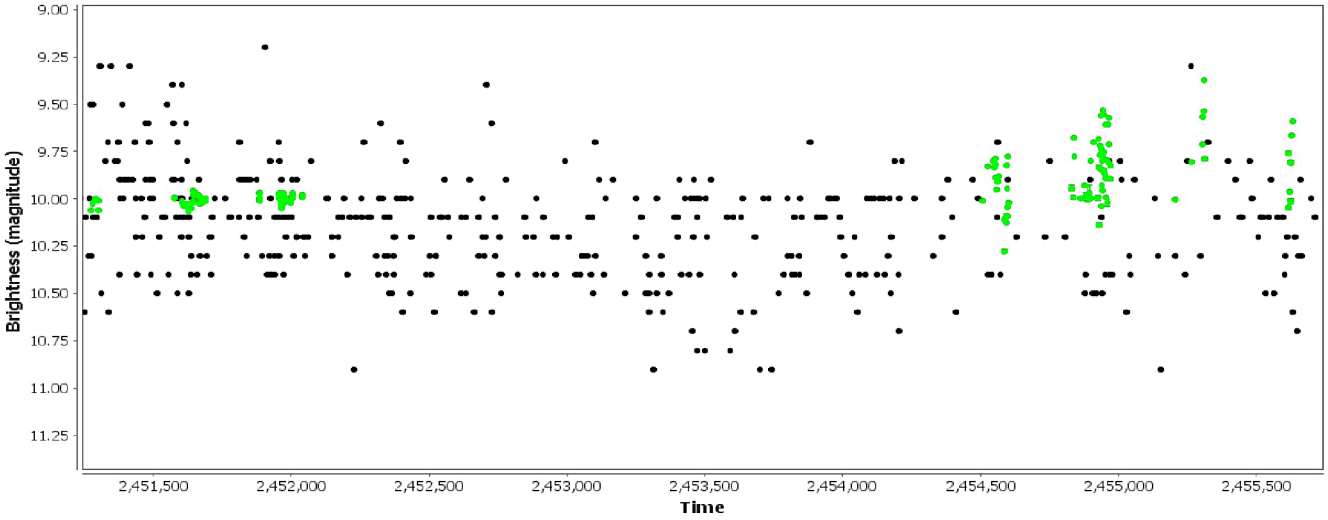

Figure 11. Light curve of AU Cam generated from vstar, JD 2451500–JD 2455500.

4.3. RY Dra

As depicted in Figure 12, RY Dra displays clear irregularity when compared to the previous self-correlation plots of SR and SRA stars, even over cycles of 6 periods. The self-correlation plot also suggests the presence of two or more pulsation modes, especially when considering its light curve (Figure 9), as there appear to be multiple maxima and minima per cycle. This behavior coincides with its classification as an SRB star. These stars are generally characterized by poorly defined periodicity and irregular changes. As in the case of R UMi, the self-correlation plots of various Julian Day time shifts display changing magnitude ranges. RY Dra has both increasing and decreasing magnitude ranges over longer Julian Day time scales, a behavior that agrees with that of its light curve.

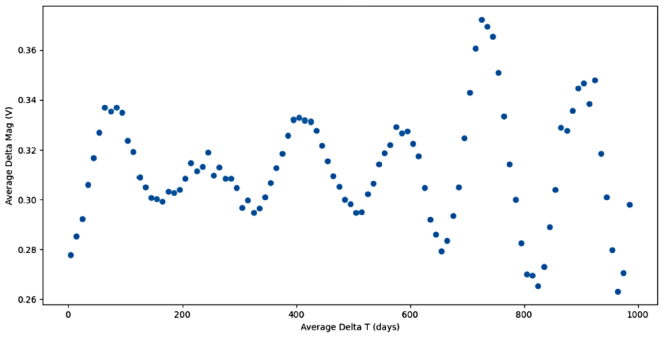

Figure 12. Self-correlation plot for RY Dra (JD 2453000–JD 2454000).

4.4. AU Cam

Vague periodicity can be seen in the light curve of AU Cam (Figure 11), and the self-correlation plot in Figure 13 even more irregular. The distribution of data points in AU Cam's light curve is relatively sparse, though this is not a sufficient indication of the star's variability type. However, the plot demonstrates a clear, gradual increase in Δmag, which is highly indicative of an SRA type variable star.

AoV and DC DFT analysis on AU Cam resulted in a period of 363.6 days. Upon a cursory glance, it appeared that this year-long period may have been a result of the seasonal Ceraski effect, briefly described by Percy *et al.* (2009). This effect causes a different perception of the magnitude difference between two stars due to the changing orientation of the star field throughout the year. The self-correlation diagrams of AU Cam further depict that the period of one year is likely spurious. Moreover, the DC DFT power spectrum exhibits a peak at a frequency of 0.000011 Hz with an amplitude nearly 6 times that of the 363.6-day period, similar to the behavior of the stars analyzed by Percy (2015). In accordance with Percy's conclusions, aliasing of AU Cam's VLF variability is the most likely cause of the one-year period.

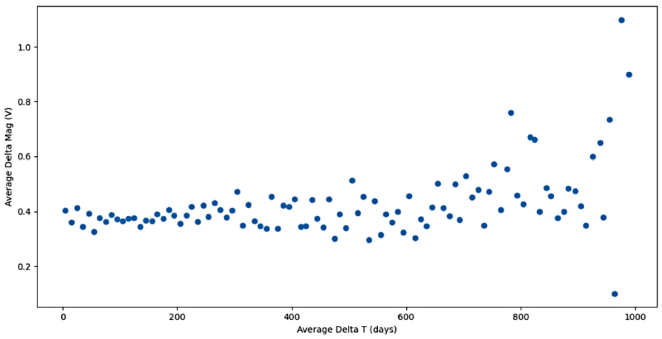

Figure 13. Self-correlation plot for AU Cam (JD 2453000–JD 2454000).

5. Conclusion

Our study supports the existing characterizations and key stellar attributes of most of the systems studied. These attributes include pulsation amplitude, GCVS variability type, and period, which we confirm via several analytical methods. The one standout case is T UMi, which appears to exhibit two pulsation modes that are, respectively, nearly 122 and 132 days longer than the VSX period. It is important to note that our proposed periods are not necessarily the most likely, as self-correlation was run on a larger JD range. Nevertheless, it is very likely that T UMi's period has increased appreciably since its last update in the VSX, and that the periods we arrived at are within an acceptable range.

Our self-correlation analysis provided no updates to the variability types of SR variables T UMi, R UMi, RY Dra, and AU Cam, though we emphasize the versatile nature of analyses of this sort. We also show how period and amplitude change through pulsation cycles, and how selecting different time scales reveals peculiar trends, specifically in the self-correlation plots of SR variables.

6. Acknowledgements

Both authors contributed equally to this work. We thank the observers and staff of the AAVSO for the data used in this research, as well as the developers of the VStar software package. We additionally relied on the International Variable Star Index database. We also thank Dr. John R. Percy and Dr. Adam W. Rengstorf for providing insight regarding period analysis with self-correlation, among other inquiries.

References

AAVSO. 2018, Variable Star Classification and Light Curves Manual, version 2.4, AAVSO, Cambridge, MA.

Benn, D. 2013, VStar data analysis software (http://www.aavso.org/vstar-overview).

Blackham, K. M. 2020, *J. Amer. Assoc. Var. Star Obs.*, **48**, 111.

Ferraz-Mello, S. 1981, *Astron. J.*, **86**, 619.

Kafka, S. 2021, variable star observations from the AAVSO International Database (https://www.aavso.org/aavso-international-database-aid).

Percy, J. R. 2015, *J. Amer. Assoc. Var. Star Obs.*, **43**, 176.

Percy, J. R., Esteves, S., Lin, A., Menezes, C., and Wu, S. 2009, *J. Amer. Assoc. Var. Star Obs.*, **37**, 71.

Percy, J. R., and Fenaux, L. 2019, *J. Amer. Assoc. Var. Star Obs.*, **47**, 202.

Percy, J. R., Golaszewska, P. 2020, *J. Amer. Assoc. Var. Star Obs.*, **48**, 165.

Percy, J. R., Kojar, T. 2013, *J. Amer. Assoc. Var. Star Obs.*, **41**, 15.

Percy, J. R., and Mohammed, F. 2004, *J. Amer. Assoc. Var. Star Obs.*, **32**, 9.

Percy, J. R., and Qiu, A. L. 2019, *J. Amer. Assoc. Var. Star Obs.*, **47**, 76.

Percy, J. R., Ralli, J. A., and Sen L. V. 1993, *Publ. Astron. Soc. Pacific*, **105**, 287.

Samus, N. N., Kazarovets, E. V., Durlevich, O. V., Kireeva, N. N., and Pastukhova, E. N., 2017, *Astron. Rep.*, **61**, 80, *General Catalogue of Variable Stars: Version GCVS 5.1* (http://www.sai.msu.su/gcvs/gcvs/index.htm).

Watson, C., Henden, A. A., and Price, C. A. 2014, AAVSO International Variable Star Index VSX (Watson+, 2006–2014, https://www.aavso.org/vsx).

The Correlation between Hα and HeI 6678 Emission Activity in the Be Star γ Cassiopeiae from 1995 to 2021

Ernst Pollmann
Observatory "Vereinigung der Sternfreunde Köln", Germany; ernst-pollmann@t-online.de

Received February 7, 2021; revised April 27, 2021; accepted April 29, 2021

Abstract The Be star γ Cas is among others well known for erratic rapid variations in its HeI emission at 6678 Å. Recently, this emission has become an important diagnostic feature to investigate the regions of disc activity close to the star. It was recognized that several factors—mass loss from the photosphere of the primary star, density variations, and collision excitations of the HeI atoms—force the emissions in HeI (at 6678 Å) to be restricted to about to 2.3 stellar radii from the center of the system. In contrast, the Hα emission may originate from anywhere in the disc. The different loci of these emissions have consequences for any potential correlation between them. Investigating such a phenomenon in this star does not require large telescopes and associated instrumentation, but does need an extended program of monitoring over many years. This is precisely the kind of program that is amenable to an amateur spectroscopic study. Thus, using data sets from long-term observation campaigns by an international consortium of amateurs over 15 years, the study presented here used equivalent width analysis to show that the emission activities of Hα and HeI 6678 are, indeed, strongly correlated.

1. Introduction

γ Cas is the prototype of the group of classical Be stars and shows emission activities in Hα and Helium at 6678 Å, originating in a circumstellar disc. A large number of fundamental and comprehensive studies on the nature of the Be star γ Cas have been carried out over the past few decades (Stee *et al.* 1998; Smith *et al.* 2012; Nemravová *et al.* 2012; Miroshnichenko *et al.* 2002; Borre *et al.* 2020), to name just a few. Therefore, at this point we deliberately refrain from describing these characteristic traits again.

γ Cas has also attracted much amateur attention (Pollmann 1997, 2009). Some prominent objects among the Be stars, such as ζ Tau, 28 Tau, δ Sco, π Aqr (to name just a few), have some certain phenomena in common, such as the quasi-periodic behavior of the equivalent width (EW) of the Hα emission and the HeI 6678 emission or absorption lines. These phenomena have been monitored in the form of long-term observations by entire groups of observers in amateur astronomy; this is especially true for the Be binary star γ Cas.

While the Hα emission of γ Cas originates in the entire volume of the Be star disk around the central star, the HeI 6678 emitting region is located much closer to the surface of the central star. In addition, the HeI 6678 emission is one of the few non-hydrogen lines in the optical spectrum that, at 1–3% of the amplitude of the neighboring continuum, is still strong enough to be analyzed well by using the neighboring continuum. Thanks to the interferometric studies by Stee *et al.* (1995, 1998) we know today (2021) the Hα-emitting regions are limited to within 18 stellar radii and those of the HeI 6678 to 2.3 stellar radii (Figure 1).

Until the 1990s, γ Cas was mainly examined spectroscopically near the Hα line. Around 1994/1995, studies were carried out by Hanuschik (1995) with the aim of finding out more about the kinematics of the circumstellar disks around Be stars. The HeI emission at 6678 Å (Figure 3) became an important diagnostic feature to investigate the regions of activity close to the star (Stee *et al.* 1998; Li *et al.* 2014).

Be stars have rotationally flattened disks (not shells, which are spherical), so matter is expelled by the star to the disk and viscosity causes the local angular momentum exchanges among particles. As a result of these exchanges some particles will gain angular momentum enough to allow them to go into orbit. Those that have lost angular momentum will fall back to the star. Phenomena resulting from these processes are observable by amateur spectrographs. Thus, the author instigated the present study, which has resulted in a very high observation density, and has led to results that are unique in amateur astronomy.

The nonphotospheric component of the HeI line can arise only from matter above the star's surface but still close enough that its HeI atoms can be influenced by the star's UV radiation field—a tighter constraint than is true for the larger region in which Hα can be influenced.

This is an essential difference from the regions of origin of the Hα emission, which is formed over the entire volume of the circumstellar star disk and generally fluctuates much more slowly over time. In the observation season 2019–2021, considerable fluctuations in the Hα EW and HeI 6678 EW were found. A growth of 1.3 Å/year of the Hα EW for the period presented here is a result of the exophotospheric material input into the Be star disk (with the HeI 6678 emission as indicator) and can be calculated from the steady increase of the Hα EW in Figure 5. In addition, both increases' progresses show a synchronous time course, with the special feature that the Hα EW minimum (November 2001) can also be found easily in the course of the HeI 6678 EW.

2. Observations

The spectra for the investigation presented here (with kind permission of the consortium members, see section 7) were obtained with 0.2-m to 0.5-m telescopes and prism spectrographs, Czerney-Turner grating spectrographs, Littrow grating spectrographs, and Echelle spectrographs, with spectral resolutions $R = \lambda/\Delta\lambda$ of 5000–25000. The spectra have been reduced with standard professional procedures (flat-field

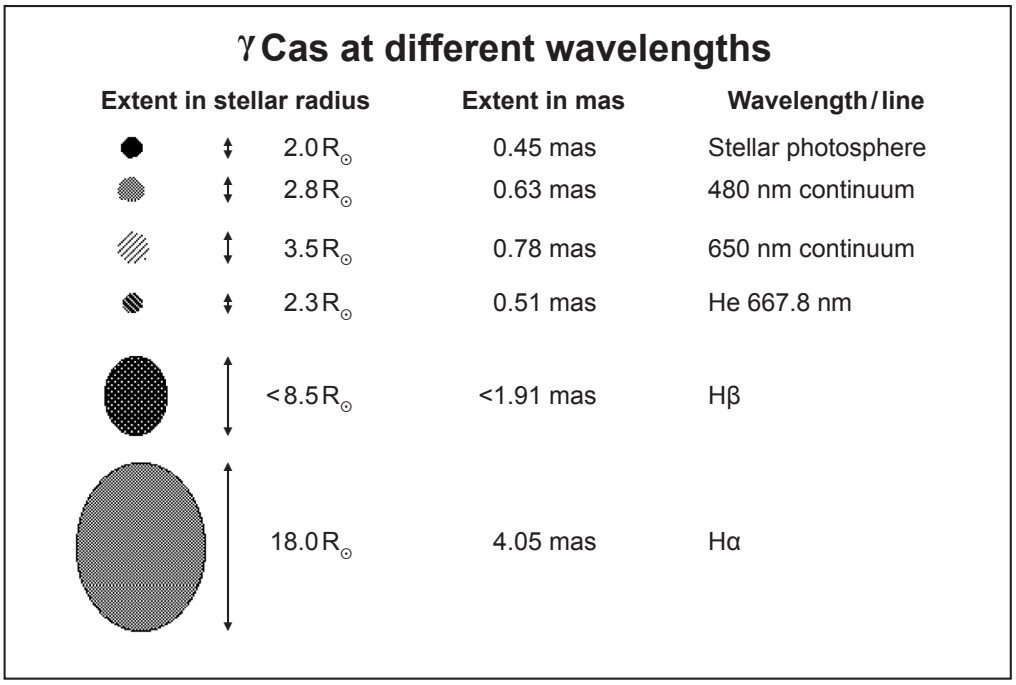

Figure 1. Schematic view of γ Cas as a function of wavelength (used with kind permission of Philippe Stee). These wavelength-dependent shapes are projections onto the sky plane, which were formed under the well founded assumption (justified) functions of envelope symmetry, flattening, and angle of inclination. In this figure the diameters are given as stellar radii. The fact that the modelled size in the HeI-line flux (in in this figure) is not larger than the visible continuum light shows that the observer cannot see HeI emission far from the star (e.g. to inner disk).

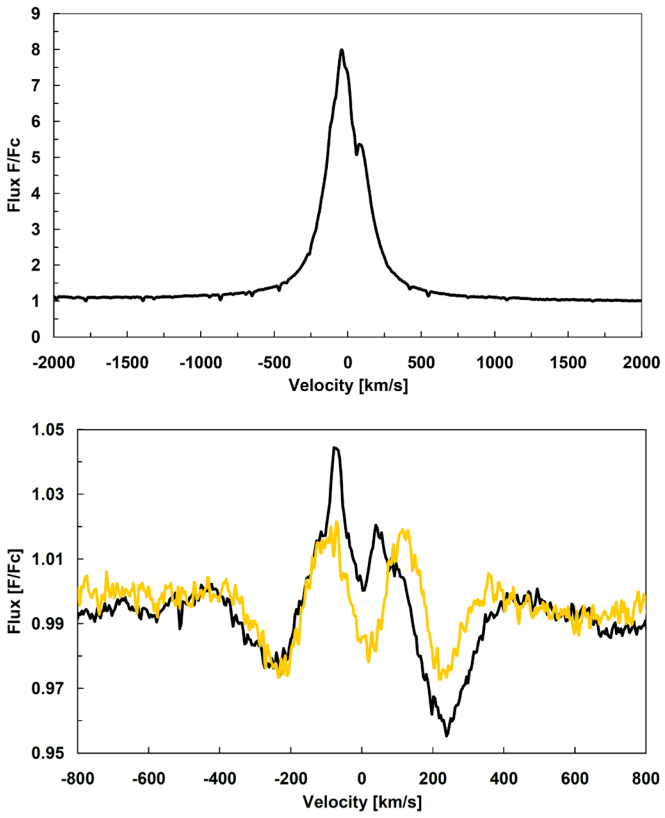

Figure 2. (top) Hα spectrum, S/N ~ 200 (2020/10/29, A. Stiewing, Arizona); (bottom) HeI6678 spectrum, S/N ~ 400 (dark line: 2020/12/10, E. Bryssinck, Belgium; light line: 2020/02/08, A. Stiewing, Arizona).

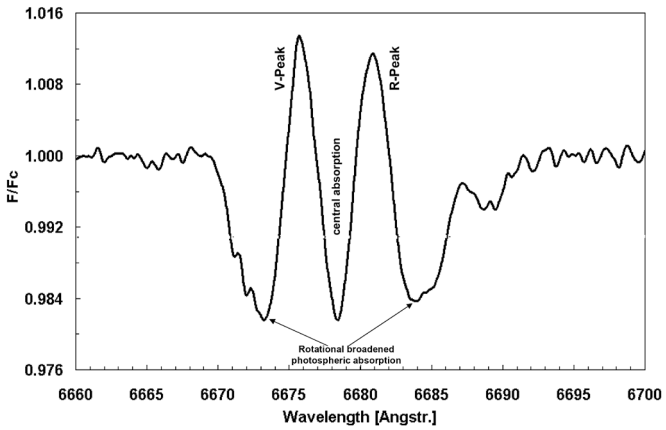

Figure 3. Characteristic features of the HeI double peak emission at 6678 Å in γ Cas.

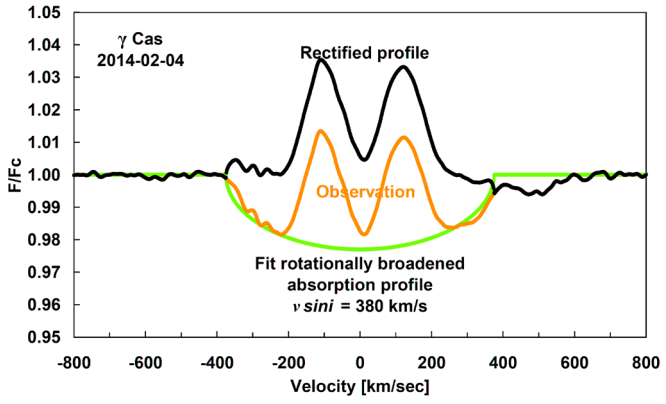

Figure 4. Subtraction of a fitted (lowest line), theoretical photospheric absorption profile with v * sin i = 380 km/s (Harmanec 2002) of the HeI double peak emission at 6678 Å in γ Cas (2014/02/04).

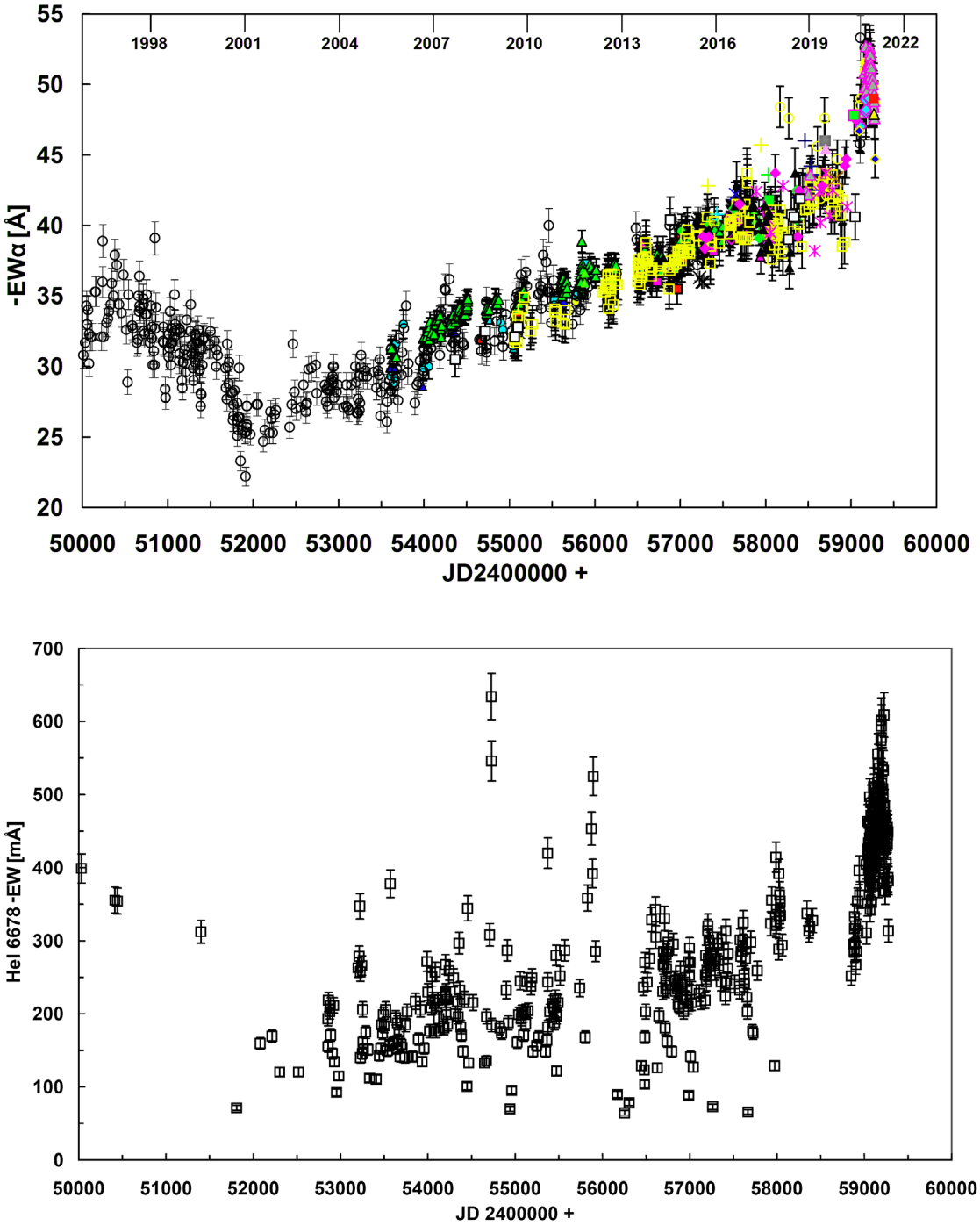

Figure 5. EW long-term monitoring of Hα (top) and HeI 6678 (bottom) by 49 observers (different color symbols) from October 1995 to November 2020.

correction, instrumental response, normalization, wavelength calibration) using the software preferred by individual observers. Typical signal/noise (S/N) of the Hα spectra was at least 100 and for HeI 6678 spectra at least 300 (mostly better). An example spectrum of Hα and HeI 6678 is shown in Figure 2.

A total of 980 spectra have been used from October 1995 to mid-January 2021, with rectification exclusively by the author in order to exclude variation of methodology across observers.

3. Equivalent width of HeI 6678

It was recognized that a time dependent mass loss from the photosphere of the primary star, density variations, and collision excitations of the HeI atoms can produce typical double peak emissions in the HeI 6678 Å line, which are due to the excitations in a range of up to about 2.3 star radii (Stee *et al.* 1998). Based on predictions of precession of disk structures, Okazaki (1991, 2000), and Berio *et al.* (1999) used interferometric modelling techniques with Hα activity to show that there is a single, radial density variation extending

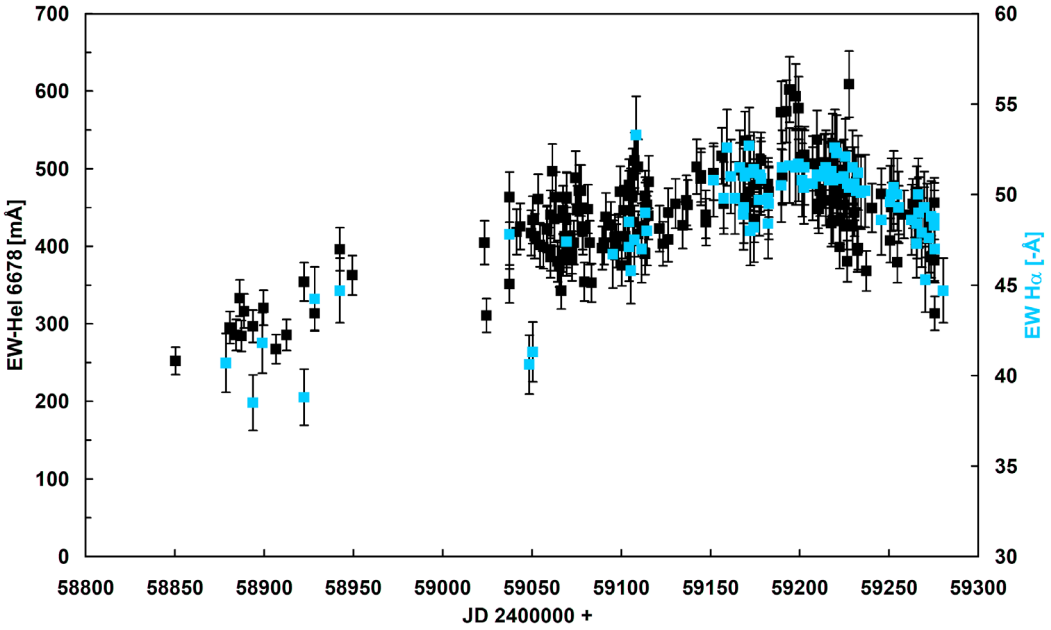

Figure 6. Particularly strong emission activity of Hα EW and HeI 6678 EW of the period after start of the intensified monitoring JD 2458850 to JD 2459321; error bars correspond to those in the text.

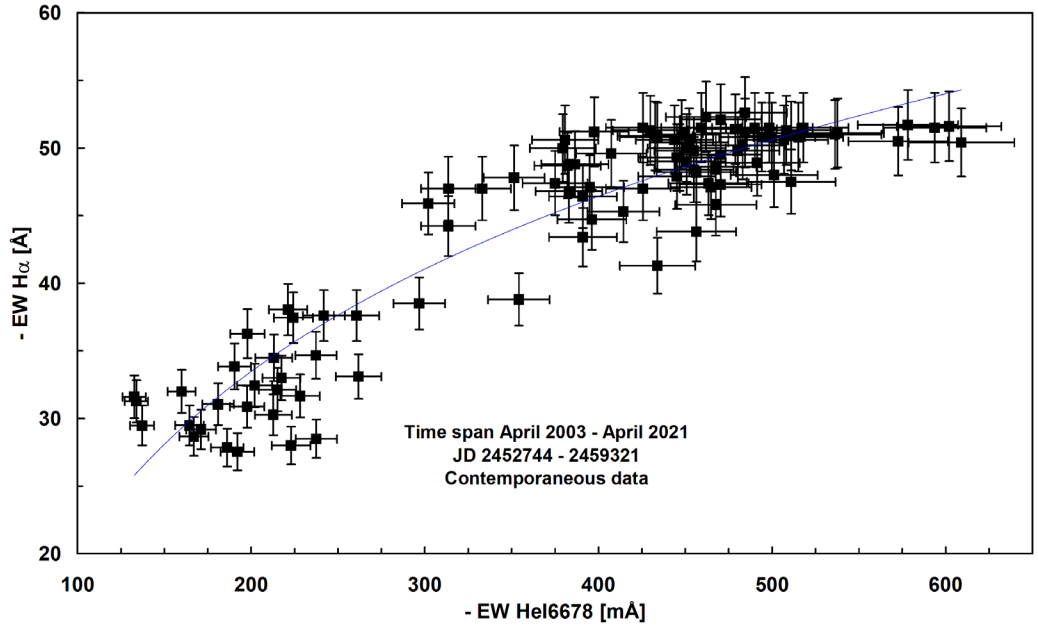

Figure 7. Clarification of the correlation of Hα EW and HeI 6678 EW; contemporaneous data of the monitoring in Figure 5. Error bars correspond to those in the text. The best-fit line is the polynomial order 2 performed with EXCEL; correlation coefficient R = 0.94! All data from Figure 7 is shown in Table 1, and will be web-archived and made available through the AAVSO *ftp site at: ftp:ftp.aavso.org/public/datasets/491-Pollmann-ewdata.txt* .

outwards from the center of the disc (a so-called "one-armed" perturbation).

Access to the shell structures in Be stars is obtained by investigating the kinematic line broadening. Stellar absorption lines in Be stars are rotationally broadened. The dimension of the half-widths (FWHM) is on the average the projected rotation velocity (v* sin i) of the Be star, where v* is the equatorial rotation velocity and (i) is the inclination of the axis in the direction of the observer (Dachs *et al.* 1986).

The total width of an emission line depends (among others) on the definition of the line wing profile and is affected by the underlying photospheric profile. In the case of a well-defined emission line, the equivalent width has to be corrected by the determination of this photospheric absorption.

The HeI 6678 profile shown in Figure 4 is a superposition of the emission line profile (produced in the star's gas disk) and the effect of the rotationally broadened photospheric absorption profile. A way to determine the effect of the rotational broadened absorption has been comprehensive described by Gray (1992) in Chapter 17. Following Dachs *et al.* (1986) and Burbidge and Burbidge (1953), we subtracted a fitted, theoretical noise-free absorption profile with v* sin i = 380 km/s (Harmanec 2002), in order to isolate the contribution of the pure emission from the constant rotationally broadened absorption. Therefore,

the corrected EW is defined as the area, normalized to the continuum intensity, between the emission line profile and that of the photospheric absorption line.

According to Chalabaev and Maillard (1983), the uncertainty of the EW determination is essentially determined by the S/N of the neighboring continuum and the flux in the spectral line. In addition, the definition of the line wings and the underlying photosphere absorption line profile (Figure 3) are important. With the equation given in Chalabaev and Maillard (1983, page 263) this results in an average error of the order of (+/–) 4–5% in practical measurements of a single observation on a given night. In this respect, this order of magnitude of the error applies to the results presented here, which were obtained with very different spectrographs (prism spectrographs, Czerney-Turner grating spectrographs, Littrow- and Echelle-spectrographs).

4. EW-results 1995–2020

The long-term monitoring presented in Figure 5 describes the period from October 1995 (JD 2450000) to January 2021 (JD 2459230). The determination of the equivalent width was carried out according the equation:

$$EW_\lambda = \int_{\lambda_1}^{\lambda_2} \frac{F_c - F_\lambda}{F_c} \, d\lambda \qquad (1)$$

with F_λ the flux at wavelength λ and F_c the continuum flux.

The EW for Hα and HeI 6678 was determined in each case in the spectral sections between 6525–6610 Å and 6670–6685 Å, with an estimated uncertainty of a single measurement in one night as mentioned above. In Figure 5 it is easy to see the steady increase in both emission contributions, although the increase in HeI 6678 shows superposed by some strong short-term fluctuations. Such fluctuations, as observed at JD 2454847–2454928 and JD 2455874–2455896, are generally associated in the HeI line spectra of active Be stars with a photospheric outburst of the Be star (e.g. Peters 1986; Smith 1989, 1995; Smith *et al.* 1997).

The rapid Hα emission increase from ~JD 2452200 onwards and the spikes in JD 2454456, JD 2455373, and JD 2455384–2455428 coincide with V brightness measurements of the APT telescope (Smith *et al.* 2012).

The apparently obvious correlation of the time courses of Hα and HeI6678 in Figures 5 and 6 is emphasized more clearly in Figure 7. This plot shows only contemporaneous EW data of Hα and HeI 6678 from spectra of the total period April 2003–April 2021 (JD 2452744–2459321).

5. Interpretation and discussion

The obvious correlation in Figures 5, 6, and 7 between the EW's of Hα and HeI 6678, generated by mass ejection from the surface of the primary star into the circumstellar disk is, however, subject to rapid fluctuations in HeI 6678, which are not directly recognizable in Hα. This is due to the fact that such a mass input is relatively small compared to the already existing massive disk and therefore may not be immediately visible. In addition, in close, interactive binaries the companion can have a strong influence on the behavior of the primary, whereas in wide systems it may be negligible. This has to be taken into account in interpretation of the behavior of the circumstellar disk. So, in that sense a question might be whether the appearance of a minimum in Hα around JD 2452000 (Figure 5, top) is related to the passage of the binary companion.

Correlation model calculations of Hα EW and UBV photometry for Be stars with increasing disk sizes of Sigut and Patel (2013) are able to explain positive and negative correlations between long-term variations in Hα EW and V brightness as observed for well known Be stars (Harmanec 1983). The very first investigation of this kind was conducted by Doazan *et al.* (1983). Their investigation shows that during and after the spectacular episode of the Be phase from 1932 to 1942, the Balmer lines and the brightness followed the same trend of variations. Pollmann *et al.* (2014) show that an increase of the Hα EW of γ Cas of ca. 10 Å observed during 15 years was accompanied by a slight magnitude increase of 0.06 mag.

6. Conclusion

The high quality of the HeI 6678 versus Hα correlation in Figures 5, 6, and 7 of better than 90% confirms among others the accuracy and practicability of the subtraction method described in section 3 of the evaluation of the HeI 6678 emission. All data from Figure 7 is shown in Table 1, and will be web-archived and made available through the AAVSO ftp site at:

ftp:ftp.aavso.org/public/datasets/491-Pollmann-ewdata.txt .

The intuitive explanation of the presented correlation is that the HeI 6678 line-forming region is contained in a much smaller volume that the region in which Hα is formed, but coincide in the inner region (Figure 1). Percentage-wise this would imply that an increase of line-emitting material within the described 2.3 stellar radii should have a much larger effect on the HeI 6678 emission as compared to the Hα emission. This is consistent with the difference in amplitude. Also, a time delay between the changes in HeI 6678 and Hα is conceivable, depending on whether the particles first emitting HeI 6678 will move outward to a larger volume. The international efforts presented here will now also be continued for other bright Be stars. In particular, projects of this kind have been initiated by Be star researchers from the University of São Paulo in collaboration with the amateur astronomical community.

7. Observer consortium

(contact address: ernst-pollmann@t-online.de)

R. Bücke, P. Fossanelli, Th. Garrel, J. Guaro, Th. Blank, P. Debreuil, St. Charbonnel, H. Kalbermatten, Ch. Netzel, E. Pollmann, Ch. Kreider, A. Wilson, E. Bertrand, O. Thizy, F. Masviel, N. Montigiani/Mannucci, M. Schwarz, B. Stober, P. Berardi, T. Lester, M. Pujol, J. Montier, J. N. Terry, L. Schanne, M. Büchner, B. Hanisch, G. Winkler, J. Guarro, P. Fosanelli, O. Garde, Th. Garrel, C. Sawicki, Th. Lemoult, Ch. Buil, P. Somogyi, J. J. Broussat, M. Keiser, S. Hess, E. Bryssinck, J. Martin, A. Stiewing, A. Maetz, Th. Daiber, Ch. Quandt, K. Alich, U. Zurmühl, D. Doctor, K. Gurney.

Table 1. Data for HeI 6678 EW and Hα EW.

HeI 6678 EW (mÅ)	*Hα EW (Å)*	*JD*	*HeI 6678 EW (mÅ)*	*Hα EW (Å)*	*JD*
223	28.0	52818.667	480	49.8	59182.199
238	28.5	53100.333	470	49.5	59182.633
192	27.5	53242.200	573	50.5	59189.598
137	29.5	53337.000	490	51.5	59190.193
167	28.7	53496.222	602	51.6	59194.198
171	29.2	53198.884	594	51.5	59197.604
165	29.5	53198.884	578	51.7	59199.221
181	31.1	53307.748	515	50.8	59201.285
186	27.9	53300.435	518	51.5	59202.630
198	30.9	53272.713	507	50.6	59207.192
213	30.3	53269.945	538	51.1	59209.655
262	33.1	53281.031	448	51.0	59210.590
217	33.0	54206.000	508	51.3	59213.633
202	32.4	53585.659	459	51.5	59214.584
215	32.1	53690.897	500	50.8	59216.588
160	32.0	53690.897	430	51.3	59217.617
134	31.3	53655.817	434	50.8	59218.598
228	31.7	53679.203	484	52.6	59219.603
133	31.6	53660.495	462	52.3	59220.594
213	34.5	53675.462	433	50.9	59222.608
198	36.3	53662.633	470	52.1	59225.584
237	34.7	53669.448	381	50.6	59226.592
190	33.9	53667.009	609	50.4	59227.609
242	37.6	53645.730	426	51.5	59229.624
261	37.6	53664.056	444	50.6	59230.599
224	37.5	53661.561	483	50.2	59231.609
221	38.0	56919.750	398	51.2	59232.599
297	38.5	58893.692	468	48.6	59245.597
354	38.8	58922.301	407	49.6	59250.621
314	44.2	58928.291	451	50.0	59251.274
396	44.7	58942.358	452	50.4	59252.602
351	47.8	59037.438	379	50.0	59254.640
434	41.3	59050.407	447	49.3	59255.294
463	47.4	59069.358	470	47.3	59265.375
465	47.1	59104.364	455	48.4	59265.645
468	45.8	59105.351	445	47.9	59268.307
511	47.5	59107.408	445	49.3	59269.610
426	47.0	59111.374	414	45.3	59270.315
451	49.0	59113.429	386	48.8	59273.597
494	50.8	59151.625	456	43.8	59275.336
455	49.8	59157.442	382	48.7	59275.340
498	51.5	59166.426	314	47.0	59275.594
491	48.9	59168.373	395	47.1	59292.609
536	51.0	59169.258	383	46.8	59293.289
501	48.0	59172.221	391	43.4	59298.286
456	48.2	59174.218	375	47.4	59299.361
479	51.4	59174.294	391	46.4	59303.292
484	51.1	59177.678	333	47.0	59303.298
511	50.9	59178.259	302	45.9	59321.314

Note: All data in Table 1 will be web-archived and made available through the AAVSO ftp site at: ftp:ftp.aavso.org/public/datasets/491-Pollmann-ewdata.txt .

8. Acknowledgements

I am very grateful to Dr. Myron Smith and Dr. K. Gurney for their critical and very helpful support in editing this paper.

References

Berio, P., *et al.* 1999, *Astron. Astrophys.*, **345**, 203.
Borre, C. C., *et al.* 2020, *Astron. Astrophys.*, **635A**, 140.
Burbidge, G. R., and Burbidge, E. M. 1953, *Astrophys. J.*, **117**, 407.
Chalaaev, A, and Maillard J. P. 1983, *Astron. Astrophys.*, **127**, 297.
Dachs, J., *et al.* 1986, *Astron. Astrophys., Suppl. Ser.*, **63**, 87.
Doazan, V., Franco, M., Rusconi, L., Sedmark, G., and Stalio, R. 1983, *Astron. Astrophys.*, **128**, 171.
Gray D. F. 1992, *The Observation and Analysis of Stellar Photospheres*, Cambridge Univ. Press, Cambridge.
Hanuschik, R. W. 1995, private communication.
Harmanec, P. 1983, *Hvar Obs. Bull.*, **7**, 55.
Harmanec, P. 2002, in *Exotic Stars as Challenges to Evolution*, ASP Conference Proceedings, eds. C. A. Tout, W. Van Hamme, ASP Confer. Series, 279, Astronomical Society of the Pacific, San Francisco, 221.
Li, H., Yan, J., Zhou, J., and Liu, Q. 2014, *Astron. J.*,**148**, 113.
Miroshnichenko, A. S., Bjorkman, K. S., and Krugov, V. D. 2002, *Publ. Astron. Soc. Pacific*, **114**, 1226.
Nemravová, J., *et al.* 2012, *Astron. Astrophys.*, **537A**, 59.
Okazaki, A. T. 1991, Publ. Astron. Soc. Japan, 43, 75.
Okazaki, A.T. 2000, in *The Be Phenomenon in Early-Type Stars*, eds. M. A. Smith, H. F. Henrichs, ASP Conf. Ser. 214, Astronomical Society of the Pacific, San Francisco, 409.
Peters, G. J. 1986, *Astrophys. J., Lett.*, **301**, L61.
Pollmann, E. 1997, *Be Star Newsl.*, **32**, 11.
Pollmann, E. 2009, *Be Star Newsl.*, **39**, 32.
Pollmann, E., Vollmann, W., and Henry, G. W. 2014, *Inf. Bull. Var. Stars*, No. 6109, 1.
Sigut, T. A. A., and Patel, P. 2013, *Astrophys. J.*, **765**, 41.
Smith, M. A. 1989, *Astrophys. J., Suppl. Ser.*, **71**, 357.
Smith, M. A. 1995, *Astrophys. J.*, **442**, 812.
Smith, M. A., Murakami, T., Ezuka, H., Anandarao, B. G., Chakraborty, A., Corcoran, M. F., and Hirata, R. 1997, *Astrophys. J.*, **481**, 467. [ADS says ApJ 481, 479]
Smith, M. A., *et al.*, 2012, *Astron. Astrophys.*, **540A**, 53.
Stee, P., de Araujo, F. X., Vakili, F., Mourard, D., Arnold, L., Bonneau, D., Morand, F., and Tallon-Bosc, I. 1995, *Astron. Astrophys.*, **300**, 219.
Stee, P., Vakili, F., Bonneau, D., and Mourard, D. 1998, *Astron. Astrophys.*, **332**, 268.

A Historical Perspective on the Diversity of Explanations for New Classes of Transient and Variable Stars

Thomas J. Maccarone
Department of Physics and Astronomy, Texas Tech University, Lubbock, TX 79409-1051; Thomas.Maccarone@ttu.edu

Received April 12, 2021; revised April 21, 2021; accepted April 21, 2021

Abstract As new classes of transients and variable stars are discovered, and theoretical models are established to work or not to work for a few members of the class, it is often the case that some researchers will make arguments on the basis of Occam's razor that all members of the class must be produced by whichever mechanism first successfully explained one of the objects. It is also frequent that this assumption will be made more implicitly. Retrospective analysis shows rather clearly that this argument fails a large fraction of the time, and in many cases, this search for false consistency has led to more fundamental astrophysical errors, a few of which are quite prominent in the history of astronomy. A corollary of this is that on numerous occasions, theoretical models to explain transients have turned out to be models that describe real—but often not yet discovered—phenomena other than the ones to which they have first been applied, albeit with minor errors that caused the model to appear to fit to a known phenomenon it did not describe. A set of examples of such events is presented here (some of which will be quite familiar to most astronomers), along with a discussion of why this phenomenon occurs, and how it may be manifesting itself at the present time. Some discussion will also be made of why and when survey designs have led to immediate separation of various transient mechanisms, generally by being overpowered in some way relative to what is needed to *detect* a new class of objects.

1. Introduction

A repeated process in the history of astronomy is that the opening of new "discovery space" will lead to the discovery of new astrophysical phenomena (see Harwit (1984) for a rather comprehensive treatment of how this process has manifested itself with the introduction of new observational capabilities). As this is done, often, classes will appear to emerge among the objects discovered. Searches for new classes of transient events in the optical bandpass have come more into fashion in recent years than they had been for several decades prior. In astronomy, as new classes of events and objects are discovered, they are ordinarily "barely" discovered—the first set of data that helps establish the new class is sufficient to establish clearly that *something* new has been found, but not to provide good diagnostics of the mechanism for productive the events or objects. In this paper, I will discuss several historical examples of this process playing itself out, and show that in many occasions, these new phenomena represent heterogeneous classes of objects. Conversely, it is also often the case that models developed for explaining one set of phenomena have minor flaws that lead to them being correct descriptions of some other phenomenon later discovered, and I will present some examples of these, as well. Finally, I will also discuss examples of cases where survey design helped identify the phenomenological differences that break the otherwise similar phenomena into two classes more easily.

2. The multiplicity of nova mechanisms

2.1. The first samples

The era of astrophotography began in the 1840s, with John Draper's successful daguerreotype of the Moon. In the late 1800s and early 1900s, largely but not entirely making use of plates, systematic studies began to be made of optical transients. It is instructive to look at an early table of what were all then called novae, containing 28 such objects mostly discovered between 1885 and 1912, but stretching back into the late 1500s (Fleming and Pickering 1912). This catalog neglects some earlier nova and supernova discoveries that have been recorded primarily by Chinese astronomers, for which the precision of the data in the historical record was deemed insufficient. This list and a few addenda represented the state of the art for thought about the nature of optical transients for quite some time. Within this rather small catalog exist supernovae of both Type Ia and Type II; classical and recurrent novae; a Mira Ceti variable; and a luminous blue variable. We present this catalog, along with current classifications for its members, in Table 1 (columns are the object name, the year of the discovery of the source, the peak apparent magnitude of the object, the class of object, and any comments that might be relevant to the objects).

Furthermore, in the year after this catalog was produced, WZ Sge was discovered. This is a very nearby dwarf nova, with a peak *apparent* magnitude similar to those of the classical novae known in the early 1900s. The original discovery paper reported that while no spectrum was obtained during the outburst, "Its sudden appearance, however, followed by a fading of brightness that was at first rapid and then more gradual, is in conformity with the typical light curve for novae" (Leavitt and Mackie 1919). Only five decades later, when its distance could be estimated based on its M-dwarf companion star, was it appreciated that its outburst was a clear clue that this was something different from that of the classical novae (Kraft 1962; Krzeminski and Kraft 1964). Other dwarf novae *had* been recognized as a different class of objects already, as U Gem showed rapid recurrence after its original discovery (Pogson 1857). (The object's discovery was first reported by J. R. Hind in a letter to *The Times* of London—see Warner (1986).) Thus at the time of the publication of Leavitt and Mackie (1919), there was a class of about 30 events which were considered to be a homogeneous set of objects by most of the leading researchers of the era, but which we know understand to have *six* separate

Table 1. The 28 "novae" from Fleming and Pickering (1912). The columns are the object name, the year of the discovery of the source, the peak apparent magnitude of the object, the class of object, and any comments that might be relevant to the objects.

Object Name	*Discovery Year*	*mV*	*Class*	*Comment*
B Cas	1572	–5	supernova	Tycho's
S And	1885	7	supernova	in M31
V Per	1887	9.2	classical nova	
N Per 1901	1901	0.0	classical nova	GK Per
T Aur	1891	4.5	classical nova	
N Gem 1903	1903	5.1	classical nova	
N Vel 1905	1905	9.7	classical nova	
RS Carinae	1895	8	classical nova	
Z Cen	1895	8	supernova	in NGC 5252
Nova Cir	1906	9.5	classical nova	typo on year in Fleming and Pickering (1912)
R Norma	1893	7	Mira Ceti variable	
T Cor B	1866	2	recurrent nova	red giant donor
T Sco	1860	7	classical nova	in globular cluster M80
Nova Ara	1910	6	classical nova	
N Oph 2	1848	5.5	classical nova	
N Oph 1	1604	–4	supernova	Kepler's
RS Oph	1898	7.7	recurrent nova	red giant donor
N Sco 2	1906	8.8	classical nova	
N Sgr 2	1910	7.5	classical nova	
N Sgr 4	1901	10.4	classical nova	
N Sgr 3	1899	8.5	classical nova	
N Sgr 1	1898	4.7	classical nova	
N Aql 2	1905	9.1	classical nova	
N Aql 1	1899	7	classical nova	
11 Vul	1670	3	classical nova	CK Vul
P Cyg	1600	3.5	luminous blue variable	
Q Cyg	1876	3	classical nova	
N Lac	1910	5	classical nova	

mechanisms: thermonuclear detonation of the entirety of a white dwarf; core collapse driven explosion of a massive star; runaway nuclear fusion on the surface of a white dwarf; pulsation of a red giant; mass ejection by a blue supergiant; and a disk instability (perhaps coupled with enhanced mass transfer of the donor star) in an accretion disk around a white dwarf.

These objects showed a broad range of similarities, within the limits of the data of the era. Where spectra could be obtained, with the exception of P Cygni (the luminous blue variable), they appeared to be spectra of gaseous nebulae (Fleming and Pickering 1912), and even P Cygni still showed the emission lines for which it is so famous. The characteristic decay times of the events were rather similar. It is thus unsurprising, especially at the dawn of systematic academic study of transient sources, that people would have put all these objects into a single class. Furthermore, it is probably desirable not to break objects up into an excessive number of subclasses until there is ample evidence to indicate that they are, indeed, caused by different phenomena.

2.2, Separation of the supernova from the novae

This growth in the size of "nova" samples took place at the dawn of extragalactic astronomy. The peak luminosities of novae were, in fact a core issue in the Shapley-Curtis debate of 1918; both participants agreed that novae had been seen in the spiral nebulae, with Shapley arguing that the novae would have to be perversely bright for S And (now known as SN 1885, in M31) to be a nova if the spiral nebulae were island universes. Curtis, on the other hand, presciently argued that S And might be a member of a different class of objects (a few years before the first really serious work on the topic was done (Lundmark 1923), and that Tycho's nova was anomalously bright as well, and might be due to that same alternative mechanism (Trimble 1995).

In relatively short order this question was resolved by Hubble's discovery of Cepheids in nearby galaxies. The Cepheids clearly established the spiral nebulae to be at ~Mpc distance scales, and hence that there was a class of nova dramatically brighter than the classical novae. It also became clear that the large majority of nova events in M31 had luminosities compatible with those of bulk of the Galactic novae, while S And was about 11 magnitudes brighter than the rest, and for more distant galaxies, it also became clear that a few of their novae were excessively bright given their distances (Lundmark 1923). The term supernova was coined, and gradually, it became clear that this was a broad class of rare, bright objects with durations and light curve shapes not dramatically different from those of classical novae with the quality of light curves available in the early 20th century (Baade and Zwicky 1934; Baade 1938). Notably, the same phenomenon occurred with the Cepheids, in the sense that the original scale of the Universe proposed by Hubble (1929) was incorrect due to the assumption that all Cepheids were the same, an assumption not rectified for quite some time (Baade 1944).

2.3. Multiple mechanisms for supernovae

The separation of the supernovae from the classical novae was eventually done in a straightforward manner using

extragalactic events. About two decades after the first well-developed suggestion (Lundmark 1923) that the novae and supernovae were separate classes of objects, Minkowski (1941) showed that there appeared to be two separate classes of *supernovae*, based on their spectral dichotomy, with the Type II supernovae showing strong hydrogen lines, and the Type I showing no really strong spectral features in early data. The Type Ib supernovae, which are core collapse supernovae from Wolf-Rayet stars (i.e. stars without hydrogen envelopes), were identified as peculiar Type I supernovae long after the Type I/Type II dichotomy was established but near the infancy of the development of serious theoretical models for supernovae (Wheeler and Levreault 1985).

When the first distinct ideas for the two mechanisms were proposed (Hoyle and Fowler 1960), a paper which got the basic ideas for both models correct, but ironically, given the authors' fame for understanding cosmic nucleosynthesis, suggested that the Type II supernovae mostly produce iron, while the Type Is mostly produce alpha elements. Only a quarter century later was it widely understood that the phenomenological boundary between Type I and Type II supernovae, in the absence or presence, respectively, of hydrogen lines, was not perfectly correlated with the explosion mechanism, and that the peculiar Type I supernovae (which we now call Type Ib and Type Ic) are core collapse supernovae from stripped stars (Wheeler and Levreault 1985).

2.4. Multiple mechanisms for dwarf novae

Over time, mostly in the 1940s and 1950s, it was also realized that a subset of accreting white dwarfs showed "dwarf novae" that were about 100,000 times fainter (M_V typically around +5 (Warner 1987)) than the classical novae (absolute magnitudes of about $M_V = -8$ (Duerbeck 1981)). For the dwarf novae, in which there are relatively sudden and extreme changes in the mass transfer rates through accretion disks around white dwarfs, there is also a breadth of phenomenology, with some attempts to explain things via a single mechanism. The dwarf novae may be produced either by some instability in the accretion disk due to changes in the ionization state of the dominant species, usually hydrogen (Meyer and Meyer-Hofmeister 1981; Smak 1984), or variations in the mass transfer rate into the accretion disk (Osaki 1970). (In the case of ultracompact binaries, helium, or in some ultracompact X-ray binaries, carbon and oxygen may be the dominant species.)

For quite some time it has been clear that the ionization instability mechanism is important. The evidence for this is particularly clear from the low mass X-ray binaries (i.e. black holes or neutron stars accreting from low mass donor stars), in which a clear demarcation is seen in a plot of mean accretion rate versus orbital period, and the systems predicted to be persistent in the disk instability model are, in fact, persistent (Lasota 2001).

Still, this does not exclude the idea that some outburst phenomenology may be driven by mass transfer variations. The new generation of optical variability surveys have started to find relatively clear evidence that some of the outbursts of accreting white dwarfs cannot be explained purely by disk instabilities. In Rivera Sandoval *et al.* (2020), SDSS J113732+405458, a double white dwarf binary with an orbital period of about 60 minutes, showed a year-long outburst. Not only is this timescale is longer than the viscous timescale for mass to flow through such a short period system's accretion disk, but also, the system became *redder* during the outburst, and maintained colors too red for the helium in the disk to be ionized, and the outburst was subluminous relative to standard dwarf novae, even for its short orbital period.

3. Gamma-ray bursts

The cosmic gamma-ray bursts represent another example of a class of object first believed to be homogeneous, but later broken into at least three separate classes with fundamentally different mechanisms (magnetar outbursts, neutron star mergers, and fireballs produced during core collapse supernovae). Interestingly, in her historical article about the first "Great Debate," the Shapley-Curtis debate, Trimble (1995) noted a point of analogy to the then contemporary debate (celebrated on the Diamond Jubilee of the original) on the origin of gamma-ray bursts. She pointed out that in 1995, there were suggestions being made that the gamma-ray bursts might be made up of two separate populations, as had been the case for the novae in Curtis' arguments in the original "Great Debate." (This was already long after the soft gamma repeaters had been identified as likely coming from a separate mechanism, due to their (as the name suggests) softer emission and repeated bursts, as well as the fact that the known objects are all either in the Galactic Plane or the Magellanic Clouds, indicating that they are produced by relatively nearby phenomena associated with massive stars.)

Still, for the broader class of gamma-ray bursts, the ones at cosmological distances, substantial numbers of members of both classes had been observed before it was widely recognized that they were from two separate populations (Kouveliotou *et al.* 1993). The gamma-ray bursts were first reported in 1973, after having been detected by the Vela satellites from 1969 to 1972 (Klebesadel *et al.* 1973).. It was understood relatively quickly that the bursts occur with quite a large range on characteristic timescales, and suggestions existed that the distribution of timescales might be bimodal (Norris *et al.* 1984), and it was well established that the bursts were isotropically and uniformly distributed (Hartmann and Blumenthal 1989). Furthermore, claims of cyclotron lines and annihilation lines in the spectra of GRBs argued for highly magnetized neutron stars at modest redshift as a mechanism (Mazets *et al.* 1982; Murakami *et al.* 1988).

The isotropy led to a preference for extragalactic models, but the lines led to a preference for Galactic models, as the locations of the annihilation lines would be shifted in the event that the bursts were at cosmological distances. Over time, skepticism grew about the observations themselves, in part because the detections of lines were not found to be repeatable with BATSE (Palmer *et al.* 1994). For quite some time, though, the prevailing view was that the GRBs were Galactic sources, and this was partly driven by the putative spectral lines, along with concerns that, at cosmological distances, rampant pair production would prevent the spectra from appearing as they are (a problem solved by the strong beaming in these systems).

This combination of preference for Galactic neutron star models and the need to reproduce an isotropic sky distribution led to a variety of "super-halo" models that managed to reproduce the isotropy via placing the GRBs in a large halo around the Milky Way, invoking neutron star kicks to do it (e.g. Lamb 1995). There were, on the other hand, some researchers who pushed for the cosmological nature of the gamma-ray bursts, but again, in an effort to unify what should not have been unified, it was suggested that the soft gamma-ray repeaters might be lensed versions of the same phenomenon as the non-repeating GRBs (Paczynski 1986).

4. General properties of new transient searches

In most cases where a new window has been opened on the transient Universe, whether due to the use of a new waveband of electromagnetic radiation, new depth of sensitivity, or new cadence of observations, *some* new class of events has been discovered, with the exceptions being in TeV gamma-ray astronomy and sub-100 MHz radio astronomy. Most of the time, when new capabilities are opened up, the increase in sensitivity is such that new phenomena can be discovered, but not necessarily well-characterized. In transient searches, the cadence and duration of the survey, along with the sensitivity, will necessarily make new classes of objects look rather similar to one another unless there has been a dramatic expansion of the capabilities in detecting transients in *multiple* dimensions (from among, for example, depth, solid angle, cadence, duration of the survey, set of wavebands); it is usually the case that only one dimension of discovery space is dramatically improved, and hence new surveys typically will discover new classes of objects that look relatively similar to one another; events which are very different from these will either be "too easy"' to detect (and hence will already have been discovered in past surveys) or "too hard"' to detect (and hence not appear at all, or at least appear so infrequently as not to be recognized as a class).

Now, we can ask what the consequences are of the facts both that (1) these new surveys are typically successful, and (2) the characteristics of the transient events will necessarily be similar in most surveys. It would be rather unlikely for a new region of discovery space to contain exactly a single class of event most of the time, unless physics prohibits any other mechanism from working in that corner of parameter space. Where there is a substantial new class of objects, then, it is *more likely* to be heterogeneous than to be homogeneous, especially if there exist several viable theoretical models for producing the sources. If homogeneous new classes were the norm, it would follow that a lot of new projects would fail to discover anything unexpected.

4.1. Occam's Blender and the heterogeneity of explanations

This conclusion can be troubling to people brought up with the idea that Occam's razor suggests that invoking two or more models to explain what appears to be a single phenomenon is fundamentally incorrect. Still, the key qualification is that often, with relatively sparse data sets at the advent of the discovery of a new broad class of objects or events, there is often not sufficient data richness to distinguish among subclasses, and there is even less frequently sufficient data quality to identify the feature that can, in hindsight, be used to separate the objects. In this situation, which frequently arises in astronomy, the most natural explanation for a new class of objects is that it is inhomogeneous; we propose adopting the term Occam's Blender for this concept. (This term was coined by Prof. Dennis Ugolini at Trinity University after the author asked some friends and colleagues for suggestions of how to describe the situation.)

A related phenomenon is that there are often ideas developed for, or incorrectly applied to, one astronomical phenomenon that re-appear to explain another phenomenon at a later time. A classic example of this is the idea of supernova shock breakouts (Colgate 1968, 1974). This idea was proposed as a purely theoretical prediction, invoked as a gamma-ray burst model (Colgate 1974), and then rejected in the era of GRB afterglows. It resurfaced when the actual shock breakouts, in the X-ray band, were discovered from supernovae (Soderberg *et al.* 2008.

Similarly, Woosley and Taam (1976) proposed runway thermonuclear burning on the surface of a neutron star as a mechanism for the gamma-ray bursts. The phenomenon is now known to occur in Nature, but to produce Type I *X-ray* bursts, as the envelopes in which this material is burning are optically thick and convert the gamma-rays produced by the nuclear interactions into larger numbers of X-rays on the way out. The Type I X-ray bursts had been discovered at the time of Woosley and Taam (1976), in a paper by Belian *et al.* (1972), but the original interpretation was that the burst was a precursor to the outburst of Cen X-4; in hindsight, it is now clear that the outburst started a few days before the Vela 5B satellite could detect it, and during the early phase of the outburst, enough matter was accreted to trigger a thermonuclear burst. Discoveries of additional Type I bursts (Grindlay *et al.* 1976; Belian *et al.* 1976) came a few months before the paper by Woosley and Taam (1976) was published. Interestingly, if it had been realized immediately that the event discovered by Belian *et al.* (1972) was from the same class as the events discovered by Grindlay *et al.* (1976), it may have led to a more immediate adoption of the nuclear fusion model; the alternative of model of scattering in a cloud of hot gas around an intermediate mass black hole Grindlay and Gursky (1976) relied on the idea that these events had seemed to occur only in globular clusters. Regardless of the early (and understandable) confusion, it was still the case that by the late 1970s/early1980s, numerous papers were written discussing the nuclear burning model in great detail (e.g. Joss 1978; Taam 1980), while very little further discussion was given to the intermediate mass black hole idea.

Retrospective examination of the gamma-ray burst models also indicates that one shouldn't get carried away and assume that all theoretical work is correct just because a few of the GRB models turned out later to be relevant for other phenomena (or similarly, because there is now evidence that both of the mechanisms first proposed for dwarf nova outbursts do, sometimes, work). It is also clear from the old literature that not every seemingly viable model for a phenomenon actually happens with substantial frequency—e.g. there is, with the benefit of hindsight, no reason to believe that gamma-ray bursts represent interstellar nuclear warfare nor Oort Cloud anti-matter comets nor many of the other less exotic, but still incorrect GRB

models (see Nemiroff (1994) for a rather extensive tabulation of models some of which are more likely than others eventually to be connected to rarer classes of astrophysical transients).

5. The present and the future

Over the past few decades, a wide variety of new classes of objects have been discovered (or have seen samples grow in size from a few oddball objects to a real class of objects). Other debates started many decades ago have remained unresolved (e.g. whether the Type Ia supernovae are produced via a single or double degenerate channel, and whether the single degenerate channel can include garden variety cataclysmic variables or only symbiotic stars with persistent supersoft emission). For the open questions, where there are multiple viable models that do not yet make any robustly testable distinct predictions, it is likely that more than one of them will turn out to be correct in many cases. This has been seen with some of the more recent newly discovered classes of objects, and remains to be determined for others.

5.1. New heterogeneous classes

Ultraluminous X-ray sources are objects not associated with the nuclei of giant galaxies and which have X-ray luminosities greater than 10^{39} erg/sec. In recent years, a few of these have shown X-ray pulsations, indicative of a hyperaccreting, highly magnetized neutron star (Bachetti *et al.* 2014). Still, there are several such objects which have properties that are problematic for the idea that *all* ULXs are accreting high magnetic field neutron stars. In particular, some of the ULXs are known to be associated with globular clusters, where high magnetic fields are very unlikely (e.g. Maccarone *et al.* 2007; Dage *et al.* 2019), while another prominent object shows state transitions and variable radio emission, characteristic of a scaled-up stellar mass black hole (Webb *et al.* 2012). The ULXs are highly likely to represent a mixture of accreting high magnetic field neutron stars and accreting black holes of both stellar and intermediate mass.

At the other end of the luminosity range, the very faint X-ray transients (Muno *et al.* 2005; Degenaar and Wijnands 2009) also represent a class of objects that was quickly established to be heterogeneous after its discovery. These are X-ray transients that are bright enough that they are highly likely to be predominantly black hole or neutron star accretors, but faint enough that they do not trigger all-sky monitors unless they are very nearby. They are likely to represent the bulk of X-ray binaries, given their relatively large numbers in the small patches of the sky in which careful searches have been made. The early discovery that one of the objects was eclipsing (Muno *et al.* 2005), along with the long-established knowledge that eclipsing X-ray binaries are underluminous, because only a component scattered in the disk wind is seen, helped set the stage for the idea that this was a heterogeneous class of objects. Now, as more of these objects have been identified, it is very clear that they are quite a mixed class, including some foreground accreting white dwarfs among them (Shaw *et al.* 2020).

5.2. New mysteries that are likely to be heterogeneous

Some other unsolved mysteries include the mechanisms for producing fast radio bursts, and the channels by which the double black hole mergers seen in LIGO data are produced. The historical evidence suggests that the use of the plural in the preceding sentence is appropriate—these are probably both heterogeneous. For the fast radio bursts, dozens of theoretical models have been proposed (https://frbtheorycat.org/index.php/Main_Page). It would be surprising if only one of them is valid. Furthermore, there are already FRBs which repeat frequently, and those that either do not repeat or repeat only infrequently. All that is known, fundamentally, about the FRBs as a class (as opposed to the relatively small subset that has been localized) is that they are extragalactic and produce fast, short bursts of radio emission, and that their discovery has been enabled in part by new hardware, and in part by people undertaking the computational effort to search for single pulses over a wide range of dispersion measures in large data sets (Lorimer *et al.* 2007).

For the gravitational wave sources, it is about as clear as anything astrophysical can be *what* they are, as the discovery data themselves give precise information on the final states of the systems; what is more uncertain is how they formed. Indeed, in recent years, four major hypotheses have been developed: standard binary stellar evolution (e.g. Belczynski *et al.* 2016); chemically homogeneous binary stellar evolution (e.g. de Mink and Mandel 2016); dynamical formation in globular clusters (e.g. Rodriguez *et al.* 2016); and formation in the accretion disks of active galactic nuclei (e.g. McKernan *et al.* 2018). At the present time, some aspects of some of the sources' data are challenging to some of the models. For example, chemically homogeneous evolution is likely to produce large spins, and at least some of the detected sources appear to have small spins; this does not exclude the idea that the chemically homogeneous evolution channel may produce some substantial fraction of the events. Fortunately, there is a growing acknowledgment of the idea that heterogeneity of explanations is likely even in papers that argue that it is possible for one of the models to explain everything (e.g. Rodriguez *et al.* 2021).

5.3. Avoiding this problem in the future?

Ideally, one wants to set up the discovery process in a manner that allows immediate separation of different classes of transients. In some cases the discovery data lend themselves to a clean and correct interpretation almost immediately, while for other phenomena, the root cause has remained elusive for a much longer period of time—see Trimble (2006) for a discussion of a large set of examples of the range of timescales from discovery to understanding in astronomy.

In some of the most fortunate cases (like the discovery of radio pulsars) the manner in which the discovery data were collected led in a relatively straightforward manner to the interpretation (Hewish *et al.* 1968). Still, it could have easily gone wrong; if we imagine a world in which Jocelyn Bell had not looked so closely at the strip charts reading her data, the pulsars might first have been recognized as a separate class of objects not via their rapid periodic variability, but via their radio spectra, which are much steeper than most, but not all, other radio sources. The availability of time resolution in the data well beyond what was required for the initial goals of the project—

detecting scintillation due to the interstellar medium—paved the way for the discovery and nearly immediate interpretation of the pulsars. The soft gamma-ray repeaters, as the name suggests, were quickly distinguished from other gamma-ray bursts because of their repetition, and, to some extent, their softer spectra. Similarly, when a second class of *X-ray* bursts, imaginatively named Type II X-ray bursts, was discovered in the "Rapid Burster," it was immediately recognized as something qualitatively different (Lewin *et al.* 1976), and this quickly led to the still-favored interpretation of magnetic gating of the accretion flow.

These examples above are all cases where the discovery data set was "overpowered" relative to what was needed to notice the phenomenon. Pulsars would have been found to scintillate, and to have unusual radio spectra, even without the high time resolution of the strip chart data. The fact that the data recording method had time resolution far in excess of what was needed for the project's aims, coupled with a particularly alert graduate student working on the project, led to the discovery of pulsars. For high energy observations, there can be extremely rapid, extremely high amplitude phenomena coupled with nearly continuous coverage of the whole sky. In these cases, durations of observations far exceed what is needed to make the discoveries. In more recent years, the Palomar Transient Factory project, by aiming for wide and shallow observations, so that the imaging does not overshoot the capability for doing spectroscopic follow-up, has generally been very successful at identifying new classes of transients, even when their light curves are relatively similar (e.g. Kasliwal *et al.* 2012). *Swift* represents another project for which the set of instruments was well designed, such that new classes of transients could be immediately identified.

This is notably *not* the case for the Vera Rubin Observatory's Legacy Survey of Space and Time—its detection limits will dramatically overshoot the resources available for spectroscopic follow-up at those fluxes, and its light curves, except in a few drilling fields, will be sampled with quite a low duty cycle, and in relatively few filters. Some potential exists to improve the discovery space if the LSST data are supplemented with e.g. strong time domain capabilities at radio and X-ray bands. Still it is *very* likely that the early stages of LSST will yield new classes of transients which are hard to follow up, and where multiple distinct mechanisms for producing the transients have rather similar observational appearances.

This should be borne in mind ahead of the survey's commencement in two ways. First, researchers should be aware that the new classes are likely to be heterogeneous. Secondly, complimentary facilities to characterize these transients based on their multiwavelength behavior (e.g. at radio and at high energies) should be supported.

6. Acknowledgements

I thank Chris Fryer, Nathalie Degenaar, Jean in't Zand, Rudy Wijnands, Aarran Shaw, Craig Heinke, Liliana Rivera Sandoval, Kristen Dage, Željka Bošnjak, and Selma de Mink for enlightening discussions, some directly motivated by this paper, and some tangential to it, that helped foment the ideas in this paper and motivate its writing. I also thank the referee for comments which improved the paper.

References

Baade, W. 1938, *Astrophys. J.*, **88**, 285.
Baade, W. 1944, *Astrophys. J.*, **100**, 137 (doi:10.1086/144650).
Baade, W., and Zwicky, F. 1934, *Proc. Natl. Acad. Sci.*, **20**, 254.
Bachetti, M., *et al.* 2014, *Nature*, **514**, 202. (doi:10.1038/nature13791).
Belczynski, K., Repetto, S., Holz, D. E., O'Shaughnessy, R., Bulik, T., Berti, E., Fryer, C., and Dominik, M. 2016, *Astrophys. J.*, **819**, 108 (doi:10.3847/0004-637X/819/2/108).
Belian, R. D., Conner, J. P., and Evans, W. D. 1972, *Astrophys. J., Lett.*, **171**, L87 (doi:10.1086/180874).
Belian, R. D., Conner, J. P., and Evans, W. D. 1976, *Astrophys. J., Lett.*, **206**, L135 (doi:10.1086/182151).
Colgate, S. A. 1968, *Can. J. Phys., Suppl.*, **46**, 476 (doi:10.1139/p68-274).
Colgate, S. A. 1974, *Astrophys. J.*, **187**, 333 (doi:10.1086/152632).
Dage, K. C., Zepf, S. E., Peacock, M. B., Bahramian, A., Noroozi, O., Kundu, A., and Maccarone, T. J. 2019, *Mon. Not. Roy. Astron. Soc.*, **485**, 1694.
de Mink, S. E., and Mandel, I. 2016, *Mon. Not. Roy. Astron. Soc.*, **460**, 3545 (doi:10.1093/mnras/stw1219).
Degenaar, N., and Wijnands, R. 2009, *Astron. Astrophys.*, **495**, 547 (doi:10.1051/0004-6361:200810654).
Duerbeck, H. W. 1981, *Publ. Astron. Soc. Pacific*, **93**, 165 (doi:10.1086/130799).
Hewish, A., Bell, S. J., Pilkington, J. D. H., Scott, P. F., and Collins, R. A. 1968, *Nature*, **217**, 709 (doi:10.1038/217709a0).
Fleming, W. P. S., and Pickering, E. C. 1912, *Ann. Harvard Coll. Obs.*, **56**, 165.
Hoyle, F., and Fowler, W. A. 1960, *Astrophys. J.*, **132**, 565 (doi:10.1086/146963).
Grindlay, J., and Gursky, H. 1976, *Astrophys. J., Lett.*, **205**, L131 (doi:10.1086/182106).
Grindlay, J., Gursky, H., Schnopper, H., Parsignault, D. R., Heise, J., Brinkman, A. C., and Schrijver, J. 1976, *Astrophys. J., Lett.*, **205**, L127 (doi:10.1086/182105).
Hartmann, D., and Blumenthal, G. R. 1989, *Astrophys. J.*, **342**, 521 (doi:10.1086/167611).
Harwit M. 1984, *Cosmic Discovery*, The MIT Press, Cambridge, MA.
Hubble, E. 1929, *Proc. Natl. Acad. Sci.*, **15**, 168 (doi:10.1073/pnas.15.3.168).
Joss, P. C. 1978, *Astrophys. J., Lett.*, **225**, L123 (doi:10.1086/182808).
Kasliwal, M. M., *et al.* 2012, *Astrophys. J.*, 755, 161 (doi:10.1088/0004-637X/755/2/161).
Klebesadel, R. W., Strong, I. B., and Olson, R. A. 1973, *Astrophys. J., Lett.*, **182**, L85 (doi:10.1086/181225).
Kouveliotou, C., Meegan, C. A., Fishman, G. J., Bhat, N. P., Briggs, M. S., Koshut, T. M., Paciesas, W. S., and Pendleton, G. N. 1993, *Astrophys. J., Lett.*, **413**, L101 (doi:10.1086/186969).

Kraft, R. P. 1962, *Astrophys. J.*, **135**, 408 (doi:10.1086/147280).
Krzeminski, W., and Kraft, R. P. 1964, *Astrophys. J.*, **140**, 921.
Lamb, D. Q. 1995, *Publ. Astron. Soc. Pacific*, **107**, 1152 (doi:10.1086/133673).
Lasota, J.-P. 2001, in *Black Holes in Binaries and Galactic Nuclei: Diagnostics, Demography and Formation*, eds. L. Kaper, E. P. J. van den Heuvel, P. A. Woudt, Springer-Verlag, Berlin, 149 (doi:10.1007/1072099527).
Leavitt, H. S., and Mackie, J. C. 1919, *Circ. Harvard Coll. Obs.*, No. 219, 1.
Lewin, W. H. G., *et al.* 1976, *Astrophys. J., Lett.*, **207**, L95 (doi:10.1086/182188).
Lorimer, D. R., Bailes, M., McLaughlin, M. A., Narkevic, D. J., and Crawford, F. 2007, *Science*, **318**, 777 (doi:10.1126/science.1147532).
Lundmark, K. 1923, *Publ. Astron. Soc. Pacific*, **35**, 95 (doi:10.1086/123277).
Maccarone, T. J., Kundu, A., Zepf, S. E., and Rhode, K. L. 2007, *Nature*, **445**, 183 (doi:10.1038/nature05434).
Mazets, E. P., *et al.* 1982, *Astrophys. Space Sci.*, **82**, 261 (doi:10.1007/BF00651438).
McKernan, B., *et al.* 2018, *Astrophys. J.*, **866**, 66 (doi:10.3847/1538-4357/aadae5).
Meyer, F., and Meyer-Hofmeister, E. 1981, *Astron. Astrophys.*, **104**, L10.
Minkowski, R. 1941, *Publ. Astron. Soc. Pacific*, **53**, 224 (doi:10.1086/125315).
Muno, M. P., Lu, J. R., Baganoff, F. K., Brandt, W. N., Garmire, G. P., Ghez, A. M., Hornstein, S. D., and Morris, M. R. 2005, *Astrophys. J.*, **633**, 228 (doi:10.1086/444586).
Murakami, T., Fujii, M., Hayashida, K., Itoh, M., and Nishimura, J. 1988, *Nature*, **335**, 234 (doi:10.1038/335234a0).
Nemiroff, R. J. 1994, *Comments Astrophys.*, **17**, 189.
Norris, J. P., Cline, T. L., Desai, U. D., and Teegarden, B. J. 1984, *Nature*, **308**, 434 (doi:10.1038/308434a0).
Osaki, Y. 1970, *Astrophys. J.*, **162**, 621 (doi:10.1086/150694).
Paczynski, B. 1986, *Astrophys. J., Lett.*, **308**, L43 (doi:10.1086/184740).
Palmer, D. M., *et al.* 1994, *Astrophys. J., Lett.*, **433**, L77 (doi:10.1086/187552).
Pogson, N. 1857, *Mon. Not. Roy. Astron. Soc.*, **17**, 200.
Rivera Sandoval, L. E., Maccarone, T. J., Cavecchi, Y., Britt, C., and Zurek, D. 2020, arXiv:2012.10356.
Rodriguez, C. L., Chatterjee, S., and Rasio, F. A. 2016, *Phys. Rev. D*, **93**, 084029 (doi:10.1103/PhysRevD.93.084029).
Rodriguez, C. L., Kremer, K., Chatterjee, S., Fragione, G., Loeb, A., Rasio, F. A., Weatherford, N. C., and Ye, C. S. 2021, *Res. Notes Amer. Astron. Soc.*, **5**, 19 (doi:10.3847/2515-5172/abdf54).
Shaw, A. W., *et al.* 2020, *Mon. Not. Roy. Astron. Soc.*, **492**, 4344 (doi:10.1093/mnras/staa105).
Smak, J. 1984, *Acta Astron.*, **34**, 161.
Soderberg, A. M., *et al.* 2008, *Nature*, **453**, 469 (doi:10.1038/nature06997).
Taam, R. E. 1980, *Astrophys. J.*, **241**, 358 (doi:10.1086/158348).
Trimble, V. 1995, *Publ. Astron. Soc. Pacific*, **107**, 1133.
Trimble, V. 2006, in *Gamma-Ray Bursts in the Swift Era*, AIP Conf. Proc. 836, AIP Publishing, Melville, NY, 3 (doi:10.1063/1.2207851).
Warner, B. 1986, *Mon. Notes Astron. Soc. S. Afr.*, **45**, 117.
Warner, B. 1987, *Mon. Not. Roy. Astron. Soc.*, **227**, 23 (doi:10.1093/mnras/227.1.23).
Webb, N., *et al.* 2012, *Science*, **337**, 554 (doi:10.1126/science.1222779).
Wheeler, J. C., and Levreault, R. 1985, *Astrophys. J., Lett.*, **294**, L17 (doi:10.1086/184500).
Woosley, S. E., and Taam, R. E. 1976, *Nature*, **263**, 101 (doi:10.1038/263101a0).

Transits, Spots, and Eclipses: The Sun's Unique Role in Outreach

Kristine Larsen
Central Connecticut State University, 1615 Stanley Street, New Britain, CT 06053; larsen@ccsu.edu

Received April 5, 2021; revised April 26, 2021; accepted April 28, 2021

Abstract The author shares her experiences exploiting the sun in the service of outreach, and encourages AAVSO observers to take advantage of the sun's ongoing reawakening from the minimum of its activity cycle to engage in both solar observing and solar-based outreach.

1. Introduction: our variable sun

Our sun is considered a variable star, showing variations in two distinct ways. First, as viewed from Earth, Mercury and Venus occasionally transit in front of the sun. The most recent opportunity was a transit of Mercury on November 11, 2019. At Central Connecticut State University (CCSU)'s Copernican Planetarium we projected a NASA live feed of the event onto the dome while a telescope with a solar filter was set up on the roof for in-person viewing (Figure 1). Anyone alive today who hasn't viewed a transit of Venus needs to have themselves cryogenically frozen, or build a time machine, because there's not going to be another opportunity until 2117. Transits of Mercury happen about every decade or so, with the next on tap for November 2032. But transits of Venus are far rarer and clustered in pairs eight years apart, with the last tandem occurring in 2004 and 2012.

Fortunately for short-lived human observers, our sun is also a variable star in the sense that it has an ever-changing number of sunspots, areas of intense magnetic activity that appear darker than the average surface (the photosphere) because they are cooler and hence less luminous. There are also hotter and thus brighter than average areas called faculae. While one might expect the brighter and dimmer areas to cancel each other out, in the case of stars similar to our sun the brighter areas tend to dominate on average, except when large sunspots are visible (Kopp *et al.* 2016). Therefore, as counter-intuitive as it might seem, the overall brightness of the sun measured over the electromagnetic spectrum (or total solar irradiance) is generally about 0.1% higher when sunspot activity is at its maximum versus where it is now, coming out of minimum, because higher sunspot activity correlates with higher amounts of faculae and other forms of energetic activity.

Figure 1. CCSU students observing the November 22, 2019, transit of Mercury.

The AAVSO is dedicated to the careful observation of stellar variability in all its forms, including that due to transits and spots. The AAVSO Exoplanet Section (https://www.aavso.org/exoplanet-section) not only provides a target list of confirmed exoplanets that are observable through standard amateur equipment, but also offers a CHOICE online course on Exoplanet Observing. More exciting is the role of AAVSO observers in the TESS (Transiting Exoplanet Survey Satellite) Follow-up Observing Program (TFOP), where amateur astronomers can play a significant role in weeding out false-positives. While there is no AAVSO observing section generally devoted to the study of spotted stars, observers have contributed observations of a number of such stars to the AAVSO International Database, for example CT Vir, MS Ser, and AX CrB. Since these stars generally vary by only a few tenths of a magnitude (or less) they are suited for CCD rather than visual observations. But there is one particular spotted star that is not only well-suited to visual observing, but has the bragging rights of owning of its own observing section—the sun. The AAVSO Solar Section (https://www.aavso.org/solar) aggregates observations from observers around the world into a monthly *Solar Bulletin*. Over time, the long-term trends of solar activity become apparent, including the semi-regular nature of the approximately 11-year-long solar cycle. The *AAVSO Solar Observing Guide* (available in seven languages) leads the interested observer through the theory and practice of safe solar observing.

While we have considered these two kinds of variable activity as separate and distinct for the sake of our discussion, anyone who has taken the opportunity to observe sunspots during a transit knows that nature is not that simple. Indeed, while the Kepler Space Telescope (RIP) proved to be a transiting exoplanet discovering fiend (discovering thousands of transiting exoplanets), it also detected other types of stellar variability, including spotted stars. At these distances we don't observe the starspots directly, but instead see the small deviations in the brightness of the stars due to transient spots and splotches. As in the case of our sun, this activity varies in three ways. First, individual spots only last for a certain length of time, typically anywhere from several hours to a few months. Second, as the

star rotates you will view different spots. Third, the overall activity waxes and wanes in a cyclical manner, for example an approximately 11-year cycle for our sun. Therefore time-series observation of these "spotty" stars not only divulges the existence of the spots, but computer models can also be used to estimate the sizes and likely latitudinal distribution of spots (Luo *et al.* 2019), along with the rotational cycle, and, if we watch it long enough, estimate the starspot cycle.

These are exactly the same types of observations we have been doing with our own sun for centuries, and in some cases, longer. Therefore, while we might have to wait a few years for the next opportunity to view a transit of our own star, the sun's natural cycle of activity (now slowly sliding out of minimum) is an excellent starting point for teaching about the properties of stars. In addition, our star, the star that most people would agree is the most important star to their personal lives, is also a powerful hook for opening up discussions of the importance and fascinating world of variable stars with the general public, including children.

Figure 2. Using colored filters to read "secret messages." Note the plastic UV beads are white/clear in the classroom light.

2. Solar outreach

Sidewalk astronomy involving the sun is always fun, as long as one takes care to make safety the number one concern. When local students from an urban high school visited our campus, I set up a telescope with a white light solar filter outside the Student Center. As they exited the building, I invited the teens to look through my filtered 6-inch Schmidt-Cassegrain, an instrument I only use for solar observing (having removed the finder scope for safety). They suspiciously squinted skyward and asked what I was looking at. I enthusiastically offered "The Sun!" After a quick safety lesson in which I explained my equipment they eagerly accepted what for most was their first look through a telescope. Most of them simply couldn't believe what they were seeing. They had heard of sunspots, but to think that you could actually see them with your own eyes seemed like magic. The icing on the cake was learning the relative size of those sunspots to our Earth. To a person, they were astounded. They had no idea of scale in the solar system; after all, to all but global travelers, the Earth seems so incredibly huge.

Projection methods are also available for solar observing, and when working with large groups, especially involving young children, projection is recommended. One option is the commercially available Sunspotter, a folded refractor that projects an image of the sun on the base of a triangular wooden frame. It is relatively easy to use, so children can help to set it up and aim it at the sun by minimizing the shadow projected by a small wooden gnomon. The Sunspotter offers enough resolution to allow for the viewing of sufficient sunspot groups and spots to track the overall sunspot cycle (Larsen 2013). Therefore, schools and other astronomy outreach groups can use the instrument as a hands-on educational tool to safely monitor solar activity over long periods of time and compare their observations to the published solar activity values (for example in the AAVSO *Solar Bulletin*). The sight of sunspots projected on the paper screen amazes children of all ages. But they are soon disappointed when the sun begins to disappear, drifting out of the field of view. The moment is infinitely teachable: why did it appear to move, they ask. Is the sun really moving, or are we moving, I reply. The best part of outreach, especially with children, really is the questions, meandering from topic to topic and, invariably, ending up at black holes, and then extraterrestrials.

If we observe transits of stars outside our solar system, what would an extraterrestrial astronomer observe if they were looking back at our sun? If they were oriented in just the right way they would see both types of activity—transits and evidence of the sunspot cycle. Wells *et al.* (2018) determined that 68 currently known exoplanets are positioned in such a way that any similar astronomical technology to our own could be used to observe at least one planet in our solar system transiting the sun. It is therefore possible that any alien civilizations that exist in our galaxy able to view our sun at the right orientation could discover the existence of our planetary system by noting the variability of our sun through transits. Such an idea is not only fascinating to astronomers, but students and the general public as well. Who knows who could be watching us right this moment?

Admittedly, the most effective outreach activities are more than a simple "one and done." Offering multiple opportunities to engage with the material more clearly demonstrates the connections between various aspects of astronomy (and relationships with physics, for example), and more accurately represents the scientific endeavor. Fortunately, there's a lot one can actually do with the sun in terms of outreach. I've hosted many three-hour Saturday morning workshops for 7th graders, and in my experience, it takes a lot of individual activities to fill that time. The sun provides a great unifying theme that bridges multiple fundamental laws of nature. For example, the various forms of light (the electromagnetic spectrum) can be easily demonstrated through the use of cheap plastic beads that change color when exposed to UV. Couple a handful of these beads with a pipe cleaner and you have a bracelet that doubles as a UV detector. Children are fascinated by the beads' ability

to detect these invisible rays, even on cloudy days. The use of filters in astronomy is easy to demonstrate, using colored plastic film and "secret messages" written in particular colors (Figure 2). Attendees apply this knowledge to pictures of the sun taken at different wavelengths.

Similarly, an exploration of the properties of bar magnets and horseshoe magnets leads to a short lesson on the magnetic field of the sun, complete with pictures of the sun showing not only how individual sunspot groups change over time, but the apparent motion of sunspots due to the sun's rotation. The similarities between bipolar sunspot groups, prominences, and the physical magnets the students had previously experimented with become readily apparent. Styrofoam models of the sun are then constructed, with the children adding their own sunspot groups, faculae, and prominences (Figure 4). We cap this off with actual observations of the sun (weather permitting), both in white light and hydrogen alpha (thanks to the availability of small, commercially available "solar telescopes").

As previously explained, children will notice that the sun drifts out of the field of view of the Sunspotter (or a telescope that is not tracking), which leads to a discussion of the rotation of the Earth. We can easily turn this around and demonstrate how the apparent motion of the sun in the sky caused by the Earth's rotation can be used to tell time. Children make simple sundials and (weather permitting) take them outside to be used. Otherwise, flashlights are handed out and they observe how the shadows shift as the "sun" appears to move through the day. Many printable templates for simple sundials can be found online, but my personal favorite is the "Pocket Sun Clock" (with accompanying lesson plan) available in the Astronomical Society of the Pacific's *The Universe at Your Fingertips* (Fraknoi 1995) (Figure 3).

The planetarium is the capstone of our time together, where I not only run through the obligatory constellation stories, but can speed up the yearly apparent motions of the sun in our sky, demonstrating the relationship between the sun and the seasons, and how this relationship changes depending on an observer's latitude. Children love watching the moon fly by as I put the sun through its annual paces along the ecliptic, pausing to point out the ever-shifting positions of the bright planets.

For those who are concerned about aligning outreach activities with educational standards (in some cases a demand of school-funded outreach such as field trips), the activities I have described above align with standards PS4.B Electromagnetic radiation, ESS1.A The universe and its stars, and ESS1.B Earth and the solar system, of the Next Generation Science Standards (NGSS), which have either been adopted or adapted by most states (NSTA 2014). There's a lot of science in sun-based activities, as well as opportunities for creativity. For example, I encourage children to decide which part of the solar-activity cycle their individual sun model represents, and design the numbers of spots, faculae, and prominences accordingly.

But undoubtedly the greatest solar outreach opportunity of recent memory was the Great American solar eclipse of August 2017. That was a very busy time for professional and amateur astronomers alike, putting in considerable efforts in outreach to assure that the public enjoyed the eclipse safely. I noticed many children in the audiences of my eclipse talks at libraries and community centers, and I was even invited to visit a local elementary school to discuss safe eclipse viewing in an age-appropriate way. I have always found children to especially appreciate silly visuals, so I was accompanied to every public eclipse talk by BB the eclipse-chasing bunny, an old plushy who has been my lucky charm at five total solar eclipses (Figure 5). BB's job in this circumstance was to demonstrate to children how to safely observe with their solar eclipse glasses (Larsen 2019).

Figure 3. Seventh graders setting up their Pocket Sun Clocks. Note the UV bead bracelets have changed color in the sunlight.

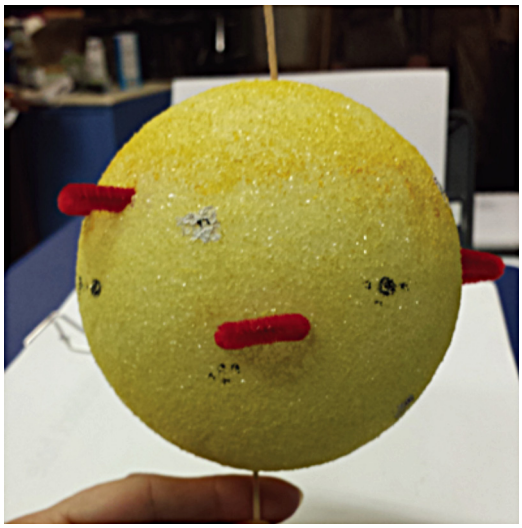

Figure 4. Solar outreach model. Faculae are made with white correction fluid, the sunspots with a black marker, and prominences with red pipe cleaners. Toothpicks represent the rotational poles.

A common question asked at these pre-eclipse outreach sessions was how eclipse glasses could be used after the main event. Again, this is a perfect opportunity to explore the solar-activity cycle. Approximately 3% of all sunspots are

Figure 5. BB the eclipse-chasing bunny at the Australia total solar eclipse in 2012.

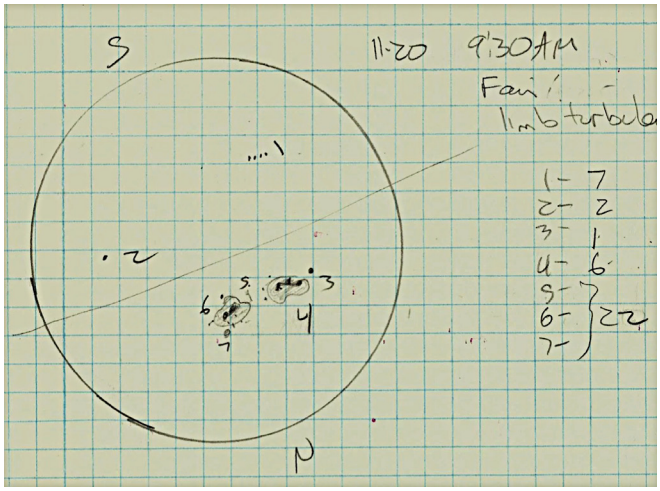

Figure 6. One of the author's early solar observations, demonstrating the learning curve for solar observing. Upon further reflection, "Groups" 5, 6, and 7 were later realized to comprise a single group.

larger than the theoretical resolving power of the human eye, ~ 70", especially near the peak of the solar cycle (Vaquero and Vázquez 2009). But observers have discerned sunspot groups less than half this size without optical aid (MacRobert 1989). It is therefore not surprising that records of sunspot observations date back two millennia, long before the invention of the telescope (Vaquero and Vázquez 2009). With the sun currently waking up from its solar minimum doldrums, it's time to dust off those solar eclipse glasses, check them for defects, and get back to the roots of solar observing (but done far more safely than the ancient methods of viewing the sun through clouds, haze, or smoked glass). It's also not too early to begin planning both our outreach and individual travel plans for the next Great American solar eclipse on April 8, 2024. While the path of totality will stretch northeast from Mexico, crossing several US states before ending in Labrador in Canada, the entire continental US will experience some of the partial phase of the eclipse. Since the sun will be about halfway to the next solar maximum at that time, we should be able to couple our viewing of the partial phases with observing sunspots. Several warm-up events will occur before then, including the October 25, 2022, partial solar eclipse visible from parts of Europe, northeastern Africa, and the Middle-east, the April 20, 2023, total/annular eclipse visible from Southeast Asia and Australia, and the October 14, 2023, annular eclipse visible from much of North America, Central America, and South America. Helpful resources are listed at the conclusion of this article.

3. A personal story

Every backyard observer, no matter how expert, started somewhere. This is true both in general, and with variable star observers more specifically. In the summer of 1989, while I was completing my Ph.D. and shortly after being hired as a faculty member at CCSU, I attended the famous Stellafane Convention on Breezy Hill in Vermont for the sixth time. At Stellafane you meet many colorful characters, and one of the most colorful in the late 1980s was Casper "Cap" Hossfield, former chair of the AAVSO Solar Section (1963–1979). Every year he would lug an eclectic array of gear up to the hill, including seismographs, a purported gravity wave detector, and his trademark Hossfield pyramid solar projection system with which he would show people sunspots. That particular year I wandered over to his set-up and looked over the pyramid with interest, the only excuse Cap needed to launch into a detailed explanation of the wonders of solar observing. Two months later, I was the proud owner of a solar filter for my six-inch Bausch and Lomb Schmidt-Cassegrain, and was submitting sunspot observations to Cap in service of the American Radio Relay League. The possibility of helping ham radio aficionados communicate more effectively by simply counting sunspots seemed too easy. I was right.

There is more to solar observing than simply counting the numbers of individual spots, because solar activity is more closely aligned with the number active regions (or "groups") visible on the sun than the total number of individual spots. An isolated spot simultaneously counts as a "group" and a "spot" because it denotes the location of a distinct active region (Figure 6). Solar activity is therefore described by the Wolf number (defined by famed solar observer Rudolf Wolf in 1848), calculated by weighting the number of groups by a factor of ten and then adding in the total number of spots: $10g+s$. It is much easier to determine the identity of individual groups when the sun is relatively quiet, such as when it is coming out of solar minimum, as it is now (http://sidc.oma.be/silso/). But as the sun approaches solar maximum and the field gets more crowded, it takes experience and consistent observations to get a good handle on where one group ends and the next begins. My decision to start solar observing near solar maximum certainly added an extra level of challenge to the activity.

After several months of patience and encouragement from Cap, he dangled another carrot in front of me, asking if I would consider sending my observations to the AAVSO, a group that monitors variable stars. What Cap could not have known was that after becoming an AAVSO observer I not only became a member, but Janet Mattei invited me to become involved in developing a grant-funded educational project, *Hands-on Astrophysics*, a means to bring astrophysics to classrooms by using variable stars. Janet afterwards tasked me with delivering

a presentation on the project at the AAVSO annual meeting, where I met Dorrit Hoffleit, who afterwards became highly influential in my research on the history of women in science. Janet then sealed the deal by encouraging me to run for AAVSO Council, and the rest, as they say, is history.

Dorrit was fond of recounting the story of how, as an intern at the Maria Mitchell Observatory, Janet Mattei started on her road to becoming the Director of the AAVSO by unexpectedly taking Dorrit's place hosting an AAVSO meeting "all because of the Nantucket fog" (Larsen 2009, 62); my road to being President of the organization (and later Secretary and Co-Solar Section Chair) started with a chance encounter at Stellafane and some spots on the sun. Everyone's pathway to variable stars is different, but it often comes down to unexpected experiences, and a mentoring hand. By offering both, we will assure the continued success of the AAVSO long after we have individually submitted our own final observations.

4. Conclusion

The sun is our star and belongs to all of us. Too often we take it for granted, and don't appreciate its identity as a variable star. The sun might reliably appear in our sky (clouds permitting) every single day, but no two sunrises are the same. Similarly, every (safe) view of the sun through a telescope has some unique quality. Even a sun devoid of spots can sometimes be seen to have faculae strung along the limb, if you trade your disappointment for patience. More importantly, no two solar cycles are the same. The numbering system used to identify individual cycles was developed by Wolf in 1861, with Cycle 1 defined to have begun in 1755 (https://www.stce.be/news/312/welcome.html). Cycle 25 began in December 2019 and is expected to peak between around 2025 (Potter 2020). What tricks does the sun have up its sleeve for this cycle? Our star will divulge the answer in its own time, so accept its invitation to watch it unfold for yourself. Remember, it is far easier to learn how to separate sunspot groups if you begin your education when the sun is relatively quiet. Now is the perfect time to start your personal solar observing journey, and the AAVSO Solar Section provides you with both the information you need to get started and the opportunity to engage in the process of scientific data collection.

Teachers with access to a solar projection system are also encouraged to invite children to keep an eye on our star, with changes visible not only from day to day, but month to month, and year to year. Imagine middle school students who begin observing the sun now, just after minimum, and continue to monitor their star until high school graduation, when it should be reaching maximum. What a powerful lesson in the truth that the ability to do science is open to us all, and that learning is a life-long endeavor.

As the sun awakens from solar minimum, let's harness a solar energy of a different kind, the energy of our enthusiasm, to light the fire of wonder in the next generation, and recruit and train the next generation of AAVSO members and observers.

5. Additional resources

American Astronomical Society 2024 Eclipse Webpage: http://eclipse.aas.org

Great American Eclipse: https://www.greatamericaneclipse.com/

International Astronomical Union Working Group on Solar Eclipses: https://sites.williams.edu/iau-eclipses/

Schatz, D., and Fraknoi, A. 2016, *Solar Science*, NSTA, Arlington.

Weather Predictions for Solar Eclipses: http://eclipsophile.com

References

Fraknoi, A., ed. 1995, *The Universe at Your Fingertips*, Astronomical Society of the Pacific, San Francisco. (https://files.eric.ed.gov/fulltext/ED399149.pdf).

Kopp, G., Krivova, N., Wu, C. J., and Lean, J. 2016, *Sol. Phys.*, **291**, 2951.

Larsen, K. 2009, *J. Amer. Assoc. Var. Star Obs.*, **37**, 52.

Larsen, K. 2013, *J. Amer. Assoc. Var. Star Obs.*, **41**, 373.

Larsen, K. 2019, in *Celebrating the 2017 Great American Eclipse*, eds. S. R. Buxner, L. shore, J. B. Jensen, Astronomical Society of the Pacific, San Francisco, 173.

Luo, T., Liang, Y., and Ip, W.-H. 2019, *Astron. J.*, **157**, 238.

MacRobert, A. M. 1989, *Sky & Telescope*, **78**, 289.

NSTA. 2014, About the Next Generation Science Standards (https://ngss.nsta.org/about.aspx).

Potter, S., ed. 2020, "Solar Cycle 25 is Here," updated Jan. 4. 2021 (https://www.nasa.gov/press-release/solar-cycle-25-is-here-nasa-noaa-scientists-explain-what-that-means).

Vaquero, J. M., and Vázquez, M., eds. 2009, *The Sun Recorded Through History*, Springer, New York.

Wells, R., Poppenhaeger, K., Watson, C. A., and Heller, R. 2018, *Mon. Not. Roy. Astron. Soc.*, **473**, 345.

The Photometric Period of V1391 Cassiopeiae (Nova Cas 2020)

Richard E. Schmidt
Burleith Observatory, 1810 35th Street NW, Washington, DC 20007; schmidt.rich@gmail.com

Received December 27, 2020; revised February 6, 2021; accepted February 17, 2021

Abstract A photometric study of Nova Cassiopeiae 2020 has been undertaken at the urban Burleith Observatory in Washington, DC, where 7,504 CCD observations were obtained over a time span of 100.16 days. A photometric period was obtained: 3.8036 ± 0.0005 h, epoch (HJD) of maximum light 2459082.59223, with amplitude 0.011 magnitude (Cousins I).

1. Introduction

V1391 Cassiopeiae (Nova Cas 2020, TCP J00114297+6611190), R.A. = $00^h11^m42.96^s$, Dec. = +66°11' 20.8" (2000), was discovered on 2020 July 27.9302 by Korotkiy and Sokolovsky (2020) at Ka-Dar Observatory, Nizhny Arkhyz, Russia. Its classification as a classical Fe II nova was made by Sokolovsky *et al.* (2020). Newly discovered novae make excellent high-cadence photometry candidates for bright-sky urban observatories. Fe II novae are typically slow declining, thus remaining in reach of small telescopes for extended periods. Amplitudes of variation are typically below 0.03 magnitude, but periods average less than 0.2 d; small observatories that are able to devote many hours acquiring sufficient images can detect such periodicity, which remains stable for many months or years. For a recent compendium of nova light curve properties see Özdönmez *et al.* (2018). Most novae lie at low galactic latitudes, and their red excess is optimal for near-infrared observations in a band such as Cousins I, which is dark under city lights. V1391 Cas represents the third recent nova for which a photometric period has been found at Burleith Observatory (Schmidt 2020a, 2020b). A fourth, Nova Per 2020, is the subject of a forthcoming paper (Schmidt 2021). A preliminary photometric period of V1391 Cas was reported to the Central Bureau for Astronomical Telegrams on 23 September 2020 (Schmidt 2020c).

2. Observations

At Burleith Observatory, Washington, DC, CCD observations were obtained with a 0.32-m PlaneWave CDK and SBIG STL-1001E CCD camera with an Astrodon Cousins Ic filter. Pixel size was 1.945 arc-seconds, yielding on average 2-pixel FWHM. Exposure times ranged from 30 to 120 seconds.

3. Reductions

Synthetic aperture photometry was performed using C-Munipack 2.1.29 (Motl 2020), with an aperture of radius 3.8 pixels. Observation times had heliocentric corrections applied. Comparison stars were selected to avoid CCD saturation.

Cousins I-band differential ensemble photometry was performed using the comparison stars in Table 1 and shown in Figure 1, from AAVSO chart sequence X25582CLS (C = comparison, K = check, Label = chart label). Nightly checks were made to rule out variability of the comparison stars.

Nightly means of observing sessions are shown in Figure 2. Example nightly observations are shown in Figures 3a–3f. The circumpolar declination of V1391 Cas enabled sessions as long as 7.2 h, as seen on 14 Oct. 2020 (Figure 3d). Table 2 lists nightly mean times (HJD – 2450000), observed mean magnitude Ic, and mean error of the magnitudes. These data are shown in Figure 2.

4. Analysis

Prior to Fourier analysis, each nightly observation set was pre-processed by subtracting nightly means and removing linear trends. Period analysis was performed using Peranso 2.60 software (Paunzen and Vanmunster 2016), applying several period analysis techniques, including the phase-folding Jurkewich method (Figure 4), two Analysis of Variance methods, the Date-Compensated Discrete Fourier Transform (DCDFT) method, and the Fourier/least-squares Lomb-Scargle method. Initial analyses use a wide spectral search of 0–10 d before refining in a smaller window such as that shown in Figure 4.

Fourier periodic analysis of variable star photometry often presents present challenges in interpretation of results. Weather conditions, daylight, and limited periods of observation create gaps in the time series. The need to observe at nearly the same time each night produces aliases in the resulting Fourier spectrum. The inherent assumption that the light curve of a variable star can be reasonably fit to a series of sine functions is only approximately true. The results reported here came from the Lomb-Scargle method, which was chosen for its use of Fourier spectral analysis combined with least-squares fitting. It is among the most familiar methods in astronomical use (VanderPlas 2018). This yielded an observed period of p = 0.158482 d (6.3101 c/d), as seen in the lower part of Figure 5. The period found by the DCDFT method differed from that from the Lomb-Scargle method by only +0.000005 d.

To test the reliability of the Lomb-Scargle method under our observing constraints, it was applied to a synthetic light curve generated from the simple sinusoid:

$$y_i = a^* \sin(2\pi / p^* (x_i - x_0)) + \varepsilon_i$$

using our observed amplitude a = 0.011 and period p = 0.158487 d. Values for y_i were computed using for each x_i, the times of our CCD observations, with x_0 being the first of these. Gaussian errors ε_i, scaled by each observed magnitude's error, were added at each point. This gives us synthetic data with a known period, but with all of the temporal gaps of our actual observation set. Using Peranso software, we obtain the resulting Lomb-Scargle

Table 1. Photometry comparison stars.

AUID	R. A. (2000) h m s	Dec. (2000) ° ′ ″	C/K	Label	Ic	Mag Err
000-BNP-452	00 12 58.25	+66 04 49.5	C	112	10.503	(0.242)
000-BNP-453	00 10 49.30	+66 06 24.0	C	126	11.207	(0.052)
000-BNP-455	00 11 32.60	+66 03 06.1	K	137	12.586	(0.053)

Table 2. Nightly mean magnitudes I_c

HJD	mag Ic	err	HJD	mag Ic	err
9070.75613*	8.905	0.002	9136.58565	9.563	0.002
9072.64919*	8.744	0.003	9137.52403	9.683	0.002
9080.48809*	9.655	0.002	9140.60407	9.903	0.002
9082.59589	9.509	0.004	9145.54884	10.423	0.003
9086.61026	9.578	0.006	9156.56631	10.492	0.003
9091.46495	9.799	0.002	9158.46183	10.316	0.003
9092.52855	10.089	0.003	9158.58060	10.316	0.002
9098.62223	10.085	0.005	9160.58690	9.706	0.003
9099.60930	10.342	0.003	9161.73181	9.515	0.003
9100.58408	10.503	0.004	9162.58105	9.513	0.003
9105.61944	9.440	0.004	9163.57182	9.543	0.003
9106.58591	9.540	0.002	9164.58537	9.398	0.003
9111.65805	9.929	0.003	9167.57344	9.890	0.003
9112.60118	10.020	0.003	9168.55022	10.243	0.003
9113.57928	10.140	0.003	9170.56898	10.769	0.003
9114.59360	10.239	0.003	9172.56174	10.932	0.003
9115.57977	10.213	0.003	9174.56764	10.727	0.002
9123.57543	10.065	0.004	9180.55862	11.170	0.003
9125.58597	9.885	0.003	9182.58765	10.752	0.003
9126.61275	10.007	0.003	9191.64513*	11.388	0.004
9129.59152	10.262	0.003	9193.91493*	12.322	0.008
9131.57959	10.019	0.003			

** Not used.*

Table 3. Summary of the resulting period information.

Period (h)	3.803568 (0.001537)
Period (d)	0.158482 (0.000067)
Frequency (c/d)	6.3098667 (0.0026667)
Mean amplitude (fit)	0.011
Number of observations	7504
Time span (d)	100.1595
Epoch (JD) of maximum	2459082.592230

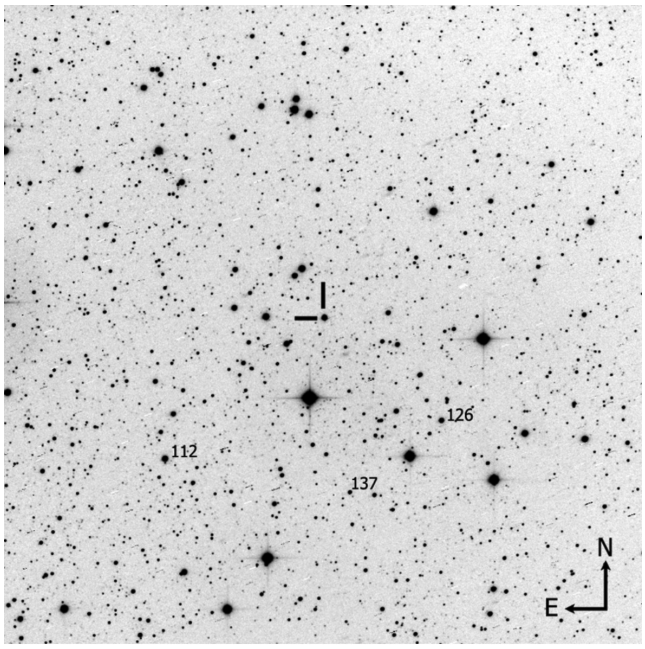

Figure 1. 30 arc-min field of Nova Cas 2020.

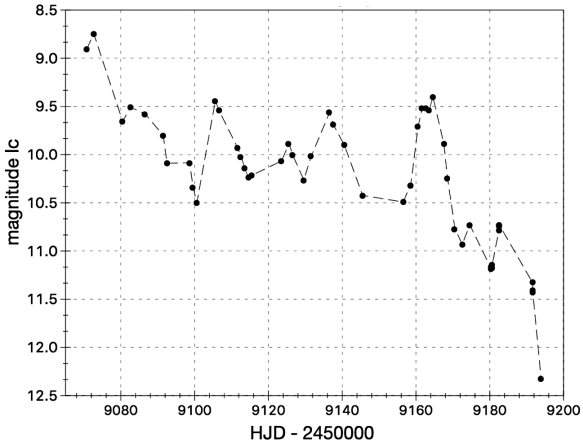

Figure 2. Nightly mean Ic magnitudes from Table 2.

periodogram of this synthetic data as seen in Figure 5 (top), with peak at 6.3101 c/d ± 0.0042 (period 0.158460 ± 0.0001 d). Figure 5 (bottom) compares the periodogram of our actual V1931 Cas observations. Note the one-cycle per day aliases bordering our peak frequency. This exercise demonstrates the reliability and accuracy of the Lomb-Scargle period analysis for signals of small amplitude in the presence of noise.

A folded double-phase plot of the most prominent period, 6.3101 c/d, is shown in Figure 6. A 225-point averaging with 128-point spline interpolation is shown (solid white line). The amplitude of this fit is 0.011 magnitude Ic.

Finally, Peranso software's Fisher Monte Carlo Randomization Test was applied. This method keeps observation times fixed while randomizing the order of the magnitude observations over 200 permutations, searching for spectral responses due solely to observational biases (Moir 1998). FAP 1 computes the probability that no period of value P is present in the data, and FAP 2 the probability that any other significant periods are present in the data. The FAP are given in a range of 0 to 1, with values below 0.01 (1%) indicating very secure solutions (Paunzen and Vanmunster 2016). For P = 3.8036 h the Peranso values of both FAP were 0.000 (probability < 0.05 %). It should be noted that the FAP only give confidence in the reality of the underlying period, but do not judge the precision or accuracy of its value. The resulting period information is summarized in Table 3.

5. Conclusion

Time-resolved photometry of new novae from small observatories can detect low-amplitude photometric periods. Less than 100 such periods have been recorded. Coincidently, the observed period of 3.8 h for Nova Cas 2020 happens to be the median value of orbital periods of novae with period less than 12 h which are found in the catalogue of galactic novae of (Özdönmez *et al.* 2018). Figure 7 shows a histogram of orbital periods from their Tables 5 and 6.

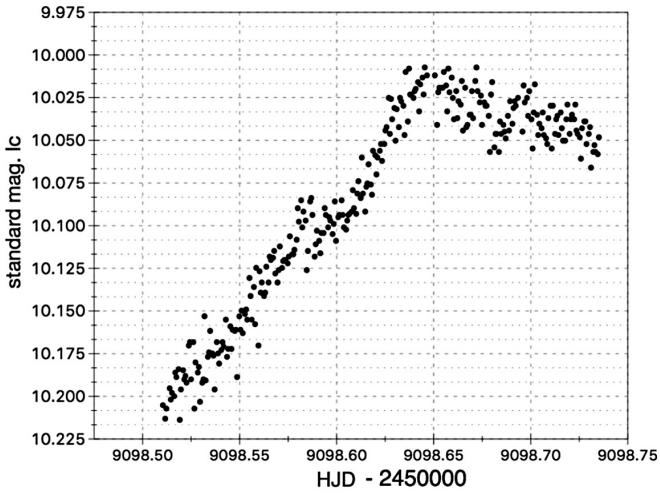

Figure 3a. Example observations 6 September 2020.

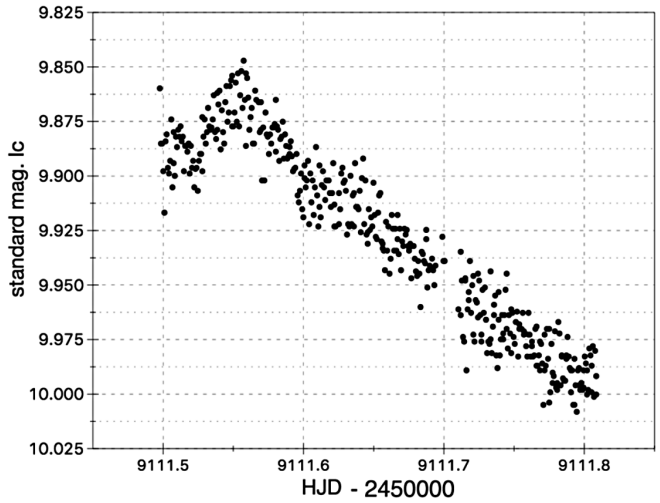

Figure 3b. Example observations 19 September 2020.

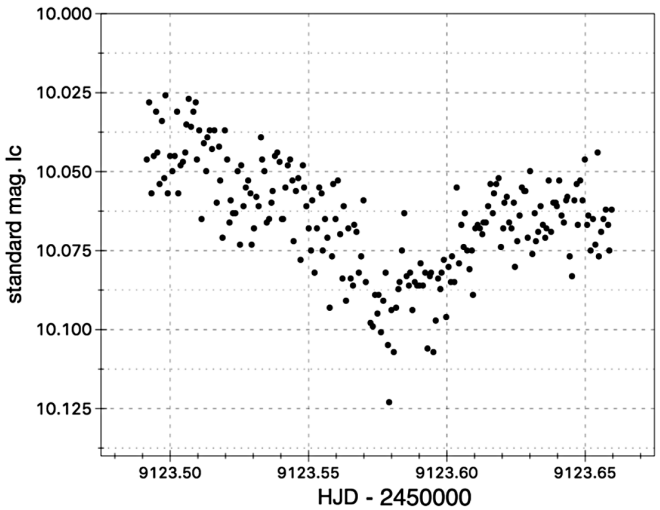

Figure 3c. Example observations 1 October 2020.

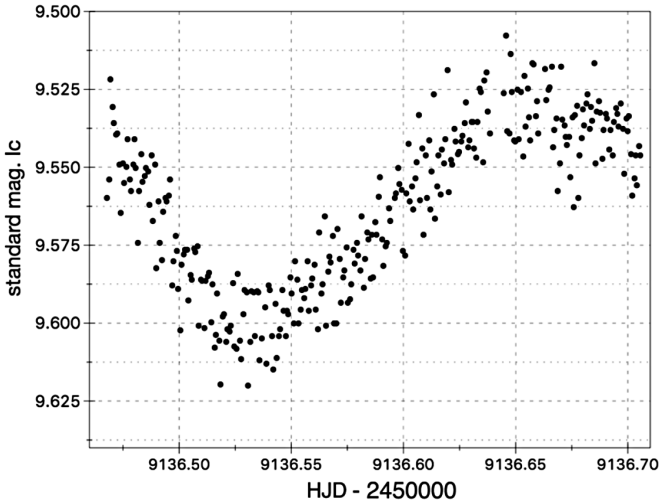

Figure 3d. Example observations 14 October 2020.

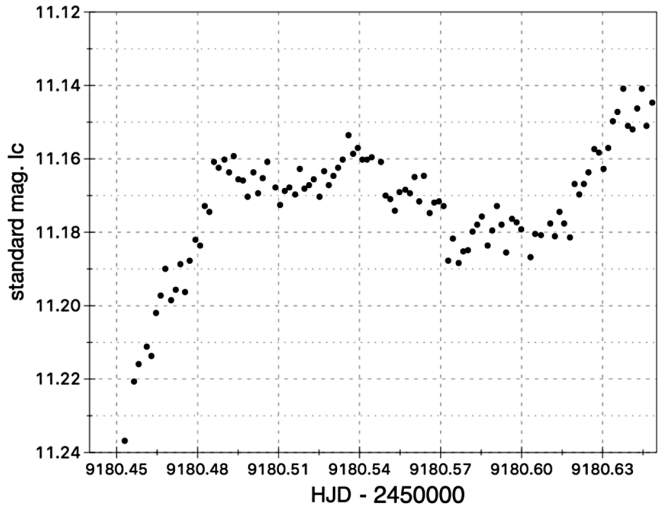

Figure 3e. Example observations 27 November 2020.

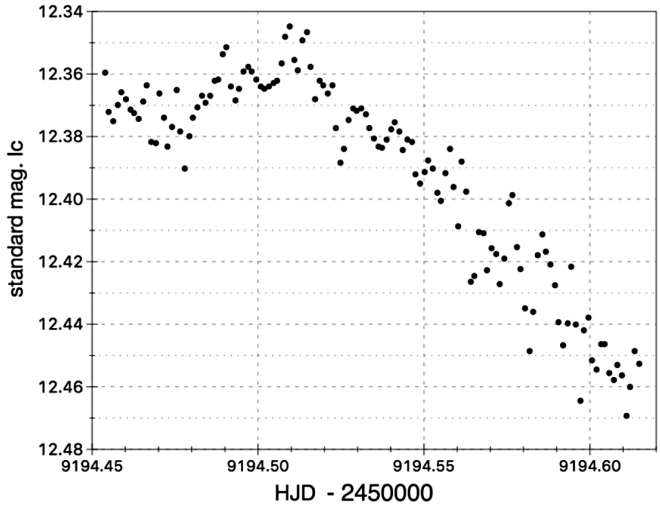

Figure 3f. Example observations 11 December 2020.

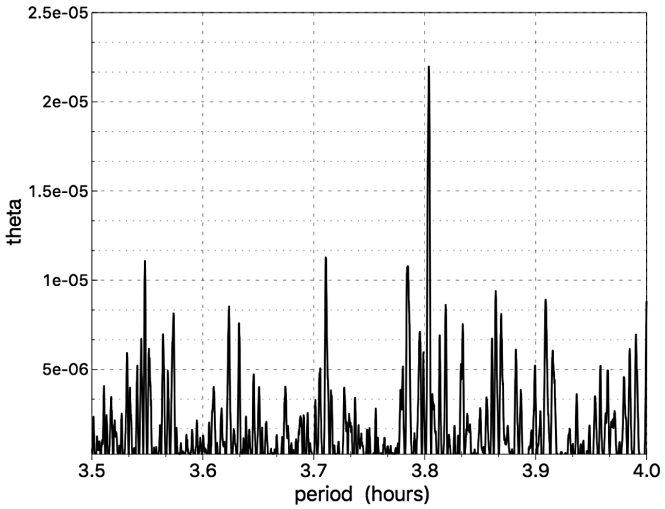

Figure 4. Jurkewich periodogram of Nova Cas 2020, with peak at 3.81 h.

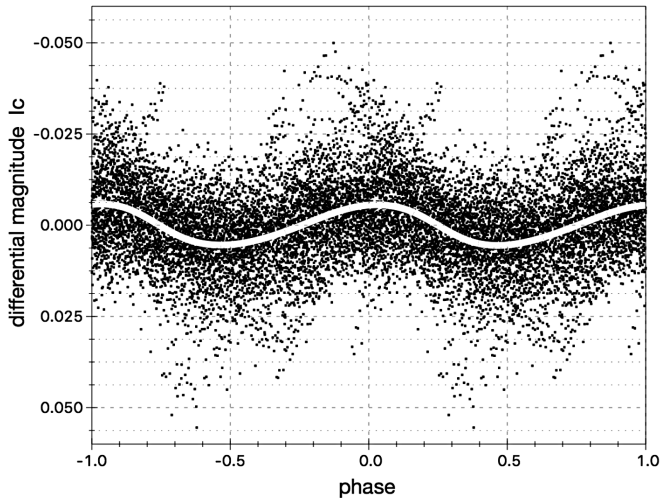

Figure 6. V1391 Cas, double phased plot with spline interpolated fit.

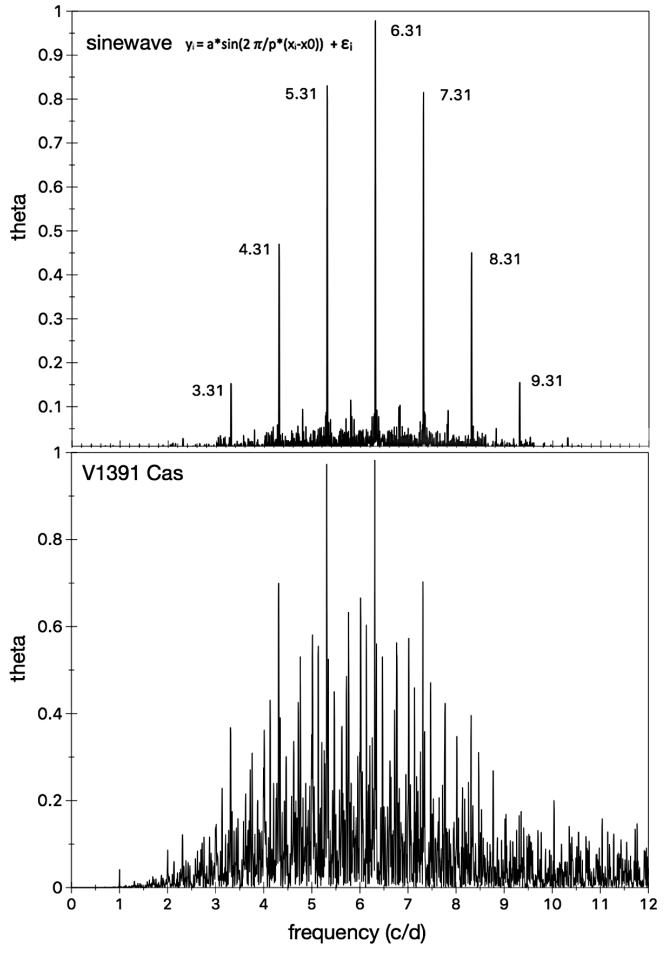

Figure 5. Lomb-Scargle periodograms of a sinusoid of frequency 6.31 c/d (top) and of our observations (bottom).

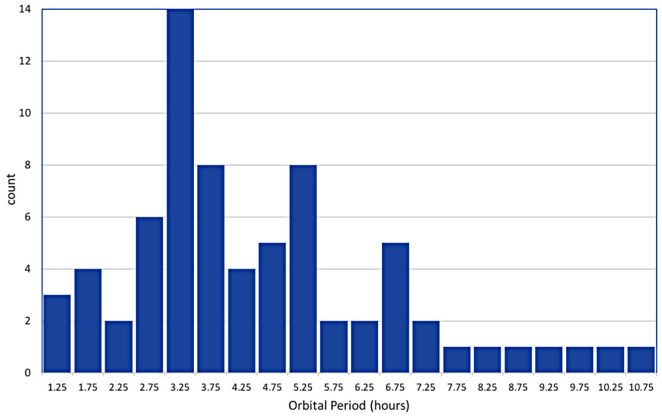

Figure 7. Distribution of novae orbital periods < 12 h, extracted by the author from Özdönmez *et al.* (2018), "A New Catalogue of Galactic Novae." The median value of these is 3.8 h.

6. Acknowledgements

The author wishes to thank James A. DeYoung, NRL/USNO (ret.) for many valuable discussions. Special thanks to the AAVSO for providing photometric standards from the AAVSO Comparison Star Database via its Variable Star Plotter utility.

References

Korotkiy, S., and Sokolovsky, K. 2020, *Cent. Bur. Astron. Telegrams*, CBAT Transient Object Followup Reports, TCP J00114297+6611190, 2020 07 27.9302.

Moir, R. 1998, *Exp. Economics*, **1**, 87.

Motl, D. 2020, C-Munipack software utilities (http://c-munipack.sourceforge.net).

Özdönmez, A., Ege, E., Güver, T., and Ak, T. 2018, *Mon. Not. Roy. Astron. Soc.*, **476**, 4162.

Paunzen, E., and Vanmunster, T. 2016, *Astron. Nachr.*, **337**, 239.

Schmidt, R. E. 2020a, *J. Amer. Assoc. Var. Star Obs.*, **48**, 13.

Schmidt, R. E. 2020b, *J. Amer. Assoc. Var. Star Obs.*, **48**, 53.

Schmidt, R. E. 2020c, *Cent. Bur. Astron. Telegrams*, No. 4857, 1.

Schmidt, R. E. 2021, *J. Amer. Assoc. Var. Star Obs.*, **49**, 99.

Sokolovsky, K., *et al.* 2020, *Astron. Telegram*, No. 13904, 1.

VanderPlas, J. T. 2018, *Astrophys. J., Suppl. Ser.*, **236**, 16.

The Photometric Period of V1112 Persei (Nova Per 2020)

Richard E. Schmidt
Burleith Observatory, 1810 35th Street NW, Washington, DC 20007; schmidt.rich@gmail.com

Received January 13, 2021; revised January 28, 2021; accepted February 2, 2021

Abstract A photometric study of V1112 Persei (Nova Persei 2020) has been undertaken at the urban Burleith Observatory in Washington, DC, where 2,400 CCD observations were obtained over a time span of 42.02 days. A photometric period was obtained: 2.2257 ± 0.0011 h, epoch (HJD) of minimum light 2459192.612, with amplitude 0.010 magnitude (Cousins I). The serendipitous discovery of two new variable stars, BD +43 984 and GSC 02891-02799, is reported.

1. Introduction

V1112 Persei, (Nova Persei 2020, TCP J04291884+4354232), R.A. $04^h\ 29^m\ 18.85^s$, Dec. +43° 54' 23.0" (2000), was discovered on 2020 November 25.807 UT by Seiji Ueda (2020) at Kushiro, Hokkaido, Japan. An independent discovery on 2020 November 25.844 UT was made by Korotki, Sokolovsky, and Smolyankina (Ueda 2020). Munari *et al.* (2020) categorized it as a classical nova. Banerjee *et al.* (2020) reported its transition into a typical Fe II nova. Novae are typically reddened, making them ideal for near-infrared observing at high cadence from bright urban sky locations. This is the fourth recent nova since 2019 with a photometric period measured at Burleith Observatory (Schmidt 2020a, 2020b, 2020c). A preliminary photometric period reported to the *Central Bureau for Astronomical Telegrams* was published on January 9, 2021 (Schmidt 2021).

2. Observations

At Burleith Observatory, CCD observations were obtained with a 0.32-m PlaneWave CDK and SBIG STL-1001E CCD camera with an Astrodon Cousins I_c filter. Flat-fields and dark frames were applied in real time using The SkyX Professional Edition version 10.5.0 (Software Bisque 2020). Exposure times ranged from 8 to 120 seconds.

3. Reductions

Synthetic aperture photometry was performed using C-Munipack 2.1.29 (Motl 2020). Differential ensemble photometry used the comparison stars from AAVSO chart sequence X25769ASF (Table 1), seen in Figure 1.

Hourly mean magnitudes of all observing sessions, including those not used in period analysis, are shown in Table 2 and Figure 2. Example observing sessions are shown in Figures 3a–3d.

4. Analysis

Observed magnitudes were pre-processed by subtracting nightly means, then detrended by removing a linear fit to remove the nova's long-term decline. Compare the result of this process, Figure 4, with the original observations in Figure 3c.

Period analysis was then performed using Peranso 3.0 software (Paunzen and Vannmuster 2016), applying several period analysis techniques including the Date-Compensated Discrete Fourier Transform (DCDFT), two Analysis of Variance (ANOVA) methods, and the generalized Lomb-Scargle method. Confidence in the results is gained when a period is found using multiple methods. DCDFT is particularly useful for variable star observations in its ability to process unevenly spaced data. Nova Persei's 5.5 magnitude drop in 42 days required exposure times varying from 8 to 120 sec. As Templeton (2004) pointed out, two factors determining the resolution of a period determination by time series analysis are the time span of observations and the Fourier sampling frequency. In practice the maximum sampling rate is usually chosen as 2 to 5 multiples of the Nyquist frequency, $f_{Ny} = 1/(2\Delta t)$ for observing interval Δt. For an average $\Delta t = 60$ sec this results in $f_{Ny} = 1/720$ day, or 30,240 Fourier samples over our span of 42 days. As Thomson (1982) remarks, "…the sample size must be extraordinarily large for the periodogram to be reasonably unbiased." Figure 5 shows the DCDFT periodogram computed with 50,000 Fourier samples. The spectrum peaks at 10.783 ± 0.006 cycles / day (with associated 1 c / d aliases), period 2.2257 ± 0.0011 h.

A folded double-phase plot, is shown in Figure 6. A 512-point averaging with 128-point spline interpolation is shown (solid line).

The period was tested for significance using the Peranso False Alarm Probability (FAP) computations. A Fisher Monte Carlo Randomization Test, which keeps observation times fixed while randomizing the order of the magnitude observations over 200 permutations, searches for spectral responses due solely to observational biases (Moir 1998). FAP 1 computes the probability that *no* period of value P is present in the data, and FAP 2 the probability that *any other* significant periods are present in the data. The FAP are given in a range of 0 to 1, with values below 0.01 (1%) indicating very secure solutions (Paunzen and Vanmunster 2016). For P = 2.2257 h the Peranso values of both FAPs were 0.000 (probability of each < 0.05%).

The resulting period information is summarized in Table 3.

5. Discovery of two field variable stars: BD +43 984 and GSC 02891-02799

In the AAVSO chart sequence X25769ASF for V1112 Per, one of the AAVSO comparison stars, BD +43 984 in Figure 1, was found to be variable. Its AUID is 000-BNS-433, chart label 105. It is a 2.9-arc second double, WDS 04303+4408 in the *Washington Double Star Catalog* (USNO 2020;

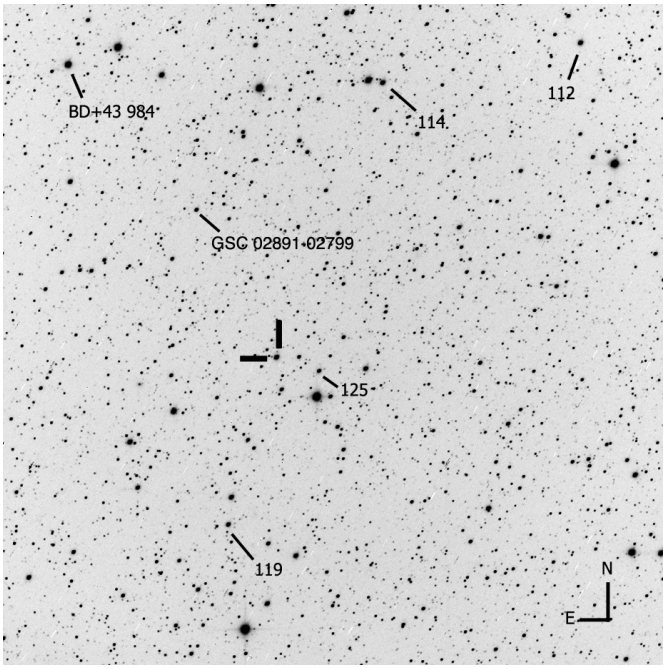

Figure 1. 30 arc-min field of V1112 Persei.

Table 1. Comparison stars (C = comparison, K = check).

AUID	R.A. (2000) h m s	Dec. (2000) ° ′ ″	C/K	Label	I_c	Mag. Error
000-BNS-435	04 27 56.78	+44 09 13.0	C	112	10.638	(0.160)
000-BNS-436	04 28 49.69	+44 07 27.6	C	114	10.687	(0.143)
000-BNS-437	04 29 32.14	+43 46 24.5	C	119	11.151	(0.140)
000-BNS-438	04 29 07.55	+43 53 42.6	K	125	11.650	(0.137)

unresolved in these CCD observations). An ANOVA time series analysis of 2,084 observations of this star yields a period of 0.3489 ± 0.0003 d, mean magnitude 9.51 in Cousins I_C, amplitude 0.023 magnitude I_c (Figure 7). ANOVA works particularly well for variables with small differences in the depths of minima, a defining characteristic of W Ursae Majoris variables (Lucy 1968), and is classified as a probable EW by (Otero 2021). It has now been added to the AAVSO VSX with a new AUID designation, 000-BNT-120.

A second field variable star, GSC 02891-02799 was also found to be a possible δ Scuti variable from an ANOVA analysis of 1,070 CCD images over a span of 29.2 d. This yielded a period of 0.1162 ± 0.0001 d (2.789 ± 0.002 h), epoch of maximum 2459224.382, with mean magnitude 11.89 in Cousins I_C, and amplitude 0.01 magnitude (Figure 8).

6. Conclusion

CCD observations of the classical nova, Nova Persei 2020, from a bright-sky urban observatory have detected a low-amplitude photometric period of 2.2257 h. The nova continued to remain photometrically active in early 2021, showing magnitude changes as much as 0.3 magnitude I_c in 6 hours (10 January 2021). Continued observations in standard bands should be of interest.

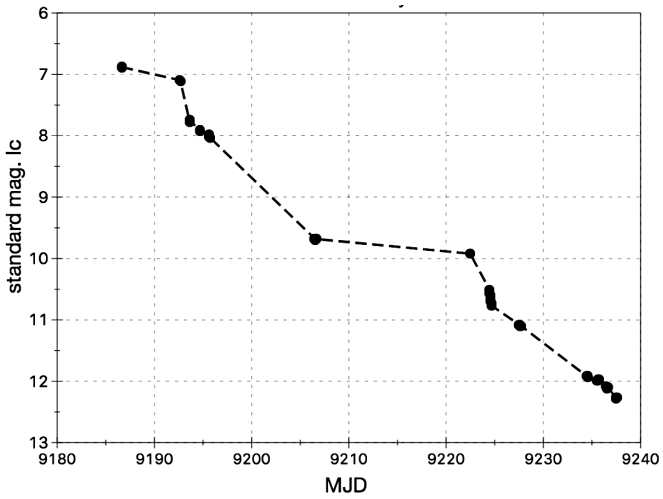

Figure 2. Hourly mean I_c magnitudes.

Table 2. Hourly mean magnitude (Ic) and magnitude error.

HJD 2450000+	Mag. I_c	Error	HJD 2450000+	Mag. I_c	Error
9186.658	6.880	0.009	9224.601	10.658	0.004
9186.679	6.884	0.009	9224.643	10.696	0.004
9192.641	7.095	0.008	9224.686	10.735	0.004
9192.677	7.107	0.009	9224.725	10.775	0.004
9193.640	7.781	0.004	9225.475	10.864	0.004
9193.675	7.741	0.004	9225.518	10.882	0.003
9194.650	7.925	0.004	9225.560	10.897	0.003
9194.686	7.914	0.004	9225.601	10.893	0.004
9195.582	7.972	0.003	9225.643	10.887	0.003
9195.624	7.984	0.003	9225.670	10.879	0.003
9195.665	8.011	0.003	9227.489	11.074	0.005
9195.700	8.028	0.003	9227.530	11.082	0.005
9206.492	9.677	0.004	9227.573	11.089	0.005
9206.534	9.698	0.003	9227.613	11.092	0.005
9206.576	9.703	0.003	9227.657	11.095	0.005
9206.613	9.688	0.003	9227.692	11.096	0.005
9206.662	9.679	0.003	9234.487	11.920	0.005
9206.687	9.683	0.003	9234.531	11.921	0.006
9222.473	9.922	0.004	9234.572	11.929	0.006
9224.475	10.510	0.005	9234.613	11.933	0.005
9224.517	10.560	0.004	9234.639	11.935	0.010
9224.560	10.601	0.004	9235.489	11.992	0.005

Table 3. Period test information summary.

Parameter	Value
Period (hours)	2.2257 ± 0.0011
Period (days)	0.09274 ± 0.00005
Mean amplitude (fit)	0.010
Number of observations	2,400
Time span (d)	42.02
Epoch (JD) of minimum	2459192.612

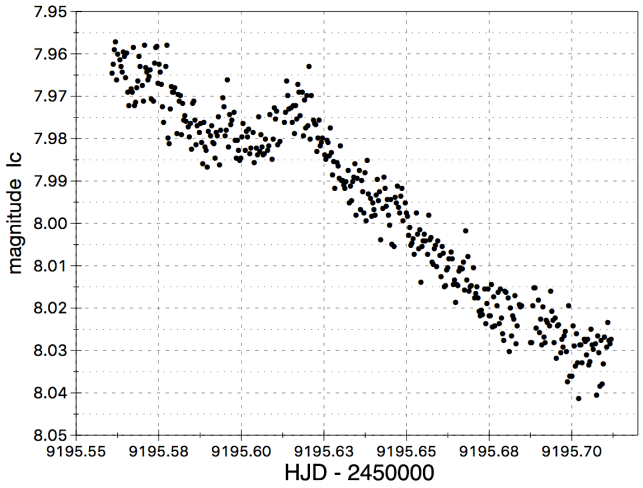

Figure 3a. Example session, December 12, 2020.

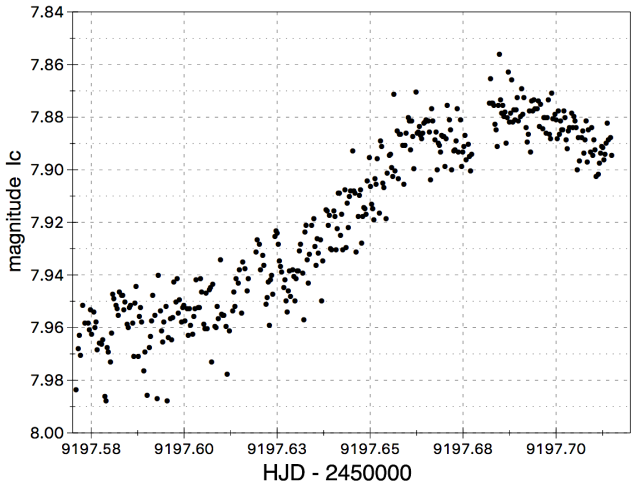

Figure 3b. Example session, December 14, 2020.

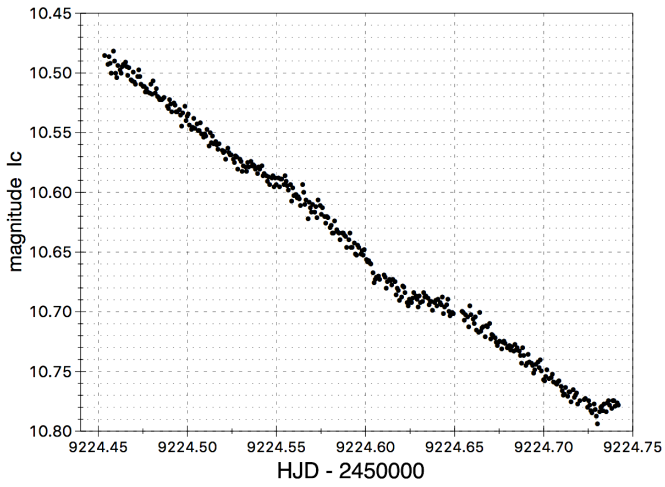

Figure 3c. Example session, January 10, 2021, with large magnitude drop.

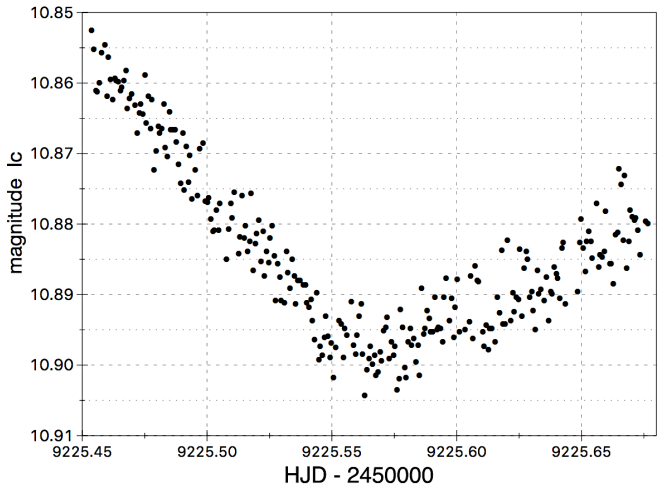

Figure 3d. Example session, January 11, 2021.

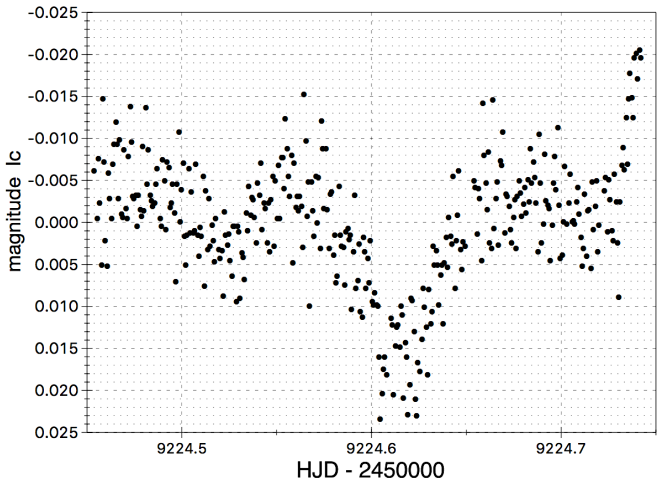

Figure 4. Observations of Figure 3c detrended.

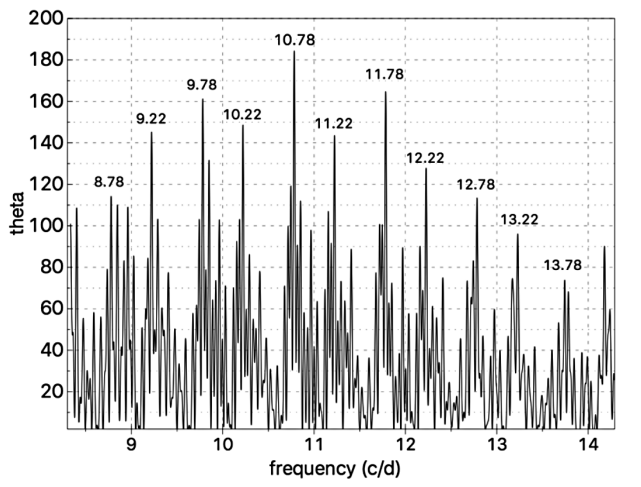

Figure 5. DCDFT spectrum.

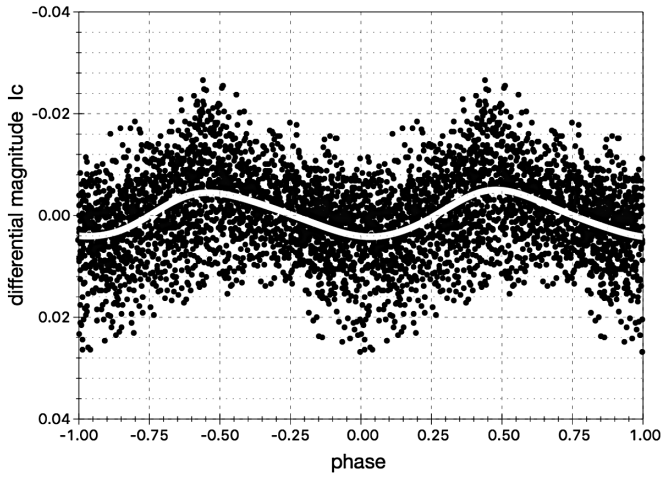

Figure 6. V1112 Persei, double phased plot with spline interpolated fit.

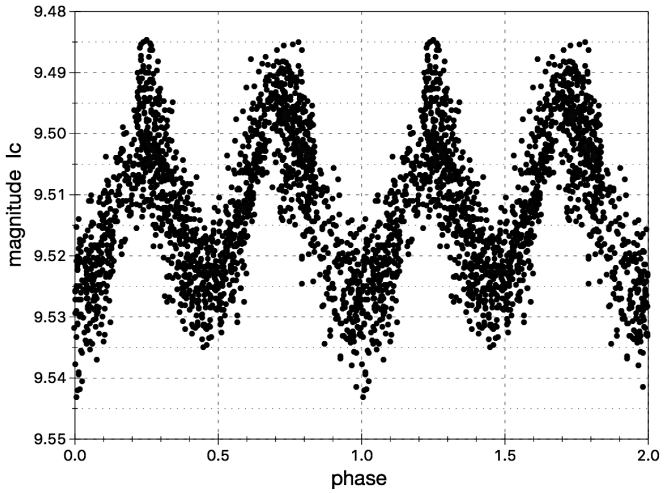

Figure 7. Variable field star BD+43 984.

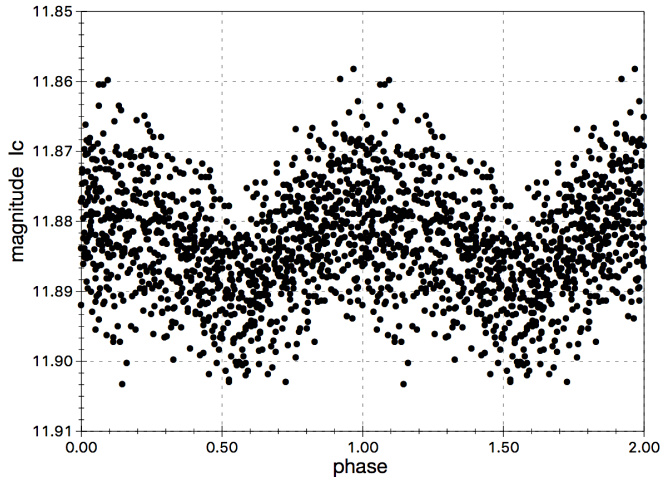

Figure 8. Variable field star GSC 02891-02799.

7. Acknowledgements

The author wishes to thank Sebastián Otero, AAVSO, and James A. DeYoung for many valuable discussions. Special thanks to the AAVSO for providing photometric standards from the AAVSO Comparison Star Database via its Variable Star Plotter utility.

References

Banerjee, D., Shahbandeh, M., Woodward, C., Evans, A., Hsiao, E., and Joshi, V. 2020, *Astron. Telegram*, No. 14256.
Lucy, L. 1968, *Astrophys. J.*, **153**, 877.
Moir, R. 1998, *Exp. Economics*, **1**, 87.
Motl, D. 2020, C-Munipack software utilities (http://c-munipack.sourceforge.net).
Munari, U., Castellani, F., Dallaporta, S., and Andreoli, V. 2020, *Astron. Telegram*, No. 14224.
Otero, S. 2021, private communication.
Paunzen, E., and Vanmunster, T. 2016, *Astron. Nachr.*, **337**, 239.
Schmidt, R. E. 2020a, *J. Amer. Assoc. Var. Star Obs.*, **48**, 13.
Schmidt, R. E. 2020b, *J. Amer. Assoc. Var. Star Obs.*, **48**, 53.
Schmidt, R. E. 2020c, *J. Amer. Assoc. Var. Star Obs.*, **49**, 95.
Schmidt, R. E. 2021, *Cent. Bur. Astron. Telegrams*, No. 4906, 1.
Software Bisque. 2020, The SkyX Professional Edition (https://www.bisque.com).
Templeton, M. 2004, *J. Amer. Assoc. Var. Star Obs.*, **32**, 41.
Thomson, D. J. 1982, *Proc. IEEE*, **70**, 1055.
Ueda, S. 2020, *Cent. Bur. Astron. Telegrams*, CBAT Transient Object Followup Reports, TCP J04291884+4354232, 2020 11 25.807.
United States Naval Observatory. 2020, *The Washington Double Star Catalog (http://www.astro.gsu.edu/wds).*

Recent Maxima of 79 Short Period Pulsating Stars

Gerard Samolyk
P. O. Box 20677, Greenfield, WI 53220; gsamolyk@wi.rr.com

Received February 8, 2021; accepted February 8, 2021

Abstract This paper contains times of maxima for 79 short period pulsating stars (primarily RR Lyrae and δ Scuti stars). They represent the CCD observations received by the AAVSO Short Period Pulsator (SPP) Section in 2020.

1. Recent observations

Table 1 contains times of maxima calculated from CCD observations made by participants in the AAVSO's Short Period Pulsator (SPP) Section. This list will be web-archived and made available through the AAVSO ftp site at:

ftp:ftp.aavso.org/public/datasets/gsamj491spp79.txt.

The error estimate is included. RR Lyr stars in this list, along with data from earlier AAVSO publications, are included in the GEOS database at:

http://rr-lyr.ast.obs-mip.fr/dbrr/dbrr-V1.0_0.php.

This database does not include δ Scuti stars. The observations were reduced by the writer using the PERANSO program (Vanmunster 2007). In the table, "TG" in the Filter (F) column indicates DSLR green band; "C" indicates a clear filter.

The linear elements in the *General Catalogue of Variable Stars* (Kholopov *et al.* 1985) were used to compute the O–C values for most stars. For a few exceptions where the GCVS elements are missing or are in significant error, light elements from another source are used: V799 Aur (AAVSO VSX site (Watson *et al.* 2014)); VY CrB (Antipin 1996); RZ Cap and DG Hya (Samolyk 2010); V2416 Cyg (Samolyk 2018); GO Hya (GEOS 2020); and GW UMa (Hintz *et al.* 2005).

References

Antipin, S. V. 1996, *Inf. Bull. Var. Stars*, No. 4343, 1.
Groupe Européen d'Observation Stellaire (GEOS) 2020, GEOS RR Lyr Database (http://rr-lyr.irap.omp.eu/dbrr/index.php).
Hintz, E. G., Bush, T. C., and Rose, M. B. 2005, *Astron. J.*, **130**, 2876.
Kholopov, P. N., *et al.* 1985, *General Catalogue of Variable Stars*, 4th ed., Moscow.
Samolyk, G. 2010, *J. Amer. Assoc. Var. Stars*, **38**, 12.
Samolyk, G. 2018, . *Amer. Assoc. Var. Stars*, **46**, 70.
Vanmunster, T. 2007, PERANSO period analysis software (http://www.peranso.com).
Watson, C., Henden, A. A., and Price, C. A. 2014, AAVSO International Variable Star Index VSX (Watson+, 2005–2020; https://www.aavso.org/vsx).

Table 1. Maxima of stars from data submitted to the AAVSO SPP Section in 2020.

Star	*JD (max) Hel. 2400000 +*	*Cycle*	*O–C (day)*	*F*	*Observer*	*Error (day)*	*Star*	*JD (max) Hel. 2400000 +*	*Cycle*	*O–C (day)*	*F*	*Observer*	*Error (day)*
SW And	59075.8391	92574	–0.5306	V	G. Samolyk	0.0009	AA Aqr	59156.5710	63079	–0.1926	V	G. Samolyk	0.0019
SW And	59114.7595	92662	–0.5308	V	K. Menzies	0.0015	BO Aqr	59085.7725	25164	0.2364	V	G. Samolyk	0.0019
SW And	59125.8167	92687	–0.5305	V	K. Menzies	0.0009	BR Aqr	59157.6395	44662	–0.2371	V	G. Samolyk	0.0009
SW And	59209.4011	92876	–0.5370	V	T. Arranz	0.0010	CY Aqr	59127.6091	406616	0.0169	V	G. Samolyk	0.0004
SW And	59210.2863	92878	–0.5363	V	T. Arranz	0.0009	CY Aqr	59127.6700	406617	0.0168	V	G. Samolyk	0.0004
XX And	59073.8592	27653	0.2952	V	G. Samolyk	0.0016	CY Aqr	59127.7310	406618	0.0167	V	G. Samolyk	0.0003
XX And	59125.8960	27725	0.2942	V	K. Menzies	0.0012	CY Aqr	59127.7921	406619	0.0168	V	G. Samolyk	0.0004
AC And	59091.7527	14891	0.5249	V	G. Samolyk	0.0009	CY Aqr	59130.6003	406665	0.0172	V	G. Samolyk	0.0004
AC And	59096.6546	14898	0.4481	V	G. Samolyk	0.0033	CY Aqr	59130.6610	406666	0.0169	V	G. Samolyk	0.0003
AC And	59171.3488	15003	0.4621	V	T. Arranz	0.0047	CY Aqr	59130.7219	406667	0.0168	V	G. Samolyk	0.0003
AC And	59176.3445	15010	0.4791	V	T. Arranz	0.0009	CY Aqr	59130.7831	406668	0.0169	V	G. Samolyk	0.0004
AC And	59186.3507	15024	0.5279	V	T. Arranz	0.0014	CY Aqr	59152.2690	407020	0.0173	V	T. Arranz	0.0005
AC And	59196.2820	15038	0.5019	V	T. Arranz	0.0015	CY Aqr	59152.3295	407021	0.0168	V	T. Arranz	0.0003
AC And	59208.3633	15055	0.4921	V	T. Arranz	0.0009	CY Aqr	59152.3906	407022	0.0169	V	T. Arranz	0.0003
AT And	59111.7804	27181	0.0001	V	G. Samolyk	0.0024	CY Aqr	59152.4522	407023	0.0174	V	T. Arranz	0.0006
AT And	59170.3787	27276	–0.0085	V	T. Arranz	0.0017	DN Aqr	59165.5624	48505	0.0446	V	G. Samolyk	0.0021
AT And	59210.4784	27341	–0.0083	V	K. Menzies	0.0021	TZ Aur	58894.4397	99552	0.0160	V	T. Arranz	0.0009
GM And	59112.6331	47359	0.0473	V	K. Menzies	0.0018	TZ Aur	59156.8625	100222	0.0168	V	G. Samolyk	0.0007
SW Aqr	59068.8183	73963	0.0001	V	G. Samolyk	0.0008	TZ Aur	59193.6799	100316	0.0169	TG	G. Conrad	0.0009
SW Aqr	59089.4872	74008	0.0004	V	T. Arranz	0.0007	TZ Aur	59200.7303	100334	0.0171	TG	G. Conrad	0.0009
SW Aqr	59138.6329	74115	0.0006	V	G. Samolyk	0.0009	BH Aur	58856.6381	35311	0.0092	V	G. Samolyk	0.0011
TZ Aqr	59081.7948	37698	0.0121	V	G. Samolyk	0.0019	BH Aur	58885.3683	35374	0.0057	V	T. Arranz	0.0012
YZ Aqr	59130.7033	43060	0.0867	V	G. Samolyk	0.0021	BH Aur	58913.6513	35436	0.0111	V	R. Sabo	0.0011

Table continued on following pages

Table 1. Maxima of stars from data submitted to the AAVSO SPP Section in 2020, cont.

Star	JD (max) Hel. 2400000 +	Cycle	O–C (day)	F	Observer	Error (day)
BH Aur	58923.6835	35458	0.0094	TG	G. Conrad	0.0017
BH Aur	59123.9070	35897	0.0094	V	K. Menzies	0.0012
BH Aur	59167.6933	35993	0.0111	V	G. Samolyk	0.0008
BH Aur	59188.6713	36039	0.0090	TG	G. Conrad	0.0016
V799 Aur	58561.3942	57296	0.0057	V	T. Arranz	0.0008
V799 Aur	58883.3631	61527	0.0051	V	T. Arranz	0.0006
V799 Aur	58883.4394	61528	0.0052	V	T. Arranz	0.0007
V799 Aur	58900.3331	61750	0.0053	V	T. Arranz	0.0006
V799 Aur	58900.4095	61751	0.0055	V	T. Arranz	0.0006
V799 Aur	59192.6258	65591	0.0066	TG	G. Conrad	0.0008
V799 Aur	59192.7015	65592	0.0062	TG	G. Conrad	0.0007
V799 Aur	59192.7773	65593	0.0059	TG	G. Conrad	0.0007
RS Boo	58944.6597	45514	–0.0357	I	G. Samolyk	0.0011
RS Boo	58964.6575	45567	–0.0369	TG	G. Conrad	0.0018
RS Boo	58988.4323	45630	–0.0344	V	T. Arranz	0.0007
RS Boo	58990.6993	45636	–0.0315	TG	G. Conrad	0.0011
RS Boo	58994.4691	45646	–0.0351	V	T. Arranz	0.0007
RS Boo	58997.4880	45654	–0.0349	V	T. Arranz	0.0007
RS Boo	59020.5108	45715	–0.0298	V	T. Arranz	0.0009
ST Boo	58942.8406	63895	0.0911	TG	G. Conrad	0.0015
ST Boo	58994.4948	63978	0.0952	V	T. Arranz	0.0016
ST Boo	58999.4760	63986	0.0981	V	T. Arranz	0.0018
ST Boo	59027.4764	64031	0.0954	V	T. Arranz	0.0015
ST Boo	59032.4566	64039	0.0973	V	T. Arranz	0.0014
ST Boo	59050.5029	64068	0.0972	V	T. Arranz	0.0014
SW Boo	58915.8827	31828	0.5503	V	G. Samolyk	0.0011
SW Boo	58975.4554	31944	0.5538	V	T. Arranz	0.0009
SW Boo	58983.6728	31960	0.5548	TG	G. Conrad	0.0017
SW Boo	58993.4312	31979	0.5561	V	T. Arranz	0.0009
SZ Boo	58915.8489	59821	0.0146	V	G. Samolyk	0.0013
SZ Boo	58981.7252	59947	0.0156	V	G. Samolyk	0.0011
SZ Boo	58987.4741	59958	0.0135	V	T. Arranz	0.0013
TV Boo	58936.7676	109826	0.1083	V	K. Menzies	0.0009
TV Boo	58986.4607	109985	0.1045	V	T. Arranz	0.0009
TV Boo	58987.3990	109988	0.1051	V	T. Arranz	0.0011
TV Boo	58991.4936	110001	0.1364	V	T. Arranz	0.0011
TV Boo	58992.4252	110004	0.1304	V	T. Arranz	0.0014
TV Boo	58996.4628	110017	0.1047	V	T. Arranz	0.0011
TV Boo	58997.3997	110020	0.1039	V	T. Arranz	0.0009
TV Boo	59006.4659	110049	0.1059	V	T. Arranz	0.0007
TV Boo	59013.6601	110072	0.1112	V	K. Menzies	0.0041
TV Boo	59022.4283	110100	0.1278	V	T. Arranz	0.0017
TV Boo	59026.4714	110113	0.1076	V	T. Arranz	0.0009
TV Boo	59036.4703	110145	0.1046	V	T. Arranz	0.0015
TV Boo	59047.4217	110180	0.1164	V	T. Arranz	0.0028
TW Boo	58945.7114	60222	–0.1102	V	G. Samolyk	0.0012
TW Boo	58999.4772	60323	–0.1040	V	T. Arranz	0.0009
TW Boo	59023.4241	60368	–0.1094	V	T. Arranz	0.0009
UU Boo	58908.8592	49952	0.3564	V	G. Samolyk	0.0009
UU Boo	59019.4388	50194	0.3612	V	T. Arranz	0.0009
UU Boo	59035.4317	50229	0.3619	V	T. Arranz	0.0008
UY Boo	58915.8160	26242	0.8706	V	G. Samolyk	0.0017
UY Boo	58998.4545	26369	0.8528	V	T. Arranz	0.0009
UY Boo	59001.7119	26374	0.8560	V	G. Samolyk	0.0012
UY Cam	58854.7074	87213	–0.0952	V	G. Samolyk	0.0022
UY Cam	58871.7990	87277	–0.0943	V	K. Menzies	0.0017
UY Cam	58904.6461	87400	–0.0934	TG	G. Conrad	0.0029
UY Cam	58908.6460	87415	–0.0992	V	G. Samolyk	0.0029
UY Cam	59157.8005	88348	–0.0952	V	G. Samolyk	0.0027
UY Cam	59190.9140	88472	–0.0949	V	K. Menzies	0.0021
RW Cnc	58895.6683	35342	0.2472	V	G. Samolyk	0.0016
RW Cnc	59182.9456	35867	0.2451	V	G. Samolyk	0.0016
TT Cnc	58901.7636	33645	0.1415	V	G. Samolyk	0.0009
TT Cnc	59182.9175	34144	0.1342	V	G. Samolyk	0.0011
VZ Cnc	57807.6531	100414	0.0155	V	N. Simmons	0.0013
VZ Cnc	57815.6905	100459	0.0266	V	N. Simmons	0.0014
RV Cap	59050.8087	56210	–0.1441	V	G. Samolyk	0.0016
RZ Cap	59073.7416	19174	0.0018	V	G. Samolyk	0.0013
VW Cap	59054.7945	107061	0.2046	V	G. Samolyk	0.0019
YZ Cap	59133.5764	56330	0.0420	V	G. Samolyk	0.0019
RR Cet	59111.8079	46888	0.0205	V	G. Samolyk	0.0009
RR Cet	59213.5660	47072	0.0214	V	K. Menzies	0.0013
RU Cet	59159.7105	32976	0.1302	V	G. Samolyk	0.0015
RV Cet	58865.5602	31684	0.2965	V	G. Samolyk	0.0021
RV Cet	59181.6318	32191	0.3028	V	G. Samolyk	0.0026
RZ Cet	59150.7592	49439	–0.2172	V	G. Samolyk	0.0015
RZ Cet	59193.6464	49523	–0.2213	V	G. Samolyk	0.0013
TY Cet	59182.7133	23961	–0.0232	V	G. Samolyk	0.0019
UU Cet	59155.6629	29612	–0.1837	V	G. Samolyk	0.0031
VY CrB	59017.6675	37242	–0.1871	V	K. Menzies	0.0008
XX Cyg	59012.7391	107940	0.0043	V	G. Samolyk	0.0005
XX Cyg	59012.8736	107941	0.0039	V	G. Samolyk	0.0008
XX Cyg	59050.6360	108221	0.0041	V	G. Samolyk	0.0006
XX Cyg	59050.7708	108222	0.0040	V	G. Samolyk	0.0005
XZ Cyg	59017.7162	31918	–2.8544	V	G. Samolyk	0.0006
XZ Cyg	59044.7862	31976	–2.8530	V	G. Samolyk	0.0013
XZ Cyg	59049.4509	31986	–2.8553	V	T. Arranz	0.0007
XZ Cyg	59055.5209	31999	–2.8524	V	T. Arranz	0.0005
XZ Cyg	59056.4546	32001	–2.8521	V	T. Arranz	0.0006
XZ Cyg	59057.3870	32003	–2.8531	V	T. Arranz	0.0006
XZ Cyg	59062.5190	32014	–2.8548	V	T. Arranz	0.0006
XZ Cyg	59063.4506	32016	–2.8566	V	T. Arranz	0.0007
XZ Cyg	59066.7142	32023	–2.8599	V	G. Samolyk	0.0009
XZ Cyg	59069.5092	32029	–2.8651	V	T. Arranz	0.0006
XZ Cyg	59070.4421	32031	–2.8656	V	T. Arranz	0.0007
XZ Cyg	59071.3746	32033	–2.8665	V	T. Arranz	0.0008
XZ Cyg	59073.7071	32038	–2.8675	V	G. Samolyk	0.0008
XZ Cyg	59080.6987	32053	–2.8764	V	G. Samolyk	0.0006
XZ Cyg	59084.4331	32061	–2.8756	V	T. Arranz	0.0008
XZ Cyg	59091.4361	32076	–2.8731	V	T. Arranz	0.0009
XZ Cyg	59092.3700	32078	–2.8726	V	T. Arranz	0.0007
XZ Cyg	59119.4409	32136	–2.8703	V	T. Arranz	0.0007
XZ Cyg	59120.3741	32138	–2.8705	V	T. Arranz	0.0007
DM Cyg	59039.7553	39197	0.0969	V	G. Samolyk	0.0009
DM Cyg	59088.4602	39313	0.0980	V	T. Arranz	0.0008
DM Cyg	59107.7751	39359	0.0994	V	K. Menzies	0.0015
DM Cyg	59154.3797	39470	0.0995	V	T. Arranz	0.0012
V2416 Cyg	59012.6590	96620	–0.0021	V	G. Samolyk	0.0015
V2416 Cyg	59012.7166	96621	–0.0004	V	G. Samolyk	0.0012
V2416 Cyg	59012.7746	96622	0.0017	V	G. Samolyk	0.0011
V2416 Cyg	59012.8308	96623	0.0020	V	G. Samolyk	0.0017
V2416 Cyg	59050.6095	97299	–0.0007	V	G. Samolyk	0.0019
V2416 Cyg	59050.6671	97300	0.0010	V	G. Samolyk	0.0014
V2416 Cyg	59050.7208	97301	–0.0012	V	G. Samolyk	0.0013
V2416 Cyg	59050.7788	97302	0.0009	V	G. Samolyk	0.0015
V2416 Cyg	59050.8337	97303	0.0000	V	G. Samolyk	0.0012
RW Dra	58933.7732	44153	0.2679	V	G. Samolyk	0.0011
RW Dra	58941.7349	44171	0.2571	V	G. Samolyk	0.0014
RW Dra	59007.7629	44320	0.2905	TG	G. Conrad	0.0015
RW Dra	59029.4405	44369	0.2651	V	T. Arranz	0.0009
RW Dra	59033.4372	44378	0.2756	V	T. Arranz	0.0010
RW Dra	59037.4368	44387	0.2889	V	T. Arranz	0.0009
RW Dra	59041.4340	44396	0.2999	V	T. Arranz	0.0009
RW Dra	59049.4035	44414	0.2969	V	T. Arranz	0.0006
RW Dra	59068.4096	44457	0.2575	V	T. Arranz	0.0012
XZ Dra	58955.8899	35735	–0.1044	V	G. Samolyk	0.0009
XZ Dra	58978.7749	35783	–0.0913	V	G. Samolyk	0.0012
XZ Dra	59041.6664	35915	–0.0974	V	G. Samolyk	0.0015
XZ Dra	59054.5313	35942	–0.0979	V	T. Arranz	0.0015
XZ Dra	59055.4837	35944	–0.0985	V	T. Arranz	0.0011
XZ Dra	59065.4829	35965	–0.1057	V	T. Arranz	0.0009
XZ Dra	59066.4366	35967	–0.1050	V	T. Arranz	0.0009

Table continued on next page

Table 1. Maxima of stars from data submitted to the AAVSO SPP Section in 2020, cont.

Star	*JD (max) Hel. 2400000 +*	*Cycle*	*O–C (day)*	*F*	*Observer*	*Error (day)*
XZ Dra	59067.3891	35969	–0.1055	V	T. Arranz	0.0009
XZ Dra	59087.4096	36011	–0.0979	V	T. Arranz	0.0008
XZ Dra	59108.3771	36055	–0.0962	V	T. Arranz	0.0012
RX Eri	58891.5821	63345	–0.0087	V	G. Samolyk	0.0012
RX Eri	59165.8255	63812	–0.0093	V	G. Samolyk	0.0012
SV Eri	59167.7516	33083	1.1163	V	G. Samolyk	0.0024
BB Eri	59153.8691	34382	0.3450	V	G. Samolyk	0.0022
RR Gem	58883.4891	44114	–0.6757	V	T. Arranz	0.0008
RR Gem	58893.4190	44139	–0.6786	V	T. Arranz	0.0007
RR Gem	58895.4026	44144	–0.6815	V	T. Arranz	0.0007
RR Gem	58899.3806	44154	–0.6766	V	T. Arranz	0.0007
RR Gem	58901.3649	44159	–0.6789	V	T. Arranz	0.0007
RR Gem	58903.3494	44164	–0.6809	V	T. Arranz	0.0006
RR Gem	58905.3401	44169	–0.6768	V	T. Arranz	0.0008
RR Gem	58907.3253	44174	–0.6781	V	T. Arranz	0.0007
RR Gem	58916.4591	44197	–0.6825	V	T. Arranz	0.0006
RR Gem	58918.4465	44202	–0.6816	V	T. Arranz	0.0009
RR Gem	58922.4208	44212	–0.6804	V	T. Arranz	0.0006
RR Gem	58932.3509	44237	–0.6831	V	T. Arranz	0.0006
RR Gem	58934.3424	44242	–0.6782	V	T. Arranz	0.0007
RR Gem	59167.9437	44830	–0.6955	V	G. Samolyk	0.0006
RR Gem	59181.8500	44865	–0.6951	V	G. Samolyk	0.0007
TW Her	58973.7575	93665	–0.0202	V	G. Samolyk	0.0008
TW Her	59035.6952	93820	–0.0206	V	G. Samolyk	0.0008
TW Her	59046.4847	93847	–0.0203	V	T. Arranz	0.0006
TW Her	59048.4828	93852	–0.0202	V	T. Arranz	0.0007
TW Her	59054.4768	93867	–0.0202	V	T. Arranz	0.0005
TW Her	59058.4728	93877	–0.0202	V	T. Arranz	0.0006
VX Her	58959.8056	81712	–0.1010	V	G. Samolyk	0.0008
VX Her	59027.6544	81861	–0.1027	V	K. Menzies	0.0008
VX Her	59034.4844	81876	–0.1033	V	T. Arranz	0.0008
VX Her	59047.6897	81905	–0.1038	V	G. Samolyk	0.0008
VZ Her	59001.7741	50446	0.0954	V	G. Samolyk	0.0007
AR Her	58945.7600	37216	–1.1490	V	G. Samolyk	0.0015
AR Her	58953.7433	37233	–1.1562	V	G. Samolyk	0.0014
AR Her	58978.6601	37286	–1.1509	V	G. Samolyk	0.0011
AR Her	58983.8158	37297	–1.1655	V	K. Menzies	0.0009
AR Her	58993.7451	37318	–1.1068	V	K. Menzies	0.0011
AR Her	58994.6831	37320	–1.1089	TG	G. Conrad	0.0021
AR Her	59000.7766	37333	–1.1257	V	G. Samolyk	0.0007
AR Her	59008.7454	37350	–1.1474	V	G. Samolyk	0.0014
AR Her	59017.6590	37369	–1.1643	V	G. Samolyk	0.0011
AR Her	59025.6918	37386	–1.1220	V	G. Samolyk	0.0012
AR Her	59028.5253	37392	–1.1087	V	T. Arranz	0.0012
AR Her	59029.4547	37394	–1.1193	V	T. Arranz	0.0011
AR Her	59030.3864	37396	–1.1277	V	T. Arranz	0.0008
AR Her	59036.4902	37409	–1.1343	V	T. Arranz	0.0007
AR Her	59037.4330	37411	–1.1315	V	T. Arranz	0.0008
AR Her	59044.4535	37426	–1.1614	V	T. Arranz	0.0009
AR Her	59059.5290	37458	–1.1268	V	T. Arranz	0.0006
AR Her	59068.4505	37477	–1.1359	V	T. Arranz	0.0009
AR Her	59069.3887	37479	–1.1377	V	T. Arranz	0.0007
DL Her	58959.8450	35075	0.0696	V	G. Samolyk	0.0011
DL Her	59028.4754	35191	0.0712	V	T. Arranz	0.0011
DL Her	59051.5466	35230	0.0689	V	T. Arranz	0.0018
DY Her	58957.8194	171689	–0.0355	V	G. Samolyk	0.0006
DY Her	58976.8442	171817	–0.0355	V	G. Samolyk	0.0006
DY Her	58990.8158	171911	–0.0352	TG	G. Conrad	0.0011
DY Her	59015.6365	172078	–0.0360	V	G. Samolyk	0.0006
DY Her	59015.7854	172079	–0.0357	V	G. Samolyk	0.0006
DY Her	59035.4043	172211	–0.0361	V	T. Arranz	0.0005
DY Her	59035.5541	172212	–0.0350	V	T. Arranz	0.0007
LS Her	59014.6701	134353	0.0148	V	G. Samolyk	0.0014
SZ Hya	58886.7391	33891	–0.2812	V	G. Samolyk	0.0009
SZ Hya	58893.7201	33904	–0.2843	V	G. Samolyk	0.0022
SZ Hya	58900.6653	33917	–0.3232	V	G. Samolyk	0.0018
SZ Hya	58907.6930	33930	–0.2797	V	G. Samolyk	0.0009
UU Hya	58898.7649	37070	0.0203	V	G. Samolyk	0.0012
DG Hya	58898.7971	8650	0.0327	V	G. Samolyk	0.0025
DH Hya	58891.8034	56678	0.1194	V	G. Samolyk	0.0013
GO Hya	58562.7648	6350	–0.0022	V	G. Samolyk	0.0029
GO Hya	58854.8860	6809	–0.0054	V	G. Samolyk	0.0024
GO Hya	58907.7172	6892	0.0017	V	G. Samolyk	0.0025
GO Hya	58944.6259	6950	–0.0029	V	G. Samolyk	0.0044
RR Leo	58886.8728	34464	0.1881	V	G. Samolyk	0.0007
RR Leo	58986.4004	34684	0.1892	V	T. Arranz	0.0007
SS Leo	58933.7248	27385	–0.1174	V	G. Samolyk	0.0015
ST Leo	58854.8968	64713	–0.0192	V	G. Samolyk	0.0009
TV Leo	58959.6982	32575	0.1348	V	G. Samolyk	0.0016
WW Leo	58945.6222	39916	0.0564	V	G. Samolyk	0.0018
AA Leo	58900.7852	32246	–0.1215	V	G. Samolyk	0.0013
U Lep	58895.5233	30170	0.0403	V	G. Samolyk	0.0013
SZ Lyn	58856.6861	172002	0.0406	V	G. Samolyk	0.0013
SZ Lyn	58856.8069	172003	0.0408	V	G. Samolyk	0.0006
SZ Lyn	58906.7084	172417	0.0409	TG	G. Conrad	0.0011
SZ Lyn	58906.8291	172418	0.0410	TG	G. Conrad	0.0011
SZ Lyn	59150.9056	174443	0.0343	V	G. Samolyk	0.0006
SZ Lyn	59156.9326	174493	0.0346	V	G. Samolyk	0.0008
SZ Lyn	59165.8517	174567	0.0341	V	G. Samolyk	0.0007
SZ Lyn	59185.7394	174732	0.0335	V	G. Samolyk	0.0007
SZ Lyn	59185.8602	174733	0.0338	V	G. Samolyk	0.0006
RR Lyr	59008.7789	28377	–0.6468	V	G. Samolyk	0.0011
RR Lyr	59061.4895	28470	–0.6549	V	T. Arranz	0.0008
RR Lyr	59065.4550	28477	–0.6575	V	T. Arranz	0.0009
RR Lyr	59069.4208	28484	–0.6598	V	T. Arranz	0.0008
RR Lyr	59074.5214	28493	–0.6610	V	T. Arranz	0.0009
RR Lyr	59096.6293	28532	–0.6609	V	N. Simmons	0.0022
RR Lyr	59103.4283	28544	–0.6643	V	T. Arranz	0.0008
RZ Lyr	59000.6752	34851	–0.0562	V	G. Samolyk	0.0011
RZ Lyr	59047.6945	34943	–0.0712	V	G. Samolyk	0.0009
RZ Lyr	59062.5208	34972	–0.0709	V	T. Arranz	0.0009
RZ Lyr	59091.6693	35029	–0.0632	V	G. Samolyk	0.0011
CX Lyr	58975.7692	42009	1.7665	V	K. Menzies	0.0012
AV Peg	59076.8193	39158	0.2108	V	G. Samolyk	0.0009
AV Peg	59121.7124	39273	0.2108	TG	G. Conrad	0.0005
AV Peg	59163.4839	39380	0.2122	V	T. Arranz	0.0005
BH Peg	59091.6929	30775	–0.1467	V	G. Samolyk	0.0018
BH Peg	59141.6938	30853	–0.1432	TG	G. Conrad	0.0025
DY Peg	59112.6145	200347	–0.0208	V	G. Samolyk	0.0004
DY Peg	59112.6864	200348	–0.0217	V	G. Samolyk	0.0005
DY Peg	59112.7601	200349	–0.0210	V	G. Samolyk	0.0005
DY Peg	59112.8331	200350	–0.0209	V	G. Samolyk	0.0005
DY Peg	59131.5748	200607	–0.0213	V	G. Samolyk	0.0006
DY Peg	59131.6492	200608	–0.0198	V	G. Samolyk	0.0008
DY Peg	59131.7198	200609	–0.0221	V	G. Samolyk	0.0006
DY Peg	59131.7931	200610	–0.0217	V	G. Samolyk	0.0008
DF Ser	58990.7166	66891	0.1092	V	G. Samolyk	0.0009
RV UMa	58891.8485	29518	0.1424	V	G. Samolyk	0.0009
RV UMa	58982.6508	29712	0.1411	V	G. Samolyk	0.0011
RV UMa	58991.5405	29731	0.1376	V	T. Arranz	0.0008
RV UMa	58992.4770	29733	0.1380	V	T. Arranz	0.0008
RV UMa	58993.4149	29735	0.1398	V	T. Arranz	0.0009
RV UMa	59190.9322	30157	0.1358	V	K. Menzies	0.0007
AE UMa	58886.5759	270670	0.0016	V	G. Samolyk	0.0009
AE UMa	58886.6641	270671	0.0038	V	G. Samolyk	0.0008
AE UMa	58886.7455	270672	–0.0008	V	G. Samolyk	0.0005
AE UMa	58886.8310	270673	–0.0013	V	G. Samolyk	0.0007
AE UMa	58886.9237	270674	0.0054	V	G. Samolyk	0.0008
AE UMa	58962.3590	271551	0.0037	V	T. Arranz	0.0007
AE UMa	58962.4440	271552	0.0027	V	T. Arranz	0.0004
GW UMa	58911.5650	34015	0.0021	V	G. Samolyk	0.0011
GW UMa	58911.7674	34016	0.0013	V	G. Samolyk	0.0015

Times of Minima for Eclipsing Binaries 2017–2020 from Stellar Skies Observatories and 2004–2009 SuperWasp Data Mining

Edward O. Wiley
Live Oaks Observatory, Stellar Skies LLC, Pontotoc, TX; ewiley@suddenlink.net

E. Whit Ludington
Caliche Observatory, Stellar Skies LLC, Pontotoc, TX; whit.ludington@gmail.com

Received March 18, 2021; revised May 23, 2021; accepted June 9, 2021

Abstract A total of 96 times of minima (ToMs) are reported for 68 eclipsing binary systems from our observations and 134 times of minima for 12 of these eclipsing binaries collected by SuperWasp data mining. We discuss our data mining criteria for minimum timing and remark on the value of data mining for filling in ToM histories.

1. Introduction

Prior to 2018 we compiled a number of observations of eclipsing binary minima, most taken from the AAVSO Legacy Program. We reported these data to the AAVSO, but we were interested in going a step further by compiling times of minima (ToMs) of our observations and beginning a program that concentrated on poorly observed eclipsing binaries. This paper reports the first of our combined research efforts and contains a number of eclipse timing of binary systems with few previously reported times of minima.

In addition to our own observations, we sought to increase the number of ToMs for some systems through data mining. Through the AAVSO Variable Star Index (VSX: Watson *et al.* 2006) we accessed SuperWasp data (Butters *et al.* 2010) for some poorly observed and well-observed eclipsing binaries. We developed criteria for accessing the quality of the SuperWasp data for suitability of estimating times of minima based on comparisons of previous data reported by Nelson (2020).

2. Equipment

Both observatories are part of the Stellar Skies LLC observatory consortium near Pontotoc, Texas (location: 30.98° N 98.94° W).

a. Live Oaks Observatory, Wiley (WEY). Mount: AstroPhysics Ap900 (German Equatorial). OTA: Celestron HD with focal reducer, 280 mm f/7. Detector: Moravian G21600 Mk.1 (1536 × 1024 pixels, 9-micron square pixels). Filters: B, V, I_c. Flats: Light box. Capture software: PD Capture. Field of View: 24 × 14 arcminutes.

b. Caliche Observatory, Ludington (LWHA). Mount: Bisque Paramount ME (German Equatorial). OTA: Meade SCT with focal reducer, 356 mm f/6.4. Detector: SBIG STT-1603ME (1536 × 1040 pixels; 9-micron square pixels). Filters: B, V, R_c, and I_c. Flats: Dusk Flats or Electro-luminescent Panel. Capture software: MaxIm DL Version 6. Field of View: 21.5 × 14.5 arcminutes.

3. Data reduction

We calibrated images using bias, dark, and flat frames. We performed aperture photometry using VPhot (AAVSO 2012) or LesvePhotometry (de Ponthière 2010) and data uploaded to the AAVSO International Database (AID). Times, magnitudes, and errors were saved as text and imported into Peranso 2.5 (Vanmunster 2013), where any times not already in Heliocentric Julian Dates (HJD) were converted to HJD. Minimum timing determination was performed using the Kwee-van Woerden (1956) algorithm except in a few cases where a fifth-order polynomial fit was employed as implemented in Peranso 2.5. Observed versus calculated (O–C) values were computed from light elements in Nelson (2020) who cites original sources. Times of minima and their associated errors were entered into Nelson spreadsheets (Nelson 2020) as a quality check.

To supplement our observational data, we accessed SuperWasp data through the VSX portal. We downloaded data for a number of these variables and found several where cadence and data density revealed eclipses that might be amenable to analysis. Data (HJD, magnitude, and errors) for each potential target were sorted by errors and all data with errors over 0.05 magnitude were eliminated. The data were then imported into Peranso 2.5 and visually inspected for potential minima. Each eclipse identified in the data was examined for (1) the cadence of eclipse data points, and (2) the errors associated with those data points. In short, if the eclipse appeared to be well-covered by data and the errors appeared reasonable, a ToM was calculated using the Kwee-van Woerden (1956) algorithm. This is an admittedly qualitative rather than quantitative selection criterion. Therefore, we employed an additional round of inspection using the resulting O–C calculations which, again, were based on light elements in Nelson (2020). We imported each ToM and error into Nelson spreadsheets (Nelson 2020) and examined the data relative to the least squares fit. SuperWasp ToMs exceeding the linear fits of previously reported ToMs taken from the literature were rejected. In most cases these discrepant ToMs differed from other SuperWasp ToMs taken at times close to the discrepant ToM. The reasoning for omission is that any radical difference between O–C linear fits on a short time scale was likely due to non-physical causes such as unsuitability of the eclipse for measurement. In some cases, we adjusted the cycle in order to obtain a solution that fit the existing Nelson least squares solution so as not to reject a valid ToM because the published period was old enough to cause the cycle count to be inaccurate.

4. Results and discussion

A total of 96 times of minima for 68 eclipsing binaries imaged by us is shown in Table 1. WEY and LWHA are Wiley and Ludington, respectively. Table 2 reports 134 ToMs for 12 eclipsing binaries taken from SuperWasp data ranging from May 2004 to 9 August 2009.

SuperWasp data mining has been used in adding data used in modeling binary systems (e.g., Alton 2020) and we were pleased to add data mining to our first paper reporting times of minima. We began our data mining efforts with 18 candidate systems, 12 of which contained at least two or more ToMs that met our criteria. Of the twelve systems, only two (V596 Aur, V640 Aur) had SuperWasp ToMs that did not fill a gap of at least one year with no ToM record in the Nelson spreadsheets.

5. Acknowledgements

This research makes use of a number of databases and programs of the AAVSO, Cambridge, Massachusetts, including the International Variable Star Index (VSX) database, VPhot, and WebObs. We used data from DR1 of the WASP data database (Butters *et al.* 2010) as provided by the WASP consortium and the computing and storage facilities at the CERIT Scientific Cloud, reg. no. CZ.1.05/3.2.00/08.0144, which is operated by Masaryk University, Czech Republic. We also used databases of the Centre de Données astronomiques de Strasbourg. We thank two colleagues, Kevin Alton and Gary Billings, whose informal reviews of the manuscript resulted in substantial improvements.

References

AAVSO. 2012, VPhot AAVSO photometric software (http://www.aavso.org/vphot).

Alton, K. B. 2020, *J. Amer. Assoc. Var. Star Obs.*, **48**, 40.

Butters, O. W, *et al.* 2010, *Astron. Astrophys.*, **520**, L10 (DOI: 10.1051/0004-6361/201015655).

de Ponthière, P. 2010, Lesvephotometry, automatic photometry software (http://www.dppobservatory.net).

Kwee, K. K., and van Woerden, H. 1956, *Bull. Astron. Inst. Netherlands*, **12**, 327.

Nelson, R. 2020, Bob Nelson's O–C Files (http://binaries.boulder.swri.edu/binaries/omc/).

Vanmunster, T. 2013, Peranso v.2.50 light curve and period analysis software (http://www.cbabelgium.com/peranso).

Watson, C., Henden, A. A., and Price, C. A. 2014, AAVSO International Variable Star Index VSX (Watson+, 2006–2014; https://www.aavso.org/vsx).

Table 1. Sample of 10 times of minima for 68 eclipsing binaries.*

System	*Class*	*Filter*	*HJD (+2400000)*	*Error*	*Cycle*	*O–C*	*Observer*
RT And	EA/RS	I_c	58811.6517	0.0001	27237	0.0057	LWHA
RT And	EA/RS	V	58811.6518	0.0001	27237	0.0058	LWHA
RT And	EA/RS	V	58111.6536	0.0001	26982	–0.0116	WEY
WZ And	EB	V	58108.6774	0.0001	24777	0.0791	WEY
IO Aqr	EA	V	58315.8046	0.0002	2443	–0.0619	LWHA
IO Aqr	EA	B	58315.8056	0.0002	2443	–0.0609	LWHA
V0596 AUR	EW	V	58825.6898	0.0001	14643.5	0.1040	WEY
V640 Aur	EW	V	58825.8086	0.0002	16892	–0.0338	WEY
V0644 Aur	EA/SD	V	58225.6448	0.0001	8632	0.0004	LWHA
CV Boo	EA	V	58262.6572	0.0001	14227	–0.0109	LWHA

**Whole cycles are primary eclipses, fractional cycles are secondary eclipses. Full table available at: ftp://ftp.aavso.org/public/datasheets/WileyLudington491-Table1.txt .*

Table 2. Sample of 10 times of minima for 12 eclipsing binaries observed by SuperWasp.*

System	*Class*	*HJD (+2400000)*	*Error*	*Cycle*	*O–C*
V600 And	EW	54318.5899	0.0005	7353.5	–0.0030
V600 And	EW	54321.5664	0.0007	7361	–0.0025
V600 And	EW	54337.6377	0.0003	7401.5	–0.0013
V0644 Aur	EA/SD	54050.6263	0.0002	3282.5	–0.0008
V0644 Aur	EA/SD	54070.5276	0.0004	3308	–0.0010
V0644 Aur	EA/SD	54111.5015	0.0004	3360.5	–0.0007
V0644 Aur	EA/SD	54115.4042	0.0004	3365.5	–0.0003
V0644 Aur	EA/SD	54122.4293	0.0002	3374.5	0.0008
V0644 Aur	EA/SD	54124.3801	0.0012	3377	0.0005

**Whole cycles are primary eclipses, fractional cycles are secondary eclipses. Full table available at: ftp://ftp.aavso.org/public/datasheets/WileyLudington491-Table2.txt .*

Recent Minima of 225 Eclipsing Binary Stars

Gerard Samolyk
P. O. Box 20677, Greenfield, WI 53220; gsamolyk@wi.rr.com

Received March 17, 2021; accepted March 18, 2021

Abstract This paper continues the publication of times of minima for eclipsing binary stars. Times of minima determined from observations received by the AAVSO Eclipsing Binaries Section from August 2020 through January 2021 are presented.

1. Recent observations

The accompanying list (Table 1) contains times of minima calculated from recent CCD observations made by participants in the AAVSO's eclipsing binary program. These observations were reduced by the observers or the writer using the method of Kwee and van Woerden (1956).

The linear elements in the *General Catalogue of Variable Stars* (GCVS; Kholopov *et al.* 1985) were used to compute the O–C values for most stars. For a few exceptions where the GCVS elements are missing or are in significant error, light elements from another source are used: CD Cam (Baldwin and Samolyk 2007), AC CMi (Samolyk 2008), CW Cas (Samolyk 1992), DV Cep (Frank and Lichtenknecker 1987), EF Ori (Baldwin and Samolyk 2005), GU Ori (Samolyk 1985).

The light elements used for QX And, GS Aqr, V409 Aql, V688 Aql, V889 Aql, LZ Lyr, DK Sct, and V1128 Tau are from TIDAK—TIming DAtabase at Krakow (http://www.as.up.krakow.pl/ephem/; Kreiner 2004).

The light elements used for V1261 Cas, V2553 Cyg, MZ Del, FW Lib, V502 Oph, VZ Psc and NN Vir are from (Paschke 2014.).

The light elements used for V407 Peg are from (Nelson 2014).

The light elements used for NY Boo, MY Cam, V362 Cas, and V2642 Oph are from the AAVSO VSX site (Watson *et al.* 2014).

O–C values listed in this paper can be directly compared with values published in the AAVSO *Observed Minima Timings of Eclipsing Binaries* monographs. The standard error is included when available. Column F indicates the filter used. A "TG" indicates DSLR green band; a "C" indicates a clear filter.

This list will be web-archived and made available through the AAVSO ftp site at ftp://ftp.aavso.org/public/datasets/gsamj491eb225.txt. This list, along with the eclipsing binary data from earlier AAVSO publications, is also included in the Lichtenknecker Database administrated by the Bundesdeutsche Arbeitsgemeinschaft für Veränderliche Sterne e. V. (BAV) at: http://www.bav-astro.de/LkDB/index.php?lang=en.

References

Baldwin, M. E., and Samolyk, G. 2005, *Observed Minima Timings of Eclipsing Binaries No. 10*, AAVSO, Cambridge, MA.

Baldwin, M. E., and Samolyk, G. 2007, *Observed Minima Timings of Eclipsing Binaries No. 12*, AAVSO, Cambridge, MA.

Frank, P., and Lichtenknecker, D. 1987, *BAV Mitt., No. 47, 1.*

Kholopov, P. N., *et al.* 1985, *General Catalogue of Variable Stars*, 4th ed., Moscow.

Kreiner, J. M. 2004, *Acta Astron.*, **54**, 207 (http://www.as.up.krakow.pl/ephem/).

Kwee K. K., and van Woerden, H. 1956, *Bull. Astron. Inst. Netherlands*, **12**, 327.

Nelson, R. 2014, Eclipsing Binary O–C Files (http://www.aavso.org/bob-nelsons-o-c-files).

Paschke, A. 2014, "O–C Gateway" (http://var.astro.cz/ocgate/).

Samolyk, G. 1985, *J. Amer. Assoc. Var. Star Obs.*, **14**, 12.

Samolyk, G. 1992, *J. Amer. Assoc. Var. Star Obs.*, **21**, 34.

Samolyk, G. 2008, *J. Amer. Assoc. Var. Star Obs.*, **36**, 171.

Watson, C., Henden, A. A., and Price, C. A. 2014, AAVSO International Variable Star Index VSX (Watson+, 2006–2014; http://www.aavso.org/vsx).

Table 1. Recent times of minima of stars in the AAVSO eclipsing binary program.

Star	*JD (min) Hel. 2400000 +*	*Cycle*	*O–C (day)*	*F*	*Observer*	*Standard Error (day)*
RT And	58423.5999	27478	–0.0143	C	L. Hazel	0.0004
RT And	59060.7077	28491	–0.0121	TG	G. Conrad	0.0001
RT And	59118.5692	28583	–0.0121	TG	A. Howell	0.0001
RT And	59157.5619	28645	–0.0130	V	G. Samolyk	0.0001
TW And	59114.7429	4874	–0.0680	V	L. Hazel	0.0001
TW And	59209.5662	4897	–0.0685	V	G. Samolyk	0.0004
UU And	59075.7868	11724	0.1125	V	G. Samolyk	0.0002
UU And	59233.3368	11830	0.1151	V	T. Arranz	0.0001
WZ And	59095.8241	26196	0.0876	V	G. Samolyk	0.0003
WZ And	59220.3486	26375	0.0894	V	T. Arranz	0.0001
XZ And	59130.8973	25900	0.2056	V	G. Samolyk	0.0001
XZ And	59167.5442	25927	0.2060	V	G. Samolyk	0.0001
XZ And	59186.5462	25941	0.2061	V	G. Samolyk	0.0001
AB And	59097.5416	69263.5	–0.0496	V	L. Corp	0.0002
AB And	59115.6297	69318	–0.0496	V	G. Samolyk	0.0001
AB And	59138.6965	69387.5	–0.0493	TG	G. Conrad	0.0004
AB And	59138.8617	69388	–0.0501	TG	G. Conrad	0.0001
AD And	59080.8426	20359.5	–0.0624	V	G. Samolyk	0.0003
AD And	59112.8935	20392	–0.0629	V	G. Samolyk	0.0002
AD And	59206.5789	20487	–0.0661	V	K. Menzies	0.0001
BD And	59076.8436	52094	0.0112	V	G. Samolyk	0.0002
BD And	59128.6874	52206	0.0099	TG	G. Conrad	0.0004
BD And	59161.5547	52277	0.0112	V	G. Samolyk	0.0001
BX And	59096.8302	36990	–0.1139	V	N. Simmons	0.0002
BX And	59104.7620	37003	–0.1136	V	L. Hazel	0.0003
BX And	59123.6753	37034	–0.1139	TG	G. Conrad	0.0003
BX And	59227.3937	37204	–0.1151	V	T. Arranz	0.0002
DS And	59127.6711	22746	0.0049	V	G. Samolyk	0.0003
QX And	59127.7592	16080	0.0094	V	G. Samolyk	0.0005
QX And	59131.8801	16090	0.0086	V	K. Menzies	0.0004
RY Aqr	59111.6196	9299	–0.1520	V	G. Samolyk	0.0001
RY Aqr	59129.3189	9308	–0.1521	V	T. Arranz	0.0001
CX Aqr	59130.5833	40787	0.0192	V	G. Samolyk	0.0001
CZ Aqr	59167.5609	18309	–0.0711	V	G. Samolyk	0.0001
GS Aqr	59105.4284	17658	–0.0068	V	X. Miret	0.0005
XZ Aql	59087.6825	8033	0.1805	V	G. Samolyk	0.0003
XZ Aql	59162.5490	8068	0.1757	V	L. Hazel	0.0002
KO Aql	59080.5032	6003	0.1086	V	T. Arranz	0.0001
KO Aql	59120.6005	6017	0.1092	V	L. Hazel	0.0001
KP Aql	59114.6002	5558.5	–0.0263	V	L. Hazel	0.0003
OO Aql	59076.4034	40378	0.0760	V	L. Corp	0.0002
OO Aql	59078.6838	40382.5	0.0758	V	G. Samolyk	0.0001
V342 Aql	59080.5448	5828	–0.0965	V	T. Arranz	0.0002
V343 Aql	59004.7481	16568	–0.0514	C	L. Hazel	0.0003
V343 Aql	59091.4447	16615	–0.0511	V	T. Arranz	0.0001
V343 Aql	59113.5747	16627	–0.0564	V	L. Hazel	0.0003
V343 Aql	59161.5390	16653	–0.0518	V	G. Samolyk	0.0001
V346 Aql	59012.7817	15451	–0.0170	C	L. Hazel	0.0002
V346 Aql	59032.6993	15469	–0.0139	V	L. Hazel	0.0006
V346 Aql	59102.3990	15532	–0.0151	V	T. Arranz	0.0001
V346 Aql	59104.6123	15534	–0.0145	V	L. Hazel	0.0002
V409 Aql	59105.4060	3223	–0.0228	V	T. Arranz	0.0005
V688 Aql	59075.4100	1690	–0.0076	V	T. Arranz	0.0006
V889 Aql	59075.4438	590.5	–1.6118	V	T. Arranz	0.0003
RX Ari	59150.7485	20155	0.0668	V	G. Samolyk	0.0001
SS Ari	59121.8020	49493	–0.4342	V	G. Samolyk	0.0002
SS Ari	59185.5409	49650	–0.4363	V	G. Samolyk	0.0002
SS Ari	59228.3714	49755.5	–0.4382	V	T. Arranz	0.0002
SS Ari	59243.3940	49792.5	–0.4373	V	T. Arranz	0.0002
SX Aur	59138.8363	15682	0.0231	V	G. Samolyk	0.0001
SX Aur	59161.8282	15701	0.0235	V	G. Samolyk	0.0005
TT Aur	59127.9018	28427	–0.0124	V	G. Samolyk	0.0001
AP Aur	59161.8714	29362.5	1.8241	V	G. Samolyk	0.0002
AP Aur	59244.7171	29508	1.8349	V	K. Menzies	0.0002
CL Aur	59092.8798	20995	0.1851	V	L. Hazel	0.0006
CL Aur	59138.9250	21032	0.1888	V	G. Samolyk	0.0002
CL Aur	59158.8345	21048	0.1885	V	L. Hazel	0.0002
CL Aur	59188.6992	21072	0.1885	V	G. Samolyk	0.0002
EM Aur	59193.7236	15479	–1.1399	V	G. Samolyk	0.0006
EP Aur	59129.8497	55533	0.0204	V	G. Samolyk	0.0002
EP Aur	59193.6765	55641	0.0184	V	G. Samolyk	0.0002
HP Aur	59150.7879	11522.5	0.0753	V	G. Samolyk	0.0001
HP Aur	59165.7275	11533	0.0754	V	G. Samolyk	0.0001
IM Aur	59153.7495	14943	–0.1411	V	G. Samolyk	0.0001
IM Aur	59153.7499	14943	–0.1407	V	N. Simmons	0.0003
TU Boo	59215.9133	80637.5	–0.1675	V	K. Menzies	0.0001
TY Boo	59225.9321	78025	0.0578	V	K. Menzies	0.0001
NY Boo	59086.4135	23500.5	0.0501	V	A. Beck	0.0006
Y Cam	59166.6097	4902	0.5113	V	L. Hazel	0.0002
AO Cam	59213.4234	20349.5	–0.0289	TG	G. Coates	0.0001
AO Cam	59213.5870	20350	–0.0302	TG	G. Coates	0.0001
CD Cam	59157.7558	8368.5	–0.0188	V	G. Samolyk	0.0006
MY Cam	59214.5275	3995	–0.1158	TG	G. Coates	0.0004
RT CMa	59157.9534	25146	–0.7843	V	G. Samolyk	0.0003
TZ CMa	59150.9163	16755	–0.2324	V	G. Samolyk	0.0002
TZ CMa	59242.6657	16803	–0.2324	V	G. Samolyk	0.0002
UU CMa	59167.9584	6725	–0.0598	V	G. Samolyk	0.0002
XZ CMi	59167.9505	28893	0.0059	V	G. Samolyk	0.0001
AC CMi	59161.9124	8283	0.0061	V	G. Samolyk	0.0001
AC CMi	59201.8051	8329	0.0069	V	G. Samolyk	0.0001
RW Cap	59096.7198	4844	–0.8206	V	G. Samolyk	0.0002
TY Cap	59076.4503	10034	0.1030	V	T. Arranz	0.0003
RZ Cas	59130.6351	13328	0.0768	V	G. Samolyk	0.0001
RZ Cas	59167.6874	13359	0.0764	V	N. Simmons	0.0001
RZ Cas	59185.6160	13374	0.0763	V	G. Samolyk	0.0001
RZ Cas	59222.6682	13405	0.0759	TG	G. Conrad	0.0003
TV Cas	59137.6245	8019	–0.0330	TG	A. Howell	0.0002
TV Cas	59157.5628	8030	–0.0333	V	G. Samolyk	0.0002
TW Cas	59152.5835	12003	0.0232	TG	G. Coates	0.0003
ZZ Cas	59041.7432	20590	0.0273	V	L. Hazel	0.0006
ZZ Cas	59138.7373	20668	0.0263	V	G. Samolyk	0.0001
AB Cas	58422.7158	11492	0.1394	C	L. Hazel	0.0002
AB Cas	59070.6220	11966	0.1474	V	L. Hazel	0.0006
AB Cas	59085.6571	11977	0.1469	V	G. Samolyk	0.0002
AE Cas	59068.6400	44337	0.0809	V	L. Hazel	0.0008
CW Cas	59098.6291	54777.5	–0.1341	V	G. Samolyk	0.0002
CW Cas	59151.5606	54943.5	–0.1341	V	L. Hazel	0.0006
CW Cas	59154.5875	54953	–0.1364	V	L. Hazel	0.0006
CW Cas	59154.7479	54953.5	–0.1354	V	L. Hazel	0.0002
CW Cas	59182.6468	55041	–0.1371	V	K. Menzies	0.0001
CW Cas	59222.3446	55165.5	–0.1379	V	T. Arranz	0.0001
DZ Cas	59112.6099	39086	–0.2192	V	G. Samolyk	0.0003
IR Cas	59017.7195	24466	0.0165	V	L. Hazel	0.0006
IR Cas	59171.5550	24692	0.0171	V	G. Samolyk	0.0002
IS Cas	59085.7901	16459	0.0745	V	L. Hazel	0.0006
IS Cas	59133.6692	16485	0.0743	V	G. Samolyk	0.0002
IS Cas	59181.5483	16511	0.0741	V	G. Samolyk	0.0001
IT Cas	59066.6607	7777	0.0730	V	G. Samolyk	0.0003
MM Cas	59058.7262	20421	0.1273	V	L. Hazel	0.0006
MM Cas	59130.5501	20483	0.1261	V	L. Hazel	0.0002
MM Cas	59138.6587	20490	0.1254	V	G. Samolyk	0.0001
MM Cas	59182.6821	20528	0.1269	V	G. Samolyk	0.0002
OR Cas	59081.6582	11938	–0.0359	V	L. Hazel	0.0006
OR Cas	59127.7510	11975	–0.0344	V	G. Samolyk	0.0001
OR Cas	59222.4243	12051	–0.0352	V	T. Arranz	0.0001
OR Cas	59232.3904	12059	–0.0348	V	T. Arranz	0.0001
OX Cas	59155.6476	7185	0.0848	V	G. Samolyk	0.0004
PV Cas	59066.8332	10762.5	–0.0031	V	G. Samolyk	0.0001
PV Cas	59081.6832	10771	–0.0321	V	G. Samolyk	0.0002
PV Cas	59095.6861	10779	–0.0329	TG	G. Conrad	0.0005

Table continued on following pages

Table 1. Recent times of minima of stars in the AAVSO eclipsing binary program (cont.).

Star	JD (min) Hel. 2400000 +	Cycle	O–C (day)	F	Observer	Standard Error (day)
PV Cas	59109.6903	10787	–0.0325	V	R. Sabo	0.0001
PV Cas	59159.6086	10815.5	–0.0026	V	G. Samolyk	0.0001
V362 Cas	59097.7608	7364	–0.0026	V	K. Menzies	0.0006
V364 Cas	59095.6568	16047.5	–0.0249	V	G. Samolyk	0.0002
V375 Cas	59066.8410	16577	0.2943	V	G. Samolyk	0.0002
V380 Cas	59130.7114	24671	–0.0758	V	G. Samolyk	0.0002
V1261 Cas	59232.3808	16445.5	0.0150	V	T. Arranz	0.0005
U Cep	58410.6464	5563	0.2201	C	L. Hazel	0.0002
U Cep	58420.6189	5567	0.2204	C	L. Hazel	0.0002
U Cep	59068.8269	5827	0.2360	V	G. Samolyk	0.0003
U Cep	59113.6988	5845	0.2331	V	L. Hazel	0.0002
U Cep	59128.6609	5851	0.2369	V	L. Hazel	0.0002
U Cep	59133.6432	5853	0.2331	V	N. Simmons	0.0001
U Cep	59133.6433	5853	0.2332	V	G. Samolyk	0.0002
U Cep	59148.6020	5859	0.2336	TG	A. Howell	0.0002
SU Cep	59181.5418	36450	0.0067	V	G. Samolyk	0.0002
WW Cep	59135.5870	22239	0.3616	V	G. Samolyk	0.0001
WZ Cep	59131.5874	74479.5	–0.2199	V	G. Samolyk	0.0002
XX Cep	58412.6830	5807	0.0252	C	L. Hazel	0.0002
XX Cep	59008.7067	6062	0.0307	C	L. Hazel	0.0006
XX Cep	59085.8401	6095	0.0323	V	G. Samolyk	0.0003
XX Cep	59153.6232	6124	0.0329	TG	A. Howell	0.0002
XX Cep	59188.6829	6139	0.0327	V	G. Samolyk	0.0002
XX Cep	59221.4046	6153	0.0318	V	T. Arranz	0.0005
DK Cep	59134.4401	25909	0.0282	V	T. Arranz	0.0001
DL Cep	59075.6491	15412	0.0679	V	G. Samolyk	0.0003
DL Cep	59155.5434	15461	0.0687	V	G. Samolyk	0.0003
DV Cep	59068.6604	10590	–0.0057	V	G. Samolyk	0.0003
DV Cep	59104.6815	10621	–0.0059	V	L. Hazel	0.0008
EG Cep	59153.6158	30405	0.0066	TG	G. Coates	0.0003
EK Cep	59153.6214	4551	0.0133	V	N. Simmons	0.0001
EK Cep	59153.6217	4551	0.0136	V	G. Samolyk	0.0001
GK Cep	59138.6633	21838	0.1604	V	N. Simmons	0.0002
NW Cep	59089.6463	517	–0.0149	V	L. Hazel	0.0012
TT Cet	59156.7201	54760	–0.0878	V	G. Samolyk	0.0002
TW Cet	59165.7012	52997.5	–0.0354	V	G. Samolyk	0.0002
TX Cet	59121.8396	21650	0.0139	V	G. Samolyk	0.0003
SS Com	59215.9153	82880.5	1.0062	V	K. Menzies	0.0002
U CrB	59068.6575	12259	0.1496	V	G. Samolyk	0.0004
W Crv	59237.9114	50479.5	0.0191	V	G. Samolyk	0.0003
Y Cyg	59081.5630	16563	–0.1164	V	T. Arranz	0.0003
Y Cyg	59129.5091	16579	–0.1116	V	T. Arranz	0.0002
SW Cyg	59016.6896	3750	–0.3806	V	L. Hazel	0.0002
SW Cyg	59112.7233	3771	–0.3827	V	G. Samolyk	0.0001
WW Cyg	59073.6714	5635	0.1571	V	G. Samolyk	0.0001
WW Cyg	59083.6251	5638	0.1575	V	L. Hazel	0.0006
WW Cyg	59133.3924	5653	0.1582	V	T. Arranz	0.0001
ZZ Cyg	58391.6994	21303	–0.0736	C	L. Hazel	0.0006
ZZ Cyg	58995.7930	22264	–0.0804	C	L. Hazel	0.0006
ZZ Cyg	58997.6808	22267	–0.0785	C	L. Hazel	0.0006
ZZ Cyg	59058.6566	22364	–0.0785	V	L. Hazel	0.0006
ZZ Cyg	59084.4289	22405	–0.0794	V	T. Arranz	0.0002
ZZ Cyg	59089.4568	22413	–0.0805	V	T. Arranz	0.0002
ZZ Cyg	59107.6865	22442	–0.0806	V	R. Sabo	0.0002
ZZ Cyg	59165.5188	22534	–0.0811	V	G. Samolyk	0.0001
AE Cyg	58348.6817	14200	–0.0053	C	L. Hazel	0.0006
BR Cyg	58990.7270	13096	0.0015	C	L. Hazel	0.0002
BR Cyg	59022.7084	13120	0.0014	V	L. Hazel	0.0002
BR Cyg	59098.6648	13177	0.0016	V	M. Durkin	0.0003
BR Cyg	59134.6443	13204	0.0019	TG	A. Howell	0.0001
CG Cyg	59081.4588	31144	0.0814	V	T. Arranz	0.0001
CG Cyg	59156.5649	31263	0.0817	V	G. Samolyk	0.0001
DK Cyg	59127.6078	44887	0.1373	V	G. Samolyk	0.0001
KV Cyg	59087.6769	10433	0.0677	V	G. Samolyk	0.0006
V346 Cyg	59081.6644	8528	0.2055	V	G. Samolyk	0.0002
V387 Cyg	59082.5913	48544	0.0187	V	K. Menzies	0.0001
V387 Cyg	59086.4352	48550	0.0190	V	T. Arranz	0.0002
V387 Cyg	59098.6064	48569	0.0188	V	G. Samolyk	0.0001
V387 Cyg	59182.5238	48700	0.0181	V	G. Samolyk	0.0001
V388 Cyg	59068.6549	19924	–0.1396	V	G. Samolyk	0.0001
V388 Cyg	59082.3993	19940	–0.1398	V	T. Arranz	0.0002
V388 Cyg	59088.4132	19947	–0.1391	V	T. Arranz	0.0001
V388 Cyg	59098.7212	19959	–0.1396	V	K. Menzies	0.0002
V388 Cyg	59137.3788	20004	–0.1386	V	T. Arranz	0.0001
V388 Cyg	59154.5599	20024	–0.1383	TG	A. Howell	0.0003
V401 Cyg	59098.5960	26193	0.0997	V	K. Menzies	0.0001
V443 Cyg	58991.7803	38134	0.0387	C	L. Hazel	0.0002
V443 Cyg	58996.7668	38140	0.0386	C	L. Hazel	0.0008
V445 Cyg	59081.7152	9721	0.3401	V	L. Hazel	0.0006
V445 Cyg	59085.5948	9723	0.3242	V	L. Hazel	0.0008
V445 Cyg	59118.7119	9740	0.3298	V	L. Hazel	0.0006
V456 Cyg	58991.7976	15799.5	0.0534	C	L. Hazel	0.0006
V456 Cyg	59095.6218	15916	0.0537	V	G. Samolyk	0.0002
V456 Cyg	59122.3575	15946	0.0537	V	T. Arranz	0.0001
V456 Cyg	59144.6379	15971	0.0543	TG	G. Conrad	0.0004
V466 Cyg	59076.4484	21775.5	0.0077	V	T. Arranz	0.0001
V477 Cyg	59193.5301	6393	–0.0447	V	G. Samolyk	0.0002
V687 Cyg	59045.7325	8278	–0.0030	V	L. Hazel	0.0006
V704 Cyg	59068.6235	37023	0.0403	V	G. Samolyk	0.0002
V704 Cyg	59092.5925	37065	0.0397	V	K. Menzies	0.0003
V704 Cyg	59103.4355	37084	0.0394	V	T. Arranz	0.0001
V836 Cyg	59087.4452	21784	0.0235	V	T. Arranz	0.0001
V836 Cyg	59102.4742	21807	0.0241	V	T. Arranz	0.0003
V836 Cyg	59140.3721	21865	0.0241	V	T. Arranz	0.0001
V995 Cyg	58981.8123	9175	0.7392	C	L. Hazel	0.0012
V1034 Cyg	59153.5810	16598	0.0213	V	G. Samolyk	0.0003
V2553 Cyg	59113.5586	4528	–0.0014	V	K. Menzies	0.0002
W Del	59039.6968	3269	0.0064	V	L. Hazel	0.0002
W Del	59087.7601	3279	0.0087	V	G. Samolyk	0.0003
TT Del	59171.5599	4855	–0.1418	V	G. Samolyk	0.0005
TY Del	59076.6639	13531	0.0810	V	G. Samolyk	0.0001
TY Del	59118.3536	13566	0.0812	V	T. Arranz	0.0001
YY Del	59068.8138	20312	0.0130	V	G. Samolyk	0.0002
YY Del	59085.4705	20333	0.0148	V	T. Arranz	0.0002
YY Del	59165.5708	20434	0.0128	V	G. Samolyk	0.0001
FZ Del	59025.7446	35369	–0.0308	V	L. Hazel	0.0002
FZ Del	59077.4361	35435	–0.0314	V	T. Arranz	0.0001
FZ Del	59156.5414	35536	–0.0306	V	G. Samolyk	0.0001
MZ Del	59076.3995	14426.5	–0.0511	V	L. Corp	0.0008
RZ Dra	59067.4743	27029.5	0.0754	V	T. Arranz	0.0002
RZ Dra	59086.4769	27064	0.0729	V	T. Arranz	0.0001
UZ Dra	59070.4348	5366	0.0031	V	T. Arranz	0.0001
TZ Eri	59163.8078	6427	0.3631	V	L. Hazel	0.0002
TZ Eri	59226.3604	6451	0.3701	V	T. Arranz	0.0001
YY Eri	59130.8742	54586	0.1705	V	G. Samolyk	0.0001
YY Eri	59175.5616	54725	0.1703	V	L. Corp	0.0002
YY Eri	59210.4448	54833.5	0.1714	V	T. Arranz	0.0003
YY Eri	59237.6107	54918	0.1709	V	G. Samolyk	0.0001
RW Gem	58436.8126	14006	0.0038	C	L. Hazel	0.0006
SX Gem	59181.8574	29374	–0.0576	V	G. Samolyk	0.0001
WW Gem	59215.8029	26847	0.0340	V	K. Menzies	0.0002
AL Gem	59137.8808	23584	0.1069	V	K. Menzies	0.0002
AL Gem	59201.8831	23630	0.1076	V	G. Samolyk	0.0002
AL Gem	59215.7961	23640	0.1073	V	K. Menzies	0.0001
RX Her	59080.6406	14568	–0.0001	V	N. Simmons	0.0001
TT Her	59075.6590	20919	0.0445	V	G. Samolyk	0.0001
UX Her	59096.6446	12541	0.1646	V	G. Samolyk	0.0001
SW Lac	59047.8366	42942.5	–0.0683	V	G. Samolyk	0.0002
SW Lac	59097.3879	43097	–0.0684	V	L. Corp	0.0003
SW Lac	59097.5470	43097.5	–0.0697	V	L. Corp	0.0002

Table continued on following pages

Table 1. Recent times of minima of stars in the AAVSO eclipsing binary program (cont.).

Star	*JD (min) Hel. 2400000 +*	*Cycle*	*O–C (day)*	*F*	*Observer*	*Standard Error (day)*	*Star*	*JD (min) Hel. 2400000 +*	*Cycle*	*O–C (day)*	*F*	*Observer*	*Standard Error (day)*
SW Lac	59115.6674	43154	–0.0700	V	G. Samolyk	0.0001	BG Peg	59091.6856	6945	–2.4728	V	G. Samolyk	0.0004
SW Lac	59135.3897	43215.5	–0.0721	V	T. Arranz	0.0001	BX Peg	59118.6712	53218	–0.1400	V	G. Samolyk	0.0001
SW Lac	59135.5513	43216	–0.0708	V	T. Arranz	0.0001	BX Peg	59159.6114	53364	–0.1413	V	G. Samolyk	0.0001
SW Lac	59190.5527	43387.5	–0.0730	V	K. Menzies	0.0001	DI Peg	59091.8796	19521	0.0158	V	G. Samolyk	0.0001
TW Lac	59163.5996	5815	0.4852	V	L. Hazel	0.0002	DI Peg	59099.7097	19532	0.0160	V	L. Hazel	0.0002
VX Lac	59092.6669	12875	0.0881	V	L. Hazel	0.0002	DI Peg	59186.5517	19654	0.0163	V	G. Samolyk	0.0001
VX Lac	59135.6472	12915	0.0886	V	G. Samolyk	0.0001	EU Peg	59082.5119	34808	0.0508	V	X. Miret	0.0003
AW Lac	59068.8066	28389	0.2216	V	G. Samolyk	0.0001	EU Peg	59095.4928	34826	0.0516	V	D. Cejudo	0.0001
CM Lac	58423.7080	19566	–0.0038	C	L. Hazel	0.0006	EU Peg	59120.0087	34860	0.0497	V	D. Cejudo	0.0002
CM Lac	59131.3770	20007	–0.0038	V	T. Arranz	0.0001	EU Peg	59120.3725	34860.5	0.0529	V	D. Cejudo	0.0004
CM Lac	59150.6333	20019	–0.0038	V	N. Simmons	0.0001	GP Peg	59150.6135	18360	–0.0591	V	G. Samolyk	0.0001
CO Lac	59080.6823	20455.5	–0.0160	V	G. Samolyk	0.0002	GP Peg	59151.5898	18361	–0.0585	TG	A. Howell	0.0003
CO Lac	59132.3735	20489	0.0112	V	T. Arranz	0.0001	GP Peg	59193.5407	18404	–0.0591	V	G. Samolyk	0.0001
CO Lac	59185.5522	20523.5	–0.0162	V	G. Samolyk	0.0001	KW Peg	59118.7618	13425	0.2391	V	G. Samolyk	0.0005
DG Lac	59076.6817	6602	–0.2428	V	G. Samolyk	0.0002	KW Peg	59159.5807	13475	0.2388	V	G. Samolyk	0.0004
DG Lac	59118.6031	6621	–0.2455	V	L. Hazel	0.0002	V407 Peg	59175.3876	3525	0.0028	V	L. Corp	0.0008
XY Leo	59182.9332	49660	0.1905	V	K. Menzies	0.0004	Z Per	58406.7623	4171	–0.3375	C	L. Hazel	0.0002
XZ Leo	59182.9250	29027	0.0803	V	K. Menzies	0.0008	Z Per	59112.7359	4402	–0.3708	V	G. Samolyk	0.0001
RS Lep	58941.6373	17656	–0.0418	V	S. Cook	0.0009	RT Per	58352.7876	29405	0.1129	C	L. Hazel	0.0002
FW Lib	59041.7538	1138	0.0875	V	S. Cook	0.0005	RT Per	59130.8434	30321	0.1180	V	G. Samolyk	0.0001
RY Lyn	59181.7115	11355	–0.0202	V	G. Samolyk	0.0003	RT Per	59165.6692	30362	0.1184	V	G. Samolyk	0.0001
RV Lyr	59083.7306	3767	–0.3221	V	L. Hazel	0.0008	RT Per	59245.5135	30456	0.1191	V	K. Menzies	0.0001
TT Lyr	59076.7931	3904	0.0185	V	S. Cook	0.0011	RV Per	59182.7563	8683	0.0077	V	G. Samolyk	0.0001
BV Lyr	59116.5905	14339	0.0370	V	L. Hazel	0.0006	ST Per	59131.8107	6304	0.3249	V	G. Samolyk	0.0001
EW Lyr	59092.3958	16725	0.3066	V	T. Arranz	0.0001	ST Per	59139.7592	6307	0.3285	V	L. Hazel	0.0006
FL Lyr	59077.3773	9575	–0.0036	V	T. Arranz	0.0001	ST Per	59155.6457	6313	0.3251	TG	A. Howell	0.0001
LZ Lyr	59032.8131	4054	0.0137	V	L. Hazel	0.0008	XZ Per	59087.8592	13529	–0.0762	V	L. Hazel	0.0006
V461 Lyr	59077.7790	4504	–0.9106	V	S. Cook	0.0009	XZ Per	59087.8606	13529	–0.0748	V	G. Samolyk	0.0002
Beta Lyr	59013.64	774.5	2.74	V	G. Samolyk	0.03	XZ Per	59162.7151	13594	–0.0765	V	L. Hazel	0.0002
Beta Lyr	59013.64	774.5	2.74	R	G. Samolyk	0.03	XZ Per	59207.6293	13633	–0.0761	V	R. Sabo	0.0001
Beta Lyr	59013.66	774.5	2.76	B	G. Samolyk	0.03	IQ Per	59157.7580	8527	–0.0103	V	N. Simmons	0.0002
Beta Lyr	59020.11	775	2.74	B	G. Samolyk	0.02	IT Per	59075.8313	19360	–0.0461	V	G. Samolyk	0.0003
Beta Lyr	59020.12	775	2.75	V	G. Samolyk	0.03	IT Per	59161.7168	19416	–0.0492	V	G. Samolyk	0.0005
Beta Lyr	59020.12	775	2.75	R	G. Samolyk	0.02	IU Per	59156.7220	15805	0.0043	V	G. Samolyk	0.0001
RU Mon	59182.8437	4865	–0.1549	V	G. Samolyk	0.0002	KW Per	59087.8546	17915	0.0205	V	G. Samolyk	0.0001
RW Mon	58434.8043	12987	–0.0881	C	L. Hazel	0.0006	KW Per	59116.7245	17946	0.0214	V	L. Hazel	0.0002
RW Mon	59185.8007	13381	–0.0928	V	G. Samolyk	0.0001	KW Per	59130.6915	17961	0.0195	V	L. Hazel	0.0002
AQ Mon	58941.6880	13090	–0.0844	V	S. Cook	0.0004	V432 Per	59076.8425	72165.5	0.0314	V	G. Samolyk	0.0004
BB Mon	59156.9676	44323	–0.0041	V	G. Samolyk	0.0001	V432 Per	59157.7204	72417	0.0478	V	G. Samolyk	0.0001
V502 Oph	59042.7233	23253	–0.0036	V	S. Cook	0.0006	Beta Per	59209.7474	4732	0.1500	V	G. Samolyk	0.0005
V508 Oph	59097.6261	40648	–0.0274	V	G. Samolyk	0.0003	Y Psc	59131.7223	3584	–0.0276	V	G. Samolyk	0.0002
V839 Oph	59118.5719	45648	0.3406	V	G. Samolyk	0.0001	RV Psc	59161.5480	62781	–0.0692	V	G. Samolyk	0.0002
V2642 Oph	59057.6968	1713	–0.0665	V	S. Cook	0.0017	RV Psc	59188.6935	62830	–0.0693	V	G. Samolyk	0.0002
EF Ori	59153.9006	4201	0.0101	V	G. Samolyk	0.0005	SX Psc	59135.3623	15914	0.0062	V	X. Miret	0.0004
EQ Ori	59153.8718	15873	–0.0340	V	G. Samolyk	0.0001	VZ Psc	59098.4672	58433.5	–0.0032	V	X. Miret	0.0007
ER Ori	59157.8153	41406	0.1537	V	G. Samolyk	0.0001	VZ Psc	59172.2811	58716	0.0049	V	L. Corp	0.0005
FL Ori	59127.8827	8885	0.0414	V	G. Samolyk	0.0001	GW Psc	59146.4320	18388.5	0.0320	V	X. Miret	0.0002
FR Ori	59127.9135	35402	0.0474	V	G. Samolyk	0.0001	UZ Pup	59237.7573	18398.5	–0.0108	V	G. Samolyk	0.0002
FZ Ori	59186.7289	37907	–0.0214	V	G. Samolyk	0.0002	U Sge	59046.7337	12399	0.0232	V	L. Hazel	0.0006
GU Ori	59153.9432	34172	–0.0709	V	G. Samolyk	0.0003	U Sge	59073.7805	12407	0.0251	V	G. Samolyk	0.0004
GU Ori	59223.6025	34320	–0.0724	V	K. Menzies	0.0002	V505 Sgr	59087.6721	12365	–0.1254	R	G. Samolyk	0.0003
U Peg	59076.5200	60208.5	–0.1765	V	L. Corp	0.0005	DK Sct	59080.7788	5404	0.0149	V	B. Ramey	0.0006
U Peg	59109.8757	60297.5	–0.1763	V	R. Sabo	0.0001	AO Ser	59013.7098	28294	–0.0110	C	L. Hazel	0.0006
U Peg	59150.5392	60406	–0.1766	V	G. Samolyk	0.0001	RW Tau	59159.8228	4867	–0.3041	V	G. Samolyk	0.0001
U Peg	59159.5337	60430	–0.1769	V	G. Samolyk	0.0001	RZ Tau	59135.8732	51625	0.0998	V	G. Samolyk	0.0001
U Peg	59186.5179	60502	–0.1770	V	G. Samolyk	0.0001	RZ Tau	59140.8605	51637	0.0990	V	K. Menzies	0.0001
TY Peg	59171.6028	6054	–0.4811	V	G. Samolyk	0.0003	TY Tau	59091.8856	35178	0.2788	V	G. Samolyk	0.0002
UX Peg	59076.7309	12075	0.0016	V	L. Hazel	0.0006	TY Tau	59186.6938	35266	0.2797	V	G. Samolyk	0.0001
UX Peg	59096.8097	12088	0.0004	V	G. Samolyk	0.0001	WY Tau	59159.7879	31407	0.0668	V	G. Samolyk	0.0003
UX Peg	59161.6846	12130	0.0014	V	G. Samolyk	0.0002	AC Tau	59161.7635	6619	0.2001	V	G. Samolyk	0.0002
AQ Peg	59111.6563	3224	0.5785	V	G. Samolyk	0.0002	AQ Tau	59167.7190	24272	0.5231	V	G. Samolyk	0.0003
AQ Peg	59139.3991	3229	0.5788	V	T. Arranz	0.0002	AQ Tau	59245.5356	24336	0.5219	V	K. Menzies	0.0003
BB Peg	59081.8653	42372	–0.0351	V	G. Samolyk	0.0002	EQ Tau	59096.8463	55320.5	–0.0473	V	G. Samolyk	0.0001
BB Peg	59153.6241	42570.5	–0.0344	V	G. Samolyk	0.0001	EQ Tau	59138.8311	55443.5	–0.0484	V	G. Samolyk	0.0001
BB Peg	59182.5439	42650.5	–0.0348	V	G. Samolyk	0.0001	EQ Tau	59172.7965	55543	–0.0471	V	R. Sabo	0.0006
BG Peg	59087.7830	6943	–2.4700	V	L. Hazel	0.0008	EQ Tau	59181.6704	55569	–0.0483	V	G. Samolyk	0.0003

Table continued on next page

Table 1. Recent times of minima of stars in the AAVSO eclipsing binary program (cont.).

Star	*JD (min) Hel. 2400000 +*	*Cycle*	*O–C (day)*	*F*	*Observer*	*Standard Error (day)*	*Star*	*JD (min) Hel. 2400000 +*	*Cycle*	*O–C (day)*	*F*	*Observer*	*Standard Error (day)*
EQ Tau	59194.6415	55607	–0.0484	V	K. Menzies	0.0001	Z Vul	59071.4672	6568	–0.0170	V	T. Arranz	0.0001
EQ Tau	59206.5886	55642	–0.0485	V	R. Sabo	0.0001	RR Vul	59076.6885	4760	–0.0805	V	L. Hazel	0.0006
EQ Tau	59225.5338	55697.5	–0.0482	V	K. Menzies	0.0003	RS Vul	59069.7834	5865	0.0299	V	S. Cook	0.0003
V1128 Tau	59175.4064	21859.5	–0.0059	V	L. Corp	0.0004	AW Vul	59008.8124	15777	–0.0365	C	L. Hazel	0.0006
V1128 Tau	59175.5592	21860	–0.0057	V	L. Corp	0.0002	AW Vul	59085.4256	15872	–0.0362	V	T. Arranz	0.0001
V Tri	59136.6182	59231	–0.0056	TG	A. Howell	0.0002	AX Vul	59136.5611	7054	–0.0404	V	L. Hazel	0.0002
X Tri	58409.5683	16373	–0.0985	C	L. Hazel	0.0002	AX Vul	59138.5855	7055	–0.0408	V	G. Samolyk	0.0001
X Tri	59082.8379	17066	–0.1028	V	L. Hazel	0.0002	AX Vul	59140.6100	7056	–0.0412	TG	A. Howell	0.0002
X Tri	59155.7011	17141	–0.1048	V	G. Samolyk	0.0001	AY Vul	59135.6616	6819	–0.1901	V	G. Samolyk	0.0005
X Tri	59220.3119	17207.5	–0.1011	V	T. Arranz	0.0003	BE Vul	59097.6399	12233	0.1046	V	L. Hazel	0.0002
RS Tri	59121.8465	11096	–0.0575	V	G. Samolyk	0.0001	BE Vul	59105.3994	12238	0.1039	V	T. Arranz	0.0001
RS Tri	59186.7503	11130	–0.0571	V	G. Samolyk	0.0002	BO Vul	59020.7250	11836	–0.0115	V	L. Hazel	0.0002
RV Tri	58367.7697	16366	–0.0439	C	L. Hazel	0.0002	BO Vul	59133.5866	11894	–0.0103	V	G. Samolyk	0.0001
RV Tri	59135.7541	17385	–0.0457	V	G. Samolyk	0.0001	BS Vul	59076.6501	33206	–0.0365	V	G. Samolyk	0.0001
XZ UMa	59157.8618	10627	–0.1588	V	G. Samolyk	0.0001	BS Vul	59167.5605	33397	–0.0367	V	G. Samolyk	0.0001
XZ UMa	59157.8619	10627	–0.1587	V	L. Hazel	0.0002	BT Vul	59038.7202	20712	0.0058	V	L. Hazel	0.0002
W UMi	59066.7724	14922	–0.2243	V	N. Simmons	0.0003	BT Vul	59118.6037	20782	0.0053	V	G. Samolyk	0.0002
RU UMi	59181.8745	33501	–0.0140	V	G. Samolyk	0.0001	BT Vul	59150.5588	20810	0.0068	V	G. Samolyk	0.0002
DL Vir	59007.6969	15364	0.1372	V	S. Cook	0.0007	BT Vul	59182.5120	20838	0.0064	V	G. Samolyk	0.0002
NN Vir	59036.7043	21919	0.0184	V	S. Cook	0.0009	BU Vul	59115.6197	44960	0.0114	V	G. Samolyk	0.0001
Z Vul	59029.7352	6551	–0.0151	V	L. Hazel	0.0002	CD Vul	59075.6459	18687	–0.0019	V	G. Samolyk	0.0002
Z Vul	59066.5584	6566	–0.0159	V	T. Arranz	0.0002							

Abstracts of Papers and Posters Presented at the 109th Annual Meeting of the AAVSO, Held as an "Online Only" Event, November 13–15, 2020

Types of Period Changes of W Virginis Stars

Pradip Karmakar
MAA Durga Villa, Bhatrapally Road, Nabapally, Barasat, West Bengal, India; pradipkarmakar39@gmail.com

Horace A. Smith
Department of Physics and Astronomy, Michigan State University, East Lansing, MI 48824; smith@pa.msu.edu

Wayne Osborn
118 Eagle Pointe Drive, Unit C, Delevan, WI 53115; wayne.osborn@cmich.edu

Abstract There are still unsolved problems in understanding the evolution of type II Cepheids of the W Virginis class. Period changes of W Vir variables have the potential to provide insight into that evolution. We illustrate this by showing the observed period changes of three W Vir variables in globular clusters. V2 in M10 shows a long-term decrease in period. V3 in M10 shows a small period increase. Sometimes, as with V1 in M12, irregular period changes make it hard to determine the long-term trend of the period change.

Search for Variability in 30 Bright Metallic-line A Stars Observed by the TESS Spacecraft

Joyce A. Guzik
Los Alamos National Laboratory, MS T082, Los Alamos, NM 87547; joy@lanl.gov

Abstract As part of the NASA TESS Guest Investigator Cycle 2 program, we received 2-minute cadence light curves for bright main-sequence metallic-line A (Am) stars. The Am stars show significant underabundances of calcium and scandium, and enhanced abundances of titanium and iron-group elements compared to the solar abundances. Catanzaro *et al.* (2019) used high resolution spectroscopy + Gaia parallaxes to derive a set of uniformly reduced parameters for these stars, including log g, v sin i, effective temperature, luminosity, and element abundances. While these stars lie in or near the delta Scuti pulsation instability region in the H-R diagram, they are not expected to pulsate because the diffusive element settling and radiative levitation processes responsible for their peculiar abundances should have also drained helium from the layer in the envelope that drives delta Scuti pulsations. Of the 30 stars observed by TESS, we find four delta Sct stars, two of which may be δ Sct/γ Dor hybrids. Of the remaining stars, we find one previously known eclipsing binary, and 16 showing variability of unconfirmed origin. We will show example light curve analyses for a delta Scuti star, for one of the higher amplitude variables, and for the eclipsing binary. Follow-up observations combined with stellar modeling will be needed to understand the causes for the variability.

Simultaneous Photometry on VSX Variables and TESS Exoplanet Candidates

Madelyn Madsen
madsenma@mnstate.edu

Abstract As a continuation of our software development as part of the TESS ground-based follow-up network, we have been able to produce the data products necessary for a TESS submission. Currently we are able to produce a photometry measurement table, light curve, seeing profile, a field of labeled apertures, and corresponding measurement files. We have made one successful submission to TESS, and we are now working on streamlining the analysis process for other submissions. We are also able to measure the photometry of variable stars in the field and have observed a possible new variable in the field we submitted to TESS.

The Quick and the Deadtime

Gregory Sivakoff
University of Alberta, Edmonton AB, Canada; sivakoff@ualberta.ca

Abstract In an ideal world, we could image sizescales as small as the distance between the Earth and the Moon. However, even the highest resolution astronomical imaging facililities, like the Event Horizon Telescope, could only do so out to distances less than 100 parsecs (326 light-years) from Earth. However, since light travels from the Earth to the Moon in about 1.3 seconds, rapid variability can probe small distances across the entire Universe—if your source is bright enough and you have a good setup. I will discuss recent rapid-variability results from relativistic jets launched by stellar-mass black holes that are feasting on the envelope of nearby stars. These results demonstrate the power (and pitfalls) of rapid variability (milliseconds to minutes). I will also discuss some of the equipment that astronomers are using to make such measurements—especially CMOS/sCMOS detectors whose useful features include minimized deadtime due to quick readout, low readout noise, and windowing.

Characterizing the O'Connell Effect in Kepler Eclipsing Binaries

Matthew Knote
Department of Aerospace, Physics, and Space Sciences, Florida Institute of Technology, 150 West University Boulevard, Melbourne, FL 32901; mknote2015@my.fit.edu

Abstract The O'Connell effect—the presence of unequal maxima in eclipsing binary light curves—is a poorly understood phenomenon that has been recognized for over a century. Several

ideas have been proposed to explain it, including chromospheric spots, effects of mass transfer, or circumstellar material, but the exact cause of the effect nevertheless remains unresolved. The Kepler mission observed nearly 3,000 eclipsing binaries, of which my analysis shows that over 200 show a significant O'Connell effect. Our goal is to analyze and characterize this sample of systems as a prelude to future projects looking to determine the physical cause of the phenomenon. I now present the results we have obtained thus far, such as a correlation between the O'Connell effect size and eclipse depth. I will also discuss some interesting classes of systems we have discovered, including systems with considerable temporal variation and systems with asymmetric minima that warrant further observations.

Disk Instabilities Caused the 2018 Outburst of AG Draconis

Helena M. Richie
University of Pittsburgh; helenarichie@pitt.edu

Abstract The symbiotic binary AG Draconis (AG Dra) has a well-established outburst behavior based on an extensive observational history. Usually the system undergoes a 9- to 15-year period of quiescence with a constant average energy emitted, during which the system's orbital period of ~ 550 d can be seen at shorter wavelengths (particularly in the U band), as well as a shorter period of ~ 355 d thought to be due to pulsations of the cool component. After a quiescent period, the marker of an active period is usually a major (cool) outburst of up to V = 8.4 mag, followed by a series of minor (hot) outbursts repeating at a period of approximately 1 year. However, in 2016 April after a 9-year period of quiescence, AG Dra exhibited unusual behavior: it began an active phase with a minor outburst followed by two more minor outbursts repeating at an interval of ~ 1 year. We present R-band observations of AG Dra's 2018 April minor outburst and an analysis of the outburst mechanism, and report on the system's activity levels following the time of its next expected outburst. By considering the brightening and cooling times, the scale of the outburst, and its temperature evolution, we have determined that this outburst was of disk instability in nature.

Using Bespoke 18-inch Newtonian and R = 3000 Spectrometer for High-Precision Observations

John Menke
22500 Old Hundred Road, Barnesville, MD 20838; John@menkescientific.com

Abstract It is quite possible to make high-precision spectroscopic measurements using rather modest (home-built) equipment. This paper describes a multi-year research effort on AZ Cas, a binary eclipsing variable with a 9-year period that has giant red and blue components. The next eclipse is in 2022 when previous observations show that we can expect substantial stellar interactions between the components. There are limited data on the system, including substantial uncertainty of the doppler shifts involved. Preliminary results give hope that doppler shifts can be measured to better than 0.1 Å (about 10 km/s) even with a spectrometer resolution of about 2 Å.

Morning Star: The Search for and Discovery of the Stars of Bethlehem According to the Gospel of Matthew

Rev. Kenneth Beckmann
3704 Derby Ridge Drive, Columbia, MO 65202; kcb@whatajoyfulcelebration.com

Abstract For more than two thousand years, the Star of Bethlehem has remained an enigma in the light of biblical scholarship and astronomical research. In 1984, the late Dr. Dorrit Hoffleit wrote an article in the Journal of the AAVSO, Volume 13, Number 1, entitled, "The Christmas Star, Novae and Pulsars." This article described Carolyn Murphy-Beehler's discovery of an ancient Christian star map of the Star of Bethlehem in the catacomb of Priscilla at Rome. Recently, I have discovered four clues and two keys that demonstrate that the Star on the star map in the catacomb and the Star in Matthew's Gospel may be one and the same Star. In this paper, I will demonstrate how two observations, one at the Star's rising and the other the Star at Midheaven, provide an indisputable argument that the Star of 5 BCE (the Star on the star map in the catacomb) accurately describes the Star Matthew speaks about in his gospel.

Automating a Small Urban College Observatory

Donald Smith
Deshawn Reid
Guilford College, 5800 West Friendly Avenue, Greensboro, NC 27410; dsmith4@guilford.edu, reid26856@gmail.com

Abstract We will report on our efforts to automate the operation and data processing of the 16-inch RCOS optical telescope at the Guilford College J. Donald Cline Observatory in Greesboro, North Carolina. We will briefly describe the hardware and software that comprise the instrument, and we will outline the Python scripts we have written to automate the observing schedule at night and the data reduction the next day. The final product is an ever-growing database of timestamped photometric measurements, from which can be easily extracted light curves for analysis. This fall, we have been carrying out our first oberving campaign on several variable stars indentified throught the AAVSO Target Tool as needing further observations. We will present our preliminary light curves and discuss the precision of the analysis, including the effects of the local light pollution conditions.

Researching Eclipsing Binaries "Down Under": Illustrating the Methods and Results of Variable Stars South

Thomas J. Richards
P.O. Box 323, Kangaroo Ground, VIC 3097, Australia; tomprettyhill@gmail.com

Abstract Southern skies teem with variables but there are relatively few research-oriented amateur astronomers to study them, so a centralized funded research organization is not realistic. Instead, Variable Stars Sourth (RASNZ) provides a very successful, virtual non-localized base for scattered southern variable star researchers to collaborate in a project-oriented manner without central services. This presentation illustrates that distributed but collaborative enterprise—rather different from the AAVSO model—by describing the very active work of the VSS's Southern Eclipsing Binaries Project. It shows how each observer carries out their own data analysis on their light curves, and how cloud collaboration is used to automatically combine their analyses and derive further results from them. The presentation also shows with examples how those data are used by observers as the basis for more advanced research where again, individuals collaborate rather than using a central service. The approach has proved to be very productive over the seven years of the project.

Measuring the Masses of White Dwarfs with X-rays: A NuSTAR Legacy Survey

Aarran Shaw
University of Alberta, Canada; aarrans@unr.edu

Abstract Magnetic cataclysmic variables are binary systems consisting of a white dwarf accreting matter from a normal, Sun-like star. The magnetic field of the white dwarf is strong enough to disrupt the accretion flow, forcing material along the magnetic field lines on to the poles of the dense star, where it forms an extremely hot shock just above its surface. The temperature of this shock is directly related to the white dwarf mass, and can be measured by studying the hard X-ray spectrum. This method is complimentary to optical radial velocity measurements, which depend on the (often not very well-known) binary inclination. With the 2012 launch of NASA's NuSTAR X-ray telescope, the hard X-ray spectrum has become much more accessible to astronomers. We present here the results from a NuSTAR Legacy survey of 19 magnetic cataclysmic variables, measuring their spectra and deriving the masses of their white dwarfs. We present the mass distribution and draw comparison with the masses of other classes of white dwarfs, commenting on the consequences our results may have on theories of accretion and novae in CVs.

Building Connection through Community-Based Astronomy

Todd Duncan
Erika Dunning
Pacific University, Department of Physics, 2043 College Way, Forest Grove, OR 97116; tduncan@pacificu.edu, dunn6387@pacificu.edu

Abstract Looking at the night sky can help us feel more connected to our fellow humans—perhaps because it reminds us that what we have in common is far greater than our differences. In addition, the process of doing astronomy research can help us feel more connected to the larger universe. This presentation will summarize what we've learned by combining the two: bringing astronomy research (in the form of variable star photometry) out into public spaces to invite conversation and participation from anyone who happens to walk by our portable observatory.

New Observations of the SX Phe Star XX Cygni

Richard Berry
Nolan Sottoway
Sol McClain
Address correspondence to: R. Berry, 22614 North Santiam Highway, Lyons, OR 87358; rberry@wvi.com

Abstract We report 20+ new times of maximum light of the short period pulsator XX Cygni measured during the August 2020 Pine Mountain Observatory "Virtual Astronomy Camp" for high-school students. Observations were made at a cadence of 10 seconds, producing dense light curves. We determined each time of maximum by fitting ~250 data points near the peak with a six-order polynomial. Assuming a constant period for the star, the standard error from the ephemeris is 0.00025 day = 22 seconds. We saw no evidence for early or late time-of-max during our observing campaign.

Discoveries of Variable Stars by Amateur Astronomers Using Data Mining on the Example of Eclipsing Binary Romanov V20

Filipp Romanov
Pobedy Street, House 3, Flat 30, Yuzhno-Morskoy, Nakhodka, Primorsky Krai, Russian Federation 692954; filipp.romanov.27.04.1997@gmail.com

Abstract I report my discovery of a high-amplitude Algol-type eclipsing variable star in the constellation Centaurus which was registered in the AAVSO's Variable Star Index (VSX) on December 3, 2018 under the name of Romanov V20. I describe the process of my analysis of data from VizieR catalogues to select this star as a candidate for searching for variability and to check if the variability of the star was known before. I inform how I used photometry data from several sky surveys to find variability, and how I researched these data in the software

VStar for light curve analysis and for period search. I explain about registering variable stars in VSX, and about my requesting from the AAVSO a chart with comparison star magnitudes and about my follow-up observations of the primary eclipse of this sufficiently bright star with a remote telescope in Australia. I produce photometric measurements of Romanov V20 from these images and compare them with data from sky surveys, and using this variable star as an example, I show that amateur astronomers can make astronomical discoveries and can conduct scientific research even without astronomical equipment, regardless of geographic location. Beisides this variable star, I am currently the discoverer of 70 other variable stars, which have also been registered in VSX since January 2016.

Star "Crawling" with Astronomical Binoculars

William Wink
1356 Butter Churn Road, Middletown, PA 17057; williamwink@yahoo.com

Abstract I discuss a technique to use small FOV astronomical binoculars to identify and observe variable stars using a DSLR and astrometry. Pictures of equipment are included as well as an example of an observation.

GW Lib and V386 Ser: CVs Containing Accreting, Pulsating White Dwarfs

Paul Szkody
Department of Astronomy, University of Washington, Box 351580, Seattle, WA 98195; Szkody@uw.edu

Abstract There are now 18 cataclysmic variables in which the white dwarf is known to be pulsating. This provides a unique opportunity to monitor the interior of the white dwarf when a dwarf nova outburst occurs and heats the white dwarf. Theory predicts the pulsations should stop when the white dearf moves out of its instability strip, and then resume at shorter pulsation periods which gradually grow as the white dwarf cools back to quiescence. We have tested this theory with optical and UV data on GW Lib and V386 Ser and find strange behavior in GW Lib while V386 Ser appears to follow the theory so far. AAVSO data contributed to both these projects and we encourage further monitoring until these systems return to quiescence.

109th Annual Meeting Research Posters

The Blazar BL Lacertae: 2018-2020 V-, R-, and I-Band CCD Photometry

Manny Rosales
Christina Singh
Wyatt Carbonell
Leslie F. Brown
Connecticut College, Physics and Astronomy Department, New London, CT; lfbro@conncoll.edu

Gary Walker
114 Cove Road, West Dennis, MA 02670; bailyhill14@gmail.com

Abstract We observed the gamma-ray loud AGN BL Lacertae (BL Lac; R.A. 22^h 02^m 43.290^s, Dec. +42° 16' 39.98" J2000; z = 0.0691) in the V, R, and I optical bands between July 2018 and September 2020 using the Walker telescope located at Sierra Remote Observatories. This source was active at these wavelengths during this time, and since August 2020 has been in a historically bright state. We present our three-year V, R, and I band light curves for BL Lac and compare its optical variations with this AGN's gamma-ray behavior as observed by NASA's Fermi-LAT.

Differential Photometry of Eclipsing Binary System V798 Her in Globular Cluster NGC 6341

Khola Anees
Department of Space Science, Institute of Space Technology, Pakistan

Shaukat Naaman Goderya
Tarleton State University, 137 Shadow Creek Lane, Aledo, TX 76008; sngoderya@gmail.com

Fazeel Mahmood Khan
Institute of Space Technology, Pakistan

Abstract We present the photometric study of an eclipsing binary star, V798 Her, in the globular cluster NGC 6341. The observations were obtained in Johnson B, V, and R filters using an 0.8-m Tarleton telescope and a CCD photometer. The observed light curves after the determination of light elements show that V798 Her is a W UMa contact binary system with a period of 0.2951110 day. Wilson Devinney Mathematical Model (2017 version) was used for the analysis and for obtaining the photometric solution of V798 Her.

Establishing a New ToM (Time of Minimum) for the Primary Eclipse of the Binary System WZ Ophiuchi

Mike Miller
221 Bluestem Drive, Georgetown, TX 78633; mikerph1951@gmail.com

Abstract In my research of Neglected Binary Stars I discovered that there was very little current data on the binary star WZ Oph. The Binary Star Database, AAVSO, Mt. Suhora Astronomical Observatory and the BRND Regional Network of Observers (Chez Astronomical Society) revealed the most recent observations of WZ Oph occurred in the mid 1990's. For this reason I concluded that it would be a challenging project for summer of 2018 to attempt to establish a new ToM(time of minima) for the primary eclipse of WZ Oph. The ToM for WZ Oph using my photometry data and Peranso software was determined to be 2458312.72315 JD heliocentric.

Identification of Bimodal Period and Long Secondary Period Carbon Red Giants Misclassified as "Miscellaneous" in VSX

Kristine Larsen
Geological Sciences Department, Central Connecticut State University; Larsen@ccsu.edu

Abstract In a 2015 *JAAVSO* paper, Percy and Huang applied VStar analysis software to AAVSO visual observations of known carbon red giants in order to better determine the periodicities of these stars. In particular, they sought to separate false periodicities (due to alias and spurious periods) from truly biperiodic stars with two pulsation periods as well as long secondary period (LSP) stars. Previous work by this author and her students has determined that while pulsating red giants in general have sufficient irregularities and multiple periodicities to confound automated classification algorithms, for example those of ASAS (All-Sky Automated Survey) and ASAS-SN (All-Sky Automated Survey for Supernovae), VStar analysis can often identify improved periods and lead to the proper classification of these stars' variability type. This project, motivated by the work of Percy and Huang, is a preliminary analysis of 250 spectral class C red giants with V-band variability that are classified as MISC in VSX (Variable Star Index) on the basis of their MISC classification in the "ASAS Catalogue of Variable Stars" (Pojmański 2002, *Acta Astron.*, **52**, 397). The goal is to better determine their periodicities, and in particular to identify biperiodic and LSP carbon red giants in order to improve the accuracy of their VSX citations.

Using High Resolution Spectroscopy to Measure Cepheid Pulsation

Kevin Gurney
14A Gladstone Road, Sheffield, S10 3GT, United Kingdom; k.gurney@shef.ac.uk

Abstract Using a high-resolution spectrograph like the Lhires III (Shelyak Instruments) it is possible, in principle, to measure radial velocities of the order of 1 km/s (Leadbeater, "Pushing the Limits," AAVSO/BAA joint meeting, 2018). Thus, within these bounds, it should be feasible to measure radial velocities associated with Cepheid pulsation. However, extracting this component of the Doppler shift from a multiple system in which orbital components play a role is challenging; it requires information on the orbital ephemeris which, in turn, may require substantial observational and modelling effort. Fortunately, such information is available in a recent paper by Gallenne *et al.* 2018, *Astrophys. J.* for the target described here, V1334 Cyg. Here, I show how measurements of the wavelength of the Hα line of V1334 Cyg can be used, in conjunction with this published model, to determine a putative pulsation profile of this Cepheid variable, and validate it against AAVSO-derived photometry.

NOTES